

Study of the antihydrogen atom and ion formation in the collisions antiproton-positronium

Pauline Comini

▶ **To cite this version:**

Pauline Comini. Study of the antihydrogen atom and ion formation in the collisions antiproton-positronium. Accelerator Physics [physics.acc-ph]. Université Pierre et Marie Curie - Paris VI, 2014. English. ⟨NNT : 2014PA066639⟩. ⟨tel-01150446⟩

HAL Id: tel-01150446

https://theses.hal.science/tel-01150446v1

Submitted on 11 May 2015

HAL is a multi-disciplinary open access archive for the deposit and dissemination of scientific research documents, whether they are published or not. The documents may come from teaching and research institutions in France or abroad, or from public or private research centers.

L'archive ouverte pluridisciplinaire **HAL**, est destinée au dépôt et à la diffusion de documents scientifiques de niveau recherche, publiés ou non, émanant des établissements d'enseignement et de recherche français ou étrangers, des laboratoires publics ou privés.



Distributed under a Creative Commons CC BY-NC-ND 4.0 - Attribution - Non-commercial use - No Derivative Works - International License

Université Pierre et Marie Curie

École Doctorale 517: Particules, Noyaux et Cosmos

Service de Physique des Particules du CEA–Saclay

Étude de la formation d'antihydrogène neutre et ionisé dans les collisions antiproton–positronium

Study of the antihydrogen atom and ion formation in the collisions antiproton–positronium

Par Pauline Comini

Thèse de doctorat de Physique

Dirigée par Yves Sacquin
et co-encadrée par Paul-Antoine Hervieux et François Nez

présentée et soutenue publiquement le 23 Octobre 2014

devant un jury composé de

M. Bertrand Laforge, LPNHE, Paris ..... Président du jury
M. Lamri Adoui, CIMAP, Caen ..... Rapporteur
M. Pierre Vanhove, CEA-IPhT, Saclay ..... Rapporteur
M. Jaume Carbonell, IPN, Orsay ..... Examinateur
M. Yasunori Yamazaki, RIKEN, Wako ..... Examinateur
M. Yves Sacquin, CEA-IRFU, Saclay ..... Directeur de thèse
M. Paul-Antoine Hervieux, IPCMS, Strasbourg ..... Invité
M. François Nez, LKB, Paris ..... Invité

Except where otherwise noted, this work is licensed under
http://creativecommons.org/licenses/by-nc-nd/3.0/

Remerciements

Voici quelques ultimes mots en français pour remercier chaleureusement les personnes qui, continuellement ou ponctuellement, m'ont apporté conseils, soutien, aide et énergie tout au long de cette thèse, voire même lors de ses prémisses pendant le stage de deuxième année de Master.

Mes premiers remerciements vont bien évidemment à mon directeur de thèse Yves Sacquin, qui s'est retrouvé, comme moi, embarqué sur un sujet éloigné de ses premières qualifications. Merci pour sa bienveillante supervision, ses truculentes anecdotes scientifiques, ses régulières sollicitations et sa traque féroce des "*permit*" récalcitrants lors des relectures.

Un immense merci ceux que je qualifierais de co-directeurs, tant leur rôle fut prépondérant dans l'encadrement de cette thèse : Paul-Antoine Hervieux et François Nez. Au premier, pour m'avoir réconciliée avec les calculs théoriques, tout en me faisant part de son admiration pour Louis de Broglie autour d'une tarte flambée, ou encore pour son soutien téléphonique qui fut très apprécié ; Paul-Antoine fut toujours disponible, même lorsque son emploi du temps lui criait le contraire. Au second pour avoir guidé mes premiers pas parmi les lasséristes avec patience et à renfort d'énergie chocolatée (suisse, bien sûr), ainsi que pour son dévouement dans le sprint final ; en quelques phrases concises, bien que parfois sibyllines, il m'a transmis de bien utiles conseils pratiques.

Yves, Paul-Antoine, François... À chacun sa manière de communiquer son enthousiasme, à chacun son humour : dans tous les cas, ce fut véritablement agréable et enrichissant de travailler avec eux !

Je continuerai en m'adressant d'abord à mes collègues du CEA. En particulier, merci à Patrice Pérez et Pascal Debu, qui m'ont présenté le projet pour la première fois et ont accepté ma candidature spontanée à un sujet de thèse qui n'était, alors, pas encore formulé. Je salue Laszlo Liszkay, Bertrand Vallage, Jean-Michel Rey et Jean-Marc Reymond, qui forment le reste d'une équipe alliant compétences et bonne humeur. Merci à tous pour leurs avis d'experts, conseils pratiques et sympathiques encouragements.

Merci – thank you – obrigada aux étudiants sur le projet GBAR à Saclay : Nicolas Ruiz, Pierre Dupré, Daniel Brook-Roberge, Tim Mortensen, Amelia Leite et, plus particulièrement, Pierre Grandemange avec lequel j'ai partagé deux années de thèse et quelques heures cumulées de pauses caféinées, lors desquelles nous commisérions sur les malédictions de mes *jobs* plantés et de son piège à positons. Ce fut un plaisir de les rencontrer et de travailler avec eux. À tous, je souhaite bonne continuation ! / It was a real pleasure to meet them and work with them. I wish them all the best!

Je tiens à saluer les collègues du SIS au CEA-Saclay – et plus particulièrement Paul Lotrus – pour leur patience et leur compréhension face aux indications, parfois vagues et versatiles, que je leur fournissais pour la réalisation de l'automate gérant les sécurités de la cabane du laser. Bravo pour le résultat !

Je voudrais également associer à ces remerciements Anne-Isabelle Étienvre, actuellement chef du Service de physique des particules de l'Irfu, pour m'avoir orientée vers Patrice, ainsi qu'Achille Stocchi, du LAL à Orsay, pour avoir soutenu ma candidature à une bourse ministérielle auprès de l'école doctorale.

Enfin, j'adresse un clin d'œil à Laurent Chevallier, mon parrain au SPP, qui a mené cette mission avec une facilité déconcertante, et à Pascal Lévêque, du SACM, qui serait triste si je l'oubliais (et merci, bien sûr, pour l'aménagement de la cabane laser).

La moitié de ma thèse s'est déroulée au laboratoire Kastler-Brossel de Jussieu. Aussi, je souhaite faire part de toute ma gratitude à l'ensemble de l'équipe 13 du LKB, permanents (François Biraben, Pierre Cladé, Saïda Guellati, Lucile Julien et, *bis repetita placent*, François Nez) et doctorants (Sandrine Galtier, Clément Courvoisier, Manuel Andia, Raphaël Jannin, ainsi qu'Hélène Fleurbaey). Je ne peux que louer l'équipe pour son accueil familial et ses réjouissantes poses-thé, accompagnées de succulents gâteaux – catégorie "lourds-légers" – faits maison. J'en profite également pour remercier plus spécifiquement François Biraben, pour son aide précieuse sur la simulation et pour ses explications et conseils qui ont ponctués mon séjour parmi l'équipe, et dont, finalement, je regrette de n'avoir pas plus profité ! De même, un grand merci à Lucile pour m'avoir fourni livres et cours nécessaires à ma mise en selle dans le monde des lasers. Et enfin merci à Saïda pour son chaleureux soutien dans la dernière ligne droite.

J'adresse également tous mes remerciements à Laurent Hilico pour ses limpides explications, en particulier concernant la détection synchrone. Merci aussi pour nous avoir laissé subtiliser, à peine déballé, le beau lambdamètre acheté par le groupe "H_2^+" (dont je salue aussi Albane Douillet et Jean-Philippe Karr) !

Je suis très reconnaissante envers le personnel de l'atelier de mécanique du LKB – Jean-Michel Isac, Pascal Travers, Gaël Coupin, Arnaud Leclercq et Saysavanh Souramasing – pour leur travail rapide et efficace, même lorsqu'ils sont surchargés. Je leur dois notamment la réalisation de tous les éléments mécaniques de l'oscillateur, et je sais qu'une certaine petite pièce en laiton percée d'une ouverture oblique leur a donné bien du fil à retordre...

Merci à Florence Thibout, pour nous avoir soufflé une délicate cellule de césium, et pour m'avoir permis d'assiter au rituel de la queue de cochon.

Et enfin merci à Brigitte Lamour et Jean-Pierre Okpisz, pour le support technique en électronique et les conversations autour d'un fer à souder ; merci de m'avoir confié du matériel en août pour monter mes photodiodes.

Au début de l'aventure, il y eut l'Institut de physique et de chimie des matériaux de Strasbourg, où j'ai passé deux mois avant d'y retourner régulièrement pendant la thèse. Je voudrais donc saluer, en plus de Paul-Antoine, Giovanni Manfredi, Omar Morandi, et lancer un *vielmols merci* à Yannick Hinschberger, pour un stage tout en bon son hard-rock bien gras.

Bon courage Mateo Valdes Dupuy, qui commence sa thèse à l'IPHC de Strasbourg sur le calcul des sections efficaces à très basse énergie.

Je remercie également Christine Tugène et Fabien Müller pour leurs rapides interventions dès lors qu'un problème survenait sur une des machines de calcul de Strasbourg.

Un large merci aux différents secrétariats de chacun des laboratoires que j'ai traversés. Je suis notamment extrêment reconnaissante envers Estelle Brunette, Émilie Chancrin, Martine Oger, Béatrice Guyot, Monique Granon, Laeticia Morel-Maréchal, Delphine Charbonneau pour leur aide efficace et sympathique.

I would like to acknowledge the GBAR collaborators for their interest (either enthusiastic, simply polite or even sometimes doubtful) during collaboration meetings, and for the ensuing fruitful discussions.

Je remercie enfin chaleureusement Messieurs Bertrand Laforge, Jaume Carbonell, Yasunori Yamazaki (*doumo arigatou gozaimashita*), Lamri Adoui et Pierre Vanhove, pour avoir accepté

de faire partie de mon jury ainsi que pour l'intérêt qu'ils ont manifesté à ce travail et les corrections qu'ils m'ont proposées ; je remercie plus particulièrement les deux derniers membres précédemment cités pour avoir endossé la difficile tâche de rapporteur sur un sujet polymorphe.

Aux antipodes de la physique, je souhaiterais saluer mes amis de la revue Disharmonies, contrepoint littéraire et culturel salutaire qui m'a permis de m'exercer à la communication scientifique. Durant ma thèse, j'ai pu retrouvé avec joie les membres de la Rédac' qui, lors de cette dernière année, n'ont cessé de m'adresser leurs encouragements.

Cette ligne est probablement celle qui sera le plus avidement lue. Qu'ils soient rassurés, leur immense contribution n'a pas été oubliée. Je tiens donc à remercier mes parents pour leur soutien indéfectible tout au long de mes études et notamment leur soutien logistique et financier qui fut... capital pour étudier à Paris. Ils ont cultivé très tôt mon goût pour la recherche (avec l'archéologie pour première entrée en matière) et pour les sciences, bien que, chimiste et biochimiste de formation, ils eussent probablement préféré que je ne m'obstinasse pas à faire de la physique... Encore merci !

Et enfin une dédicace au renard furtif, qui, tout au long de ces trois années, fut à la fois le solide phare dans la tempête, le brave saint-Bernard au tonneau à moitié plein, le redouté œil critique, le détonnateur d'idées, en plus de ses qualités d'inlassable cobaye gastronomique, d'enthousiaste guide de voyage et de mœlleux coussin.

Contents

I Introduction to the GBAR experiment **1**

1 Some matter about Antimatter **3**
1.1 Breve discovery history . . . 3
1.2 Positronium and antihydrogen: some properties . . . 4
1.2.1 The bound state of e^- and e^+: Positronium . . . 4
1.2.2 The bound state of $\bar{p}$ and e^+: Antihydrogen . . . 7

2 Description of the GBAR experiment **9**
2.1 Antimatter and Gravitation . . . 9
2.2 The GBAR experiment . . . 10
2.2.1 Proposal of experiment . . . 10
2.2.2 Challenges of the GBAR experiment . . . 13
2.2.3 The $\bar{H}^+$ ion and its matter equivalent: H^- . . . 13
2.3 Presentation of the present thesis . . . 14
2.3.1 Earlier reference works on the $\bar{p}$–Ps collisions . . . 14
2.3.2 Purpose and outline of the thesis . . . 16

II Cross section calculations for Antihydrogen and Antihydrogen plus production **19**

3 Continuum Distorted Wave – Final State (CDW–FS) **21**
3.1 Origin of the model . . . 21
3.1.1 The family of Continuum Distorted Wave models . . . 21
3.1.2 Continuum Coulomb wave functions . . . 22
3.2 CDW–FS for positronium production . . . 23
3.2.1 First introduction of the CDW–FS model . . . 23
3.2.2 Characteristics and limitations of the model . . . 24

4 Analytical calculations **27**
4.1 Antihydrogen production . . . 27
4.1.1 General case: $l_h,\ l_p \geq 0$ . . . 27
4.1.2 Conversion from inverse to direct reaction . . . 30
4.2 Antihydrogen positive ion production . . . 31
4.2.1 General case: $l_p,\ l_h \geq 0$ . . . 31
4.2.2 Conversion from inverse to direct reaction . . . 35

5 Complementary studies **37**
5.1 Electronic correlations . . . 37
5.1.1 "Uncorrelated" Chandrasekhar wave function . . . 37
5.1.2 "Correlated" Chandrasekhar wave function . . . 37
5.1.3 Le Sech wave function . . . 38
5.2 *Capture–excitation* and f – g processes . . . 39
5.2.1 *Capture–excitation* . . . 39
5.2.2 f and g processes . . . 42
5.3 Coulomb - Born Approximation . . . 42

6 Results of the cross section computations **45**
6.1 First reaction . . . 46
6.1.1 CDW–FS results . . . 46
6.1.2 CBA results . . . 50
6.2 Second reaction . . . 53
6.2.1 The uncorrelated Chandrasekhar wave function: first investigations and positron capture processes . . . 53
6.2.2 The correlated Chandrasekhar and Le Sech wave functions: selected cases and electronic correlations . . . 57

7 Comparisons between models and with experimental data **63**
7.1 CDW–FS vs. CBA . . . 63
7.2 Comparison with previous theoretical works . . . 66
7.2.1 Three-body reaction . . . 66
7.2.2 Four-body reaction . . . 68
7.3 Comparison with experimental data for reaction 1 . . . 71

8 Conclusions of the cross section calculations **75**

III Simulation and design of the GBAR reaction chamber **79**

9 Description of the simulation **81**
9.1 The positronium populations . . . 81
9.1.1 Optical Bloch equations . . . 81
9.1.2 Transition and photo-ionisation probabilities . . . 82
9.2 Rate equations for antimatter production . . . 83
9.2.1 Antihydrogen production . . . 83
9.2.2 Antihydrogen positive ion production . . . 84
9.2.3 Solving . . . 85
9.3 Parameters . . . 85
9.3.1 Positron beam and positronium formation . . . 85
9.3.2 Laser beam . . . 87
9.3.3 Antiproton beam . . . 89
9.3.4 Geometry of the reaction chamber . . . 92

10 Results of the simulation **95**
10.1 Working with 6-keV antiprotons . . . 95
10.1.1 First parameter scans with the monoenergetic beam . . . 95
10.1.2 Antiprotons deceleration simulated at 6 keV . . . 100
10.2 Working with 1 keV antiprotons and 3D-state positronium . . . 101
10.2.1 First investigations with a mono-energetic beam . . . 101
10.2.2 Results with a realistic simulation of an antiproton pulse decelerated to 1 keV . . . 106
10.3 Positronium excitation at Saclay and hydrogen production . . . 107
10.3.1 Positronium spectroscopy experiment . . . 108
10.3.2 Hydrogen production cross section experiment . . . 111

11 Conclusions and suggested future developments **117**
11.1 Proposition for the design and realisation of reaction chamber based on the simulation results . . . 117
11.2 Ameliorations to the simulation . . . 118

IV Laser for positronium excitation into the state 3D **119**

12 Description of the laser **121**
12.1 Requirements . . . 121
12.1.1 Natural linewidth of the transition and Doppler broadening . . . 121
12.1.2 In the prospect of an experiment at CEA . . . 122
12.2 General description of the laser system . . . 123
12.2.1 CW Ti:Sa laser . . . 124
12.2.2 Oscillator . . . 126
12.2.3 Amplification and frequency doubling . . . 129
12.3 Alignment diagnostics, selective elements and controls . . . 131
12.3.1 Alignment diagnostics . . . 131
12.3.2 Rotation direction and wavelength selection for the CW Ti:Sa laser . . . 132
12.3.3 Servo loop . . . 134
12.4 Characterisation of the laser beam . . . 136
12.4.1 Wavelength measurement . . . 136
12.4.2 Power, energy and pulse length . . . 136
12.4.3 Chirp . . . 138

13 Preparation of the positronium spectroscopy experiment at CEA **143**
13.1 The Saclay set-up simulated with a caesium cell . . . 143
13.1.1 Atomic caesium . . . 143
13.1.2 Description of the future set-up at LKB . . . 144
13.1.3 Supplementary remarks . . . 147
13.2 Preparation of the experiment at CEA-Saclay . . . 149
13.2.1 Installation of the laser hut on the GBAR zone . . . 149
13.2.2 Operation of the laser at CEA-Saclay and safety procedures . . . 150

14 Conclusion: status of laser system **153**

V Conclusion **155**

VI Appendices **167**

A Wave functions for hydrogen-like atoms **169**

B Reaction thresholds **171**
B.1 Thresholds of the GBAR reactions 171
B.1.1 Antihydrogen formation 171
B.1.2 Antihydrogen plus formation 172
B.2 Thresholds of the break-up reactions 172

C Mathematical tools **177**
C.1 *3j* symbols 177
C.2 *6j* symbols 178
C.3 *9j* symbols 179

D CDW–FS analytical expressions for particular cases **181**
D.1 Particular cases of antihydrogen formation 181
D.1.1 Only *s*-states of positronium 181
D.1.2 Only *s*-states of antihydrogen 182
D.1.3 *s*-states of both positronium and antihydrogen 183
D.2 Particular cases of antihydrogen plus formation 184
D.2.1 Only *s*-states of positronium 184
D.2.2 Only *s*-states of antihydrogen 185
D.2.3 *s*-states of both positronium and antihydrogen 186

Part I

Introduction to the GBAR experiment

Chapter 1

Some matter about Antimatter

As an introduction to the present thesis, it has been chosen to first give some chronological indications on the physics of antimatter, which is less than one century old. This will be the opportunity to introduce the main protagonists in the GBAR experiment and in this thesis: the positron, and its bound states with electron and antiproton, which are the positronium, the antihydrogen atom and the positively charged ion of antihydrogen (the latter in chapter 2).

1.1 Breve discovery history

The first theoretical prediction of an antiparticle dates back to 1928, with an article published by Paul Dirac [1]. Dirac had developed a relativistic version of the Schrödinger equation describing the motion of an electron (more generally, applicable to fermions of spin $\frac{\hbar}{2}$). The equation, now known as the Dirac equation, could also be verified by a particle with the same mass as the electron, but of positive charge and negative energy. This particle was unknown by then, which left two alternatives: either Dirac's equation was wrong, or a new particle, which would annihilate with an electron, was to be discovered. This *anti*-electron was identified in 1932. Carl Anderson used a cloud chamber (a chamber saturated with water vapour in which charged particles leaves a droplet track: the density of the droplets gives indications about the type of particle) to study cosmic showers; the chamber was positioned in a magnetic field, bending these tracks. In order to identify the direction from which the particles originated, a plate of lead was added in the chamber so the particles would lose energy in it and their tracks would have a stronger bend after the plate. From this set-up, Anderson observed particles leaving tracks of droplets similar to the ones of an electron (thus indicating that they had the same mass and absolute charge), but the magnetic field was deflecting them in the opposite direction of the one for the electron [2]. Anderson proposed to call the anti-electron a *positron*, that we will note e^+ in the following. With this new positive particle available, it was theorised that a bound state of an electron and an anti-electron could be created; this bound state received the name *positronium*, that we will sometimes abbreviate to Ps in the following, and was discovered in 1951 by Martin Deutsch [3].

It was not before 1955 that the first antiprotons, $\bar{p}$, were observed by Emilio Segré and Owen Chamberlain at the Bevatron; they were formed in collisions between GeV protons and a copper target, selected from the resulting particle beam by deflecting magnets (negative charge and energy selection), and their time of flight was measured to finally determine their mass [4]. Right after, the antineutron [5] was added to the antiparticle collection. This collection would rapidly grow richer as new leptons and hadrons, and finally quarks, were discovered in cosmic rays or at particle accelerators. After the discovery of the nucleus-less positronium atom in 1951,

it would take 44 years to report the observation of another anti-atom, the antihydrogen ($\bar{\mathrm{H}}$) [6]. In the interval, the first compound antinuclei, antideuterium, had been discovered [7].

As this mirror family of matter was progressively revealed, with antiparticles seemingly having the same mass, spin, lifetime and opposite charge, magnetic moment as their matter counterparts, one question arose: why is the universe only made with matter? Or, as an alternate formulation: why matter and antimatter have not completely annihilated in the early moments of the universe, since they should have been produced in equal amounts? This problem is referred as the *baryogenesis* problem. A first glimpse of a possible answer came from the observation of CP (charge conjugation + parity symmetry) violation in weak interactions, using the neutral kaons K_0 and $\bar{K_0}$ [8, 9, 10]. This demonstrated the existence of an asymmetry between matter and antimatter, although not being sufficient to explain the matter excess constituting the observable universe.

Antimatter studies now mainly aim at trapping and cooling antiprotons and antihydrogen atoms in order to perform precise CPT tests; the CPT symmetry adds the symmetry by time reversal, T, to CP. It is in fact the CPT invariance that imposes the same masses, spins, opposite charge, etc. for a particle and its antiparticle, with the particular interpretation of the T-symmetry developed by Feynman [11], considering that antiparticles are particles moving backwards in time. In order to understand the baryogenesis, a possible CPT violation is investigated, by comparing the most precise frequency measurements of the same transition in an antimatter system and its matter mirror, or in positronium, and looking for a deviation. So far, it has been for instance measured that the relative mass difference between electron and positron is less than $8{\cdot}10^{-9}$ [12], while the proton-antiproton charge-to-mass ratio has been measured to the 10^{-11} level of precision, with $\left|\frac{q_{\bar{\mathrm{p}}}}{m_{\bar{\mathrm{p}}}}\right| / \left(\frac{q_{\mathrm{p}}}{m_{\mathrm{p}}}\right) = 0.99999999991 \pm 9 \cdot 10^{-11}$ [13], considered as one of the most stringent test of CPT symmetry. We can also cite the measurement of mass ratio between antiproton and electron, performed using an exotic atom, the antiprotonic helium (one electron is replaced by an antiproton in high-n shell) [14]. For other comparisons regarding the charge, the gyromagnetic factor or the magnetic moment, see [15].

In the following section, we will focus on the positronium and the antihydrogen atoms, since they are at the core of the GBAR experiment.

1.2 Positronium and antihydrogen: some properties

1.2.1 The bound state of e^- and e^+: Positronium

For a first approach, the positronium atom can be seen as a particular type of hydrogen-like atom, and its energy levels can be deduced from the one obtained for hydrogen: the reduced mass of hydrogen, almost equal to the mass m_e of the electron, has instead to be replaced by the reduced mass of positronium, which is exactly $\frac{m_e}{2}$. In consequence, the energy of the positronium levels, in a non-relativistic framework, is half the one of the hydrogen levels, that is:

$$E_n = -\frac{\alpha m_e c^2}{4n^2}, \tag{1.1}$$

where n (written n_p in the following) is the principal quantum number, α the fine structure constant and c the speed of light. Throughout this document, we will use equation 1.1 to give the values of the energy levels in positronium. In atomic units ($m_e = e = \hbar = \frac{1}{4\pi\epsilon_0} = 1$), equation 1.1 simply becomes $E_{n_p} = -\frac{1}{4n_p^2}$ (with 1 a.u. $\approx$ 27.2114 eV). In addition to the relation between

the hydrogen and positronium energy levels, we also deduce that the lifetime and radius of the positronium states are twice the ones of the hydrogen states.

However, this description does not fully include the interactions between the electron and the positron, in particular the possibility for positronium to annihilate. This is accomplished by the Breit equation, which is a further development of the relativistic single-particle Dirac equation: it is formulated for two or more fermions, encompassing the electromagnetic interactions between the particles. In the case of positronium, the hamiltonian in the Breit equation is constituted of the two hamiltonians of the free particles, the Coulomb potential (the three of them forming the unperturbed hamiltonian which gives the energy levels of equation 1.1) and an operator of interaction with second order terms, in $1/c^2$ (terms only depending on the momentum and position operators, which are purely orbital terms; terms depending on the product of the orbital angular momentum and total spin operators, called spin-orbit terms; terms proportional to the square of the total spin operator, thus related to spin-spin interactions). The derivation and full expression of the Breit hamiltonian for positronium can be found in paragraph 84 of [16].

These interaction terms are responsible for corrections in the energy levels of equation 1.1 depending on the orbital angular momentum (L) et total angular momentum (J): the energy levels are split resulting in the positronium fine structure; because of the appearance of the total spin operator, $\mathbf{S}$, a distinction is also made between the two possible spin states of positronium: S can be either equal to 0 (anti-parallel spins) or 1 (parallel spins). The former is a singlet-state called *para*-positronium while the latter is the *ortho*-positronium triplet state. When ground state positronium is formed, it has a $\frac{1}{4}$ probability to be para-positronium and a $\frac{3}{4}$ probability to be ortho-positronium. The para and ortho-positronium do not have the same energy levels any more (hyperfine splitting) and, in particular, their ground state have a very different annihilation lifetime which can be calculated with the Breit equation. The para-positronium ground state, 1^1S_0, annihilates in 125 ps, while the ground state of ortho-positronium, 1^3S_0, mean lifetime is 142 ns. For the following, we will only be interested into the ortho-positronium since it has the longer lifetime and is thus better suited to be used in the GBAR experiment.

Though it gives a sufficient description of positronium, the Breit equation also has its own limitations: it only includes α^2 corrections to the energy levels and is not invariant under Lorentz transformation. For a covariant equation with higher order corrections, one can use the Bethe-Salpeter equation [17] and for the most accurate calculations, quantum electrodynamics (QED) is required. For the positronium application intended in GBAR, the results given by the Breit equation are totally satisfactory, and for the positronium wave functions, we will in fact use the wave functions for hydrogen-like atoms, as given in [18] for instance (the corresponding formulas are enclosed in appendix A). In figure 1.1, we give a diagram representation of the fine structure of ortho-positronium, as it can be calculated from [19] (energy levels at the second order, in α^2; with third or fourth order, see for instance [20]), and we give some measured transition frequencies. We remind that, in spectroscopic notations, the levels are noted $n^{2S+1}L_J$, with the letters $S, P, D, ...$ used for $L = 0, 1, 2, ...$ respectively. When the fine structure in not considered, the levels will be either referred as n_pL-states or $\mathrm{Ps}(n_p, l_p)$ in the following.

Since positronium is a purely leptonic atom, its physical properties are free from QCD corrections and it is therefore well suited for QED tests. In positronium, there is no dependency in a nuclear charge or radius and, assuming CPT invariance, the mass ratio of the positronium atom is 1: this means that the corrections to the positronium energy levels only depends on the

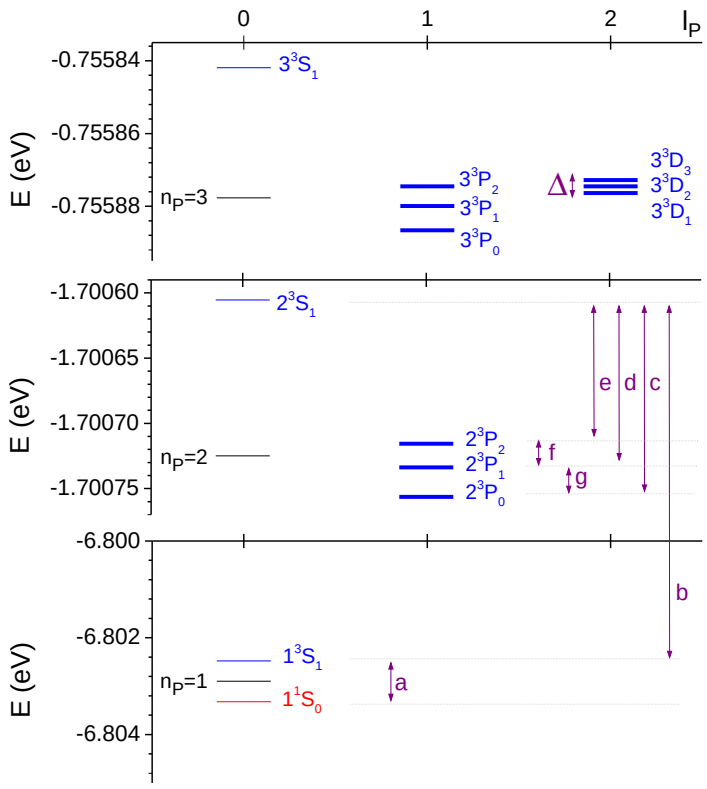


Figure 1.1: The energy levels of ortho-positronium arranged according their orbital quantum number, l_p: in black, the Schrödinger levels, in blue, the fine structure obtained from [19]. In red, the ground state of para-positronium is also displayed. The transition frequencies for the transitions identified with a letter are reported in table 1.2 below.

Transition	Exp. (MHz)	Theo. (MHz) [21]
(a)	203389.10(74) [22]	203392.010(500)
(b)	1233607216.40(320) [12]	1233607222.170(600)
(c)	18499.65(120)(400) [23]	18498.246(90)
(d)	13012.42(67)(154) [23]	13012.407(90)
(e)	8624.38(54)(140) [23]	8626.709(90)
(f)	4388.04(86)(210) [23]	4385.698(10)
(g)	5487.23(140)(430) [23]	5485.839(10)
$1^3S - 2^3P$	1233592000(10000) [24]	-
Δ	-	850
$1^3S - 3^3D$	-	1462062300

Figure 1.2: Transition frequencies in MHz for several transitions in ortho-positronium and for the ground state hyperfine splitting. In [24], a wavelength measurement of the $1^3S - 2^3P$ transition is reported (243.024(0.002) nm). The last two values, computed from the values obtained with the formulas in [19] are given for information.

knowledge of the electron mass and of the fine structure constant, α. This explains the wide interest toward the spectroscopy of positronium, several results of which have been included in figure 1.1. This subject is thoroughly discussed in [25].

1.2.2 The bound state of $\bar{p}$ and e^+: Antihydrogen

In the original discovery of antihydrogen [6], the antihydrogen atoms were formed in flight, during collisions between antiprotons and a low-density, high-Z target (xenon): the interaction of an antiproton with the Coulomb field of a xenon nucleus can induce the creation of an e^+-e^- pair from which the antiproton can combine with the positron. Other formation methods are called *at rest*, since the formation of antihydrogen is obtained by the mixing of cold antiprotons with cold positrons, and antihydrogen is then formed from the three-body interaction involving one antiproton and two positrons (the positron left unbound take away the excess energy).

In parallel with the increased precision of the measurements, technical improvements allowed the successive CERN experiments on antiproton and antihydrogen to establish records in the number of antihydrogen atoms trapped, in their confinement lifetime and cooling. For instance, first cool antihydrogen atoms [26, 27], longest lifetime in a trap [28], first spectroscopy measurement [29], first beam of antihydrogen [30].

Since no evidence of CPT violation has been shown, we will always consider in the following that the antihydrogen is absolutely equivalent to the hydrogen atom, and we will therefore use the wave functions and radiative lifetimes of hydrogen to describe $\bar{H}$.

Chapter 2

Description of the GBAR experiment

2.1 Antimatter and Gravitation

The CPT tests on antimatter previously evoked only test the Standard Model of particle physics, but it is well-known that the Standard Model does not include gravitation. We should note that the results on the antiproton mass reported above only concern the *inertial* mass (m_i for matter, $\bar{m}_i$ for antimatter). Nothing has been mentioned about the *gravitational* mass (m_g for matter, $\bar{m}_g$ for antimatter). The CPT invariance only imposes that an antimatter system follows the same law of gravitation as a matter system, but gives no indication on a matter-antimatter system (an antiproton in the gravitational field of the Earth for instance): we could have $\bar{m}_g \neq m_g$. Therefore, there is an open field for tests questioning the behaviour of antimatter with respect to gravitation.

However, the Weak Equivalence Principle (WEP) states that the inertial and gravitational mass are equal; since theory and experiments agree to say that $\bar{m}_i = m_i$, this implies that $\bar{m}_g = m_g$, unless antimatter violates the WEP. For a review on the subject of *antigravity* (i.e. the gravitational repulsion between matter and antimatter), in particular the arguments against it and, even so, the possibility of antigravity components in modified gravity theories, see the reference work by Nieto and Goldman [31]. Either for placing constraints on the existing different gravity models and for testing the WEP (and CPT invariance) in the case of antimatter, precise measurements of $\bar{g}$, the gravitational acceleration of antimatter in the gravitational field of Earth, are required.

Experimentally, attempts have been made to perform gravity tests on positrons and antiprotons. However, these species are charged, and thus sensitive to parasitic electric or magnetic fields, which prevent to make accurate measurement: indeed, the effect of the Earth gravity on an antiproton is so weak that it is often compared to the effect of a single charge placed just a few centimetres away from the antiparticle. This obliged to work on neutral antimatter species. The candidates are antineutron [32] and antihydrogen, but only antihydrogen can be trapped and cool. Another possibility is for instance working on positronium, as a GBAR collaborator intends to do. [33]

We should however note that the p-$\bar{\text{p}}$ charge-to-mass ratio measurement has been used to deduce an upper limit on the discrepancy between the gravitational acceleration on Earth of matter and antimatter: it was found that $|\bar{g} - g| < 5 \cdot 10^{-4} g$ [34]; but the assumptions made to obtain the result are often contested and the result itself is not regarded as direct measurement by some authors. This justifies the use of a different approach to produce another measurement.

There are three competing experiment at CERN that intend to address the question of the gravitational behaviour of antihydrogen. The first one is ALPHA, which was not originally designed for that purpose but provided a first exclusion measurement: statistically analysing the distribution of antihydrogen annihilation events in their trap, they deduced that the results were incompatible with a m_g/m_i ratio greater than 110 and smaller than -65.[35] The second direct concurrent is AEgIS, which is based on a Moiré interferometer for mK antihydrogen atoms [36], and the last one, not yet installed at CERN, is GBAR. Another experiment, AGE, as been proposed at Fermilab. Finally, there is the experiment, based on positronium, being implemented at ETH Zürich. [33]

2.2 The GBAR experiment

In order to make a direct observation of the effect of gravitation on antimatter, the aim in GBAR, as in AEgIS, is to record the influence of Earth's gravity in the trajectory of antihydrogen atoms. In GBAR, the antihydrogen atoms will be at rest before they undergo a free fall. This gave the name of the experiment: *Gravitational Behaviour of Antihydrogen at Rest*.

2.2.1 Proposal of experiment

The conception of the GBAR experiment has been built around the original idea proposed by Walz and Hänsch [37] of *sympathetically* cooling positive ions of antihydrogen, $\bar{\mathrm{H}}^+$ (one antiproton bound with two positrons). This process is used to bring the ions at rest before photo-detaching one of their positron to retrieve the neutral atom. The GBAR experiment can be divided into three parts: the production of the antihydrogen positive ions (described in the following section A.), their trapping and laser-cooling, and the neutral antihydrogen free-fall itself (these last two parts have been gathered in section B.).

A. Production of $\bar{\mathrm{H}}^+$
The largest part of the experiment is only dedicated to the production of these antihydrogen positive ions. This requires antiprotons and a source of positrons. As a matter of fact, the GBAR experiment does not intend to produce the ions by mixing cold antiprotons with cold positrons (as evoked earlier for other antihydrogen experiments). Instead, the experimental scheme propose to use positronium as the positron provider and the synthesis of $\bar{\mathrm{H}}^+$ would be the results of two consecutive reactions. First, an antiproton colliding with a positronium atom can capture a first positron and form antihydrogen:

$$\bar{p} \ + \ \mathrm{Ps}^{(*)} \rightarrow \ \bar{\mathrm{H}}^{(*)} \ + \ e^-; \tag{2.1}$$

then, this antihydrogen atom can encounter a second positronium atom and capture another positron to eventually form $\bar{\mathrm{H}}^+$:

$$\bar{\mathrm{H}}^{(*)} \ + \ \mathrm{Ps}^{(*)} \ \rightarrow \ \bar{\mathrm{H}}^+ \ + \ e^-. \tag{2.2}$$

The stars indicate the possibility that excited positronium is used and that excited antihydrogen is produced as an intermediate state. In the GBAR proposal, positronium excited into state 3D has been retained. The energy foreseen for the antiprotons is in the range 1 to 10 keV.

Since one antiproton should interact with two positronium atoms, an intense target of positronium is needed. This requires both an intense source of positrons and a way of confining the positronium atoms produced in a small volume. This part is in charge of CEA-Saclay. The

intense source of positrons is obtained with the combination of a intense linac-based positron source (for the description of the demonstrator installed at CEA-Saclay, see [38, 39]) and a Penning-Malmberg accumulation trap [40, 41]. The linear accelerator used at CERN, built by the polish National Centre for Nuclear Research, will produce 10 MeV electrons impacting at tungsten target: the resulting Bremsstrahlung has enough energy to produce e^+-e^- pairs. The electrons and positrons are magnetically separated and the positrons are then moderated to a few eV. The slow positron pulse obtained is compressed with a buncher prior to injection in the trap.

This trap possesses a set of 27 ring electrodes to create trapping potentials, surrounded by a 5 T solenoid for radial confinement. Before the injection of the positrons, the trap is first loaded with an electron plasma: the electrons are used to cool the positrons in order to allow their trapping. A scheme has been developed to accumulate the positrons from the pulsed beam coming from the linac. The multi-ring trap is provided by the collaborators from RIKEN, Japan, where it was already used for positron accumulation from a radioactive source. In the following, we will sometimes refer to the positron trap as the RIKEN trap.

The accumulated positron are ejected in less than 100 ns toward the positron-to-positronium converter. This converter is made of nanoporous silica [42]: the positrons are dumped in the silica matrix at 3 keV and straggle to interconnected pores where they capture an electron and form positronium. The positronium atoms then diffuse out of the converter into vacuum. The silica films tested for GBAR have pores of 3-4 nm diameter: they showed a 30-35 % e^+–*o*-Ps conversion efficiency, and the positronium re-emitted had a typical energy of about 50 meV.[43, 44] The dynamics of positronium in the pores is theoretically studied by the collaborators from the Institut de physique et de chimie des matériaux de Strasbourg (IPCMS) [45, 46]. In the GBAR proposal, the converter is inside a small tube (1 mm^2 diameter and 10 to 20 mm length): the positrons are injected inside the tube and implanted in the converter: the positronium formed is re-emitted in the tube where it is mostly confined. The goal announced in the GBAR proposal is to trap a few 10^{10} positrons and get a positronium density of 10^{12} cm^{-3}.

The antiprotons will also be injected in the positronium tube. Antiprotons are provided by CERN, at the Antiproton Decelerator (AD) facility. A new antiproton decelerator, ELENA, will provide, every 110 s, a 75 ns bunch of 4.5 10^6 $\bar{p}$ at 100 keV.[47] However, this is expected to be too energetic for the purpose of $\bar{H}^+$ production. Therefore, the GBAR experiment will use an additional decelerator, fabricated at CSNSM, Orsay, to decrease the energy of the antiprotons from 100 keV to a few keV. The design of the decelerator is based on an existing ion decelerator at ISOLDE, CERN.

A schematic summary of this part of the experiment is given in figure 2.1.

B. Cooling of $\bar{H}^+$ and $\bar{H}$ free fall

The $\bar{H}^+$ ions produced in the interaction region of GBAR will exit the positronium tube at the same kinetic energy as the antiprotons. A magnetic separator will isolate the anti-ions from the rest of the antiprotons and the antihydrogen atoms; the $\bar{H}^+$ can then be focused in the capture trap where they will undergo their first cooling process.

The capture trap is the first linear RF Paul trap of the GBAR experiment. It is filled with a crystallised cloud of beryllium ions, $^9Be^+$, constantly Doppler-cooled with a 313 nm laser. The antihydrogen ions entering this crystal will lose energy in it by Coulomb interaction with the beryllium (*sympathetic* cooling). In order to capture the energetic $\bar{H}^+$ ions, 10^6 Be^+ are needed. This stage allows to reach a temperature of 10 mK for the anti-ions (100 neV energy). This is however still too fast to perform the free fall experiment. A second cooling stage is thus required,

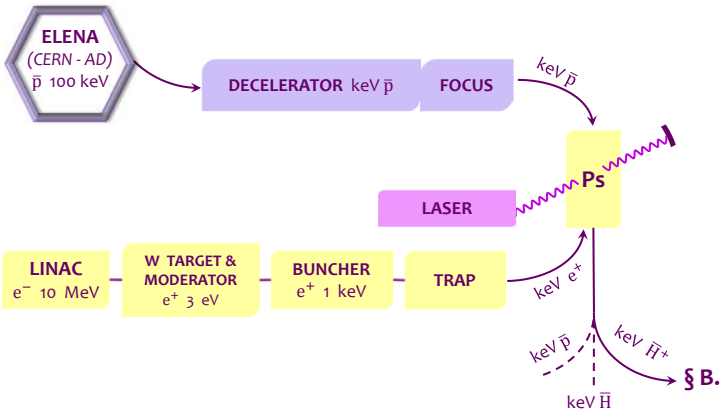


Figure 2.1: The production of $\bar{H}^+$ ions in GBAR at CERN.

in the precision trap.

Each cold $\bar{H}^+$ ion of the capture trap is shuttled to the second linear RF Paul trap, where a single Doppler-cooled Be^+ awaits; this precision trap is inserted inside the detection chamber. This time, the ion pair is cooled by Raman side-band cooling [48], a technique allowing to decrease the energy to 1 neV (10 μK). The precision trap has 200 μm electrodes and a distance between chips of electrodes of less than 1 mm. Its design is very light in order to leave access for lasers and for the falling antihydrogen atoms.

Indeed, once the $\bar{H}^+$ ion has reached an energy of 1 neV (corresponding to a speed of a few metres per second), a horizontally polarised 1,644 nm laser is used to photodetach one positron from the ion: a neutral atom of antihydrogen is obtain, which escapes the precision trap from its sides and falls freely in the vacuum chamber until it annihilates on a plate at the bottom. This chamber is surrounded with tracking detectors (micro-mesh gaseous detectors called MicroMegas) to record the tracks of the pions coming from the annihilation of the antiproton. This tracks are used to reconstruct the annihilation vertex. The time between the photodetachment and the annihilation gives the time of the free fall, Δt. Knowing the height between the antihydrogen ion in the trap and the detection plate, Δz, one can deduce the value of $\bar{m}_g\bar{g}$ from:

$$\Delta z = \frac{1}{2}\frac{\bar{m}_g}{\bar{m}_i}\bar{g}\Delta t^2 + v_{0,z}\Delta t. \tag{2.3}$$

With this experimental scheme, a 1 % precision measurement of $\bar{g}$ should be obtained within a few months of antiproton beam time. The main limiting parameter on the precision is the initial vertical speed of the antihydrogen atom, $v_{0,z}$. Other parameters inducing uncertainties are the recoil of the atom after photo-ionisation, the position of $\bar{H}^+$ in the last trap and the time measurement. An upgrade of the GBAR experiment is foreseen to reach a precision better than 10^{-4}, using the quantum gravitational states. [49]

The capture trap and both 313 nm and 1,644 nm lasers are realised by the Laboratoire Kastler-Brossel in Paris, the precision trap by the collaborators of Johannes Gutenberg University in Mainz, and the detection chamber by the ETH-Zürich, with the participation of CEA-Saclay for the MicroMegas detectors.

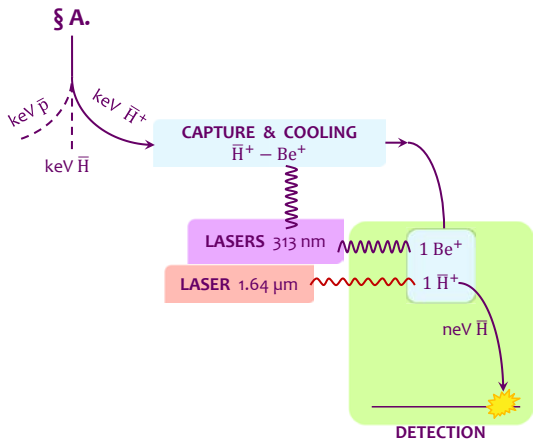


Figure 2.2: The cooling of $\bar{H}^+$ ions in GBAR and the free fall of cold antihydrogen.

2.2.2 Challenges of the GBAR experiment

The proposal of the experiment [50] has been submitted to the CERN SPSC in 2011 and has been accepted in March 2012. The GBAR project was partly made feasible thanks to the new antiproton decelerator, ELENA that we will installed at the AD. 2015 will be the year of ELENA commissioning, with the goal of delivering the first antiproton beam to GBAR in 2017. The different parts of the GBAR experiment have to be ready by then, and this implies the realisation of important milestones prior to the installation at CERN. In particular:

1. Realisation of an intense linac-positron source and record accumulation of 10^{10} positrons;

2. Deceleration from 100 keV to 1 keV and focusing of a (anti)proton pulse in a small tube;

3. Definition of the parameters of the interaction region;

4. Demonstration of the capture and cooling of ions with high mass-to-charge ratio, starting with H_2^+.

2.2.3 The $\bar{H}^+$ ion and its matter equivalent: H^-

The GBAR experiment relies on the production of the antihydrogen ion, $\bar{H}^+$. So far, no antihydrogen experiment reported the observation of this ion, which would be the first antimatter ion to be produced. The largest part of the GBAR experiment – the linac-based source, positron trap, Ps production and $\bar{p}$ decelerator – is thus dedicated to the optimised production of this anti-ion.

With its two positrons bound to an antiproton, $\bar{H}^+$ is in fact the antimatter counterpart of the negative hydrogen ion, H^-, and, for the needs of the calculations, we will of course assume that $\bar{H}^+$ can be described using the known properties of H^-. The main difference between $\bar{H}^+$

and H^-, is the way of producing it: H^- can be easily obtained from plasmas formed out of dihydrogen gas.

A survey dedicated to the negative hydrogen ion has been done by Rau [51], providing a large bibliography related to the subject. We summarise here the main features of this ion. Apart from doubly-excited states, the H^- ion only exists in its ground state, and this ground state is indeed a bound state only due to the strong electronic correlations in this 3-body system. For instance, the use of the Hartree-Fock method to find the approximate wave function of the H^- ground state predicts that the system is not bound! This problem was progressively solved with the introduction of variational methods by Hylleraas [52]. The energy of H^- (-14.360 eV) was indeed lower than the ground state energy of hydrogen (-13.606 eV). The electron binding energy in H^- is thus 0.754 eV, hence the 1.644 μm infra-red laser used for the photodetachment. In fact, the photo-ionisation cross-section of H^- is null at threshold and gradually increases to a maximum reached at about twice the threshold energy (see for instance [53] for experimental values).

The many-parameter trial wave functions used in the Hylleraas method are not convenient for the cross section calculation of collisional processes, for instance. The first step toward simpler approximated wave functions was done by Chandrasekhar [54], who proposed a two-parameter and a three-parameter wave functions, introducing radial and angular electronic correlations and considering that the two electrons do not occupy the same energy levels. These wave functions give a sufficiently good value of the binding energy and are simple enough to be still used today. In Part II, we will give their expression and highlight the importance of achieving the correct description of the electronic correlations in H^-, which are the reason for the system being bound.

In the GBAR proposal, it has been suggested that excited positronium into a state n_p=3 shall be used to take advantage of a nearly-resonant behaviour of the $\bar{H}^+$ formation cross sections at low energy. This comes from the following observation: in the case of ground state antihydrogen and n_p=3 state of positronium, the energy available in the centre of mass at the threshold of reaction 2.6 is the sum of the binding energies:

$$-\frac{1}{2n_h^2}-\frac{1}{4n_p^2}=-\frac{1}{2}-\frac{1}{36}=-0.52778 a.u.,$$

which, in electron-volts, is 14.362 eV. This appears to be very close to the energy of $\bar{H}^+$ (H^-), -14.360 eV: from a pure energy balance consideration, we expect that the capture of the positron in Ps into $\bar{H}^+$ will be optimal for very low impact kinetic energy.

2.3 Presentation of the present thesis

2.3.1 Earlier reference works on the $\bar{p}$–Ps collisions

The formation of antihydrogen from antiproton and positronium (reaction 2.1) can be more precisely written with the clear appearance of the $\bar{H}$ and Ps states considered (via the use of the quantum numbers (n, l, m)):

$$\mathrm{Ps}(n_p, l_p, m_p) \; + \; \bar{p} \; \rightarrow \; e^- \; + \; \bar{\mathrm{H}}(n_h, l_h, m_h). \tag{2.4}$$

It is the reverse charge-conjugated reaction of positronium formation from positron collision with hydrogen:

$$e^+ \; + \; \mathrm{H}(n_h, l_h, m_h) \; \rightarrow \; \mathrm{Ps}(n_p, l_p, m_p) \; + \; p. \tag{2.5}$$

Similarly, we can rewrite reaction 2.2 with the designation of the $\bar{\mathrm{H}}$ and Ps states:

$$\mathrm{Ps}(n_p, l_p, m_p) \; + \; \bar{\mathrm{H}}(n_h, l_h, m_h) \; \rightarrow \; e^- \; + \; \bar{\mathrm{H}}^+. \tag{2.6}$$

Its charge-conjugated inverse is then the positronium formation from positron binding with an electron of H^-:

$$e^+ \; + \; \mathrm{H}^- \; \rightarrow \; \mathrm{Ps}(n_p, l_p, m_p) \; + \; \mathrm{H}(n_h, l_h, m_h). \tag{2.7}$$

Throughout the thesis, reactions 2.1 & 2.2 and reactions 2.4 & 2.6 will be indiscriminately referred as the "GBAR equations", although with a slight preference toward the latter ones.

The formation of positronium in collisions between a positron and an atomic hydrogen target (reaction 2.5) has already been widely studied for it is the prototype of a 3-body charge exchange reaction, where the three particles involved are distinguishable. But even more than providing a testing ground for atomic collision theories, this reaction, and more precisely its charge conjugated inverse (reaction 2.4) as considered in GBAR, in fact stirred interest for antimatter experiment very early. Indeed, in the 1980s when a sub-GeV beam of antiprotons was available at CERN's LEAR facility, the possibility of efficiently producing antihydrogen atoms using ground state positronium had already been discussed [55]. The importance of using low energy antiprotons was stressed and a note added by the authors of [55] also suggested to investigate the production of excited states of $\bar{\mathrm{H}}$. These cross sections were computed for instance by Igarashi, Toshima & Shirai using hyperspherical coupled-channel calculation [56] and by Mitroy using Unitarised Born Approximation (UBA) [57]. In the latter, the production of $\bar{\mathrm{H}}$ states up to $n_h = 7$ was considered for Ps energies between 0 and 4 eV and, furthermore, for positronium being itself excited (from $n_p = 1$ to 4). Mitroy thus showed that high-n_h antihydrogen levels provide the main contribution to the total $\bar{\mathrm{H}}$ formation cross section. This was later confirmed by a more accurate Close Coupling (CC) calculation [58]. Mitroy also pointed out the interest of having the positronium excited to a state $n_p = 3$ or 4 since these states lead to the highest cross sections below 1 eV centre of mass energy.

Around the same period, experimental values became available for both direct and reverse reactions of 2.5: (*i*) Weber *et al.* [59] and Zhou *et al.* [60] performed scattering experiments of positrons on, respectively, a mixture of H / H_2 and H_2, and deduced from their measurements the total cross section for Ps formation from ground state hydrogen (in the range 0 to $\simeq$ 200 eV positron energy). Their experimental measurements are in good agreement with each other and with available 2-centre CC calculations [61, 62, 63]. The maximum of the cross section is found to be about 3.5 πa_0^2 around 1 Ryd positron energy; (*ii*) three experimental values of hydrogen formation from protons and ground state positronium are also available in the range 11 to 16 keV (proton energy) [64]. The CC calculations of Mitroy & Ryzhikh [58] gives lower values but is almost within the error bars.

More recent theoretical calculations include: 2-centre CC approach by Kadyrov & Bray [65] where the production of Ps(*1s* to *2p*) from ground state hydrogen is considered, modified Faddeev equations [66, 67] for Ps(*1s*)-H(*1s* to *2p*) and Ps(*2s*,*2p*)-H(n_h=2), and also Continuum Distorted Wave - Eikonal Final State (CDW-EFS) [68, 69] for H(*1s*)-Ps(n_p=1 to 5).

If reaction 2.5 is a fundamental 3-body charge exchange reaction, then the reaction of positronium formation from collisions between positrons and H^- ions (reaction 2.7) would be the 4-body equivalent. However, the literature is much less abundant on that process, certainly because of its complexity and the extra care required to describe correctly the highly correlated system that is H^-. Usually, the main motivation in studying reaction 2.7 lies in astrophysics, where it

is supposed to be a major contribution of the 511 keV annihilation line observed.

Straton and Drachman used the Coulomb Born Approximation (CBA) with two wave functions for H^- to compute the cross sections of reaction 2.7 at four different positron energies (0.1, 0.5, 1 and 100 eV) when Ps and H are in their ground state [70]. Chaudhuri highlighted the importance of the choice of the H^- wave function and demonstrated the influence of the correlation description on the total cross section above 50 eV positron energy [71]. Biswas [72] used 2-channel exchange coupled-channel theory to compute the cross section of the reverse process studied in [70], but took a plane wave for the exit channel, and thus did not take into account the long range Coulomb interaction between e^+ and H^-. This resulted in a total cross section going to zero close to the threshold when a finite value is expected. The most complete studies currently available are those of McAlinden *et al.* [73] and Roy and Sinha [74], who both considered the formation of H^- from H(*1s*) + Ps(*1s* to *2p*), using respectively a coupled pseudo-states approach and Coulomb Modified Eikonal Approximation (CMEA). Both concluded to the predominance of Ps(*2p*) at low energy. No experimental result for this 4-body reaction can be found in the literature.

From this rapid review of the different studies dedicated to reactions 2.5 to 2.6, we underline the general lack of computations for excited states of (anti)hydrogen above $n_h = 2$ and, maybe more importantly for GBAR, for positronium excited in a $n_{Ps} = 3$ state. This is particularly true for the second reactions involving four bodies in Coulomb interactions, which furthermore suffers from the absence of experimental data.

Until now, the two set of equations have not been studied as an ensemble of two consecutive reactions. Taken as a whole, they can either describe the stripping of an H^- ion passing through a gaz of positronium or, in the reverse point of view, the production of H^- ions from protons interacting with positronium. These two processes could probably be experimentally studied more easily than the single 4-body process. And of course, from the antimatter point of view, the coupling of reactions 2.4 with 2.6 corresponds to the formation of $\bar{H}^+$ from antiprotons and positronium in GBAR that we will at the centre of the present work.

2.3.2 Purpose and outline of the thesis

The main objective of the thesis is to provide a complete set of cross sections for the GBAR reactions, within a unique theoretical framework, with particular care given to the lesser-studied second reaction. This would become the most extensive study of reactions 2.7 and 2.6. From these cross sections, we intend to identify what should be the kinetic energy of the antiprotons, when they make collisions with positronium, to optimally form the $\bar{H}^+$ ions; we will also investigate different states of ortho-positronium and check that Ps(3d) is indeed the most interesting one to enhance the production of $\bar{H}^+$ ions. In that case, the laser that will be used at CERN to excite the positronium into state 3D can already be built and tested.

The major part of the thesis has therefore been dedicated to the theoretical study of the collisional processes involved in the formation of the antihydrogen atoms and ions in the scope of the GBAR experiment: this corresponds to Part II and Part III. The experimental work of the thesis, consisting in the building of a laser system dedicated to positronium excitation, is presented in Part IV.

- In Part II, we describe the extensive theoretical calculations of the cross sections for reactions 2.4 and 2.6, in the framework of two perturbative theory models, namely Continuum

Distorted Wave – Final State (CDW–FS) and Coulomb-Born Approximation (CBA). This work has been carried out under the supervision of Paul-Antoine Hervieux from IPCMS. We first introduce the CDW–FS model by presenting the Continuum Distorted Wave model family from which it inherits its characteristics. The basis of the analytical calculation are explained and the final expressions of the cross sections are given. The derivation of the CBA cross sections from the CDW–FS model is then explained. The cross section results are finally detailed for positronium excited up to state 3D and antihydrogen up to 5D.

- Part III introduces a simple simulation of the interaction region where the formation of antihydrogen atoms and ions takes place. This simulation, which makes use of the calculated cross sections and focusses on the interesting antiproton energies highlighted by the results of Part II, allows to explore the importance of the different experimental parameters in the final $\bar{H}^+$ yield. We first list the experimental parameters and justify some assumptions that have been made when experimental input was insufficient. Then, each parameter is individually scanned to understand their influence on the antihydrogen ion production. The simulation, developed for the GBAR experiment at CERN, can be adapted to the needs of a positronium spectroscopy experiment or a hydrogen production cross sections measurement at CEA-Saclay.

- Finally, Part IV describes the laser system dedicated to the positronium excitation into state 3D, both for a positonium spectroscopy experiment foreseen at CEA-Saclay and for the optimisation of the antihydrogen ion production in the CERN experiment. After summarising the different effects inducing a broadening or a shift in the 3D line of positronium, we give a technical description of the laser system built at the Laboratoire Kastler-Brossel (LKB) under the supervision of François Nez, and provide practical details orientated toward non-laser specialists. Characterisation of the different laser beams is included. The last chapter is fully dedicated to the utilisation of the laser at CEA-Saclay: we present an experiment which is currently being implemented at LKB to evaluate the possibility of detecting the fluorescence of positronium and we describe, in a few words, the preparation of the laser experimental area at Saclay.

We wrote this thesis also as a reference document for the GBAR collaboration concerning the cross sections of antihydrogen atom and ion production, a paper for anyone willing to take over from the author on the simulation development or the laser. With that didactic purpose declared, we tried to write a document that is accessible for non-specialists in atomic collisions or laser physics, like the author was at the beginning of the thesis.

Part II

Cross section calculations for Antihydrogen and Antihydrogen plus production

Chapter 3

Continuum Distorted Wave – Final State (CDW–FS)

3.1 Origin of the model

3.1.1 The family of Continuum Distorted Wave models

The model called Continuum Distorted Wave (CDW) laid the foundation for a whole branch of collisional theories, among which is the one that has been chosen to compute the cross sections for GBAR. CDW belongs to the family of the perturbation theories and was first introduced to describe charge transfer between heavy particles, that is at least with the mass of a proton, at high energies but still non-relativistic. [75] The transferred charge, an electron, is bound to an atom, while simultaneously in the continuum of an ion. This is a three-body problem involving three Coulomb interactions (two nuclei and one transferred charge). Due to the presence of a charged species – the ion – in the continuum, the First Born Approximation, while being well-suited for excitation reaction, is not sufficient to study the process. [76] The influence of the long-ranged Coulomb potential created by the ion on the bound electron should be included in the description of the initial state (and also in the final state if the residual target is charged). The motion of an electron in the continuum of an ion is described by a Coulomb wave function; the introduction of a Coulomb wave in the initial state (respectively final state) wave function will thus accounts for the distortion due to the Coulomb potential of the charged projectile (respectively residual target). Hence the name of the model: *Continuum Distorted Wave*. The CDW model is equivalent to a second order perturbation theory. The mathematical expression of the continuum Coulomb wave function is given in section 3.1.2.

Since the CDW model was successfully applied to charge transfer in ion-atom collisions, it has been later extended to ionisation in atom-ion collisions [76, 77], and then, for charge exchange reactions, generalised to the continuum of an electron [78] instead of an ion. The latter case is the one of most interest for us, since the capture of a bound positron by an electron to form positronium corresponds to the reversed process of the one involved in antihydrogen and antihydrogen plus production in GBAR. This positron capture by an electron is different from the electron capture by a proton/ion because, in the latter, the motion of the projectile with respect to the target can be treated classically (except at very low energies), whereas for the light particle-projectile, such an approximation cannot be done.

The use of the continuum Coulomb wave functions to describe the initial and final states of the collision process gives the exact boundary conditions. However, specially in the case of ionisation, CDW was reproached to have a faulty normalisation for the initial state wave

function, and this gave rise to new approximations to improve the model. For instance, CDW-EIS, for Eikonal Inital State, replaces the Coulomb wave function by its eikonal approximation in the initial state. [79] CDW theory also has non-relativistic and relativistic versions. In the energy range of GBAR, only the non-relativistic theory is needed. It should also be noted that neglecting the Coulomb interaction in the continuum leads back to a plane wave to describe the propagating particle. For a complete review of the use of CDW, see [76].

3.1.2 Continuum Coulomb wave functions

Coulomb wave functions are first defined as exact solutions of the Coulomb wave equation, which writes:

$$\frac{d^2w}{d\rho^2} + \left(1 - \frac{2\eta}{\rho} - \frac{l(l+1)}{\rho^2}\right) w = 0, \tag{3.1}$$

where η is a real number and l is a non negative integer. [80] This equation is a special case of the radial Schrödinger equation for an electron in a central potential $V(r)$:

$$\left\{-\frac{\hbar^2}{2mr^2}\frac{d}{dr}\left(r^2\frac{d}{dr}\right) + \frac{\hbar^2\, l(l+1)}{2mr^2} + V(r)\right\} R(r) = ER(r). \tag{3.2}$$

Indeed, let's take the radial part $R(r) = \frac{1}{r}P(r)$. Equation 3.2 becomes

$$\frac{d^2P}{dr^2} - \frac{l(l+1)}{r^2}P(r) + \frac{2m}{\hbar^2}\left(E - V(r)\right)P(r) = 0. \tag{3.3}$$

If $V(r)$ is the Coulomb potential created by a proton, then equation 3.3 is, in atomic units:

$$\frac{d^2P}{dr^2} - \frac{l(l+1)}{r^2}P(r) + \left(2E - \frac{2}{r}\right)P(r) = 0. \tag{3.4}$$

This equation is valid for both bound states and continuum states. When looking for the continuum states of the proton, E is positive and equal to $\frac{k^2}{2}$, in atomic units, where $\vec{\mathbf{k}}$ is the wave vector of the electron and k its norm. Taking $\rho = kr$ and dividing equation 3.4 by $2E = k^2$, eq. 3.4 indeed becomes Eq. 3.1 with $\eta = k^{-1}$. The general solutions of eq. 3.1 are of the form:

$$w(l, \eta, \rho) = C_1 F_l(\eta, \rho) + C_2 G_l(\eta, \rho), \tag{3.5}$$

where the F_l functions are called *regular* solutions whereas the G_l functions are the *irregular* solutions; C_1 and C_2 are two multiplicative constants. The G_l functions grow exponentially as r increases: they cannot be used as physical solution for a propagating wave (and are not considered any more afterwards), contrary to the F_l functions which exhibit an oscillating behaviour. The general expression of the F_l functions is [80]:

$$F_l(\eta, \rho) = C_l(\eta)\rho^{l+1}e^{\mp i\rho}\,{}_1F_1(l + 1 \mp i\eta; 2l + 2; \pm 2i\rho), \tag{3.6}$$

with

$$C_l(\eta) = \frac{2^l e^{-\pi\frac{\eta}{2}}|\Gamma(l + 1 + i\eta)|}{(2l + 1)!}. \tag{3.7}$$

${}_1F_1$ is called *confluent hypergeometric function*, and also *Coulomb function*. Later in chapter 4, we will use the notation $F_l(kr) \equiv F_l(\eta, \rho)$ for the radial part of the multi-pole expansion of the

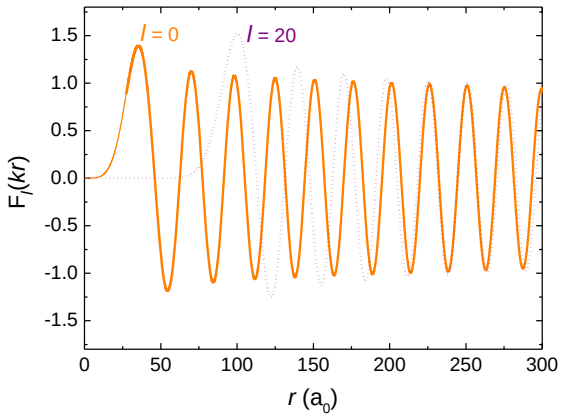


Figure 3.1: Examples of radial parts of continuum Coulomb wave functions for a 1 eV positron moving in the Coulomb potential of a proton. The first maximum of $F_l(kr)$ corresponds to the classical turning point.

Coulomb wave functions $\mathcal{F}_{\boldsymbol{k}}(\boldsymbol{r})$. On figure 3.1, two examples of Coulomb wave function radial parts have been drawn as a function of r, for different values of the l parameters (0 and 20) and a fixed value of k. In the CDW theory, the treatment is slightly different. The electron is first and foremost bound in an atom, while simultaneously in the continuum of a charged particle which induces distortion to the bound state. The Coulomb wave functions introduced are then related to the distorting potential, and the refinement degree of the CDW-related theory comes from the choice of the distorting potential. In the charge exchange problem addressed by CDW, the Schrödinger equation describing the motion of the electron is independent from the internuclear separation $\vec{\mathbf{R}}$: terms proportional to the internuclear potential can thus be conveniently added to the distorting potential.

3.2 CDW–FS for positronium production

3.2.1 First introduction of the CDW–FS model

A. Three-body CDW–FS for hydrogen-like ions

The CDW–FS has been first introduced by Fojón *et al.* [81] in the case of charge transfer collisions involving positrons and hydrogen-like targets (He^+, Li^{2+}, etc.). In this article, the formation of positronium is considered, which places Ps in the final state, to the contrary of the first GBAR reaction (eq. 2.5). The particular feature of the CDW–FS approximation is the addition of a distortion potential to the final channel, leading to the use of two Coulomb wave functions: one for the positron and one for the electron bound in the positronium which both move in the continuum of the residual target. This is a further refinement of the model proposed by Mandal *et al.* [82] is the case of positronium formation from ground state hydrogen. The use of the Coulomb wave functions also ensures the correct asymptotic conditions.

The article by Fojón *et al.* [81] describes the derivation of the CDW–FS transition matrix element expression, along with the possible approximations proceeding from the use of light projectile particles, and explains step by step the analytical development of the transition matrix element toward a computable expression. The GBAR three-body CDW–FS cross section calculations presented in chapter 4 have been adapted from the calculations of [81] and, since the analytical development stages are similar, they are not fully detailed here (only useful mathe-

matical relations are given in appendix C).

B. Four-body formulation for metastable Helium
After applying the CDW–FS to the case of positronium formation from alkali targets [83], with a good agreement obtained between the theoretical results for potassium and related experiment, the model received a further extension as the formation of positronium from helium and alkaline-earth metals was investigated. This time, the transfer-excitation reactions involved four bodies (a target formed of the atomic nucleus and inner shell electrons, two outer-shell electrons and the positron projectile), requiring to develop a four-body CDW–FS approximation. [84] The extended model was then applied to the case of metastable helium – (1s2s) excited states – and a description of the corresponding four-body CDW–FS calculation is given in [85]. The similitude between the metastable helium system and the H^- system led to the application of four-body CDW–FS to the second reaction of $\bar{H}^+$ formation in GBAR.

3.2.2 Characteristics and limitations of the model

A. Main features of CDW–FS
Among the characteristics of the CDW–FS, we select here three main features that qualified the model for the computation of the $\bar{H}$ and $\bar{H}^+$ formation cross sections for GBAR:

- The careful treatment of the exact boundary conditions, in particular for the positronium in the final state;
- The same level of approximation for both the 3-body and 4-body formulations, giving an equal treatment to the two GBAR reactions;
- The flexibility of the model, allowing the computation of many excited states cases, provided that the convergence of the discrete sums and integrals has been checked.

B. Domain of validity
The domain of validity of the CDW–FS model covers intermediate and high energies, as most of the CDW theories. The intermediate energy region is not a very well defined region: it is often considered to start above two or three times the threshold values, which, in some of our cases, could be already at zero energy (*cf* appendix B). This can also be defined in terms of transferred energy compared to impact energy, or even corresponds to a projectile velocity greater than the mean orbital velocity of the electron (in both the initial and final states). Using the latter definition, the intermediate energy region can be considered to start around 13 keV in the worse case. This is obviously above the expected energies of interest for GBAR which should be below 10 keV. In general, CDW theories are thought to have a more extended domain of validity than expected. [86, 68] In any case, values close to the threshold should not be expected to be correct, but the relative behaviour of the cross sections should be a reliable information. The best way to obtain the correct behaviour at low energies is to compare CDW with Close Coupling calculations or, even better, Faddeev calculations, which give exact results at the threshold: CDW–FS results could then be connected to these calculations, which are limited far from the thresholds. At high energies, most of the perturbative theories give comparable results: though this energy region is of less interest for GBAR, the computation of the cross sections in this energy range allows to check the validity of CDW–FS calculations by comparing with other established theoretical results.

C. Post-prior discrepancy

The *post/prior* discrepancy can arise from rearrangement collisions, like the ones we are interested in for GBAR. Indeed, in rearrangement collisions, the particles are different in the initial and the final states, implying that the interaction potential in the exit channel is different from the one in the entrance channel. When writing the transition matrix element corresponding to the reaction, a choice has thus to be made between the potential perturbating the initial state, V_i, and the one of the final state, V_f. In the former case, the *prior* from of the theory is obtained, while in the latter case, it is called the *post* form. Obviously, there is little chance that V_i and V_f, with their adequate asymptotic conditions, lead to the same results for the transition matrix element. This is what is called the *post/prior* discrepancy. Perturbation theories are more or less sensitive to it, and, in general, it is emphasised toward low energies.

Several authors give both *prior* and *post* forms of the theoretical models and compare the obtained results. For instance, Straton and Drachman [70] did it for their orthogonalised Fock-Tani model and for CBA. In the case of CDW, the *post/prior* discrepancy has been studied by Bransden *et al.* [86]. The observed effect can be as large as half an order of magnitude discrepancy between the two. This should be kept in mind for CDW–FS. Since we based our calculations on the original CDW–FS work by Fojòn [81], we used the *prior* formulation of the CDW–FS theory; developing the *post* formulation would be an entirely new study that could not be done in the time of this thesis.

Chapter 4

Analytical calculations

This chapter has been built from the material published in the *New Journal of Physics* article. [87] Complements are given in appendices B and C: first, in appendix B, are given the thresholds for all the considered reactions (both direct and reverse); in appendix C, mathematical tools used in the analytical computation of the cross sections are detailed (mainly various formulas involving spherical harmonic functions, *3-j*, *6-j* and *9-j* symbols). The cross sections for antihydrogen and antihydrogen plus are given in the general case for any excited state of positronium and antihydrogen. For particular cases, that is $l_h = 0$ and/or $l_p = 0$, the cross sections are given in appendix D.

4.1 Antihydrogen production

4.1.1 General case: $l_h,\ l_p \geq 0$

The capture of an electron with positronium formation in e^+-H collisions is considered (reaction (2.5)). Figure 4.1 describes the coordinates used in this section; for further discussion and details about the CDW-FS model of this reaction and on the choice of the coordinates, see [81].

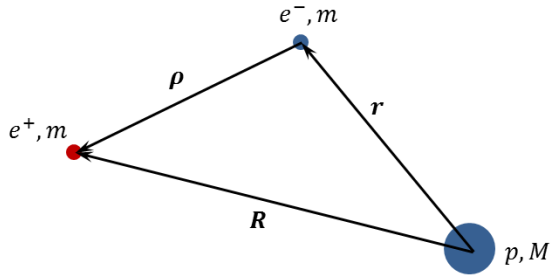


Figure 4.1: Coordinates used for reaction (2.5).

The wave function corresponding to the entrance channel is

$$\xi_\alpha^{(+)} = \varphi_{n_h l_h m_h}(\boldsymbol{r}) \mathcal{F}_{\boldsymbol{k}_\alpha}^{(+)}(\boldsymbol{R}), \tag{4.1}$$

where $\varphi_{n_h l_h m_h}(\boldsymbol{r}) = R_{n_h l_h}(r) Y_{l_h m_h}(\hat{\boldsymbol{r}})$ is the wave function of the electron in the hydrogen atom in the $(n_h l_h m_h)$ state and $\mathcal{F}_{\boldsymbol{k}_\alpha}^{(+)}(\boldsymbol{R})$ is the Coulomb wave function of the positron in the continuum

of the hydrogen target. The final state is described by the wave function

$$\xi_\beta^{(-)} = \psi_{n_p l_p m_p}(\boldsymbol{\rho}) \mathcal{F}_{\boldsymbol{k}_-}^{(-)}(\boldsymbol{r}) \mathcal{F}_{\boldsymbol{k}_+}^{(-)}(\boldsymbol{R}), \tag{4.2}$$

where $\psi_{n_p l_p m_p}(\boldsymbol{\rho}) = \tilde{R}_{n_p l_p}(\rho) Y_{l_p m_p}(\hat{\boldsymbol{\rho}})$ is the wave function of the electron bound in the positronium atom, formed in the $(n_p l_p m_p)$ state, $\mathcal{F}_{\boldsymbol{k}_-}^{(-)}(\boldsymbol{r})$ and $\mathcal{F}_{\boldsymbol{k}_+}^{(-)}(\boldsymbol{R})$ are respectively the Coulomb wave functions of the outgoing electron and positron in the continuum of the residual proton of charge Z_T=1. The Coulomb wave functions write as

$$\mathcal{F}_{\boldsymbol{k}_\alpha}^{(+)}(\boldsymbol{R}) = N_{\alpha+} \exp\left[i \frac{\boldsymbol{k}_\alpha}{\mu_\alpha}.\boldsymbol{R}\right] \; {}_1F_1\left(-i\alpha_+; 1; -i\frac{\boldsymbol{k}_\alpha}{\mu_\alpha}.\boldsymbol{R} + i\frac{k_\alpha}{\mu_\alpha}R\right), \tag{4.3}$$

with $\alpha_+ = (Z_T - 1)\frac{\mu_\alpha}{k_\alpha} = 0$ since the charge $Z_T - 1$ of the hydrogen target is 0 (in which case, the Coulomb wave function actually reduces to a plane wave) and $N_{\alpha+} = \Gamma(1 + i\alpha_+) \exp\left(-\frac{\pi}{2}\alpha_+\right)$. $\boldsymbol{k}_\alpha$ is the wavevector of the reduced positron in the entrance channel and μ_α is the reduced mass of the positron-target system ($\mu_\alpha = \frac{m(M+m)}{M+2m} \simeq m$);

$$\mathcal{F}_{\boldsymbol{k}_+}^{(-)}(\boldsymbol{R}) = N_{\beta+} \exp\left[i \frac{\boldsymbol{k}_+}{\mu_\beta}.\boldsymbol{R}\right] \; {}_1F_1\left(i\beta_+; 1; -i\frac{\boldsymbol{k}_+}{\mu_\beta}.\boldsymbol{R} - i\frac{k_+}{\mu_\beta}R\right), \tag{4.4}$$

with $\beta_+ = Z_T \frac{\mu_\beta}{k_+}$ and $N_{\beta+} = \Gamma(1 - i\beta_+) \exp\left(-\frac{\pi}{2}\beta_+\right)$. $\boldsymbol{k}_+$ is the wavevector of the reduced positron in the exit channel and μ_β is the reduced mass of the positronium-residual target system ($\mu_\beta = \frac{2m \times M}{M+2m} \simeq 2m$);

$$\mathcal{F}_{\boldsymbol{k}_-}^{(-)}(\boldsymbol{r}) = N_{\beta-} \exp\left[i \frac{\boldsymbol{k}_-}{\mu_\beta}.\boldsymbol{r}\right] \; {}_1F_1\left(-i\beta_-; 1; -i\frac{\boldsymbol{k}_-}{\mu_\beta}.\boldsymbol{r} - i\frac{k_-}{\mu_\beta}r\right), \tag{4.5}$$

with $\beta_- = Z_T \frac{\mu_\beta}{k_-}$ and $N_{\beta-} = \Gamma(1+i\beta_-) \exp\left(+\frac{\pi}{2}\beta_-\right)$. $\boldsymbol{k}_-$ is the wavevector of the reduced electron in the exit channel. $\boldsymbol{k}_+ \simeq \boldsymbol{k}_- \simeq \frac{\boldsymbol{k}_\beta}{\mu_\beta}$, where $\boldsymbol{k}_\beta$ is the wavevector of the reduced positronium in the exit channel. Even if the exit channel of reaction (2.5) is not Coulombic as it contains two species with only one having the overall charge, the CDW-FS model includes distortions in the final channel which are related to the Coulomb continuum states of the positron and the electron (of the positronium atom) in the field of the residual target (the proton). Therefore, the continuum wave functions (4.4) and (4.5) do not reduce to plane waves. If no distortions are included in the final channel, the Coulomb Born approximation (CBA) is obtained. This situation is similar to the one described in [81]. These results will be discussed in section 7.1.

In order to compute the transition matrix element, the following partial wave expansion of the Coulomb wave functions has been used

$$\mathcal{F}_{\boldsymbol{k}}^{(\pm)}(\boldsymbol{r}) = 4\pi \sum_{lm} (i)^l \, e^{\pm i\delta_l} \, \frac{1}{kr} \, F_l(kr) \, Y_{lm}^*(\hat{\boldsymbol{k}}) \, Y_{lm}(\hat{\boldsymbol{r}}), \tag{4.6}$$

where the functions $F_l(kr)$ are the Coulomb radial functions with the Sommerfeld parameters $\eta = \beta_\pm$ or $\eta = \alpha_+$, and δ_l are the usual Coulomb phase shifts $\delta_l = \arg\Gamma(l + 1 + i\eta)$.

The spherical harmonic function $Y_{l_p m_p}(\hat{\boldsymbol{\rho}})$ has been treated using the development (equation 29 in [88])

$$\begin{aligned} Y_{LM}(\hat{\boldsymbol{\rho}}) &= \rho^{-L}(-1)^{L+M}\sum_{\lambda\mu}\left(\frac{\hat{L}!\;\hat{L}\;4\pi}{\hat{\lambda}!\;\widehat{(L-\lambda)!}}\right)^{\frac{1}{2}} R^{L-\lambda}r^{\lambda}\begin{pmatrix} L-\lambda & \lambda & L \\ M-\mu & \mu & -M\end{pmatrix} \\ &\times \quad Y_{L-\lambda\;M-\mu}(\hat{\boldsymbol{R}})\;Y_{\lambda\mu}(-\hat{\boldsymbol{r}}), \end{aligned} \tag{4.7}$$

where $0 \le \lambda \le L$ and $-\lambda \le \mu \le \lambda$.

The perturbative potential in the entrance channel *(initial state)* is

$$V_\alpha = \left(\frac{1}{R} - \frac{1}{\rho}\right). \tag{4.8}$$

The transition matrix element is then

$$\begin{aligned} T^{(-)}_{\alpha\beta} &= \left\langle \xi^{(-)}_\beta \right| V_\alpha \left| \xi^{(+)}_\alpha \right\rangle \\ &= (-1)^{l_p+m_h}\;\frac{(4\pi)^{\frac{3}{2}}}{k_+k_\alpha k_-}\;\hat{l}_h^{\frac{1}{2}}\hat{l}_p^{\frac{1}{2}}(\hat{l}_p!)^{\frac{1}{2}}\sum_{l_i\mathcal{L}}\;i^{l_i}\;e^{i\delta_{l_i}}\;\hat{\mathcal{L}}^{\frac{1}{2}}\hat{l}_i\;\mathcal{S}_{l_i\mathcal{L}}\;Y_{\mathcal{L}m_h-m_p}(\hat{\boldsymbol{k}}_\beta), \end{aligned} \tag{4.9}$$

with

$$\begin{aligned} \mathcal{S}_{l_i\mathcal{L}} &= \sum_{l_f l l' L L'}\;\sum_{0\le\lambda\le l_p} i^{-l-l_f}\;e^{i(\delta_l+\delta_{l_f})}\;\mathcal{A}^{\lambda l_f l l' L L'}_{l_i\mathcal{L}}\mathcal{R}^{\lambda l l'}_{l_i l_f}, \\ \mathcal{A}^{\lambda l_f l l' L L'}_{l_i\mathcal{L}} &= (-1)^{\lambda}\left(\frac{\hat{l}_f\hat{l}\hat{l}'\hat{L}\hat{L}'}{((2\lambda)!(2(l_p-\lambda))!)^{\frac{1}{2}}}\right)^{\frac{1}{2}} \\ &\times\begin{pmatrix} l_f & l & \mathcal{L}\\ 0 & 0 & 0\end{pmatrix}\begin{pmatrix} l' & l_h & L\\ 0 & 0 & 0\end{pmatrix}\begin{pmatrix} l_p-\lambda & l' & L'\\ 0 & 0 & 0\end{pmatrix}\begin{pmatrix} \lambda & l & L\\ 0 & 0 & 0\end{pmatrix} \\ &\times\begin{pmatrix} l_f & L' & l_i\\ 0 & 0 & 0\end{pmatrix}\sum_{\mu m_f}(-1)^{m_f}\begin{pmatrix} \lambda & l & L\\ \mu & m_f+m_p-m_h & m_h-m_p-\mu-m_f\end{pmatrix} \\ &\times\begin{pmatrix} l_p-\lambda & \lambda & l_p\\ -m_p-\mu & \mu & m_p\end{pmatrix}\begin{pmatrix} l_p-\lambda & l' & L'\\ -m_p-\mu & \mu+m_p+m_f & -m_f\end{pmatrix} \\ &\times\begin{pmatrix} l_f & L' & l_i\\ -m_f & m_f & 0\end{pmatrix}\begin{pmatrix} l_f & l & \mathcal{L}\\ m_f & m_h-m_p-m_f & m_p-m_h\end{pmatrix} \\ &\times\begin{pmatrix} l' & l_h & L\\ -m_f-m_p-\mu & m_h & m_f+m_p+\mu-m_h\end{pmatrix}, \\ \mathcal{R}^{\lambda l l'}_{l_i l_f} &= \int_0^\infty dR\;R^{l_p-\lambda}\;F_{l_f}(k_+R)\;\mathcal{V}_{\lambda l l'}(R)\;F_{l_i}(k_\alpha R), \\ \mathcal{V}_{\lambda l l'}(R) &= \int_0^\infty dr\;r^{\lambda+1}\;\mathcal{R}_{n_h l_h}(r)\;\mathcal{J}^{l_p}_{l'}(r,R)\;F_l(k_-r), \\ \mathcal{J}^{l_p}_{l'}(r,R) &= \frac{1}{2}\int_{-1}^{1} du\;\rho^{-l_p}\;\tilde{\mathcal{R}}_{n_p l_p}(\rho)\left(\frac{1}{R}-\frac{1}{\rho}\right)P_{l'}(u). \end{aligned} \tag{4.10}$$

In the above expression, the variable u is defined as $\rho = \sqrt{r^2 + R^2 + 2rRu}$ and $\hat{l}$ indicates $\hat{l} = 2l + 1$. $\mathrm{P}_{l'}$ is the Legendre polynomial of degree l', coming from the multipole expansion

$$\rho^{-l_p}\ \tilde{\mathcal{R}}_{n_p l_p}(\rho)\ \left(\frac{1}{R} - \frac{1}{\rho}\right)\ =\ 4\pi \sum_{l'm'}\ \mathcal{J}_{l'}^{l_p}(r,R)\ Y^*_{l'm'}(\hat{\boldsymbol{R}})\ Y_{l'm'}(\hat{\boldsymbol{r}}). \tag{4.11}$$

The CDW–FS total cross section for $\mathrm{Ps}(n_p, l_p)$ formation from $\mathrm{H}(n_h, l_h)$ (reaction (2.5)) is given by

$$\begin{aligned}
\sigma^{3B,1}_{n_h l_h;\ n_p l_p} &= \frac{1}{\hat{l}_h} \sum_{m_h m_p} \frac{1}{4\pi^2}\ \frac{k_\beta}{k_\alpha}\ \mu_\alpha \mu_\beta \int d\hat{\boldsymbol{k}}_\beta \left| T^{(-)}_{\alpha\beta} \right|^2 \\
&= 16\pi\ \frac{k_\beta}{k_-^2\, k_+^2\, k_\alpha^3}\ \mu_\alpha \mu_\beta\ \hat{l}_p ! \hat{l}_p \sum_{m_h m_p} \sum_{l_i l'_i \mathcal{L}}\ i^{l_i - l'_i}\ e^{\,i(\delta_{l_i} - \delta_{l'_i})}\ \hat{l}_i \hat{l}'_i \hat{\mathcal{L}}\ \left(\mathcal{S}^*_{l'_i \mathcal{L}} \times \mathcal{S}_{l_i \mathcal{L}} \right)
\end{aligned} \tag{4.12}$$

This is the first record of CDW–FS cross sections calculated for any excited state of hydrogen and positronium: so far, l_p had always been kept equal to zero [81] (with the exception of $\mathrm{Ps}(2p)$ in [83], but the angular part of the $\mathrm{Ps}(2p)$ wave function had in fact been taken equal to $1/\sqrt{(4\pi)}$).

4.1.2 Conversion from inverse to direct reaction

The previous cross section is given for the inverse reaction of the one of interest for GBAR, since it has been adapted from other studies considering the formation of positronium. This cross section for positronium formation can easily be related to the cross section for antihydrogen formation. [55] To obtain the cross sections for the direct reaction for antihydrogen production (equation 2.4), the following kinetic transformation is applied, assuming microreversibility [89, 55] and, obviously, invariance by charge conjugation:

$$\sigma^{3B,2}_{n_h l_h;\ n_p l_p} = \frac{\hat{l}_h}{\hat{l}_p} \frac{k_\alpha^2}{k_\beta^2} \sigma^{3B,1}_{n_h l_h;\ n_p l_p} \tag{4.13}$$

where $\frac{1}{2}\frac{k_\beta^2}{2m}$ is almost the kinetic energy of the positronium atom in the centre of mass and $\frac{1}{2}\frac{k_\alpha^2}{m}$ almost the kinetic energy of the electron/positron in the centre of mass. To obtain this relation, one can write and compare the expressions of $\sigma^{3B,1}_{n_h l_h;\ n_p l_p}$ and $\sigma^{3B,2}_{n_h l_h;\ n_p l_p}$, respectively the cross sections for reactions 2.5 and 2.4. We already wrote in the previous section:

$$\sigma^{3B,1}_{n_h l_h;\ n_p l_p}\ =\ \frac{1}{\hat{l}_h} \sum_{m_h m_p} \frac{1}{4\pi^2}\ \frac{k_\beta}{k_\alpha}\ \mu_\alpha \mu_\beta \int d\hat{\boldsymbol{k}}_\beta \left| T^{(-)}_{\alpha\beta} \right|^2, \tag{4.14}$$

where the sum over the possible magnetic quantum numbers in the final state has been made($\sum_{m_p}$) while the average has been made over the initial states ($\frac{1}{\hat{l}_h} \sum_{m_h}$). According to what has been done previously, $\boldsymbol{k}_\alpha$ is the wavevector of the reduced particle in the entrance channel, reasonably assumed to be equal to the one of the positron in the present case, and $\boldsymbol{k}_\beta$ the wavevector of the reduced particle in the exit channel, which is almost equal to the one of the positronium. Similarly, one can write (with i and f indexing the *initial* and *final* states in reaction 2.4):

$$\sigma^{3B,2}_{n_h l_h;\ n_p l_p} = \frac{1}{\hat{l}_p} \sum_{m_h m_p} \frac{1}{4\pi^2}\ \frac{k_f}{k_i}\ \mu_i \mu_f \int d\hat{\boldsymbol{k}}_f \left| T^{(-)}_{if} \right|^2, \tag{4.15}$$

where $\boldsymbol{k}_i$ the wavevector of the reduced particle in the entrance channel of 2.4, almost equal to the wavevector of the positronium, and $\boldsymbol{k}_f$ the wavevector of the reduced particle in the exit channel of 2.4, which can be taken to be equal to the one of the electron. We thus have $\boldsymbol{k}_i \approx \boldsymbol{k}_\beta$ and $\boldsymbol{k}_f \approx \boldsymbol{k}_\alpha$. The same thing can be written for the mass of the reduced particles: $\mu_i \approx \mu_\beta$ and $\mu_f \approx \mu_\alpha$. The detailed balance principle (also called microreversibility principle) allows to write the equality of the two transition matrix elements:

$$\left|T^{(-)}_{\alpha\beta}\right| = \left|T^{(-)}_{if}\right|, \tag{4.16}$$

and this leads to the relation

$$\sum_{m_h m_p} \int d\hat{\boldsymbol{k}}_f \left|T^{(-)}_{if}\right| \;=\; 4\pi^2 \hat{l}_h \frac{k_\alpha}{k_\beta} \frac{1}{\mu_\alpha \mu_\beta} \sigma^{3B,1}_{n_h l_h;\; n_p l_p}, \tag{4.17}$$

from which one can express $\sigma^{3B,2}_{n_h l_h;\; n_p l_p}$ as given in 4.13.

4.2 Antihydrogen positive ion production

4.2.1 General case: $l_p,\ l_h \geq 0$

We develop here the very general case where both l_h and l_p are different from 0 (the particular cases when $l_h = 0$, $l_p = 0$ and $l_h = l_p = 0$ are described in appendix D) and the wave function for H^- is of the form

$$\Phi_\alpha(\boldsymbol{r}_1, \boldsymbol{r}_2) \;=\; f(r_1, r_2)\,(1 + g(r_{12}))\,, \tag{4.18}$$

where r_{12} is defined as $r_{12} = |\boldsymbol{r}_1 - \boldsymbol{r}_2|$. This wave function has been treated using a partial wave expansion which can be written as follows

$$\Phi_\alpha(\boldsymbol{r}_1, \boldsymbol{r}_2) \;=\; 4\pi \sum_{l_t m_t} \tilde{h}_{l_t}(r_1, r_2)\; Y^*_{l_t m_t}(\hat{\boldsymbol{r}}_1)\; Y_{l_t m_t}(\hat{\boldsymbol{r}}_2) \tag{4.19}$$

with

$$\left\{ \begin{array}{rcll} \tilde{h}_0 & = & f + \tilde{g}_0 & \text{if } l_t = 0, \\ \tilde{h}_{l_t} & = & \tilde{g}_{l_t} & \text{for } \mathrm{l_t} \neq 0, \end{array} \right. \tag{4.20}$$

and

$$\tilde{g}_{l_t}(r_1, r_2) \;=\; \frac{f(r_1, r_2)}{2} \int_{-1}^{1} du\; g(r_{12})\; P_{l_t}(u), \tag{4.21}$$

where $r_{12} = \sqrt{r_1^2 + r_2^2 + 2 r_1 r_2 u}$.

Figure 4.2 describes the coordinates used for the 4-body reaction, similarly to [85] and derived from [84]. The wave function of the initial state is

$$\xi^{(+)}_\alpha = \Phi_\alpha(\boldsymbol{r}_1, \boldsymbol{r}_2) \mathcal{F}^{(+)}_{\boldsymbol{k}_\alpha}(\boldsymbol{R}), \tag{4.22}$$

with the Coulomb wave function $\mathcal{F}^{(+)}_{\boldsymbol{k}_\alpha}(\boldsymbol{R})$ describing the positron in the continuum of H^- (see Eq. (4.3)). $\boldsymbol{k}_\alpha$ is the wavevector of the reduced positron in the entrance channel with $\mu_\alpha =$

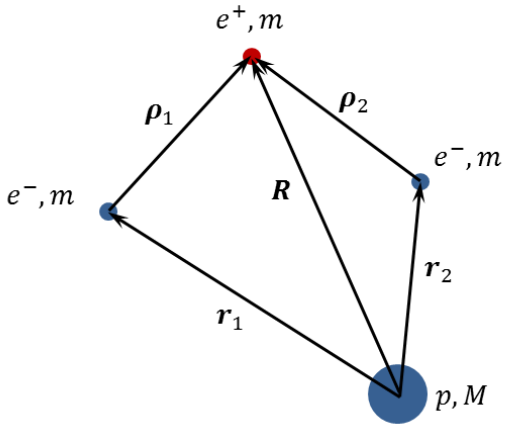


Figure 4.2: Coordinates used for reaction (2.7).

$\frac{m(M+2m)}{M+3m} \simeq m$ the reduced mass of the positron-H^- target system. The wave function for the final state is

$$\xi_\beta^{(-)} = \frac{1}{\sqrt{2}} \left\{ \psi_\beta(\boldsymbol{\rho}_1) \mathcal{F}_{\boldsymbol{k}_-}^{(-)}(\boldsymbol{r}_1) \varphi_{n_h l_h m_h}(\boldsymbol{r}_2) \; + \; \psi_\beta(\boldsymbol{\rho}_2) \mathcal{F}_{\boldsymbol{k}_-}^{(-)}(\boldsymbol{r}_2) \varphi_{n_h l_h m_h}(\boldsymbol{r}_1) \right\} \mathcal{F}_{\boldsymbol{k}_+}^{(-)}(\boldsymbol{R}), \qquad (4.23)$$

where $\psi_\beta(\boldsymbol{\rho}_i)\mathcal{F}_{\boldsymbol{k}_-}^{(-)}(\boldsymbol{r}_i)$ describes electron i captured in the outgoing positronium while electron j remains in the residual hydrogen atom ($\varphi_{n_h l_h m_h}(\boldsymbol{r}_j)$); $\mathcal{F}_{\boldsymbol{k}_+}^{(-)}(\boldsymbol{R})$ is the Coulomb wave function of the outgoing positron (see Eq. (4.4)). $\boldsymbol{k}_\beta$ is the wavevector of the reduced positronium in the exit channel; we also define $\mu_\beta = \frac{2m(M+m)}{M+3m} \simeq 2m$, the reduced mass of the positronium-residual target system. As defined in the previous section, $\boldsymbol{k}_+ \simeq \boldsymbol{k}_- \simeq \frac{\boldsymbol{k}_\beta}{\mu_\beta}$. Again, a partial wave expansion of the Coulomb wave functions has been used (see Eq. (4.6)). The Sommerfeld parameters are $\alpha_+ = (Z_T - 2)\frac{\mu_\alpha}{k_\alpha}$, $\beta_+ = (Z_T - 1)\frac{\mu_\beta}{k_+}$ and $\beta_- = (Z_T - 1)\frac{\mu_\beta}{k_-}$; since the proton charge $Z_T = 1$, we have $\beta_\pm = 0$: therefore, it should be noted that the Coulomb wave functions for the electron and the positron in the exit channel are actually plane waves. The Coulomb phase shifts δ_l are defined as in the previous section. The ^1S symmetry of the initial state of H^- imposes the symmetry in the final state, hence the choice of the expression (4.23) for $\xi_\beta^{(-)}$.

The chosen short-range perturbative potential is

$$V_\alpha = \left(\frac{2}{R} - \frac{1}{\rho_1} - \frac{1}{\rho_2} \right), \qquad (4.24)$$

and the 4-body CDW-FS matrix element $T_{\alpha\beta}^{(-)}$ reads as

$$\begin{aligned} T_{\alpha\beta}^{(-)} &= \left\langle \xi_\beta^{(-)} \middle| V_\alpha \middle| \xi_\alpha^{(+)} \right\rangle \\ &= \int d\boldsymbol{R} \; \mathcal{F}_{\boldsymbol{k}_+}^{(-)*}(\boldsymbol{R}) \; V_T(\boldsymbol{R}) \; \mathcal{F}_{\boldsymbol{k}_\alpha}^{(+)}(\boldsymbol{R}), \end{aligned} \qquad (4.25)$$

with

$$\begin{aligned} V_T(\boldsymbol{R}) &= \sqrt{2}\int\int d\boldsymbol{r}_1 d\boldsymbol{r}_2 \tilde{R}_{n_p l_p}(\rho_1) Y^*_{l_p m_p}(\hat{\boldsymbol{\rho}}_1)\ \mathcal{F}^{(-)*}_{\boldsymbol{k}_-}(\boldsymbol{r}_1) \\ &\qquad \times R_{n_h l_h}(\boldsymbol{r}_2) Y^*_{l_h m_h}(\hat{\boldsymbol{r}}_2)\left(\frac{1}{R}-\frac{1}{\rho_1}\right)\Phi_\alpha(\boldsymbol{r}_1,\boldsymbol{r}_2) \\ &+ \sqrt{2}\int\int d\boldsymbol{r}_1 d\boldsymbol{r}_2 \tilde{R}_{n_p l_p}(\rho_1) Y^*_{l_p m_p}(\hat{\boldsymbol{\rho}}_1)\ \mathcal{F}^{(-)*}_{\boldsymbol{k}_-}(\boldsymbol{r}_1) \\ &\qquad \times R_{n_h l_h}(\boldsymbol{r}_2) Y^*_{l_h m_h}(\hat{\boldsymbol{r}}_2)\left(\frac{1}{R}-\frac{1}{\rho_2}\right)\Phi_\alpha(\boldsymbol{r}_1,\boldsymbol{r}_2) \\ &\equiv V_{cap}(\boldsymbol{R}) + V_{exc}(\boldsymbol{R}), \end{aligned} \tag{4.26}$$

where "*cap*" stands for *capture* and "*exc*" for *excitation*, notations that are justified in the case of the uncorrelated Chandrasekhar wave function (see 5.1.1). The transition matrix element $T^{(-)}_{\alpha\beta}$ can thus be written as a sum of two terms, t_{cap} and t_{exc}. After some calculations, the former term may be expressed as

$$\begin{aligned} t_{cap} &= \int d\boldsymbol{R}\ \mathcal{F}^{(-)*}_{\boldsymbol{k}_+}(\boldsymbol{R})\ V_{cap}(\boldsymbol{R})\ \mathcal{F}^{(+)}_{\boldsymbol{k}_\alpha}(\boldsymbol{R}) \\ &= (-1)^{l_p}\ \sqrt{2}\ \frac{(4\pi)^{\frac{5}{2}}}{k_- k_\alpha k_+}\ \left(\hat{l}_p!\hat{l}_p\hat{l}_h\right)^{\frac{1}{2}}\ \sum_{l_i\mathcal{L}}\ i^{l_i}\ e^{i\delta_{l_i}}\ \hat{l}_i\hat{\mathcal{L}}^{\frac{1}{2}}\ \mathcal{S}_{l_i\mathcal{L}}\ Y_{\mathcal{L}\ -m_p-m_h}(\hat{\boldsymbol{k}}_\beta), \end{aligned} \tag{4.27}$$

where

$$\begin{aligned} \mathcal{S}_{l_i\mathcal{L}} &= \sum_{l_f l l' L L' \lambda}\ i^{-l-l_f}\ e^{i(\delta_l+\delta_{l_f})}\ \mathcal{A}^{l_f l l' L L' \lambda}_{l_i\mathcal{L}}\ \mathcal{R}_{l_f l l' \lambda l_i}, \\ \mathcal{A}^{l_f l l' L L' \lambda}_{l_i\mathcal{L}} &= (-1)^\lambda\ \frac{\hat{l}_f\hat{l}\hat{l}'\hat{L}\hat{L}'}{((2\lambda)!(2(l_p-\lambda))!)^{\frac{1}{2}}} \begin{pmatrix} l_h & l' & L \\ 0 & 0 & 0 \end{pmatrix} \begin{pmatrix} l & \lambda & L \\ 0 & 0 & 0 \end{pmatrix} \\ &\quad \times \begin{pmatrix} l' & l_i & L' \\ 0 & 0 & 0 \end{pmatrix} \begin{pmatrix} l_f & l_p-\lambda & L' \\ 0 & 0 & 0 \end{pmatrix} \begin{pmatrix} l_f & l & \mathcal{L} \\ 0 & 0 & 0 \end{pmatrix} \\ &\quad \times \sum_{\mu m'} (-1)^{m'} \begin{pmatrix} l_p-\lambda & \lambda & l_p \\ -m_p-\mu & \mu & m_p \end{pmatrix} \begin{pmatrix} l_h & l' & L \\ -m_h & m' & m_h-m' \end{pmatrix} \\ &\quad \times \begin{pmatrix} l' & l_i & L' \\ -m' & 0 & m' \end{pmatrix} \begin{pmatrix} l_f & l & \mathcal{L} \\ -m'-m_p-\mu & m'+\mu-m_h & m_p+m_h \end{pmatrix} \\ &\quad \times \begin{pmatrix} l & \lambda & L \\ m_h-m'-\mu & \mu & m'-m_h \end{pmatrix} \begin{pmatrix} l_f & l_p-\lambda & L' \\ m'+m_p+\mu & -m_p-\mu & -m' \end{pmatrix}, \\ \mathcal{R}_{l_f l l' \lambda l_i} &= \int_0^\infty dR\ R^{l_p-\lambda}\ F_{l_f}(k_+R)\ \mathcal{V}_{\lambda l l'}(R)\ F_{l_i}(k_\alpha R), \end{aligned}$$

$$
\begin{aligned}
\mathcal{V}_{\lambda l l'}(R) &= \int_0^\infty dr\ r^{\lambda+1}\ \mathcal{L}_{n_h l_h}(r)\ \mathcal{J}^{l_p}_{l'}(r,R)\ F_l(k_- R), \\
\mathcal{J}^{l_p}_{l'}(r,R) &= \frac{1}{2}\int_{-1}^{1} du\ \rho^{-l_p}\ R_{n_p l_p}(\rho)\left(\frac{1}{R}-\frac{1}{\rho}\right) P_{l'}(u), \\
\mathcal{L}_{n_h l_h}(r_1) &= \int_0^\infty dr_2\ r_2^2\ R_{n_h l_h}(r_2)\ \tilde{h}_{l_h}(r_1,r_2). \qquad (4.28)
\end{aligned}
$$

Similarly the *excitation* transition matrix element is given by

$$
\begin{aligned}
t_{exc} &= \int d\boldsymbol{R}\ \mathcal{F}^{(-)*}_{\boldsymbol{k}_+}(\boldsymbol{R})\ V_{exc}(\boldsymbol{R})\ \mathcal{F}^{(+)}_{\boldsymbol{k}_\alpha}(\boldsymbol{R}) \\
&= (-1)^{l_p}\ \sqrt{2}\ \frac{(4\pi)^{\frac{5}{2}}}{k_- k_\alpha k_+}\ \left(\hat{l}_p!\hat{l}_p\hat{l}_h\right)^{\frac{1}{2}}\ \sum_{l_i\tilde{l}} i^{l_i}\ e^{i\delta_{l_i}}\ \hat{l}_i\hat{\tilde{l}}^{\frac{1}{2}}\ \tilde{\mathcal{S}}_{l_i\tilde{l}}\ Y_{\tilde{l}\ -m_p-m_h}(\hat{\boldsymbol{k}}_\beta), \qquad (4.29)
\end{aligned}
$$

with

$$
\begin{aligned}
\tilde{\mathcal{S}}_{l_i\tilde{l}} &= \sum_{l_f l_t \Lambda l l' \lambda L L' \tilde{L}} i^{-l-l_f}\ e^{i(\delta_l+\delta_{l_f})}\ \tilde{\mathcal{A}}^{l_f l_t \Lambda l l' \lambda L L' \tilde{L}}_{l_i\tilde{l}}\ \tilde{\mathcal{R}}_{l_f l_t \Lambda l l' \lambda l_i}, \\
\tilde{\mathcal{A}}^{l_f l_t \Lambda l l' \lambda L L' \tilde{L}}_{l_i\tilde{l}} &= (-1)^\lambda\ \frac{\hat{l_f}\hat{l_t}\hat{\Lambda}\hat{l}\hat{l'}\hat{L}\hat{L'}\hat{\tilde{L}}}{((2\lambda)!(2(l_p-\lambda))!)^{\frac{1}{2}}}
\begin{pmatrix} l_h & l_t & \Lambda \\ 0 & 0 & 0 \end{pmatrix}
\begin{pmatrix} l' & l_t & \tilde{L} \\ 0 & 0 & 0 \end{pmatrix}
\begin{pmatrix} l & \lambda & \tilde{L} \\ 0 & 0 & 0 \end{pmatrix} \\
&\quad \times \begin{pmatrix} \Lambda & l_i & L \\ 0 & 0 & 0 \end{pmatrix}
\begin{pmatrix} l' & L & L' \\ 0 & 0 & 0 \end{pmatrix}
\begin{pmatrix} l_f & l_p-\lambda & L' \\ 0 & 0 & 0 \end{pmatrix}
\begin{pmatrix} l_f & l & \tilde{l} \\ 0 & 0 & 0 \end{pmatrix} \\
&\quad \times \sum_{\mu m m_t} (-1)^{m+\mu}
\begin{pmatrix} \Lambda & l_i & L \\ m_t-m_h & 0 & m_h-m_t \end{pmatrix}
\begin{pmatrix} l_h & l_t & \Lambda \\ -m_h & m_t & m_h-m_t \end{pmatrix} \\
&\quad \times \begin{pmatrix} l' & l_t & \tilde{L} \\ m+m_t-\mu & -m_t & \mu-m \end{pmatrix}
\begin{pmatrix} l_f & l & \tilde{l} \\ -m_p-m_h-m & m & m_p+m_h \end{pmatrix} \\
&\quad \times \begin{pmatrix} l_p-\lambda & \lambda & l_p \\ -m_p-\mu & \mu & m_p \end{pmatrix}
\begin{pmatrix} l' & L & L' \\ \mu-m-m_t & m_t-m_h & m+m_h-\mu \end{pmatrix} \\
&\quad \times \begin{pmatrix} l_f & l_p-\lambda & L' \\ m_p+m_h+m & -m_p-\mu & \mu-m-m_h \end{pmatrix}
\begin{pmatrix} l & \lambda & \tilde{L} \\ -m & \mu & m-\mu \end{pmatrix}, \\
\tilde{\mathcal{R}}_{l_f l_t \Lambda l l' \lambda l_i} &= \int_0^\infty dR\ R^{l_p-\lambda}\ F_{l_f}(k_+ R)\ \tilde{\mathcal{V}}^{\Lambda l_t}_{\lambda l l'}(R\ ) F_{l_i}(k_\alpha R), \\
\tilde{\mathcal{V}}^{\Lambda l_t}_{\lambda l l'}(R) &= \int_0^\infty dr_1\ r_1^{\lambda+1}\ \tilde{\mathcal{J}}^{l_p}_{l'}(r_1,R)\ F_l(k_- r_1)\ \tilde{\mathcal{L}}^{\Lambda l_t}_{n_h l_h}(r_1,R), \\
\tilde{\mathcal{L}}^{\Lambda l_t}_{n_h l_h}(r_1,R) &= \frac{1}{\hat{\Lambda}}\int_0^\infty dr_2\ r_2^2\ R_{n_h l_h}(r_2)\left(\frac{r_<^\Lambda}{r_>^{\Lambda+1}}-\frac{\delta_{\Lambda 0}}{R}\right)\tilde{h}_{l_t}(r_1,r_2), \\
\tilde{\mathcal{J}}^{l_p}_{l'}(r_1,R) &= \frac{1}{2}\int_{-1}^{1} du\ R_{n_p l_p}(\rho_1)\ \rho_1^{l_p}\ P_{l'}(u). \qquad (4.30)
\end{aligned}
$$

$r_<$ (respectively $r_>$) is defined as $min(r_2, R)$ (resp. $max(r_2, R)$). The total cross section for a given state (n_h, l_h) of H and a given state (n_p, l_p) of Ps (reaction (2.7)) is given by

$$\begin{aligned}
\sigma^{4B,3}_{n_h l_h;\ n_p l_p} &= \frac{1}{4\pi^2}\,\frac{k_\beta}{k_\alpha}\,\mu_\alpha\mu_\beta \sum_{m_p m_h}\int d\hat{\boldsymbol{k}}_\beta\,|T_{\alpha\beta}|^2 \\
&= \frac{1}{4\pi^2}\,\frac{k_\beta}{k_\alpha}\,\mu_\alpha\mu_\beta\,\frac{2(4\pi)^5}{(k_- k_\alpha k_+)^2}\,\hat{l}_p!\hat{l}_p\hat{l}_h \sum_{m_p m_h}\sum_{l_i l_i' \tilde{l}} i^{l_i - l_i'}\, e^{i(\delta_{l_i}-\delta_{l_i'})}\,\hat{l}_i\hat{l}_i'\hat{\tilde{l}} \\
&\quad\times\left\{(\mathcal{S}^*_{l_i'\tilde{l}}\times\mathcal{S}_{l_i\tilde{l}} + \tilde{\mathcal{S}}^*_{l_i'\tilde{l}}\times\tilde{\mathcal{S}}_{l_i\tilde{l}} + \left[\mathcal{S}^*_{l_i'\tilde{l}}\times\tilde{\mathcal{S}}_{l_i\tilde{l}} + c.c.\right]\right\}. \qquad (4.31)
\end{aligned}$$

with

$$|T_{\alpha\beta}|^2 \;=\; t^*_{exc}\times t_{exc} + t^*_{exc}\times t_{cap} + t^*_{cap}\times t_{exc} + t^*_{cap}\times t_{cap}$$

4.2.2 Conversion from inverse to direct reaction

Based on the same assumptions explained in section 4.1.2, the GBAR cross sections of the positive antihydrogen ion formation, noted $\sigma^{4B,4}_{n_h l_h;\ n_p l_p}$, can be related to the previously obtained cross sections $\sigma^{4B,3}_{n_h l_h;\ n_p l_p}$. This relation is:

$$\sigma^{4B,4}_{n_h l_h;\ n_p l_p} = \frac{1}{\hat{l}_p\hat{l}_h}\frac{k_\alpha^2}{k_\beta^2}\sigma^{4B,3}_{n_h l_h;\ n_p l_p}, \qquad (4.32)$$

where, as they were defined in the previous section, k_α designs the wavevector of the positron (the electron for reaction 2.6), while k_β corresponds to the wavevector of the positronium.

Chapter 5

Complementary studies

5.1 Electronic correlations

Since the exact wave function for H^- is not analytically known, except for a series expansion given by Bethe [52], an approximate wave function has to be used in the CDW–FS calculations. In the computation of the 4-body CDW–FS cross section presented in the previous section, a general form had been used for the H^- wave function. It is a S-wave that writes:

$$\Phi_\alpha(\boldsymbol{r}_1, \boldsymbol{r}_2) \;=\; f(r_1, r_2)\,(1 + g(r_{12}))\,, \tag{5.1}$$

In this expression, the angular correlation between the two electrons is held in the term $g(r_{12})$, and both $f(r_1, r_2)$ and $g(r_{12})$ include radial correlations. Three different wave functions, which fit this general formula, have been chosen for modelling H^-. They all give different description for the electron correlations.

5.1.1 "Uncorrelated" Chandrasekhar wave function

The first one is the "uncorrelated" Chandrasekhar wave function (label UC in the following). [54] It was first introduced by Chandrasekhar as a better alternative to the many-parameter functions inspired by a similitude between He and H^-. Its form was thought in terms of electronic screening and hydrogen polarisability; the values of the screening constants were sought to minimise the binding energy of H^- in order to obtain a stable bound state. The result is a simple and convenient wave function which, despite its misguiding name, does take into account radial correlations between the two electrons of H^- but indeed does not consider angular correlations. It is usually considered as a sufficient level of description for H^-. $\Phi_\alpha^{UC}(\boldsymbol{r}_1, \boldsymbol{r}_2)$ is given by

$$\left\{ \begin{array}{rcc} f(r_1, r_2) & = & \frac{N_1}{4\pi}\left(e^{-a_{uc}r_1 - b_{uc}r_2} + e^{-a_{uc}r_2 - b_{uc}r_1}\right) \\ g(r_{12}) & = & 0, \end{array} \right.$$

where $a_{uc} = 1.0392$, $b_{uc} = 0.2831$ and the normalisation constant $N_1 = 0.3948$. The binding energy of H^- computed with this function is $E_{H^-} = -0.5133$, which has to be compared with the exact theoretical value, -0.5277 [90].

5.1.2 "Correlated" Chandrasekhar wave function

The previous UC wave function can be modified by introducing $g \neq 0$, so that it now takes into account angular correlations. This "correlated" Chandrasekhar wave function (label CC) was

introduced in the same article as the UC wave function. $\Phi_\alpha^{CC}(\boldsymbol{r}_1, \boldsymbol{r}_2)$ is defined by:

$$\left\{ \begin{array}{rcl} f(r_1, r_2) & = & \frac{N_2}{4\pi} \left(e^{-a_{cc} r_1 - b_{cc} r_2} + e^{-a_{cc} r_2 - b_{cc} r_1} \right) \\ g(r_{12}) & = & D\ r_{12}, \end{array} \right.$$

where $a_{cc} = 1.0748,\ b_{cc} = 0.4776,\ D = 0.3121$ and the normalisation constant $N_2 = 0.3942$. The binding energy is then $E_{H^-} = -0.5259$. For both UC and CC wave functions, the normalisation constants and the binding energies have been checked. This had been also motivated by the discovery of a misprint in the article of Chaudhuri [71]: in that paper, the CC wave function was given with a negative sign for the parameter D. The sign and value in the original article of Chandrasekhar are the correct one.

5.1.3 Le Sech wave function

The last wave function chosen to describe H^- is the Le Sech wave function (label LS in the following), in its three-parameter form as proposed in [91] (in the same article, Le Sech also proposed a two-parameter wave function that has not been considered here). This wave function $\Phi_\alpha^{LS}(\boldsymbol{r}_1, \boldsymbol{r}_2)$ decomposes as follows

$$\left\{ \begin{array}{rcl} f(r_1, r_2) & = & N_3 e^{-r_1 - r_2} \left(\cosh(\lambda r_1) + \cosh(\lambda r_2) + \beta\, (r_1 - r_2)^2 \right) \\ g(r_{12}) & = & \gamma\ r_{12} e^{-\alpha r_{12}}, \end{array} \right.$$

where $\alpha = 0.05,\ \beta = 0.04,\ \gamma = 0.50,\ \lambda = 0.57$ and the normalisation constant $N_3 = 0.03615$ [92]. In the parameter optimisation carried out by Le Sech, γ is fixed and the variational parameters are α, β and λ. The binding energy calculated with the Le Sech wave function is $E_{H^-} = -0.5270$, which is very close to the exact theoretical value, -0.5277. This wave function has been emphasised as a very accurate description of H^- [93].

Table 5.1 shows the contribution of the different angular components in the H^- wave function and the convergence of the normalisation when using the partial wave expansion (4.19); in this table, a_{l_t} is defined by $a_{l_t} = (4\pi)^2 \int\int dr_1\ dr_2\ r_1^2\ r_2^2\ \left| \tilde{h}_{l_t}(r_1, r_2) \right|^2$ (for $\tilde{h}_{l_t}$, see equation 4.2.1).

a_{l_t}	UC	CC	LS
a_0	1	0.9955	0.9959
a_1	0	4.454×10^{-3}	3.954×10^{-3}
a_2	0	5.326×10^{-5}	9.444×10^{-5}
a_3	0	4.165×10^{-6}	7.776×10^{-6}
a_5	0	1.568×10^{-7}	2.966×10^{-7}
a_{10}	0	1.604×10^{-9}	3.042×10^{-9}
a_{30}	0	9.029×10^{-13}	1.714×10^{-12}

Table 5.1: Convergence of the H^- partial wave expansion.

Since the Le Sech wave function is the supposed best description of H^-, the CDW–FS 4-body results will be detailed with this wave function in section 6.2. The comparison between the different H^- wave functions and the consequent discussion on the influence of the electronic correlation description are carried out in section 6.2.2.

5.2 *Capture–excitation* and $f - g$ processes

When using the uncorrelated Chandrasekhar wave function for H^-, further simplifications can be obtained for the expression of the transition matrix element. As previously presented, the UC wave function writes:

$$\Phi_\alpha^{UC}(\boldsymbol{r}_1, \boldsymbol{r}_2) = \frac{N_1}{4\pi}\left(e^{-a_{uc}r_1 - b_{uc}r_2} + e^{-a_{uc}r_2 - b_{uc}r_1}\right) \tag{5.2}$$

Another way to write the expression is (in the following, the simplified notations $a = a_{uc}$ and $b = b_{uc}$ are used):

$$\Phi_\alpha^{UC}(\boldsymbol{r}_1, \boldsymbol{r}_2) = \frac{1}{\sqrt{2}}\left(\varphi_a(\boldsymbol{r}_1)\varphi_b(\boldsymbol{r}_2) + \varphi_a(\boldsymbol{r}_2)\varphi_b(\boldsymbol{r}_1)\right). \tag{5.3}$$

This notation reveals two *1s*-type orbital wave functions in H^-, $\varphi_a(\boldsymbol{r}_i) = \left(\frac{\sqrt{2}N_1}{4\pi}\right)^{\frac{1}{2}} e^{-ar_i}$ and $\varphi_b(\boldsymbol{r}_i) = \left(\frac{\sqrt{2}N_1}{4\pi}\right)^{\frac{1}{2}} e^{-br_i}$. The first thing which the use of φ_a and φ_b allows easily is to write the transition matrix element as:

$$^{4B,UC}T_{\alpha\beta}^- = t^{ab} + t^{ba}, \tag{5.4}$$

and since the two electrons in H^- are indistinguishable, $^{4B,UC}T_{\alpha\beta}^-$ is the coherent sum of two processes that will be discussed in 5.2.2.

5.2.1 *Capture–excitation*

As already introduced in 4.2, the transition matrix element can also be seen as the sum of a *capture* term and an *excitation* term. This will be justified below for the UC wave function. The previously introduced t^{ij} (with ij standing for either ab or ba) terms write:

$$t^{ij} = \int d\boldsymbol{R}\, \mathcal{F}_{\boldsymbol{k}_\beta}^{(-)^*}(\boldsymbol{R})\, V^{ij}(\boldsymbol{R})\, \mathcal{F}_{\boldsymbol{k}_\alpha}^{(+)}(\boldsymbol{R}). \tag{5.5}$$

Due to the absence of angular dependence in the UC wave function, the $\boldsymbol{r}_1$ and $\boldsymbol{r}_2$ terms in $V^{ij}(\boldsymbol{R})$ are fully separable:

$$\begin{aligned}
V^{ij}(\boldsymbol{R}) &= \int d\boldsymbol{r}_1\, \Psi_f^*(\boldsymbol{\rho}_1)\, \mathcal{F}_{\boldsymbol{k}_\beta}^{(-)^*}(\boldsymbol{r}_1)\, \left(\frac{1}{R} - \frac{1}{\rho_1}\right)\, \varphi_i(\boldsymbol{r}_1) \times \int d\boldsymbol{r}_2\, \varphi_{n_h l_h m_h}^*(\boldsymbol{r}_2)\, \varphi_j(\boldsymbol{r}_2) \\
&+ \int d\boldsymbol{r}_1\, \Psi_f^*(\boldsymbol{\rho}_1)\, \mathcal{F}_{\boldsymbol{k}_\beta}^{(-)^*}(\boldsymbol{r}_1)\, \varphi_i(\boldsymbol{r}_1) \times \int d\boldsymbol{r}_2\, \varphi_{n_h l_h m_h}^*(\boldsymbol{r}_2)\, \left(\frac{1}{R} - \frac{1}{\rho_2}\right)\, \varphi_j(\boldsymbol{r}_2) \\
&= \left\{\int d\boldsymbol{r}_1\, \Psi_f^*(\boldsymbol{\rho}_1)\, \mathcal{F}_{\boldsymbol{k}_\beta}^{(-)^*}(\boldsymbol{r}_1)\, \left(\frac{1}{R} - \frac{1}{\rho_1}\right)\, \varphi_i(\boldsymbol{r}_1)\right\} \times \langle n_h l_h m_h | j\rangle \\
&+ \left\{\int d\boldsymbol{r}_1\, \Psi_f^*(\boldsymbol{\rho}_1)\, \mathcal{F}_{\boldsymbol{k}_\beta}^{(-)^*}(\boldsymbol{r}_1)\, \varphi_i(\boldsymbol{r}_1)\right\} \times\, \mathcal{K}_{n_h l_h m_h}^j(\boldsymbol{R}) \\
&\equiv V_{cap}^{ij}(\boldsymbol{R}) + V_{exc}^{ij}(\boldsymbol{R})\,.
\end{aligned} \tag{5.6}$$

According to this, the matrix element t^{ij} may thus be expressed as

$$t^{ij} = t_{cap}^{ij} + t_{exc}^{ij}\,, \tag{5.7}$$

where, we recall, *cap* stands for *capture* and *exc* for *excitation*. The matrix elements t_{cap}^{ij} and t_{exc}^{ij} may be obtained replacing V^{ij} in Eq. (5.5) by V_{cap}^{ij} and V_{exc}^{ij}, respectively. The transition matrix element can now be rewritten as another sum of two terms:

$$^{4B,UC}T_{\alpha\beta}^{-} = t_{cap} + t_{exc}, \tag{5.8}$$

with $t_{cap} = t_{cap}^{ab} + t_{cap}^{ba}$ and $t_{exc} = t_{exc}^{ab} + t_{exc}^{ba}$.

Let's now have a closer look at the expressions of t_{cap}^{ij} and t_{exc}^{ij}. The term

$$\int d\boldsymbol{r}_1 \; \Psi_f^*(\boldsymbol{\rho}_1) \; \mathcal{F}_{\boldsymbol{k}_\beta}^{(-)^*}(\boldsymbol{r}_1) \; \left(\frac{1}{R} - \frac{1}{\rho_1}\right) \; \varphi_i(\boldsymbol{r}_1) \tag{5.9}$$

in t_{cap}^{ij} mostly describes the transition of the electron initially in the bound state i in H^- into a new bound state, the positronium, and in the continuum of the remaining hydrogen atom: this is what we call the *capture*. This process is pondered by the overlap between the wave function of the electron in the hydrogen atom and the wave function of the H^- electron initially in state j: $\langle n_h l_h m_h | j \rangle$. Due to this scalar product, it is worthwhile to notice that, in fact, the term of *capture* is equal to zero for $l_h \neq 0$. For that reason, one can *a priori* expects that the formation of H^- from states of hydrogen with non-zero orbital quantum number shall not be very efficient.

The term t_{exc}^{ij} encloses the transition, under the action of the potential $\left(\frac{1}{R} - \frac{1}{\rho_2}\right)$, of the electron that remains bound to the proton, from state j in H^- to state (n_h, l_h, m_h) in the hydrogen atom. Indeed, this *excitation* description corresponds to the term

$$\mathcal{K}_{n_h l_h m_h}^{j}(\boldsymbol{R}) = \int d\boldsymbol{r}_2 \; \varphi_{n_h l_h m_h}^*(\boldsymbol{r}_2) \; \left(\frac{1}{R} - \frac{1}{\rho_2}\right) \; \varphi_j(\boldsymbol{r}_2). \tag{5.10}$$

For the convenience of further calculations, $\mathcal{K}_{n_h l_h m_h}^{j}(\boldsymbol{R})$ can also be written as

$$\mathcal{K}_{n_h l_h m_h}^{j}(\boldsymbol{R}) = \mathcal{L}_{n_h l_h}^{j}(R) \; Y_{l_h m_h}^*(\hat{\boldsymbol{R}}), \tag{5.11}$$

with

$$\mathcal{L}_{n_h l_h}^{j}(R) = \frac{\sqrt{4\pi}}{\hat{l_h}} \; \int_0^\infty dr \; r^2 \; R_{n_h l_h}(r) \; \left(\frac{r_<^{l_h}}{r_>^{l_h+1}} - \frac{\delta_{l_h 0}}{R}\right) \; R_j(r). \tag{5.12}$$

The total cross section with the uncorrelated Chandrasekhar wave function can be written as

$$\begin{aligned}
\sigma_{n_h l_h;\; n_p l_p}^{4B,3-UC} &= \frac{1}{4\pi^2} \; \frac{k_\beta}{k_\alpha} \; \mu_\alpha \mu_\beta \sum_{m_p m_h} \int d\hat{\boldsymbol{k}}_\beta \, |T_{\alpha\beta}|^2 \,, \\
|T_{\alpha\beta}|^2 &= t_{cap}^{ab\;*} \times t_{cap}^{ab} + t_{exc}^{ab\;*} \times t_{exc}^{ab} + \left[t_{cap}^{ab\;*} \times t_{exc}^{ab} + c.c. \right] \\
&\quad + t_{cap}^{ab\;*} \times t_{cap}^{ba} + t_{exc}^{ab\;*} \times t_{exc}^{ba} + \left[t_{cap}^{ab\;*} \times t_{exc}^{ba} + c.c. \right] \\
&\quad + \; \{ a \leftrightarrow b \} \,.
\end{aligned} \tag{5.13}$$

As it has already been said, if m_h or l_h are different from zero, most of these terms are null. The expression of the pure *capture* terms is

$$\sum_{m_p m_h} \int d\hat{\boldsymbol{k}}_\beta \; t_{cap}^{ij\;*} \times t_{cap}^{kq} \;=\; \frac{(4\pi)^3}{(k_+ k_- k_\alpha)^2} \; \hat{l_p}! \hat{l_p} \; \sum_{l_i \tilde{l}} \; \hat{l_i} \hat{\tilde{l}} \; \left(\mathcal{W}_{l_i \tilde{l}}^{ij\;*} \times \mathcal{W}_{l_i \tilde{l}}^{kq} \right) \tag{5.14}$$

with

$$
\begin{aligned}
\mathcal{W}^{ij}_{l_i\tilde{l}} &= \sum_{l_f l l' \lambda L} i^{-l-l_f}\; e^{i(\delta_l+\delta_{l_f})}\; \mathcal{B}^{l_f l l' \lambda L}_{l_i\tilde{l}}\; \mathcal{R}^{ij}_{l_f l l' \lambda l_i}\;, \\
\mathcal{B}^{l_f l l' \lambda L}_{l_i\tilde{l}} &= (-1)^{\lambda}\; \frac{\hat{l}_f \hat{l} \hat{\tilde{l}}' \hat{L}}{((2\lambda)!(2(l_p-\lambda))!)^{\frac{1}{2}}} \left\{ \begin{array}{ccc} l & \lambda & l' \\ l_f & l_p-\lambda & L \\ \tilde{l} & l_p & l_i \end{array} \right\} \\
&\quad \times \left(\begin{array}{ccc} \lambda & l' & l \\ 0 & 0 & 0 \end{array} \right) \left(\begin{array}{ccc} l' & l_i & L \\ 0 & 0 & 0 \end{array} \right) \left(\begin{array}{ccc} l_f & l_p-\lambda & L \\ 0 & 0 & 0 \end{array} \right) \left(\begin{array}{ccc} l & l_f & \tilde{l} \\ 0 & 0 & 0 \end{array} \right), \\
\mathcal{R}^{ij}_{l_f l l' \lambda l_i} &= \int_0^{\infty} dR\; R^{l_p-\lambda}\; F_{l_f}(k_+ R)\; \mathcal{V}^{ij}_{l l' \lambda}(R)\; F_{l_i}(k_\alpha R), \\
\mathcal{V}^{ij}_{l l' \lambda}(R) &= \langle n_h l_h m_h | j \rangle \times \int_0^{\infty} dr\; r^{\lambda+1}\; F_l(k_- r)\; \mathcal{J}^{l_p}_{l'}(r,R)\; R_i(r).
\end{aligned}
\tag{5.15}
$$

Pure *excitation* terms can be written as follows

$$
\sum_{m_p m_h} \int d\hat{\boldsymbol{k}}_\beta\; t^{ij\;*}_{exc} \times t^{kq}_{exc} = \frac{(4\pi)^3}{(k_+ k_- k_\alpha)^2}\; \hat{l}_p! \hat{l}_p \hat{l}_h \sum_{l_i \tilde{l} L}\; \hat{l}_i \hat{\tilde{l}} \hat{L}\; \left(\tilde{\mathcal{W}}^{ij\;*}_{l_i \tilde{l} L} \times \tilde{\mathcal{W}}^{kq}_{l_i \tilde{l} L} \right) \tag{5.16}
$$

with

$$
\begin{aligned}
\tilde{\mathcal{W}}^{ij}_{l_i\tilde{l}L} &= \sum_{l_f l l' \lambda L'} i^{-l-l_f}\; e^{i(\delta_l+\delta_{l_f})}\; \tilde{\mathcal{B}}^{l_f l l' \lambda L'}_{l_i\tilde{l}L}\; \tilde{\mathcal{R}}^{ij}_{l_f l l' \lambda l_i}\;, \\
\tilde{\mathcal{B}}^{l_f l l' \lambda L'}_{l_i\tilde{l}L} &= (-1)^{\lambda}\; \frac{\hat{l}_f \hat{l} \hat{\tilde{l}}' \hat{L}'}{((2\lambda)!(2(l_p-\lambda))!)^{\frac{1}{2}}} \left\{ \begin{array}{ccc} l & \lambda & L' \\ l_f & l_p-\lambda & L \\ \tilde{l} & l_p & L \end{array} \right\} \left(\begin{array}{ccc} l_h & l_i & L \\ 0 & 0 & 0 \end{array} \right) \\
&\quad \times \left(\begin{array}{ccc} \lambda & l' & l \\ 0 & 0 & 0 \end{array} \right) \left(\begin{array}{ccc} l' & L & L' \\ 0 & 0 & 0 \end{array} \right) \left(\begin{array}{ccc} l_f & l_p-\lambda & L' \\ 0 & 0 & 0 \end{array} \right) \left(\begin{array}{ccc} l & l_f & \tilde{l} \\ 0 & 0 & 0 \end{array} \right), \\
\tilde{\mathcal{R}}^{ij}_{l_f l l' \lambda l_i} &= \int_0^{\infty} dR\; R^{l_p-\lambda}\; F_{l_f}(k_+ R)\; \tilde{\mathcal{V}}^{i}_{l l' \lambda}(R)\; \tilde{\mathcal{L}}^{j}_{n_h l_h}(R)\; F_{l_i}(k_\alpha R), \\
\tilde{\mathcal{V}}^{i}_{l l' \lambda}(R) &= \int_0^{\infty} dr\; r^{\lambda+1}\; F_l(k_- r)\; \tilde{\mathcal{J}}^{l_p}_{l'}(r,R)\; R_i(r), \\
\tilde{\mathcal{L}}^{j}_{n_h l_h}(R) &= \frac{\mathcal{L}^{j}_{n_h l_h}(R)}{\sqrt{4\pi}}.
\end{aligned}
\tag{5.17}
$$

Finally, the cross terms can be expressed with the previously introduced quantities. For instance

$$
\begin{aligned}
\sum_{m_p m_h} \int d\hat{\boldsymbol{k}}_\beta\; t^{ij\;*}_{cap} \times t^{kq}_{exc} &= \frac{(4\pi)^3}{(k_+ k_- k_\alpha)^2}\; \hat{l}_p! \hat{l}_p \sum_{l_i \tilde{l}}\; \hat{l}_i \hat{\tilde{l}}\; \left(\mathcal{W}^{ij\;*}_{l_i \tilde{l}} \times \tilde{\mathcal{X}}^{kq}_{l_i \tilde{l}} \right), \\
\tilde{\mathcal{X}}^{kq}_{l_i \tilde{l}} &= (-1)^{l_i}\; \hat{l}_i^{\frac{1}{2}}\; \tilde{\mathcal{W}}^{kq}_{l_i \tilde{l} l_i,\; l_h=0}.
\end{aligned}
\tag{5.18}
$$

Historically, the UC wave function has been the first one investigated for this thesis. In that

case, the denominations *capture* and *excitation* are straightforward and, though less obvious, they were nonetheless inherited by the following developments with the correlated Chandrasekhar and Le Sech wave functions. This explains why the names *capture* and *excitation* have been kept in section 4.2.

5.2.2 *f* and *g* processes

Another possible partition of the cross section expression obtained with the UC wave function exacerbates the different roles of the two electrons in H^-, depending on the orbital they belong to. In the simplistic UC vision, the H^- ion can be seen as a two level system $|a\rangle$ and $|b\rangle$, with one electron in each level, a being the closest to the nucleus while b is the further. This is easily seen in the expression of the UC wave function previously written. The transition matrix element can then be reorganised as *ab*, *ba* and *cross ab–ba* terms. The *ab* (respectively *ba*) term describes the capture of electron a (resp. b) into the positronium while the remaining electron b (resp. a) is excited in the residual hydrogen atom. The two possibilities are represented in figure 5.1. This correspond to the f and g processes described in [85] for CDW–FS applied to the metastable Helium.

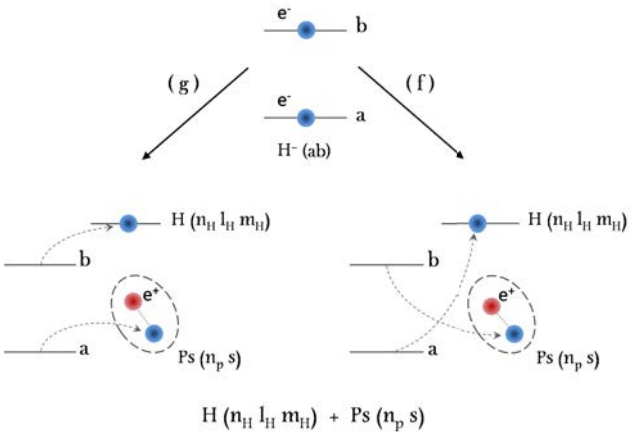


Figure 5.1: Illustration of the f and g processes.

The use of the uncorrelated Chandrasekhar wave function, though being a slightly insufficient description of the highly correlated species H^-, gives an insight of the importance of the different processes occurring during the charge exchange reaction.

5.3 Coulomb - Born Approximation

From the previously presented CDW–FS cross sections, results can be obtained corresponding to another theoretical model, the Coulomb-Born Approximation (CBA). In the CBA formalism, in its *prior* form, the Coulomb distortions in the entrance channel are taken into account and included using the same Coulomb wave function as in CDW–FS; the perturbating potential is also the same. However, the Coulomb distortions due to the charged residual target are neglected

in the exit channel and plane waves are used for the outgoing light particles, as it would be in the Born approximation types. The mathematical transition between CDW–FS and CBA is simply obtained by setting the Sommerfeld parameters $\beta_{\pm}$ of the final state to zero, since the Coulomb wave functions thus reduce to plane waves.

The CBA approximation has been described by Fujiwara [94] in the case of electron capture by a proton from a hydrogen-like heavy ion. Neglecting the internuclear potential, this was latter corrected by Mukherjee *et al.* [95] in the case of collisions between a proton and He^+. For a positron projectile, CBA cross sections have been computed and compared to the CDW results presented in [81].

The first thing that should be noticed is that the 4-body formulations of CDW–FS and CBA are equivalent. Indeed, since we chose to work with the reversed reactions (i.e. positronium formation), there is no charged species in the final state and the Coulomb wave function used in CDW–FS is, in fact, already a plane wave.

If the CBA results for the 4-body reaction will be obtained without any further effort, this cannot be said for the 3-body reaction. The 3-body CBA will be an all-new calculation and it will be interesting to compare it with CDW–FS, which, with its status of a more refined model, is naively expected to give better results than CBA.

Chapter 6

Results of the cross section computations

Throughout this chapter, only results on the total cross sections will be discussed. As a matter of fact, the differential cross sections, thought their expressions have been written in the previous chapter, have not been computed. From the beginning of the thesis, it had been decided to orientate the work so it would closely follow the experimental needs; in the GBAR experiment, only the total production of the $\bar{\mathrm{H}}^+$ matters. Since changes in the antiproton phase space are negligible in the inelastic collisions with the much lighter positronium atoms, differential cross sections have limited interest.

Of course, the differential cross sections could have nonetheless been computed: the reason why this was not done is simply for lack of time. However, if cross section measurements were to be made at Saclay using protons, as it is intended to, then the detection of the free positron ejected by the reactions becomes the main signal for the detection: it would then be of uttermost interest to compute the differential cross sections to anticipate the solid angle that the detector should cover. A PhD thesis has just started on the subject of the differential cross sections and will provide the complement to the present work.

The computer programs used for the numerical calculations of the cross sections have been adapted from pre-existing FORTRAN 77 codes: their are the codes uses in the previous CDW–FS studies of positronium production from hydrogen-like ions [81] and positronium formation in collisions with metastable Helium [85]. By modifying these codes, the differential cross sections can be extracted for future use. The calculations have been carried out in Strasbourg and at CEA-Saclay. For the most complicated cases of the 3-body reaction (Ps($3d$) with highly excited states of hydrogen), the computation of the cross sections for fifty values of the projectile positron energy could take up to four days, for each (n_h, l_h, m_h)-(n_p, l_p, m_p) pair. Overall, 561 partial cross sections have been computed for reaction 2.4 and 84 total cross sections for reaction 2.6 (including the CBA calculations and computations using the different wavefunctions for H^-). Since the 3-body cross section for a pair (n_h, l_h, m_h)-(n_p, l_p, m_p) is equal to the one for the pair $(n_h, l_h, -m_h)$-$(n_p, l_p, -m_p)$, some computational effort could be saved. As the energy of the projectile positron is increased, the number of partial waves needed to obtained a converged result increases. Because of the relations between the orbital quantum number of the partial waves, the total number of partial wave functions computed is defined by fixing the maximum of only two of these numbers for the 3-body reaction ("l_i^{max}" and "l'^{max}") and of three of these numbers for the four-body reaction ("l_i^{max}", "l'^{max}" and "l_t^{max}"). For the 3-body CDW–FS cross sections, we used $l_i^{max} = 60$ and $l'^{max} = 30$ and observed that the results had converged at least

at the eighth significant digit at low energies. For the CBA results, computed at the beginning of 2014, we work with $l_i^{max} = 40$ and $l'^{max} = 20$, which is sufficient at very low energies to have a convergence at the fourth significant digit. In the case of the 4-body reaction cross sections, we used $l_i^{max} = 40$, $l'^{max} = 20$ and $l_t^{max} = 19$, and we obtain converged results at the tenth significant digit.

The analytical expressions of the cross sections have been calculated in atomic units. The numerical cross sections have been divided by π, thus turning them into units of πa_0^2, where a_0 is the Bohr radius of the proton; these units have been kept to display the numerical results in the following sections. To convert in cm^2 the conversion factor is: $1\ \pi a_0^2 \approx 0.88 \cdot 10^{-16}\ cm^2$.

6.1 First reaction

6.1.1 CDW–FS results

CDW–FS cross sections for reaction (2.5) have been computed for six states of the positronium atom, from Ps(*1s*) to Ps(*3d*), and for thirteen states of hydrogen, from H(*1s*) to H(*5d*) (and up to H(*5g*) for ground-state positronium). The energy considered for reaction (2.5) ranges from 0 to 50 eV positron energy and the results presented here for reaction (2.4) focus on the 0 and 30 keV antiproton energy region. As said previously in section 3.2.2, the energy region of interest for GBAR, that is 0 to 10 keV, is most probably outside the domain of validity of CDW–FS, but computation in that region nevertheless holds valuable information. On the other hand, the region above 20 keV is of lesser concern for the GBAR experiment; however, numerical calculations at these energies provide a mean to verify the concordance of the present CDW–FS calculations with other theories. Finally, the energy region from 10 to 20 keV has a practical interest when considering ground state positronium only: indeed, it is in that energy range that the experimental data of Merrison *et al.* [64] have been obtained.

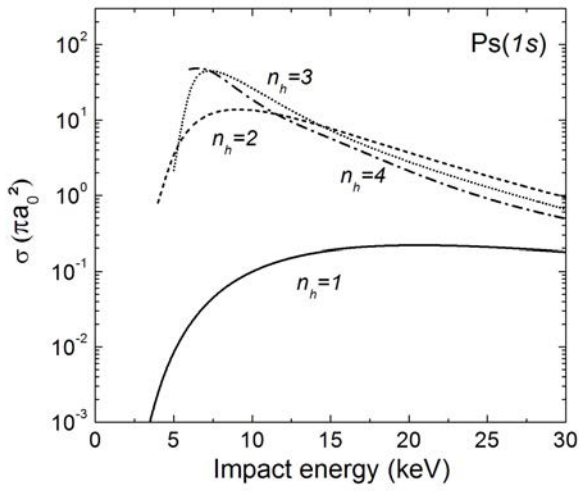
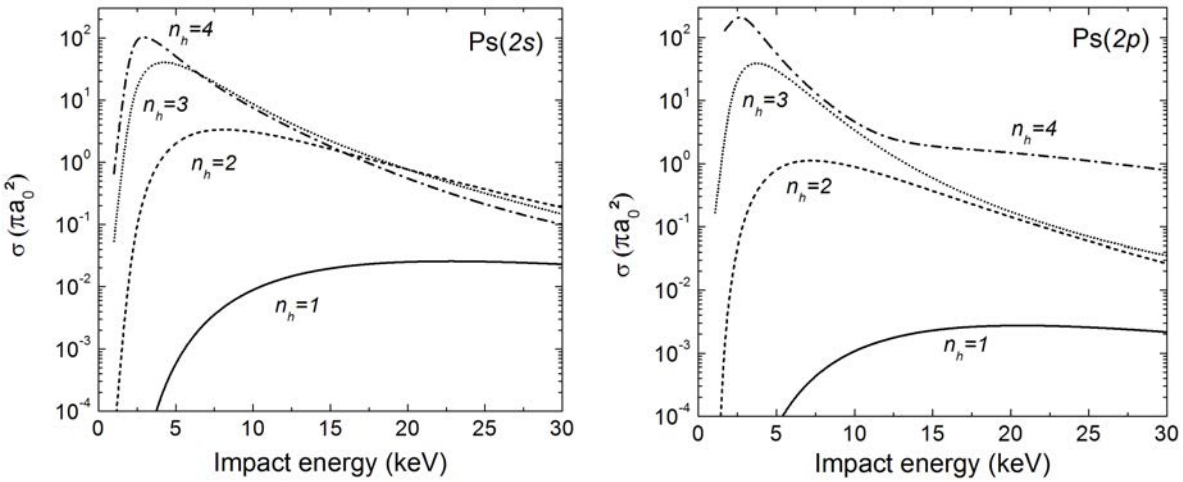


Figure 6.1: Antihydrogen production cross sections from ground state positronium as a function of antiproton impact energy.

Figures 6.1 to 6.3 present, for Ps(*1s*) to Ps(*3d*), the cross sections of antihydrogen formation $\sigma^{3B,2}_{n_h l_h;\ n_p l_p}$ for $n_h = 1$ to 4, as a function of the antiproton impact kinetic energy. These cross

sections demonstrate, for any positronium state, the large production of the higher excited states of $\bar{\mathrm{H}}$, $\bar{\mathrm{H}}(1s)$ production being almost negligible at low energies in all cases. A drop of the cross sections can be observed toward the thresholds for the lower values of n_h. As the principal quantum number considered n_h increases, so does the maximum of the corresponding cross section; simultaneously, this maximum is shifted toward lower energies. Since the thresholds for reaction 2.4 increase with n_h (see appendix B), this tends to make the maximum of the cross section happen just after the threshold for the higher values of n_h; this can be easily seen for instance in figures 6.1 and 6.2b for $n_h = 4$.

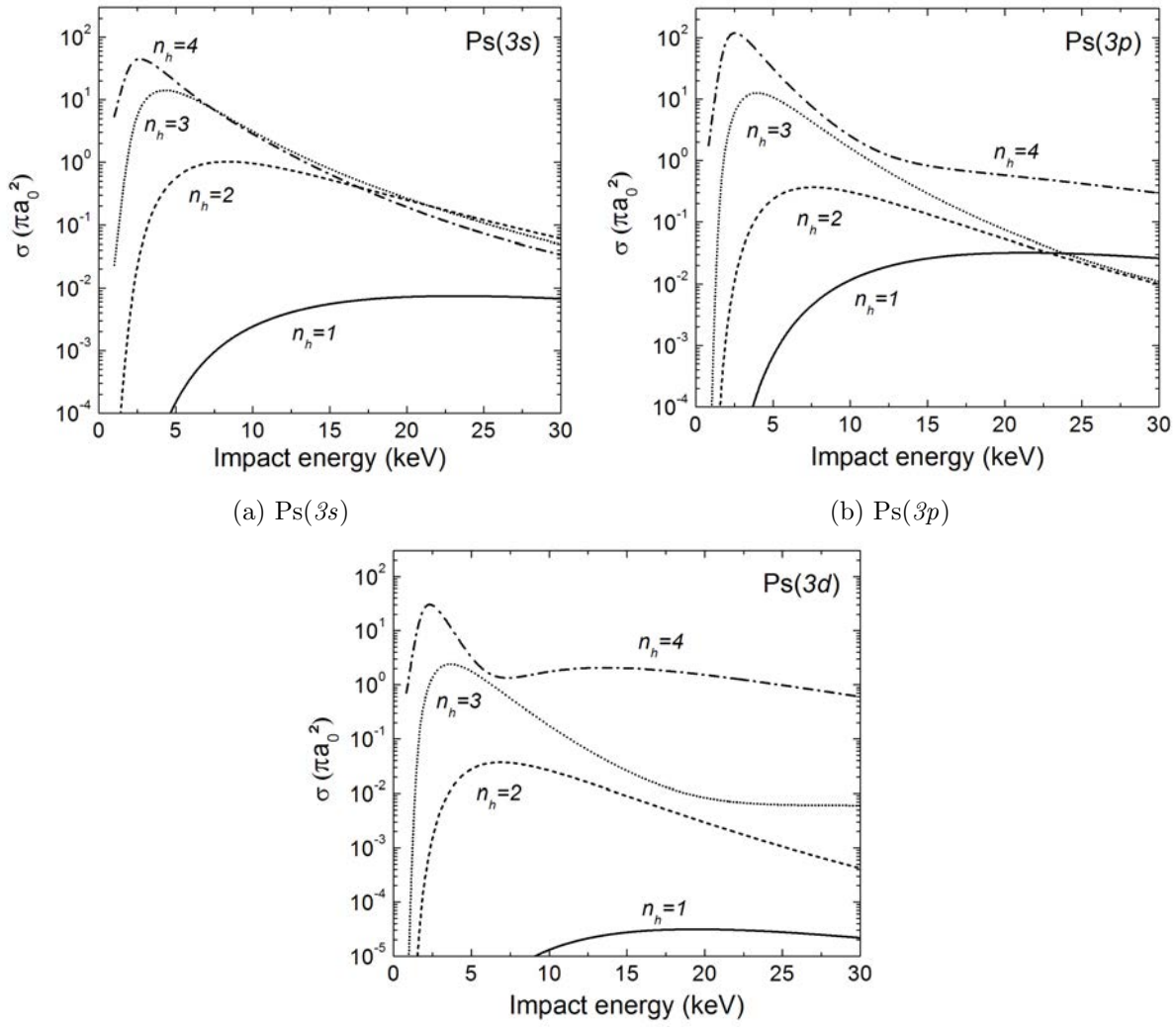


(a) Ps($2s$) (b) Ps($2p$)

Figure 6.2: Antihydrogen production cross sections from positronium excited in a state $n_p = 2$ as a function of antiproton impact energy.

A second, wide maximum is sometimes observed: from the results available, it seems to occur for $l_p \neq 0$ solely. On figure 6.2b (Ps($2p$)) and 6.3b (Ps($3p$)), it appears for $n_h = 4$, and is more like a smooth and wide shoulder on the cross section starting at about 12 keV, while on figure 6.3c (Ps($3d$)), it appears for both $n_h = 3$ and $n_h = 4$, though at larger energies for the former, and is a true local maximum for the latter at about 14 keV. In fact, this behaviour already comes from the cross sections for (n_h, l_h), as shown on the example of Ps($2p$) for $n_h = 4$ in figure 6.4. We have no physical explanation for these second maxima yet, and they do not seem to be related to numerical artefacts. If they are proven to indeed exist, they would have a non negligible incidence for GBAR since they suggest that excited antihydrogen atoms could be sufficiently produced at energies of the order of 15 keV, which is easier to make from the point of view of the antiproton decelerator realisation.

In order to further illustrate the importance of the higher excited states of antihydrogen, figure 6.5 displays the cross sections, for Ps($3d$), of the summed production of antihydrogen up to $H(3d)$, $H(4f)$ and $H(5d)$. In that example, it should be noticed that taking into account the states $n_h = 5$ drastically changes the features of the total antihydrogen production. For instance, the main maximum, at about 3-4 keV when considering only states up to $n_h = 3$, and shifted at 2-2.5 keV when going up to H($4f$), is further shifted to approximatively 500 eV, where, in fact, $n_h = 5$ states are the only contributors to this summed cross sections. Also, the second maximum is now shifted to 7 keV and is almost as important as the first maximum; and again,



(a) Ps(*3s*)

(b) Ps(*3p*)

(c) Ps(*3d*)

Figure 6.3: Antihydrogen production cross sections from positronium excited in a state $n_p = 3$ as a function of antiproton impact energy.

the main contributors to that maximum are the $n_h = 5$ states. Of course, the cross section computation have been stopped at H(*5d*), so the conclusions would certainly even be different if taking into account higher excited states.

Figure 6.4 shows the details, in the case of Ps(*2p*) and $n_h = 4$, of the different contribution of the l_h states. The relative behaviour of the cross sections in this example is similar in any other (n_h, l_h)-(n_p, l_p) case. It shows that, for a given n_h, the production of *s*-state antihydrogen is always the lowest contribution, whereas the formation of states with non-zero orbital quantum number gets more and more favoured as l_h increases. For the highest l_h state, this hierarchy can be slightly perturbed toward thresholds and toward the intermediate energy region, as can be seen in figure 6.4 for the $\bar{\mathrm{H}}(4f)$.

In the prospect of the GBAR experiment for which the highest production rate of antihydrogen atoms is sought, figure 6.6 compares the different states of positronium, when all the contributions

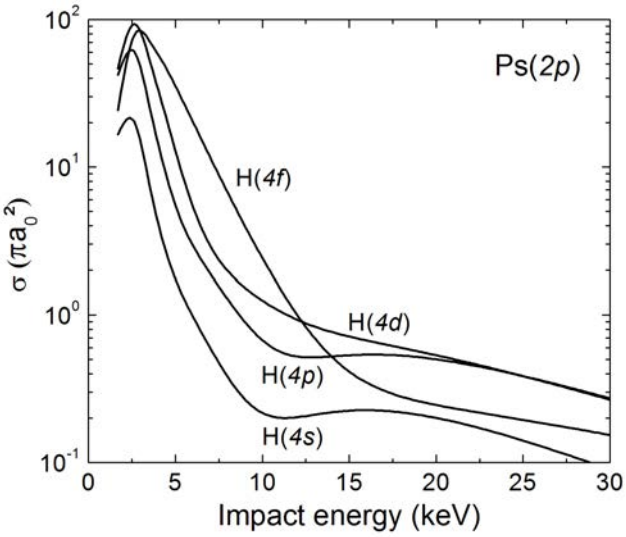


Figure 6.4: Cross sections of antihydrogen production in the states $n_h = 4$ for Ps(*2p*), as a function of the antiproton impact energy.

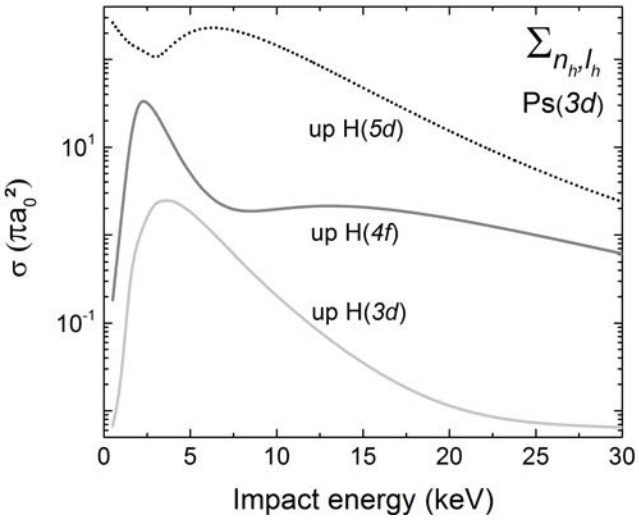


Figure 6.5: Summed cross sections of antihydrogen production from Ps(*3d*), up to the states $\bar{\mathrm{H}}$(*3d*), $\bar{\mathrm{H}}$(*4f*) and $\bar{\mathrm{H}}$(*5d*), as a function of the antiproton impact energy.

of $\bar{\mathrm{H}}$ states are summed from (*1s*) to (*5d*). The maximum of $\bar{\mathrm{H}}$ production occurs around 6 keV antiproton energy when the positronium is in its ground state and, because of threshold constraints for $n_h > 1$, $\bar{\mathrm{H}}$ formation from Ps(*1s*) appears to be completely negligible below 5 keV. For excited states of positronium, the production of antihydrogen atoms peaks in the region 2 to 3 keV, except for the already discussed case of Ps(*3d*). The highest total cross section is obtained for Ps(*2p*) at 2 keV: this maximum dominates the others by at least a factor 2. If we were to conclude from the results shown in this figure, Ps(*2p*) would be the optimum choice for producing large amounts of antihydrogen atoms at 2 keV (its use can even be extended to the region 1 to 4 keV). If an antiproton beam of less than 1 keV can be realised, then, Ps(*3p*) or Ps(*3d*) can be used with the same results. If working at 6 keV, either for technical constraint on

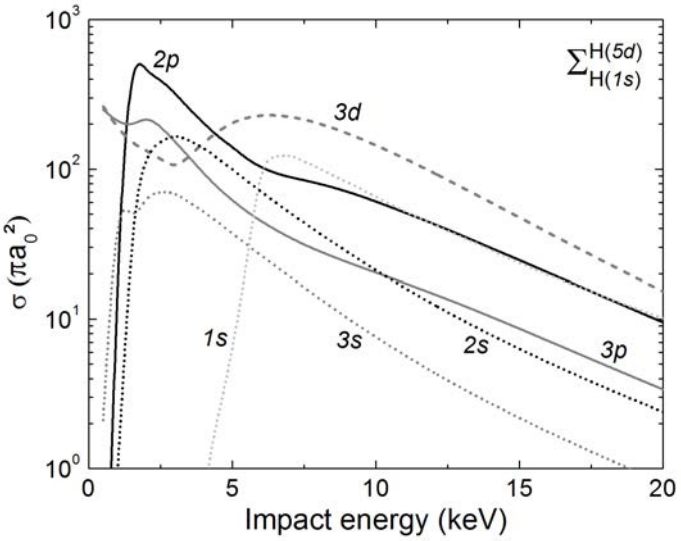


Figure 6.6: Cross sections of antihydrogen production up to $\bar{H}(5d)$ for Ps(*1s*) to Ps(*3d*), as a function of antiproton impact energy.

the decelerator or in order to make use of the ground state positronium, the results presented in figure 6.6 suggest that positonium excitation into the state 3D still has some interest to enhance the production of excited antihydrogen atoms.

Obviously, the best impact energy for the first reaction, and the optimal positronium state going accordingly, might not be the same for the second reaction; also, as it as been pointed out when discussing figure 6.5, the presented summed cross section in fact mainly reflects the behaviour of the $n_h = 5$ states: largely producing these states to the disadvantage of other states may have no interest for the optimisation of the second reaction.

6.1.2 CBA results

As explained before, the CBA results are a by-product of the CDW–FS calculations. Though CBA does not treat the long-range Coulomb interactions in the exit channel, and, from that point of view, is less accurate than CDW–FS *on the paper*, it can nonetheless be a sufficient description of reaction 2.4. It may also turn out to be more adequate. The comparison between CDW–FS and CBA will be done in section 7.1.

Similarly to the previous section, the CBA results are presented in figures 6.7 to 6.9 for each state of positronium considered in this thesis. For graphical clarity, the cross sections have been summed over the l_h states of antihydrogen and are given for each n_h states.

One of the first comments that can be done on the CBA cross concerns the behaviour of the cross sections at low energies: except for ground state positronium, the cross section are otherwise sharply increasing toward the thresholds. For any excited state of positronium, the CBA cross section suggest to use antiprotons with the smallest kinetic energy possible (notwithstanding threshold limitations that arise when considering the production of the higher excited states of antihydrogen).

The second comment, excluding Ps(*1s*) once again, is on the preponderance of the excited antihydrogen production: in the energy range investigated, the formation of $\bar{H}(1s)$ atoms almost always has the lowest cross sections, with a difference of at least three orders of magnitude at the thresholds between the cross section for ground state antihydrogen production and the production

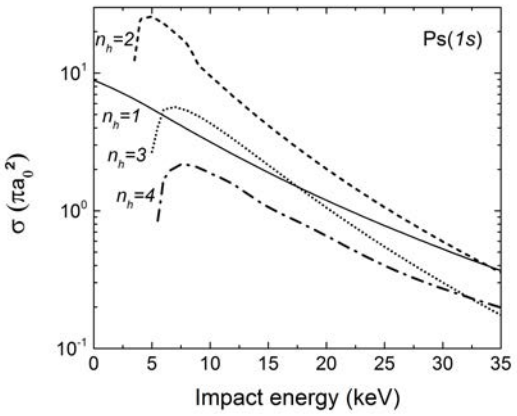
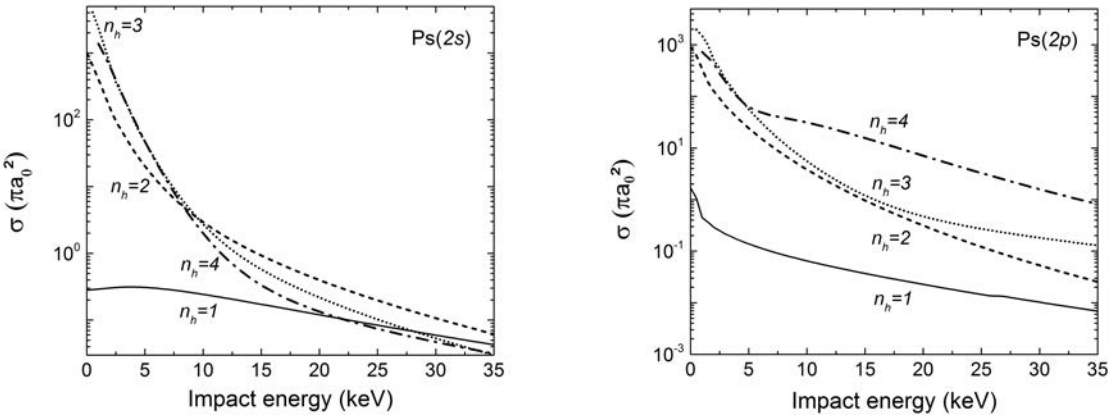


Figure 6.7: $\bar{\mathrm{H}}$ production cross sections from ground state positronium (n_p=1), obtained in the framework of the CBA theory. For each n_h state of antihydrogen, the cross sections have been summed over the l_h states.



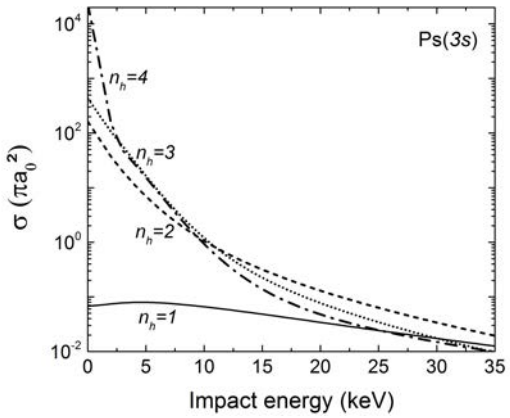
(a) Ps(*2s*) (b) Ps(*2p*)

Figure 6.8: Same as for Figure 6.7 but for n_p=2.

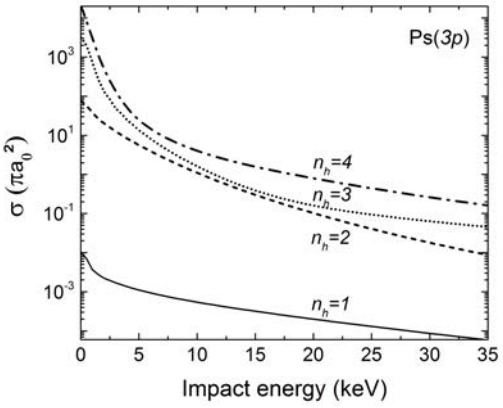
of any other exited state of antihydrogen. Two cases can still be distinguished: *s*-states of excited positronium, for which the production of excited antihydrogen largely dominates at low energy but becomes comparable to the production of ground state antihydrogen above, roughly, 20 keV; and the $l_p \neq 0$ states of positronium for which the production of excited of antihydrogen is always preponderant in the energy range considered. Keeping the same separation for the excited states of positronium, it can be observed that, in the latter case, the hierarchy between the cross sections for each n_h state is clearly defined: the higher the n_h considered is, the larger are the cross sections. For the former case of l_p=0 states of excited positronium, the difference between the excited states of antihydrogen is less pronounced: to a lower extend, the same hierarchy as for $l_p \neq 0$ is observed when the impact kinetic energy is near the threshold values, while this hierarchy is reversed (for $n_h \geq 2$) above 10 keV.

Finally, one can remark the wide shoulders appearing and modelling the shape of the cross sections for $n_h = 4$ with Ps(*2p*) and Ps(3d); a similar behaviour can be guessed to start at higher energy for n_h=3.

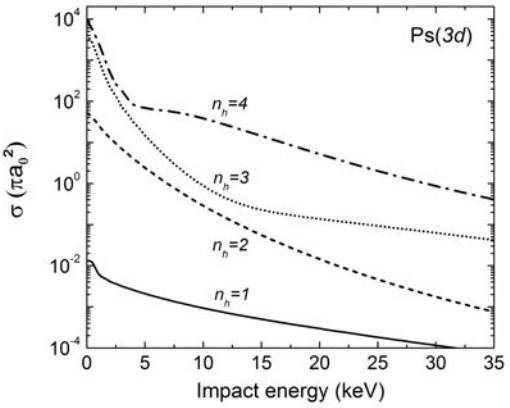
So far, the case of ground state positronium has been discarded from the previous comments



(a) Ps(*3s*)



(b) Ps(*3p*)



(c) Ps(*3d*)

Figure 6.9: Same as for Figure 6.7 but for n_p=3.

since it exhibits a singular behaviour. For $n_h \geq 2$, the cross sections drop close to the thresholds, thus displaying a maximum that shifts from 5 to 7 keV as n_h increases. The production of n_h=2 states of antihydrogen is the one leading to the highest cross sections and, from then, as n_h increases, the cross sections are getting lower and lower (passing below the cross section for $\bar{\mathrm{H}}(1s)$ for $n_h \geq 4$).

For each state of positronium the cross sections have now been summed over the computed n_h states and the comparison between the total antihydrogen production cross sections thus obtained is shown in figure 6.10, restricted to the energy region 0 to 20 keV. From this figure, the largest antihydrogen production, all $\bar{\mathrm{H}}$ states included up to n_h=4, is obtained for n_p=3 states of positronium, below 1 keV. In that energy range, the different n_p=3 states appear to be equivalent. Going to slightly higher energies, Ps(*2s*) and Ps(*2p*) offer very similar cross sections to n_p=3, and there is no real advantage in choosing one of the excited state of positronium over the others. Above 7 keV, when the cross section obtained with Ps(*1s*) becomes comparable to the other ones, the cross sections reorganise into two groups, with the highest antihydrogen production obtained for Ps(2p), Ps(3d) and Ps(1s); the second group, made of Ps(*2s*), Ps(*3s*) and Ps(3p), ends with approximately one order of magnitude lower cross sections at 20 keV (and even lower for Ps(*3s*)).

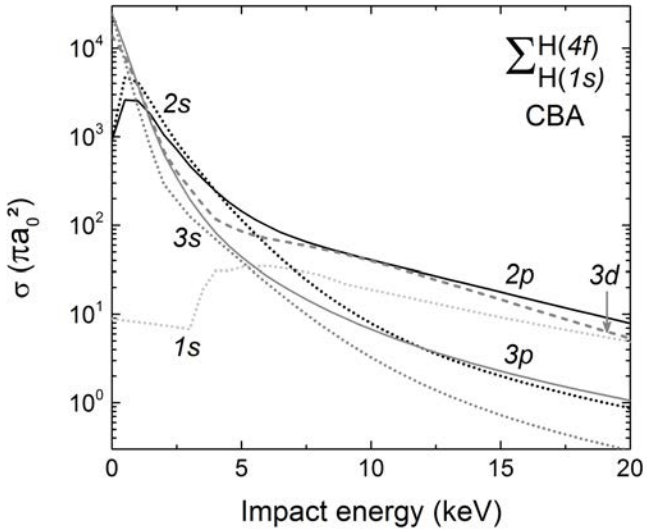


Figure 6.10: CBA cross sections of total antihydrogen production, the contribution of the different states of antihydrogen being summed up to $\bar{H}(4f)$, for Ps($1s$) to Ps($3d$), and as a function of antiproton impact energy.

6.2 Second reaction

6.2.1 The uncorrelated Chandrasekhar wave function: first investigations and positron capture processes

A. Total cross sections

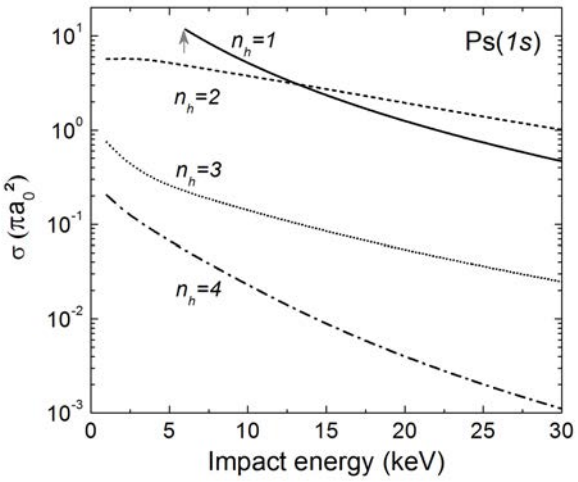
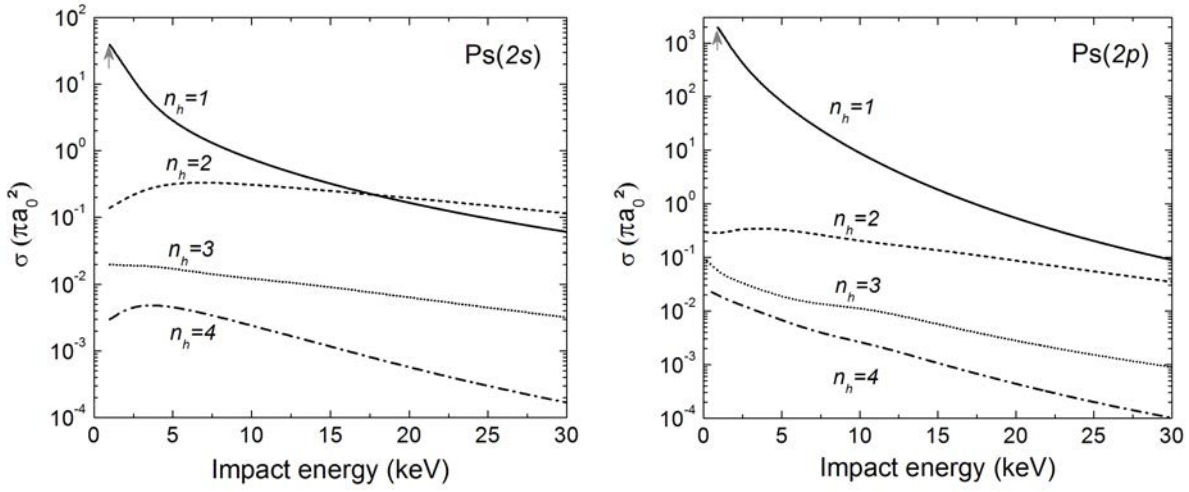


Figure 6.11: $\bar{H}^+$ production cross sections from ground state positronium as a function of antihydrogen impact energy; the arrow indicates the threshold of the $\bar{H}(1s)$ channel.

The cross sections for reaction (2.7) have been first computed using the uncorrelated Chandrasekhar wave function, since the absence of angular correlation in that wave function allows for faster numerical computing. As for the 3-body reaction, positronium in states ($1s$) to ($3d$) have been investigated and excited states of hydrogen up to ($4f$) have been considered. The results,

converted for reaction (2.6) using the relation given in section 4.2.2, are presented in figures 6.11 to 6.13, for initial antihydrogen impact kinetic energy between 0 and 30 keV. Again, only low energies are of interest for GBAR but the cross sections have been computed at higher energies for the purpose of comparison with other theoretical models. Similarly to what has been done in the previous section on reaction 2.4, the contribution of the antihydrogen excited states have been summed over l_h. As an example of the cross sections dependence in the orbital quantum number l_h, more detailed results are shown in figure 6.15 for Ps(*2p*) and in a state $n_h = 4$.



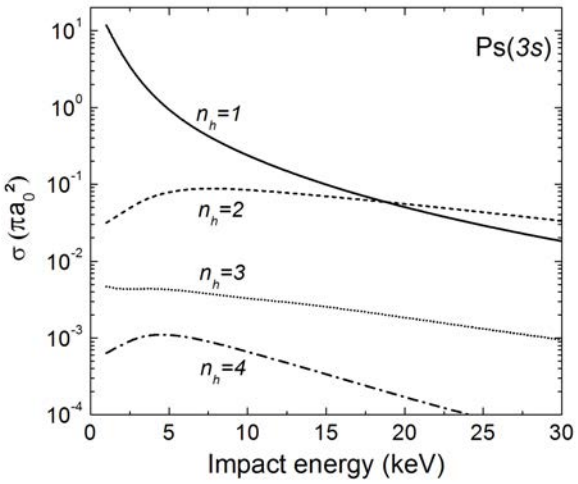
(a) Ps(*2s*) (b) Ps(*2p*)

Figure 6.12: $\bar{H}^+$ production cross sections from positronium excited in a state n_p=2 as a function of antihydrogen impact energy; the arrows mark the threshold of the $\bar{H}(1s)$ channel.

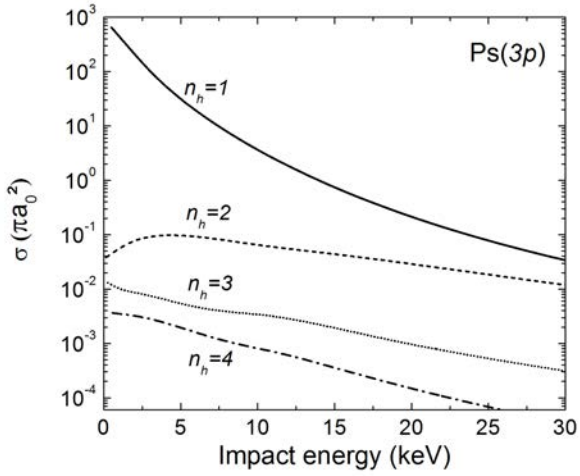
The general behaviour of the 4-body reaction cross sections is a dramatic increase of the $\bar{H}^+$ production toward the thresholds (see appendix B) when the antihydrogen in the entrance channel is in its ground state. This behaviour is less pronounced when the positronium is in its ground state too, but is really emphasised for excited states of positronium. This had already been noted by McAlinden *et al.* (who gave a $\frac{1}{E}$ law to estimate the cross section of reaction (2.7) at very low positron impact energies) and by Roy *et al.* [73, 74] for positronium (*1s*) to (*2p*); it is now also demonstrated for $n_p = 3$.

The other general tendency, over all the energy range considered, is a shift of the cross sections toward lower values when n_h increases. This decrease of the cross sections with n_h is amplified as l_p goes up. Two cases can be distinguished: l_p=0 and $l_p \neq$0. Indeed, for *s*-states of positronium, values of the cross sections for $\bar{H}^+$ formation from $\bar{H}(1s)$ are very similar: they are all of the order of 10 πa_0^2 at threshold and decrease with the impact energy, until, around 10-15 keV, they become comparable to the cross sections when $\bar{H}$ is in the n_h=2 states in the entrance channel. Among the *s*-states of positronium, Ps(*1s*) is slightly singular since the threshold of the reaction with $\bar{H}(1s)$ is already at almost 6 keV: in that case, the corresponding cross section never largely dominates the cross sections for $n_h = 2$ states of antihydrogen. On the contrary, for the $l_p \neq$0 states of positronium, the channel where the antihydrogen is in its ground state is always dominant; toward the thresholds, the difference between $\bar{H}^+$ formation cross section from ground and $n_h = 2$ states of $\bar{H}$ is at least 3 orders of magnitude.

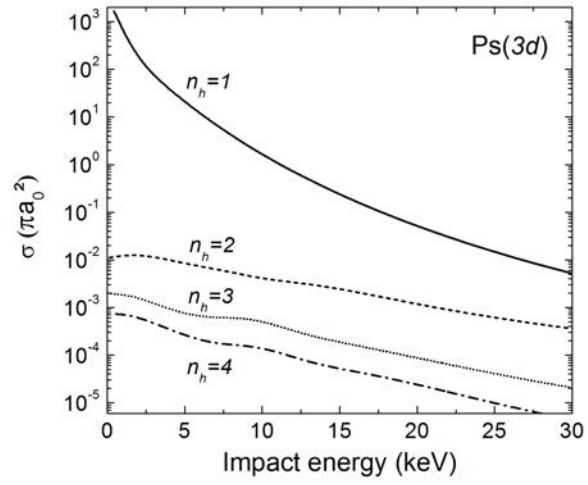
Also, below 5 keV, these cross sections are at least one or two orders of magnitude higher



(a) Ps(*3s*)



(b) Ps(*3p*)



(c) Ps(*3d*)

Figure 6.13: $\bar{H}^+$ production cross sections from positronium excited in a state n_p=3 as a function of antihydrogen impact energy.

than the ones with *s*-state positronium, as can be seen in figure 6.14 which compares the different states of positronium when only ground state antihydrogen is considered in the entrance channel. From this figure, considering that the cross section for excited states of antihydrogen are in general too small to significantly contribute to the $\bar{H}^+$ production, we can assess that the best positronium state for reaction 2.6 is Ps(*2p*), with optimal use between 1 and 2 keV. Then come Ps(*3p*) and Ps(*3d*), which should be chosen if working below 1 keV. From a practical point of view, the second reaction cannot be achieved with 100% excited positronium: only a fraction can be excited and the rest remains in the ground state. In that case, if we want to use this Ps(*1s*) anyway, we should work around 6 keV; at this energy, only Ps(*2p*) has a cross section larger enough (about 5 times), and positronium excitation in the *2p*-state could slightly enhance the $\bar{H}^+$ production.

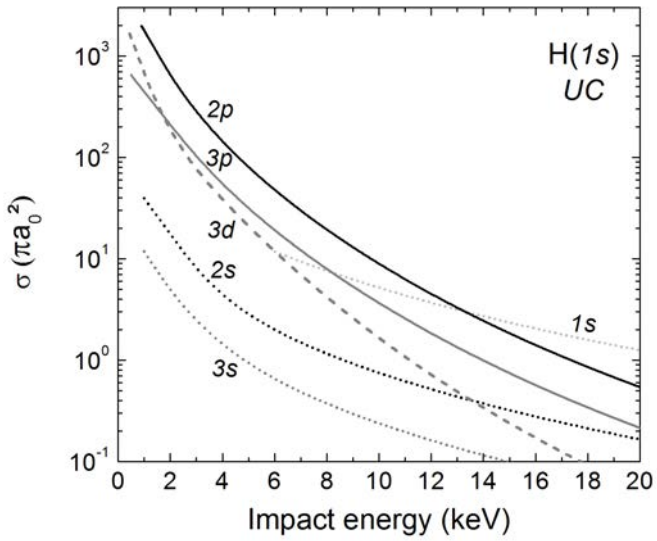


Figure 6.14: Comparison between the different positronium states for reaction (2.6) when $\bar{\mathrm{H}}$ is in the ground state, in the case of the uncorrelated Chandrasekhar wave function.

The cross sections presented in figure 6.15 are representative of the behaviour for $n_h \geq 3$ and $l_p > 0$. There has been no other general pattern found in the behaviour of the partial cross section for the different (n_h, l_h) states. In the case addressed in figure 6.15 (Ps(*2p*) and the four $n_h = 4$ states), the $\bar{\mathrm{H}}^+$ ions are preferentially produced from *s*-state and *p*-state antihydrogen atoms in close competition and then, to a lower extend, from *d*-states. For *s*-state antihydrogen atoms, the cross sections always exhibit the same structure with a shoulder or a maximum in the region 10 to 15 keV. In the case of *s*-state positronium (l_p=0), not presented here, $\bar{\mathrm{H}}^+$ production will be favoured for l_h=0, but when n_h=4, it is now the *p*-state antihydrogen channel which dominates the one with *s*-state antihydrogen. And for any state of positronium, when $\bar{\mathrm{H}}$ is in a state n_h=2 in the entrance channel, it is $\bar{\mathrm{H}}$(*2s*) that leads preferentially to $\bar{\mathrm{H}}^+$ formation.

B. Results on the *capture–excitation* and *f–g* processes

This section might be of lesser interest for the GBAR problematic, but is an interesting theoretical by-product: it holds some clue on the mechanisms involved in the formation of the $\bar{\mathrm{H}}^+$ ions. Based on the comments and equations given in section 5.2 for the UC wave function, it has been possible to investigate the respective contributions of the *capture* and the *excitation* terms to the total cross section by taking either the t_{exc}^{ij} or t_{cap}^{ij} terms equal to zero in the FORTRAN code. This is shown in figure 6.16a in the case of Ps(*2p*) and $\bar{\mathrm{H}}$(*4s*), for which an intriguing shoulder was found at 10 keV (we remind that it is not the only case but is true in general for *s*-states of antihydrogen).

This observed shoulder in the cross section is explained by a maximum in the *capture* process at these energies. In a classical description, the capture of the positron in the positronium should be optimal when the speed of the antihydrogen projectile is equal to the mean orbital speed of the positron. In general, it is observed at around once or twice this value.

Concerning the *excitation* process, it is largely dominant below 5 keV, and, in fact, is the main contributor process to the total cross section. This was to be expected since the $n_h = 4$

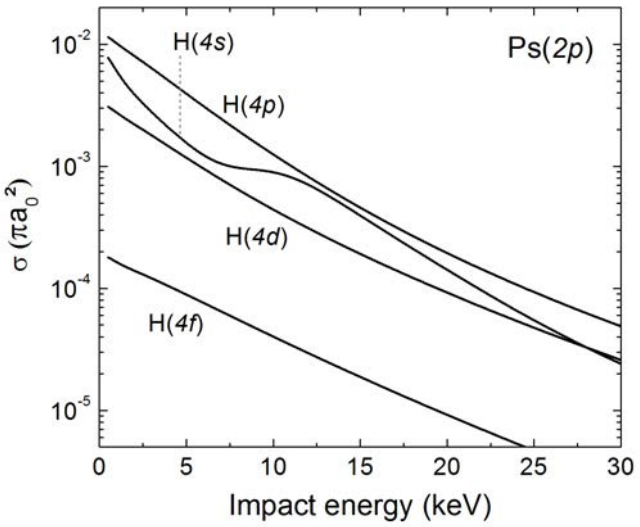


Figure 6.15: $\bar{H}^+$ production cross sections from Ps(*2p*) and the different n_h=4 states of antihydrogen.

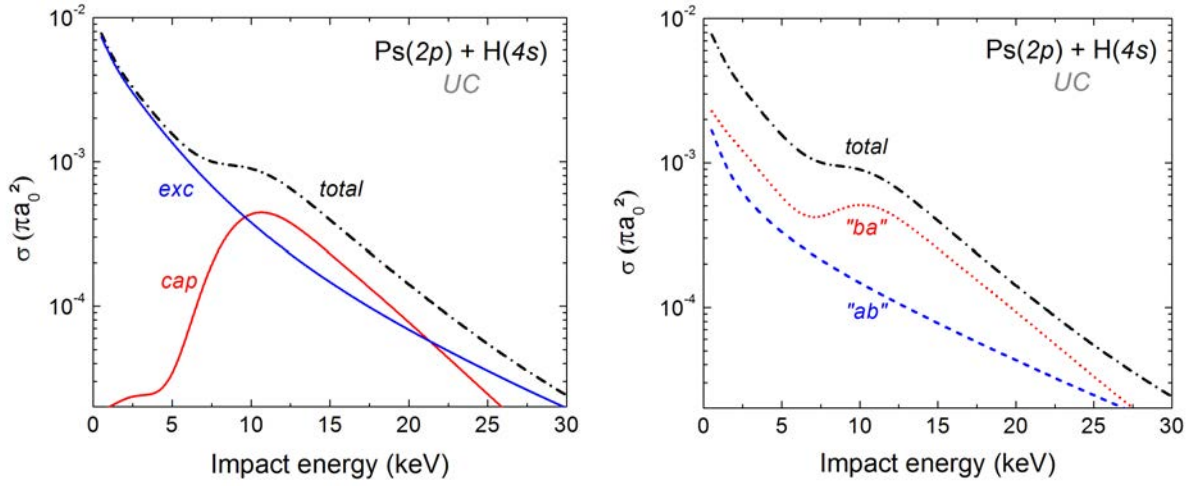
energy levels are very different from the a and b states of $\bar{H}^+$ (as described by the UC wave function for H^-), and we can imagine, in a simplistic vision, that the $\bar{H}$ must rearranged itself to form $\bar{H}^+$. The cross terms, not presented here, are completely negligible above 10 keV since the *capture* term goes to zero.

Similarly, the contributions of the processes ab and ba can be investigated by taking respectively t^{ba} or t^{ab} equal to zero. The results are presented in figure 6.16b and show that the main contribution to the total cross section of $\bar{H}^+$ is the ba process, which corresponds to the de-excitation of the positron initially in the antihydrogen atom toward the lower level a of $\bar{H}^+$ while, simultaneously, the positron in the positronium is captured in the outer level b of $\bar{H}^+$. This process is probably the one requiring a minimum of rearrangement. Nevertheless, the process ab is far from being negligible, but is mainly described by the *excitation* term: it can be pictured as if this positron in the positronium was also in a continuum state of $\bar{H}^+$ and then de-excite toward the inner level a, while the positron already in the antihydrogen atom is excited to the level b.

6.2.2 The correlated Chandrasekhar and Le Sech wave functions: selected cases and electronic correlations

From the previous results with the uncorrelated Chandrasekhar wave function, several cases of interest for GBAR have been selected for investigation with the correlated Chandrasekhar wave function and the Le Sech wave function. Since the formation of $\bar{H}^+$ ions from excited states of antihydrogen atoms is very small, only $\bar{H}(1s)$ and $(2s)$ has been considered. $\bar{H}(2s)$ has been kept to get a glimpse at where the $n_h = 2$ cross sections should be relative to the cross sections for ground state antihydrogen. Also, it is a metastable state of (anti)hydrogen which will be populated from the radiative cascade of the higher excited states of antihydrogen. This is especially of interest for Ps(*1s*) when working at 6 keV since the $n_h = 2$ cross sections with the UC wave function are of the same order as for $n_h = 1$.

To do so, only the case $l_h = 0$, detailed in appendix D, is needed and has been numerically



(a) *capture* and *excitation* (b) *"ab"* and *"ba"*

Figure 6.16: Contributions of the different processes involved in the formation of $\bar{H}^+$ from Ps(*2p*) and $\bar{H}$(*4s*).

computed. Other cases can of course be calculated using the formulas given in section 4.2 and in appendix D but at the cost of long computational time. The results are presented in figures 6.17 to 6.19, where they are also compared to the ones obtained with the uncorrelated Chandrasekhar wave function.

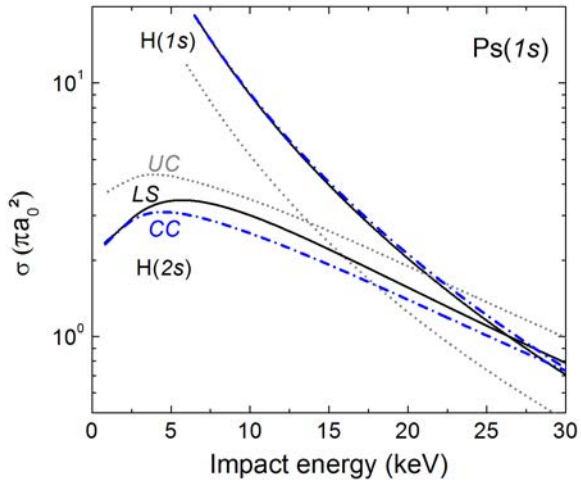
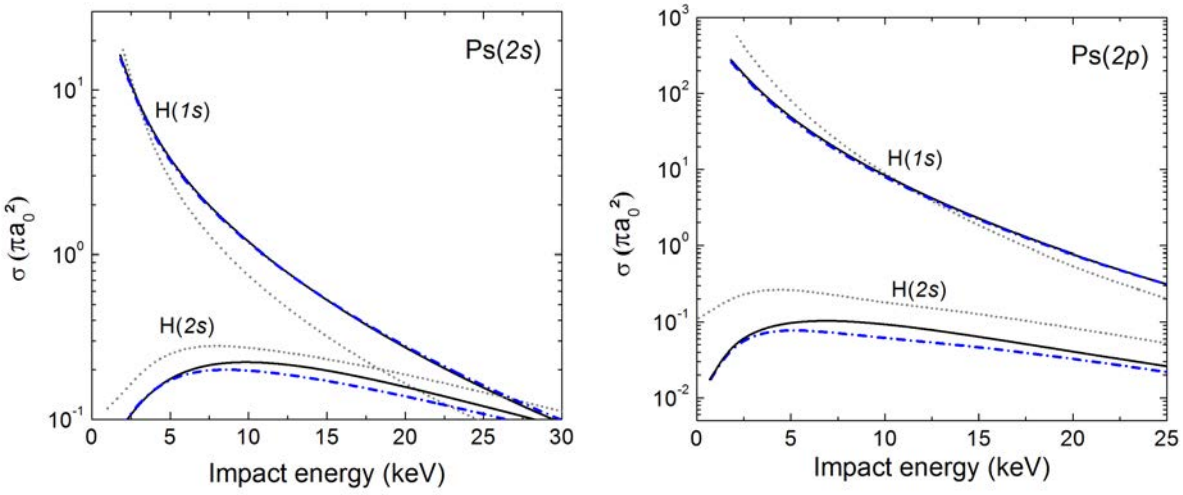


Figure 6.17: $\bar{H}^+$ production cross sections from ground state positronium (n_p=1). Comparison between the three H^- wave functions investigated: (grey) dotted lines for UC , (blue) dash-dot lines for CC and (black) solid lines for LS. The upper lines correspond to ground state antihydrogen in the entrance channel and the lines below are for the *2s*-state of antihydrogen.

The first observation is that the angular correlations taken into account in the correlated Chandrasekhar and Le Sech wave functions have an important effect on the total cross sections in all the energy range investigated, and thus cannot be overlooked as a small correction (there



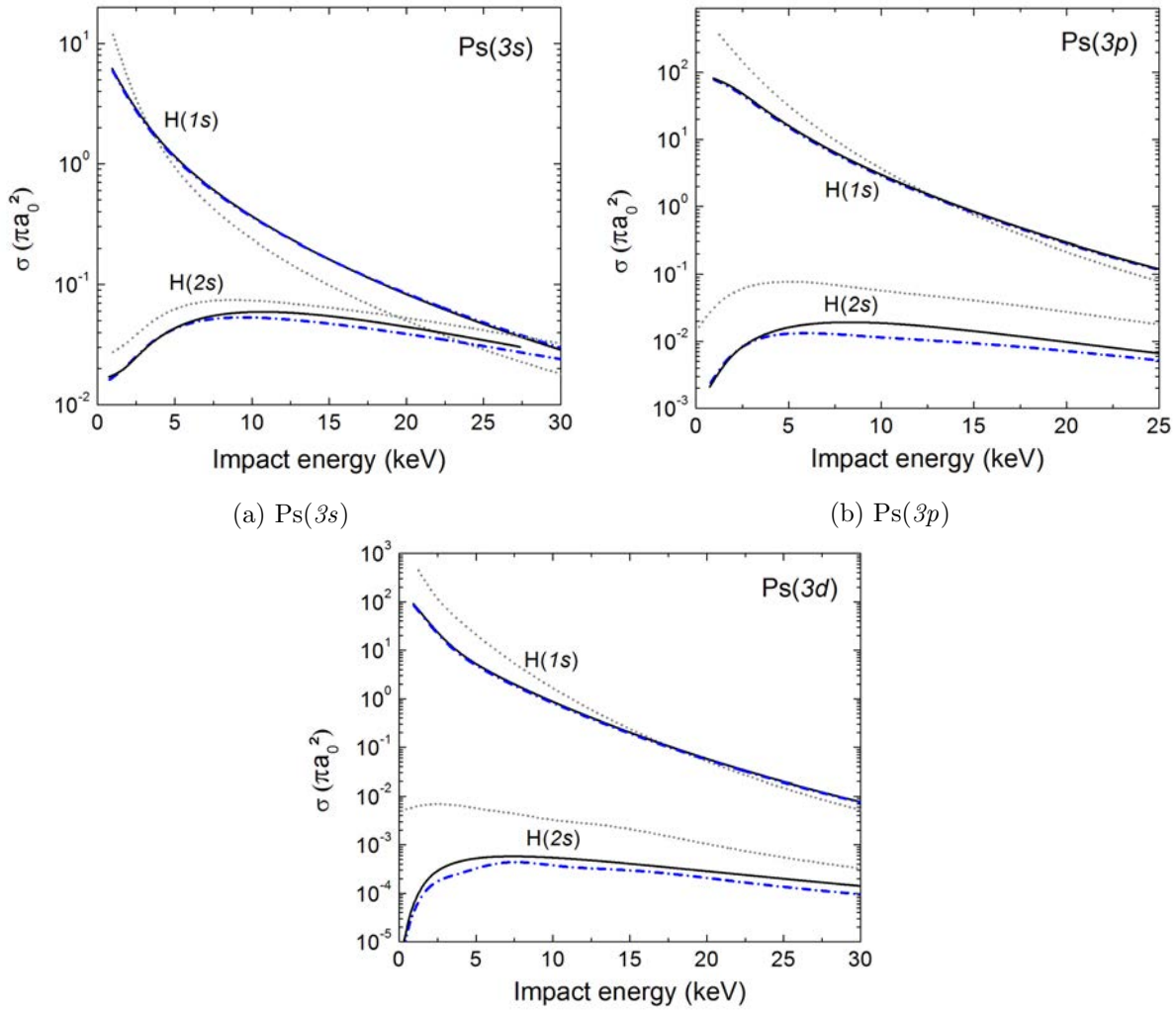
(a) Ps(*2s*) (b) Ps(*2p*)

Figure 6.18: Same as for Figure 6.17 but for n_p=2.

effect would probably be even more accentuated in the differential cross sections). However, there is little difference between the CC and the LS wave functions: for $\bar{\mathrm{H}}(1s)$ in the entrance channel, the CC and LS wave functions give the same results within 1 % below 10 keV. The most notable difference between these two wave functions is observed for $\bar{\mathrm{H}}(2s)$ above, roughly, 5 keV; below, the cross sections obtained with the CC and the LS wave functions converge toward threshold. This means that the collisional model is not sensitive to the level of description of these angular correlations at low energy, close to the reaction thresholds. This remains to be confirmed with the differential cross sections.

By comparison with the results obtained with the uncorrelated Chandrasekhar wave function (which, we remind, is already an attempt to take into account the radial correlations), one of the observed effect of the angular correlations is, when $\bar{\mathrm{H}}$ is excited, to decrease the cross sections. This damping is smaller when the positronium is in a state $l_p = 0$, but can be more than one order of magnitude at thresholds otherwise. When the antihydrogen is in its ground state, the addition of angular correlations induces an increase of the cross section for ground state positronium by almost a factor 2, while for excited states of positronium, the cross sections intersect the ones obtained with the UC wave function; in general, the cross sections computed with the CC and LS wave functions decrease at low energies and increase at higher energies. This crossing occurs at 3-4 keV for Ps(*2s*) and (*3s*), 12-13 keV for Ps(*2p*) and (*3p*), and finally 18 keV for Ps(*3d*). In the case of Ps(*3p*) and Ps(*3d*), the decrease at low energy is larger than for the other positronium states, losing almost one order of magnitude at the threshold.

The large predominance of the $\bar{\mathrm{H}}(1s)$ channel below 20 keV is confirmed with the correlated Chandrasekhar and Le Sech wave functions. The expected nearly-resonant behaviour for n_p=3 is indeed observed, but, in the prospect of the GBAR experiment, does not lead to a very sharp increase of the $\bar{\mathrm{H}}^+$ production, unless using Ps(*3d*) well below 1 keV antiproton energy. In the case of the Le Sech wave function, figure 6.20 compares, for each state of positronium investigated, the cross sections of $\bar{\mathrm{H}}^+$ production when $\bar{\mathrm{H}}$ is in its ground state in the entrance channel. It is very similar to what has been shown previously for the UC wave function, with Ps(*2p*) dominating all the other processes below 6 keV; however, it can be remarked that Ps(*3p*) is more



(a) Ps(*3s*)

(b) Ps(*3p*)

(c) Ps(*3d*)

Figure 6.19: Same as for Figure 6.17 but for n_p=3.

interesting than Ps(*3d*) above 1 keV. Finally, if working above 10 keV, Ps(*1s*) is the dominant channel.

Since the correlated Chandrasekhar wave function and the Le Sech wave function give the same results for ground state antihydrogen, we decided to use only the Le Sech wave function in the following since it is the most accurate, analytically. Compared to the uncorrelated Chandrasekhar wave function, it also bears more contraints (lower cross sections) and thus shall be chosen to limit overestimation of the total $\bar{H}^+$ production yield in GBAR.

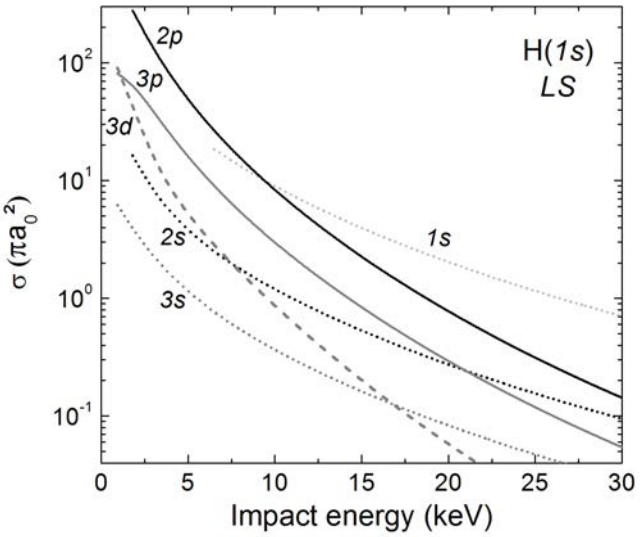


Figure 6.20: Comparison between the different positronium states for reaction 2.6 when $\bar{\mathrm{H}}$ is in the ground state - the Le Sech wave function has been used for H^-.

Chapter 7

Comparisons between models and with experimental data

7.1 CDW–FS vs. CBA

The results obtained with both CDW–FS and CBA have been independently described in sections 6.1.1 and 6.1.2 respectively, but not compared yet. To carry out this comparison, it has been chosen to plot on the same figures the CDW–FS and CBA cross sections for each positronium states, for ground state antihydrogen and for the total cross sections summed over the $\bar{\mathrm{H}}$ states. Figure 7.1 focuses on ground state positronium, figure 7.2 displays the cross section for n_p=2 and figure 7.3 addresses the case of n_p=3. The summed cross sections include the antihydrogen states from $\bar{\mathrm{H}}(1s)$ to $\bar{\mathrm{H}}(4f)$.

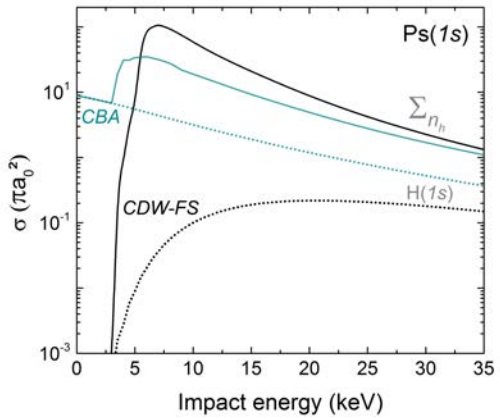
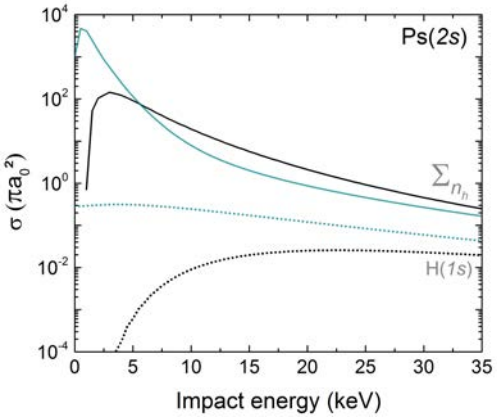
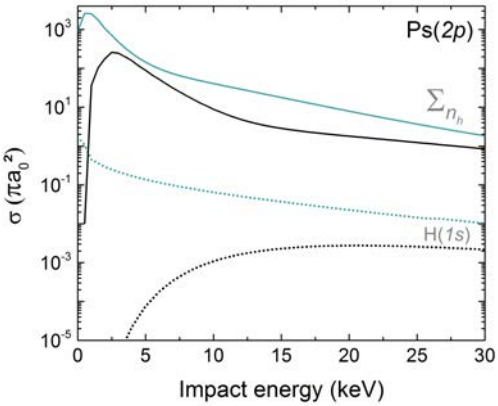


Figure 7.1: CDW–FS (black) and CBA (teal) $\bar{\mathrm{H}}$ production cross sections compared for ground state positronium. The dotted lines correspond to the formation of ground state antihydrogen only while the solid lines are the summed cross sections of antihydrogen production up to $\bar{\mathrm{H}}(4f)$.

As we could expect, the CDW–FS and CBA cross sections are on the edge of joining at high energies, where both models have their usual domain of validity. This is in fact true for any state of antihydrogen, though they are not all displayed here, with the quite surprising exception of ground state $\bar{\mathrm{H}}$ with Ps($3p$). Yet, we can note that, in general, CDW–FS and CBA are in approximate agreement for the total production of excited antihydrogen atoms as soon as the impact kinetic energy is above 5 keV. We can there make a small distinction between l_p=0 and

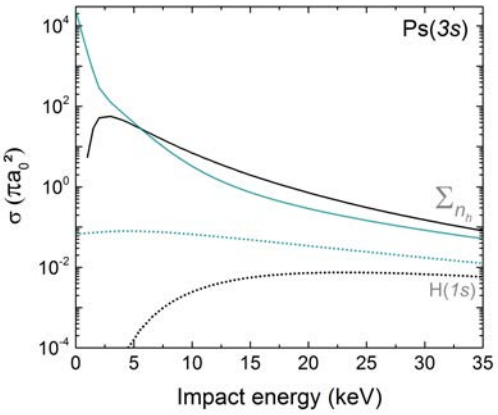


(a) Ps(*2s*)

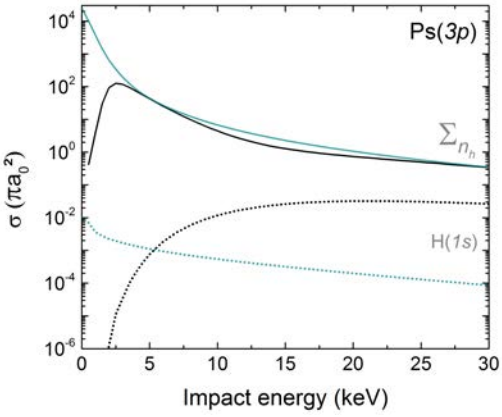


(b) Ps(*2p*)

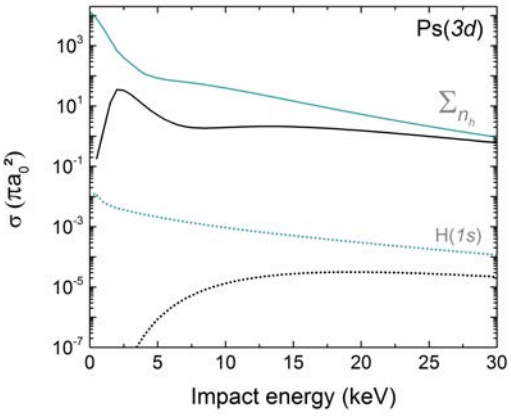
Figure 7.2: Same as for Figure 7.1 but for n_p=2.



(a) Ps(*3s*)



(b) Ps(*3p*)



(c) Ps(*3d*)

Figure 7.3: Same as for Figure 7.1 but for n_p=3.

$l_p \neq 0$ states of positronium, since, for the formers, the total antihydrogen production cross sections calculated with CBA become smaller than the CDW–FS ones, whereas in the latter case, the CBA cross sections remain higher above 5 keV.

However, as it could also be expected from the descriptions done in section 6.1, the two models totally disagree at low energies: not only do they give very different values, separated by several orders of magnitude, but their behaviour itself is also radically opposite. We thus observe that, after reaching a maximum, the CDW–FS cross sections drop to extremely low values – we can say zero – toward the thresholds for ground state antihydrogen, while the same cross sections obtained with the CBA model reach a finite value or even continue to increase until 0 keV. For the production of excited states of $\bar{\mathrm{H}}$, a similar remark can be made (excluding Ps(*1s*)): with CDW–FS, the total summed cross sections have their maximum around 3 keV, while with CBA, they continue to sharply increase, placing the maximum below 1 keV for n_p=2 states of positronium or being nearly resonant at 0 keV when the positronium is in a n_p=3 state.

The very different behaviours toward thresholds between cross sections computed with either a plane wave or a Coulomb wave function had already been pointed out in [96] (there for the case of photoelectric effect in hydrogen). We remark that this only occurs for the excited states of positronium; for ground state positronium, CBA has a reversed behaviour compared to CDW–FS: except for $\bar{\mathrm{H}}(1s)$ where the CDW–FS cross section may probably be largely underestimated at low energies, for the excited states of antihydrogen, we remember that the CBA cross sections decrease with n_h above n_h=2, and so the higher excited production is limited, while with CDW–FS, as n_h increases, so does the cross sections just above the thresholds.

The origin of this discrepancy between the two models, when the positronium is excited, can be seen by considering the final state in the formation of positronium from collisions between a positron and a hydrogen atom (reaction for which cross sections have been computed): in this final state, the incident positron is now bound to the electron taken from the hydrogen and the two particles forming the positronium are propagating in the continuum of the residual proton. In CBA, plane waves are used to describe the propagating positron and electron: this means that, at infinity, the particles are assumed to be free from the influence of the long-range Coulomb potential of the proton. This should indeed ease the liberation of the electron to form the positronium. On the contrary, in CDW–FS, the electron still feels the Coulomb potential of the proton. This potential is screened by the positron, but if the positron and the electron are far from each other (which is the case when the positronium is excited), the screening is weaker and we can imagine that the extraction of the electron from the influence of the proton is more difficult, especially at low energies. This would account for lower cross sections than for CBA.

The discrepancy between CDW–FS and CBA would probably be less pronounced or even absent if the direct reaction cross sections had been computed, since, in that case, the final state is the electron propagating in the continuum of the neutral antihydrogen: the CDW–FS approximation would reduce to the CBA approximation. Therefore, the disagreement between the two models is a form of *post/prior* discrepancy.

CDW–FS and CBA can thus lead to radically different conclusions for GBAR: they agree on the fact that it is optimal to work below 5 keV with excited positronium, in which case the antihydrogen atoms produced are excited, but CDW–FS gives an optimal energy of 2-3 keV, with Ps(*2p*) being the best option, while CBA suggests to go below 1 keV and does not really point at a particular excited state of positronium. Since they have both their weakness, the choice between the two of them will depend on the comparison with other theories (section 7.2) and with the experimental data available (section 7.3).

7.2 Comparison with previous theoretical works

7.2.1 Three-body reaction

For this comparison, we selected only a few theoretical studies. For a comparison among the models not included here, in particular for close-coupling models, see for instance [65, 69]. We have also limited the selected models to the ones computing the cross sections of the direct GBAR 3-body reaction (equation 2.4).

We start this comparison with the production of hydrogen or antihydrogen from the ground state of positronium, shown in figure 7.4. We give the total cross sections summed over the final excited states of H (or $\bar{\text{H}}$): our CDW–FS and CBA results are compared to the combined CC($1\bar{3}$,$\bar{8}$) and CC($2\bar{8}$,3) results of Mitroy & Ryzhikh [58]. We then used the modified Faddeev results from Hu & Caballero [67]: they give a total cross section for the summed contributions of Ps in the states 2S and 2P, and for the summed formation of $\bar{\text{H}}$ in the states n_h=1 and 2. This study spans a narrow energy range, from 5 to 70 eV antiproton kinetic energy: we will therefore carry out a comparison on the values at threshold, for which Faddeev-type theories are expected to be highly accurate. This comparison is presented in figure 7.5. Finally, we turned to the UBA calculation of Mitroy [57] for a comparison between CBA, CDW–FS and UBA cross sections of (anti)hydrogen formation from Ps(*3d*), displayed in figure 7.6.

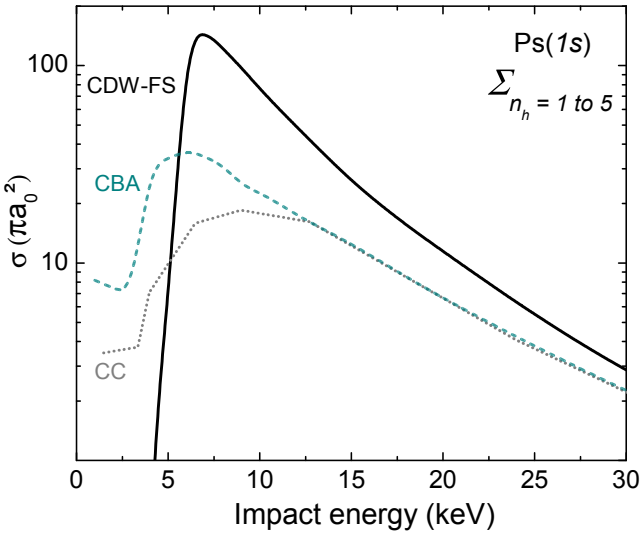


Figure 7.4: Comparison of the theoretical results for Ps(*1s*) in the entrance channel of the first reaction. The solid black line corresponds to the CDW-FS results taking into account the hydrogen states up to H(*5d*) whereas the grey dotted line is the CC estimation of the total hydrogen production from Mitroy & Ryzhikh [58], using the $\frac{1}{n^3}$ scaling for the states above H(*3d*). Our CBA results, summed over the states of hydrogen up to H(*5d*) are also included (teal dashed line).

From figure 7.4, we observe that the behaviour of the CBA cross sections matches the one of the CC cross sections of [58]: in particular, we find for both a finite value at threshold and a maximum in the range 5 to 10 keV. The agreement between the models is even better toward higher energies (above 12 keV): they predict the same values for the total (anti)hydrogen formation. The position of the maximum of the summed cross sections obtained with CDW–FS,

at about 7 keV, is in better agreement with the maximum position observed in CC than was the CBA results. However, we mainly observe that CDW–FS gives much higher cross sections, with a one order of magnitude discrepancy with respect to CC at the maximum of the cross sections. The behaviour of CDW–FS toward higher energies becomes more compatible with both CBA and CC. These results suggest that CBA should probably be preferred over CDW–FS in the case of ground state positronium.

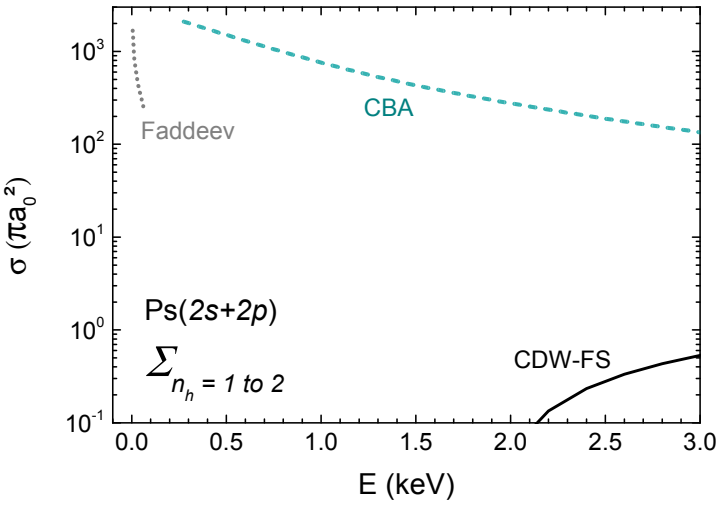


Figure 7.5: Comparison of the CDW–FS (solid black line) and CBA (teal dashed line) results to the modified Faddeev results of Hu and Caballero [67] (grey dotted line), in the case of positronium in a state n_p=2 and antihydrogen in a state $n_h \leq$2 (summed cross sections of Ps(*2s*) and Ps(*2p*) for the summed contributions of $\bar{\text{H}}$(*1s*), (*2s*) and (*2p*)).

The first remark to be made, regarding the results displayed in figure 7.5, is that CDW–FS fails completely to reproduce the threshold behaviour predicted by both the modified Faddeev model (expected to be accurate) and CBA. For cross sections involving the lower excited states of antihydrogen, CDW–FS is most probably ill-suited to low energy computations. On the contrary, the CBA results have a better behaviour toward threshold, with a large increase of the cross section when the energy decreases; extrapolating the CBA cross section to the energy range covered by the results from [67], we would probably obtain similar cross section values. However, the CBA results do not exhibit a cross section increase toward threshold as sharp as the modified Faddeev results, and, as the antiproton impact kinetic energy increases, CBA leads to much higher cross sections than the modified Faddeev results suggest. We can note a comment made by the authors of [67]: their threshold value should be considered as a lower limit value, although most probably very close to the exact value.

We finally analyse the comparison proposed in figure 7.6 for Ps(*3d*). The UBA treatment of the 3-body reaction is less refined than the CBA and CDW–FS ones. Therefore, the comparison cannot be taken as a validation (or invalidation) of our models. This remark made, we note that UBA, CBA and CDW–FS all have increased cross sections toward threshold, but that for CDW–FS, it only occurs when the n_h=5 states are included. For $n_h \leq 4$, CDW–FS does not probably have the correct behaviour at threshold. We also note that there is almost always a one

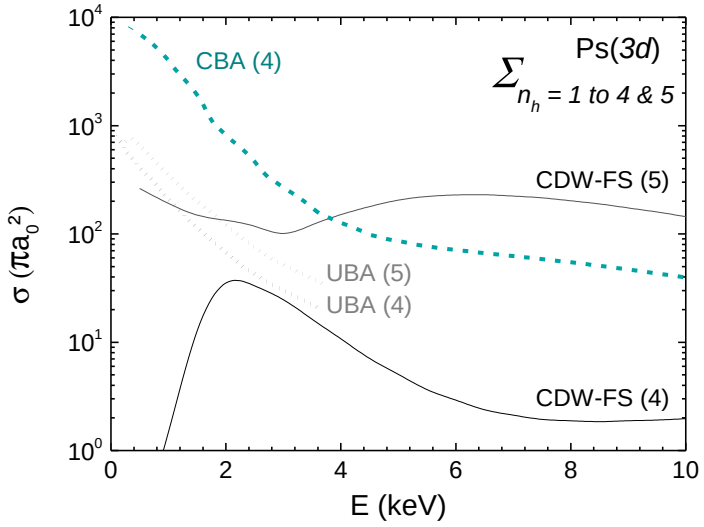


Figure 7.6: Comparison between the CDW–FS (solid black line), CBA (teal dashed line) and UBA [57] (grey dotted line) results of total hydrogen formation cross section when the positronium is excited into state 3D. The contributions of the hydrogen states have been summed up to n_4=4 and n_h=5 (except for CBA); this corresponds respectively to labels (4) and (5) in the figure.

order of magnitude discrepancy between the CBA and the UBA cross sections. On the contrary, we observe that UBA and CDW–FS are compatible at least over the range 2 to 4 keV for the cross section using $n_h \leq 4$ and in the range 1.5 to 3 keV when $n_h = 5$ states of hydrogen are added.

In general, these comparisons underline a faulty behaviour of CDW–FS toward the threshold. In order to draw further conclusions, other theoretical studies for excited states of hydrogen and of positronium (in particular for $n_p \geq 2$) would be needed.

7.2.2 Four-body reaction

Since no experimental results are yet available for the 4-body reaction, only a comparison with other theoretical models can be undertaken. So far, all the authors who investigated the 4-body reaction have kept the hydrogen atom in its ground state; we thus have no mean to confront the results we obtained for excited states of antihydrogen to other model calculations. Thus, for ground state antihydrogen, figure 7.7 focuses on ground state positronium while figure 7.8 details the cases of Ps(*2s*) and Ps(*2p*).

To carry out the comparison with the 4-body CDW–FS results (with both uncorrelated Chandrasekhar and Le Sech wave functions), we mainly focus on the coupled pseudo-states computations of McAlinden *et al.* [73], who used an approached wave function for H^-, and on the Coulomb modified eikonal approximation calculations (CMEA) of Roy and Sinha [74], who chose the uncorrelated Chandrasekhar wave function.

In the case of ground states positronium only, other theoretical studies are available: the two-channel close-coupling calculation of Biswas [72] and the CBA values obtained by Straton and Drachman [70] are thus displayed in figure 7.7. Biswas used a Chandrasekhar wave function (presumably the UC, though it is not specified), as did Straton and Drachman. The close-

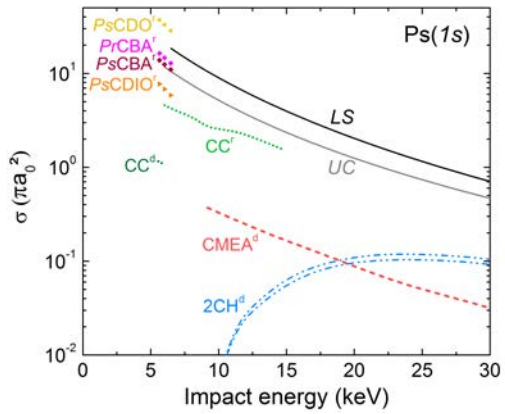
coupling calculation at threshold for the Ps(*1s*)+H(*1s*) channel performed by Blackwood *et al.* [97] is also included. The calculation by Chaudhuri [71], though carrying a discussion between several wave functions for H^- as been discarded from figure 7.7 for it gives results only above 50 keV.

Several of these others theoretical studies in fact considered the reaction of positronium formation, as we did for the computations. To avoid spurious discrepancy that may arise from the approximations done in the reversing of the cross sections (for instance in the choice of the energy of H^-, which can either be taken as the exact value or the value obtained with the considered wave function), the primary results of ground state positronium production are also plotted separately in figure 7.7b. This offers a comparison between our $\sigma^{4B,1}_{n_h l_h;\ n_p l_p}$ CDW–FS cross sections and the coupled-channel calculations of McAlinden et al. [73] and the CBA calculations of Straton and Drachman [70] in their original form.

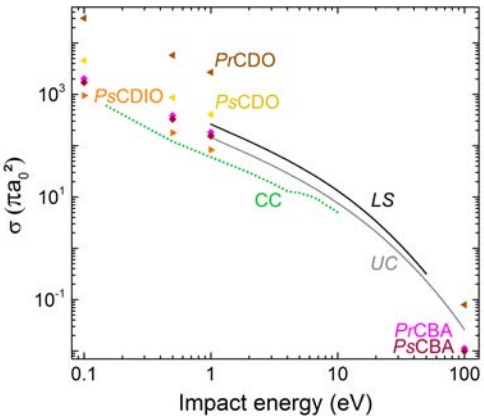
In most of the cases, although the general behaviour of the cross sections is similar, the CDW–FS results are in disagreement with the other theories calculations, giving higher cross sections. The notable exception is for Ps(*2s*) below 5 keV, where all the models seem to agree toward the threshold. Otherwise, the discrepancy can be greater than one order of magnitude. The discrepancy has nonetheless to be put into perspective: for *s*-states of positronium, the CDW–FS results are most of the time only two or three times higher than other calculation, and, looking at the cross sections displayed in figure 7.7b, we can in fact say that the CDW–FS results for the reverse reaction (2.7) are in rather good agreement with the results of Straton and Drachman, as well as the ones of McAlinden *et al.*. Let's note that the results of Biswas are strikingly different from any other: this is due to the plane wave treatment of the outgoing positron in the final state of H^- formation. Without taking into account the Coulomb interaction between these two charged species in the final state, Biswas calculations fail to give the correct behaviour at low energies, since a finite value of the cross section is then expected at the threshold. This illustrates the importance of using the correct boundary conditions.

The difference between CDW–FS and CMEA is understandable, since both models are not adapted to low energy and, in particular, they are subdued to the *post/prior* discrepancy which is emphasised toward the low energy region. More precisely, while we worked with the *prior* form of the CDW–FS cross section for the reverse reaction (Ps production), the CMEA model, *prior* form, developed by Roy and Sinha was on the contrary for the direct reaction of H^- formation. This is probably one of the reason for the disagreement at low energies. This can also explain why, in the medium energy region above 20 keV, both CDW–FS and CMEA, despite they should be valid, still disagree. However, from the *post* and *prior* CBA results from Straton and Drachman, which agree very well with our CDW–FS results supposed to be equivalent to CBA, we can see that the *post/prior* discrepancy, when using the uncorrelated Chandrasekhar wave function, is probably of the order of 10 %. We can hope for a similarly small effect with the Le Sech wave function. So, unless CMEA is on the contrary very sensitive to the *post/prior* discrepancy, this might not be the main explanation for its disagreement with CDW–FS. The other important difference between the CMEA and CDW–FS models lies in the treatment of the asymptotic states, which is exact in the case of CDW–FS. This could be a better explanation.

However, the latter argument cannot be used when comparing to the coupled-channel calculation, which is intended to be accurate in the low energy region. Nonetheless, the model developed by McAlinden *et al.*, though already including 19 pseudostates in the calculation, is itself not free from approximations. In particular, the wave function they used for H^- (a split shell function involving one electron in the H(*1s*) state and the other in a linear combination of *s*-orbitals) gives a ground state energy of -0.513 a.u., a value similar to what is obtained



(a) $\bar{\mathrm{H}}^+$ production cross sections from ground state antihydrogen and ground state positronium computed with different models. The *Pr*CDO results of Straton and Drachman are not represented here for they give far higher values of the cross sections.

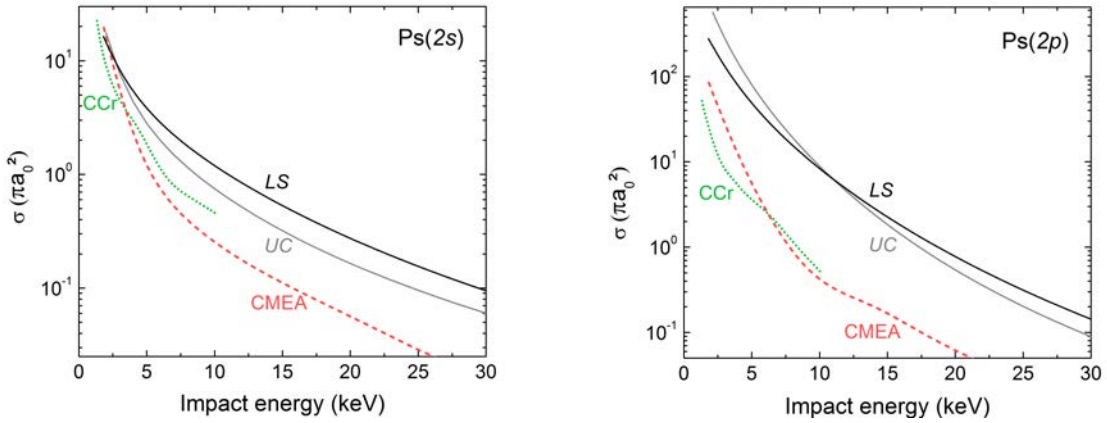


(b) Cross sections for the reverse reaction kept in the original form; the impact energy is the one of the positron in the collision between positron and H^- ion, which is at rest. To display the low energy values as well as the cross sections computed at 100 eV, a log scale as be chosen for the impact energy.

Figure 7.7: The cross sections relative to the four body reaction for ground state (anti)hydrogen and ground state positronium computed with different models. The present CDW–FS calculations are represented by the black solid line labelled *LS* for the Le Sech wave function and the grey solid line with label *UC* for the uncorrelated Chandrasekhar wave function. For the other theoretical calculations, in figure 7.7a, a small *d* (for *direct*) in exponent indicates that the cross sections have been computed for the direct reaction of H^- production, while a small *r* means that the reverse reaction, that is the positronium production, was considered. The light red dashed line labelled CMEA^d is for the results of Roy and Sinha [74] and the pseudo-state approach results of McAlinden *et al.* [73] correspond to the light green dotted line labelled CC^r (shortened to CC in figure 7.7b); the dark green dotted line with label CC^d is the calculation at threshold done by Blackwood *et al.* [97]. The CBA results of Straton and Drachman [70] are the square scatter points: pink and labelled *Pr*CBA^r for the *prior* form, and crimson with label *Ps*CBA^r for the *post* form. By the same author, the orthogonalised Fock-Tani calculations in their *post* and *prior* forms are represented by left turned triangles respectively dark yellow with label *Ps*$\mathrm{CDO}^{(r)}$ and brown with label *Pr*CDO; the *post* iso-orthogonalised results are the orange right turned triangles labelled *Ps*CDIO^r. Finally, the close-coupling calculations of Biswas [72], both two channel and two channel model exchange, are the blue dash-dot lines labelled $\mathrm{2CH}^d$.

with the uncorrelated Chandrasekhar wave function. In the conclusions of their paper [73], the authors suggested that they would investigate other wave functions for H^- (citing the one of Pekeris [90]); but no results have been made available yet. Also, their article was orientated toward positronium production: due to the type of their theoretical approach, they should have then included excited states of the produced hydrogen, in particular n_h=2 states, which they did not, as their calculation is already heavy and slow-converging.

The rather good agreement with the CDW–FS results and the CC results of McAlinden *et al.* [73], which are within less than an order of magnitude, is also an encouraging sign on the acceptable validity of CDW–FS at low energies. However, for Ps(*1s*), the threshold calculation of Blackwood *et al.* [97], probably closer to the exact value, suggests the contrary! All these ob-



(a) Ps(*2s*) (b) Ps(*2p*)

Figure 7.8: $\bar{H}^+$ production cross sections from ground state antihydrogen and n_p=2 states of positronium computed with different models. The present CDW–FS calculations are represented by the black solid line labelled *LS* for the Le Sech wave function and the grey solid line with label *UC* for the uncorrelated Chandrasekhar wave function. The light red dashed line labelled CMEA is for the results of Roy and Sinha [74] and the pseudo-state approach results of McAlinden *et al.* [73] correspond to the green dotted line labelled CC^r.

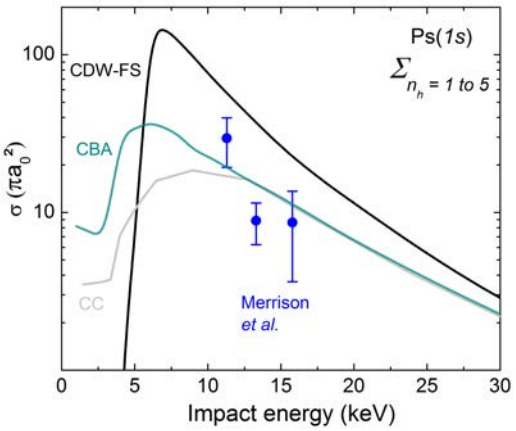
servations stress the difficulty of choosing one model over the others and that the present results should be handled with peculiar care when used to predict experimental behaviours, either for GBAR or for other future projects. Experimental data are definitely needed in this debate.

7.3 Comparison with experimental data for reaction 1

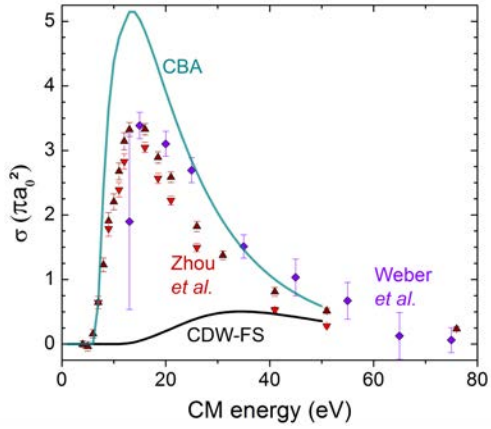
The best test to conclude on the validity of a theory is obviously to confront it to experimental results. As said previously, this cannot be done for the second reaction yet. Concerning the first reaction, several experiments gave results for the production of positronium from ground state hydrogen [59, 60] and only one experiment [64] was able to measure the cross section, at three different energies, of the hydrogen production from collisions between ground state positronium and protons. Since the configuration of the latter experiment is close to what will be done with antiprotons in GBAR, we will mainly use these results for the comparison.

In the experiment reported by Merrison *et al.*, no distinction could be made between the different states of hydrogen produced. The cross section measured thus corresponds to the sum of our $\sigma^{3B,2}_{n_h l_h;\, n_p l_p}$ cross sections over all the antihydrogen states. Here, we stopped at $5g$. In figure 7.9a, we have re-used figure 7.4 presented before and we compare these three experimental values with both our CDW–FS and CBA results, and also the CC($\bar{1}\bar{3}$,$\bar{8}$) and CC($\bar{2}\bar{8}$,3) calculations by Mitroy & Ryzhikh [58] to give some perspective.

In the case of positronium formation from ground state hydrogen, the state of the positronium produced is never measured, so, again, we need to make the comparison with a sum of cross sections, this time over all the positronium states. Obviously, we also chose not to convert these experimental results into cross sections of hydrogen production and thus use our $\sigma^{3B,1}_{n_h l_h;\, n_p l_p}$ cross sections obtained with CDW–FS and CBA. This is displayed in 7.9b, where both the experimental results of Weber *et al.* and Zhou *et al.* have been used.



(a) Hydrogen production from ground state positronium. The experimental results of Merrison *et al.* [64] are the blue circle points. The light grey line corresponds to the close-coupling results (label CC) of Mitroy and Ryzhikh [58].



(b) Positronium production from ground state hydrogen. The purple diamonds are the experimental values found by Weber *et al.* [59] whereas the red and dark red triangles are the data from Zhou *et al.* [60] (the red ones being their lower limit of the cross section). For a comparison between these experiment data and other theoretical models, in particular close-coupling models, see for instance [65].

Figure 7.9: Comparison between experimental data available concerning reactions 2.4 and 2.5, and the related CDW–FS and CBA results. The CDW–FS calculations are represented by the black solid line and CBA by the teal solid lines.

The present theoretical calculations do reproduce the behaviour suggested by the experimental data of Merrison *et al.*. In the small energy region experimentally covered, the CBA results are in very good agreement with the measured total hydrogen production; from the previous discussion on the CBA results, we remember that further excited states of antihydrogen would add a negligible contribution to the summed cross section presented in figure 7.9a. In the absence of experimental data on the repartition of the excited states of hydrogen in the total produced, we take this good match between CBA and the experiment by Merrison *et al.* as a validation of the CBA model for antihydrogen formation from ground state positronium. Despite an overestimation by, roughly, a factor 2, the CDW–FS predictions remain acceptable for a perturbative theory: based on this comparison with experimental data, CDW–FS should not be discarded.

If, on one hand, CDW–FS overestimates antihydrogen production from ground state positronium, on the other hand, it largely underestimates the production of positronium from ground state hydrogen, and even fails to reproduce the maximum observed around 14 eV by both Weber *et al.* and Zhou *et al.*; on the contrary, CBA finds the same maximum in the cross section, though it overestimates it by a bit less than 60 %. Despite this evident failure of the CDW–FS theory for the 3-body reactions involving ground state (anti)hydrogen, it should be reminded that, in the case of GBAR, we expect ground state antihydrogen production to be less consequent than excited $\bar{\text{H}}$, especially for excited positronium: thus, CDW–FS cannot be rejected. Concerning CBA, the excellent agreement between the theoretical and the experimental behaviour (in particular the place of the maximum) is another argument in favour of the validity of the Coulomb-Born approximation.

In conclusion, with the experimental data available, it seems that CBA could be more appropriate than CDW–FS to make predictions on the production of antihydrogen atoms. However,

we had already noticed the probable weakness of CDW–FS for reactions involving ground state hydrogen, while for excited states of antihydrogen, the behaviour of the CDW–FS cross sections seems more reasonable – in particular close to the thresholds where, on the contrary, the peaking CBA cross sections obtained for excited positronium are certainly not reliable. The experimental results we based the comparisons on already represent a important and difficult achievement, but data concerning the excited states of positronium would have been of greater help for the GBAR experiment. Additional experimental data are in need.

Since we are not able to fully reject or validate the CDW–FS and CBA theoretical models, we will continue to use both of them in the following part. We will nonetheless keep in mind that CDW–FS slightly over-estimates the production of antihydrogen when the positronium is in its ground state, but is probably better suited than CBA for the excited states of positronium; CDW–FS will thus be our reference to address the needs of the GBAR experiment.

Chapter 8

Conclusions of the cross section calculations

We summarise here the most important results found for the two reactions, focusing on the important parameters for the GBAR experiment. As it has been already underlined, no quantitative conclusions can be drawn, especially close to the reaction thresholds. The results focussed mainly on the relative behaviour of the cross section. Since the 3-body and 4-body reactions have been studied with the same model, using the same approximations, this reasoning can also be carried out between them (and on the combination of these two reactions).

The cross section computation for reaction 2.4 in the framework of the CDW–FS theory showed that the production of antihydrogen atoms is optimal at energies between 1 and 7 keV, maximum toward the thresholds and enhanced by the excitation of positronium, in particular Ps(*2p*) and in general for $l_p \neq 0$ states. The antihydrogen atoms are produced in excited states, and the higher is n_h, the larger are the cross sections (when the positronium is excited). When computed in the framework of the CBA theory, the behaviour of the cross sections is different at the thresholds where, for excited states of positronium, CBA gives much higher values of the cross sections, suggesting to work at very low energies. When compared to other theoretical works and experimental data, CBA seems to give more reliable results than CDW–FS in the case of ground state positronium and also ground state antihydrogen, but probably not any more for the excited states. CDW–FS will thus remain our reference for the cross sections of GBAR's first reaction.

The distinction between CDW–FS and CBA does not exist for reaction 2.6 since the two 4-body models are then equivalent (but this only because we considered the reversed reaction, 2.7, to make the calculations). The results for this second reaction suggest that only ground state antihydrogen has sufficiently large cross sections to indeed produce the $\bar{H}^+$. In that case, the cross sections peak at the thresholds, with the larger values obtained for excited states of positronum with $l_p \neq 0$, and, even more, they are almost resonant at zero energy with positronium in either state (*3p*) or (*3d*). No comparison with experimental data could yet be done, but comparison with the few other theoretical works on that reaction shows that they are all in a rather good agreement, in particular when the correlated wave function proposed by Le Sech is used to described $\bar{H}^+$.

From this, we can already have a feeling of which positronium state can be used for both reactions – that is Ps(*2p*), Ps(*3p*) and Ps(*3d*) – and in which energy range – probably around 1-2 keV. It seems that a "lesser effort" solution remains: no positronium excitation, with 6 keV antiprotons: in that case, we have lower cross sections but it requires less experimental effort

around the reaction chamber. It can be noted that cross section calculations have been initiated with positronium excited into states 4S to 4D. However, preliminary results suggest that there is no interest for GBAR in using these positronium states for the production of the antihydrogen positive ion.

So far, the results for the two reactions have been presented in a disconnected manner. However, we should keep in mind that the products of the first reaction are the only one available to make the second reaction. This trivial remark has some consequences that had not been foreseen in the GBAR proposal. Ground state antihydrogen is almost not produced in the first reaction: it seems that no use can be made from the very large cross sections obtained with this state in the second reaction, while the excited states of $\bar{\mathrm{H}}$ are apparently of lesser interest for the 4-body reaction. But since the antihydrogen atoms are abundantly produced in highly excited states, their low probability to form $\bar{\mathrm{H}}^+$ ions might be compensated by their number. Nevertheless, it seems like the benefit of positronium excitation cannot be utilised simultaneously for both reactions. In order to take advantage of the very large 4-body cross sections obtained for ground state antihydrogen, the solution is in fact to give enough time for the excited antihydrogen atoms produced to undergo radiative relaxation to the ground state.

To illustrate this idea, figure 8.1 presents a rough approximation of the CDW–FS cross sections for the two reactions combined (using the cross sections obtained with uncorrelated Chandrasekhar wave function). Two configurations have been assumed. In the first one, the antihydrogen atoms produced have no time to de-excite before the second reaction; the global cross section of the two consecutive reactions is then given by equation 8.1. In the second configuration, the collisions between excited antihydrogen atoms and the positronium atoms are supposed to be totally inefficient and are neglected; however, it is assumed that a fraction of these excited $\bar{\mathrm{H}}$ were able to de-excite to the ground state which is used for the second reaction. In that case, the global cross section has been calculated using Eq. (8.2). In both cases, it is assumed that the proportions of positronium in the ground state $(1-f)$ and in the (n_p, l_p) excited state (f) are fixed during the whole process. These cross sections are thus given for 100 % Ps($1s$) (f=0) and for 30 % Ps($2p$) (f=0.3 ; n_p=2, l_p=1). In the second configuration, we arbitrary fixed that 20 % (ε) of the excited $\bar{\mathrm{H}}$ produced in the first reaction had time to de-excite to the ground state before undergoing the second reaction.

$$\begin{aligned}
\sigma^{(2)}_{n_p l_p;f} &= (1-f)^2 \sum_{n_h l_h} \left(\sigma^{3B,2}_{n_h l_h;\ 10} \times \sigma^{4B,4}_{n_h l_h;\ 10} \right) \\
&+ f(1-f) \sum_{n_h l_h} \left(\sigma^{3B,2}_{n_h l_h;\ 10} \times \sigma^{4B,4}_{10;\ n_p l_p} + \sigma^{3B,2}_{n_h l_h;\ n_p l_p} \times \sigma^{4B,4}_{n_h l_h;\ 10} \right) \\
&+ f^2 \sum_{n_h l_h} \left(\sigma^{3B,2}_{n_h l_h;\ n_p l_p} \times \sigma^{4B,4}_{10;\ n_p l_p} \right). \qquad (8.1)
\end{aligned}$$

$$\begin{aligned}
\sigma^{(2)}_{n_p l_p;f} &= \left[(1-f) \sum_{n_h l_h} \sigma^{3B,2}_{n_h l_h;\ 10} + f \sum_{n_h l_h} \sigma^{3B,2}_{n_h l_h;\ n_p l_p} \right] \\
&\times \varepsilon \times \left[(1-f)\, \sigma^{4B,4}_{10;\ 10} + f\, \sigma^{4B,4}_{10;\ n_p l_p} \right]. \qquad (8.2)
\end{aligned}$$

From figure 8.1, it can be deduced that, indeed, the large number of excited $\bar{\mathrm{H}}$ atoms produced cannot compensate for the very weak cross sections of the second reaction; ground state

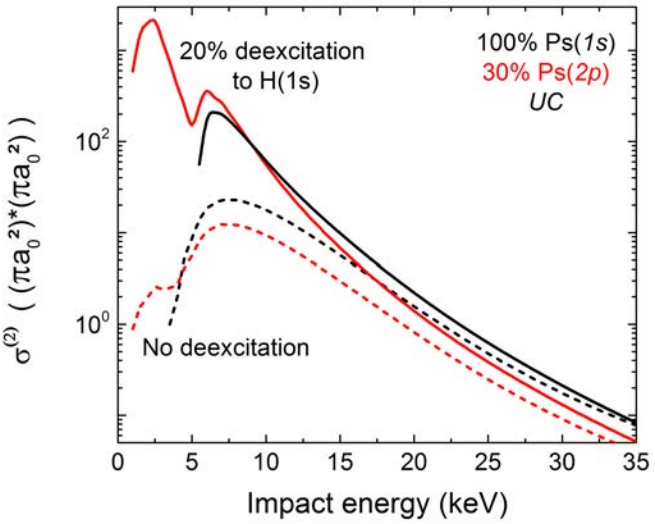


Figure 8.1: Comparison between the global $\bar{H}^+$ production cross sections, in the case of the UC wave function, when a fraction of the excited antihydrogen atoms had time to radiatively cascade down to ground state for the second reaction (solid curves) or not (dashed curves). Antihydrogen production up to $\bar{H}(4f)$ has been taken into account. The influence of positronium excitation is also demonstrated with either 100 % of Ps(*1s*) (black) or 30 % of Ps(*2p*) (red).

antihydrogen must be obtained between the two reactions. This can be done by letting the $\bar{H}$ atoms de-excite, and, in that case, the gain on the global cross section is important. The gain of positronium excitation is also indisputable. The uselessness of the antihydrogen atoms still excited for the second reaction being now definitely established, we can reproduce a similar figure with the results obtained for the Le Sech wave function. The cross sections calculated with equation 8.2 are displayed in figure 8.2, with the following parameters: 100 % Ps(*1s*) (f=0), 30 % Ps(*2p*) (f=0.3 ; n_p=2, l_p=1), and 50 % Ps(*3d*) (f=0.5 ; n_p=3, l_p=2) – values that are thought to be experimentally feasible – and ε=20 %.

Since the best way to proceed for GBAR is to let antihydrogen de-excite, then the positronium cloud in the reaction chamber should be long but still dense enough so that the antihydrogen atoms can de-excite in flight and, once in the ground state, still find some excited positronium to undergo the second reaction. This thus implies a change in the design of the reaction chamber, which should be longer and maybe thinner than initially thought; then it also has consequences on the injection of the positron and the antiprotons in that chamber. The geometry and dynamic aspects of the problem will be further addressed in the following section, thanks to a calculation simulating the physical processes and the evolution of the reactions in the chamber.

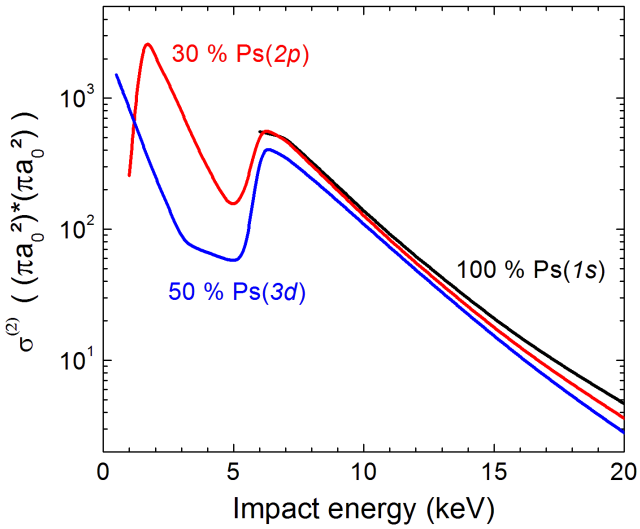


Figure 8.2: Comparison between the global $\bar{H}^+$ production cross sections, in the case of the Le Sech wave function, for different simple solutions of positronium excitation; it has been assumed that 20% of all the antihydrogen produced are in the ground state for the second reaction and that they are the only one to contribute to the $\bar{H}^+$ formation. Antihydrogen production up to $\bar{H}(5d)$ has been taken into account here.

Part III

Simulation and design of the GBAR reaction chamber

Chapter 9

Description of the simulation

In the previous part, an extensive description of the antihydrogen ion production reactions has been obtained in terms of cross sections. However, the insufficiency of the sole cross sections was already outlined when, for instance, we have remarked that antihydrogen de-excitation was required between the two reactions. The evolution of the positronium populations, firstly due to the positronium annihilation and then because of a potential positronium excitation, also calls for a time-dependent treatment of the positronium–antiprotons system. The dynamical description of GBAR's interaction cell has thus been initiated with a simple simulation.

The present chapter will describe the equations and many parameters used in the simulation, while the following chapters will discuss the parameter dependence and the $\bar{H}^+$ production results obtained, as well as the improvements that can be done to aim at a more realistic description.

The simulation of the interaction region using the computed cross sections is a calculation based on evolution of populations with time, and is segmented into two parts: the first one treats the positronium production and excitation and, once the populations of positronium known at all time, the second one is dedicated to the calculation of the antihydrogen atoms and ions populations. This formulation of the simulation has been originally proposed by François Biraben, from LKB.

9.1 The positronium populations

9.1.1 Optical Bloch equations

The interaction between the positronium atoms and the excitation laser beam is treated within the formalism of the density matrix, from which are derived the optical Bloch equations. The optical Bloch equations are particularly adapted to describe the evolution of a two-level system interacting with an intense electro-magnetic field and are necessary when the considered levels both have a finite lifetime (indeed, in that case, we have an *open system*, whereas a treatment involving the Schrödinger equation requires the system to be isolated to ensure energy conservation). The two-level systems of interest for GBAR are Ps(*1s*)-Ps(*2p*) or Ps(*1s*)-Ps(*3d*). The 2P and 3D excited states have a lifetime of, respectively, 3.2 ns and 31 ns; the ground state is also unstable since it annihilates, with a lifetime, τ, of 142 ns for the ortho-positronium. In addition of having unstable levels, ground state positronium will be simultaneously created in the reaction chamber and the excited states can be photo-detached. For all these reasons, and also because we will use intense laser pulses, the use of the optical Bloch equations is indeed justified. In the following, we will focus on the 1S-3D two-photon transition, since the study of the 1S-2P transition with the simulation has not been done yet.

The hermitian density operator is represented by a matrix, ρ, whose diagonal elements are called the *populations*, while the elements off diagonal are the *coherences*. The equation ruling the evolution of the density matrix, and from which are derived the optical Bloch equations, is obtained applying the Liouville theorem:

$$\dot{\rho} = \frac{1}{i\hbar}[H, \rho] + \gamma\rho, \tag{9.1}$$

where H is the Hamiltonian and $\gamma\rho$ is the relaxation matrix describing the spontaneous emission, the annihilation, etc. The Hamiltonian is the sum of the unperturbed Hamiltonian of the system (two-level system, here) and of the interaction with the electric field, -$\mathbf{d} \cdot \mathbf{E}$ ($\mathbf{d}$ is electric dipole moment).

Designing the ground state positronium as level *gg* and the excited state as level *ee*, the probability to find the positronium in the ground state (respectively in the excited state) is the population ρ_{gg} (respectively ρ_{ee}), while the coherences ρ_{ge} and ρ_{eg} represent the probability of finding the positronium in a coherent superposition of both states. For the two-level system *gg-ee* of positronium exposed to laser radiation resonant with the corresponding transition, the optical Bloch equations are:

$$\dot{\rho}_{gg} = p + I_L\left(-i\frac{\Omega}{2}\rho_{eg} + i\frac{\Omega}{2}\rho_{ge}\right) + \Gamma_e\rho_{ee} - \frac{\rho_{gg}}{\tau} \tag{9.2}$$

$$\dot{\rho}_{eg} = I_L\left(i\frac{\Omega}{2}\rho_{ee} - i\frac{\Omega}{2}\rho_{gg}\right) - \frac{\Gamma_e + \frac{1}{\tau}}{2}\rho_{eg} \tag{9.3}$$

$$\dot{\rho}_{ee} = I_L\left(i\frac{\Omega}{2}\rho_{eg} - i\frac{\Omega}{2}\rho_{ge}\right) - \Gamma_e\rho_{ee} - I_L\Gamma_{photo}\rho_{ee}, \tag{9.4}$$

with the following relation between the two coherences:

$$\rho_{ge} = \rho_{eg}*, \tag{9.5}$$

where the source term p has been added to account for the production rate of ground state positronium, I_L is the profile of the laser, Γ_e is the de-excitation rate from 3D to 1S ($\Gamma_e = \frac{1}{\tau_{3D}}$, with τ_{3D} the lifetime of the 3D level), Ω is the generalised Rabi frequency, equal to $\sqrt{\Gamma_e\Gamma_g}$, where Γ_g is the transition probability from the ground state to the excited state (two-photon transition probability for 1S-3D), and Γ_{photo} is the photo-ionisation probability of the 3D level. The coherences represent virtual intermediate states ensuring the coupling between the populations. The power density of the laser light is hidden in the two-photon transition probability Γ_g, as it will be shown in the following section.

9.1.2 Transition and photo-ionisation probabilities

The density matrix description uses transitions and photo-ionisation probabilities that have to be computed. In this section, their general analytical expressions and numerical values are given.

For a Doppler free resonant two-photon transition (obtained using two counter-propagating beams), the transition probability Γ_g can for instance by found in [98] and its general expression is:

$$\Gamma_g = \frac{n^2\omega^2}{\epsilon_0^2\hbar^2}\left|\sum_r \frac{\langle e|\mathbf{d}\cdot\varepsilon|r\rangle\langle r|\mathbf{d}\cdot\varepsilon|g\rangle}{\omega - \omega_{rg}}\right|^2 \frac{\Gamma_e}{(2\omega - \omega_{eg})^2 + \left(\frac{\Gamma_e}{2}\right)^2}. \tag{9.6}$$

In that expression, $\mathbf{d}$ is the operator of the electric dipole moment, ε is the polarisation of the laser, $|g\rangle$ is the ground state, $|e\rangle$ is the considered excited state of natural width Γ_e, the states

$|r\rangle$ are the intermediate states (they can be continuum states), for any state i, $\omega_{ig} = \frac{1}{\hbar}(E_i - E_g)$ and ω is the frequency of the laser; since we supposed that we are at the resonance, $2\omega = \omega_{eg}$ and the term

$$\frac{\Gamma_e}{(2\omega - \omega_{eg})^2 + \left(\frac{\Gamma_e}{2}\right)^2}$$

is in fact equal to $\frac{4}{\Gamma_e}$. In equation 9.6, the factor n is the number of photons per unit of volume in one beam, which can be related to the intensity of the laser by $I = \frac{n\hbar\omega}{c}$, in W/m^2. Assuming that the laser used is polarised along the z axis, one can introduce the two-photon operator Q_{2ph} written as:

$$Q_{2ph} = \sum_r \frac{z|r\rangle\langle r|z}{\omega - \omega_{rg}}, \tag{9.7}$$

in atomic units. Then, for the excitation of the 3^3D_3 fine structure level of the positronium, Γ_g can be rewritten as:

$$\Gamma_g = \sqrt{\frac{7}{15}}\left(\frac{4\pi a_0^2}{mc^2\alpha}\right)^2 |\langle e|Q_{2ph}|g\rangle|^2 \frac{4I^2}{\Gamma_e}. \tag{9.8}$$

The matrix elements $\langle e|Q_{2ph}|g\rangle$ for positronium can be deduced from the ones of hydrogen. Indeed, since the transition frequencies in positronium are half the ones in hydrogen and the radius of the positronium states are on the contrary twice the ones of hydrogen (hence a doubled electric dipole moment), the matrix elements $\langle e|Q_{2ph}|g\rangle$ for positronium are eight times the ones of hydrogen. In hydrogen, they have been calculated in [99] and the interesting values for GBAR have been reported in the proposal [50]. In the particular case of the 1S-3D transition in positronium, we have $\langle e|Q_{2ph}|g\rangle = 8 \times 5.87 = 46.96$ a.u.

We can now define a singular value of the light power density, I, that we will note I_0, satisfying the relation $\Gamma_g = \Gamma_e$. From equation 9.8, and after numerical application, we found that $I_0 = 8.538$ GW/m^2. The excited state cannot be considerably populated until Γ_g becomes larger than Γ_e, that is when the laser power used is larger than I_0.

We will now compute the probability of photo-ionising the 3D state of positronium when the power density is I. In the configuration of the Doppler-free two-photon transition with two laser beams counter-propagating, the photo-ionisation probability Γ_{photo} is:

$$\Gamma_{photo} = 4\pi I \frac{a_0^2}{mc^2\alpha}\gamma_{photo}, \tag{9.9}$$

with $\gamma_{photo} = 0.4584$ a.u. for hydrogen and thus 3.6676 a.u. for positronium [50]. In the case of I is equal to I_0, we have $\Gamma_{photo} \approx 0.057\,\Gamma_e$. Therefore, the photo-ionisation of Ps($3d$), although not totally negligible, will not cause important loses of positronium atoms.

9.2 Rate equations for antimatter production

The antihydrogen atom and ion production is treated using rate equations on the $\bar{H}$ and $\bar{H}^+$ populations.

9.2.1 Antihydrogen production

The rate equation describing the evolution of the $\bar{H}$ population with time is the following:

$$\dot{\boldsymbol{p}}_{\bar{H}} = N_{\bar{p}}\boldsymbol{\Gamma}_{(1)} + \bar{\bar{\Gamma}}_{rad} \times \boldsymbol{p}_{\bar{H}}, \tag{9.10}$$

where $\boldsymbol{p}_{\bar{\mathrm{H}}}$ is the 13-vector of the antihydrogen populations (from $(1s)$ to $(5d)$, for which CDW-FS and CBA results are available). The first term corresponds to the formation of the antihydrogen atoms from the collisions between the positronium and the antiprotons; $N_{\bar{\mathrm{p}}}$ is the number of antiprotons crossing the reaction chamber and $\boldsymbol{\Gamma}_{(1)}$ is the 13-vector of the $\bar{\mathrm{H}}$ formation probabilities per unit of time defined as:

$$\begin{aligned}\boldsymbol{\Gamma}_{(1)} &= \boldsymbol{\Gamma}_{(1)}(Ps_{1s}, \bar{\mathrm{H}}_{n_h,l_h}) + \boldsymbol{\Gamma}_{(1)}(Ps_{3d}, \bar{\mathrm{H}}_{n_h,l_h}) \\ &= n_{Ps}\rho_{1s}v\boldsymbol{\sigma}_{(1)}(Ps_{1s}, \bar{\mathrm{H}}_{n_h,l_h}) + n_{Ps}\rho_{3d}v\boldsymbol{\sigma}_{(1)}(Ps_{3d}, \bar{\mathrm{H}}_{n_h,l_h}),\end{aligned} \tag{9.11}$$

with $\boldsymbol{\sigma}_{(1)}$ the CDW–FS or CBA cross sections for reaction 2.4, n_{Ps} the total number of orthopositronium atoms produced, v the speed of the antiprotons and ρ_{1s} and ρ_{3d} the populations of respectively Ps$(1s)$ and Ps$(3d)$. The latter populations are computed using the previously introduced optical Bloch equations. The second term in 9.10 describes the successive radiative relaxations of the antihydrogen excited states with $\bar{\bar{\Gamma}}_{rad}$ being the 13×13 radiation matrix of the first 13 (n_h, l_h) states of hydrogen. [100]

9.2.2 Antihydrogen positive ion production

The evolution of the $\bar{\mathrm{H}}^+$ population with time is ruled by the following rate equation:

$$\dot{\boldsymbol{p}}_{\bar{\mathrm{H}}^+} = {}^t\boldsymbol{\Gamma}_{(2)} \times \boldsymbol{p}_{\bar{\mathrm{H}}} - \Gamma_{det} \times I_L, \tag{9.12}$$

where $\boldsymbol{p}_{\bar{\mathrm{H}}^+}$ is the population of $\bar{\mathrm{H}}^+$ ions.

The first term corresponds to the formation of the $\bar{\mathrm{H}}^+$ ions from the collisions between the antihydrogen atoms and the positronium; $\boldsymbol{p}_{\bar{\mathrm{H}}}$ is the previously defined 13-vector of the antihydrogen populations and $\boldsymbol{\Gamma}_{(2)}$ is the 13-vector of the $\bar{\mathrm{H}}^+$ formation probabilities per unit of time defined by:

$$\begin{aligned}\boldsymbol{\Gamma}_{(2)} &= \boldsymbol{\Gamma}_{(2)}(Ps_{1s}, \bar{\mathrm{H}}_{n_h,l_h}) + \boldsymbol{\Gamma}_{(2)}(Ps_{3d}, \bar{\mathrm{H}}_{n_h,l_h}) \\ &= n_{Ps}\rho_{1s}v\boldsymbol{\sigma}_{(2)}(Ps_{1s}, \bar{\mathrm{H}}_{n_h,l_h}) + n_{Ps}\rho_{3d}v\boldsymbol{\sigma}_{(2)}(Ps_{3d}, \bar{\mathrm{H}}_{n_h,l_h})\end{aligned} \tag{9.13}$$

with $\boldsymbol{\sigma}_{(2)}$ the CDW-FS or CBA cross sections for reaction 2.6, n_{Ps} the total number of orthopositronium atoms produced, v the speed of the antihydrogen atoms and ρ_{1s} and ρ_{3d} the populations of respectively Ps$(1s)$ and Ps$(3d)$. In practice, the cross sections used in the simulation are the one obtained with the Le Sech wave function, and only $\bar{\mathrm{H}}^+$ production from $\bar{\mathrm{H}}(1s)$ and $(2s)$ is considered. Besides, the interest of taking into account the 2S state of $\bar{\mathrm{H}}$ for the second reaction will be investigated, since it is a metastable state that can be significantly populated during the relaxation of the excited antihydrogen atoms.

The second term in equation 9.2.2 has been introduced to take into account the destruction of the antihydrogen ions by laser photodetachment: it is proportional to the number of ions already created and to Γ_{det}, which is the photodetachment probability of $\bar{\mathrm{H}}^+$ for the laser intensity of concern, that has to be pondered by the laser profile I_L.

The photodetachment probability is linked to the $\bar{\mathrm{H}}^+$ photodetachment cross section as follows:

$$\Gamma_{det} = \frac{I}{h\nu}\sigma_{det}(\nu), \tag{9.14}$$

where I is the intensity of the light in W/cm^2 (which is twice the intensity of the laser beam in the case of the excitation scheme using two counter-propagating beams), $h\nu$ is the energy of a photon at the relevant laser frequency and $\sigma_{det}(\nu)$ is the photodetachment cross section at this

frequency. $\sigma_{det}(\nu)$ has been both experimental measured [53] and theoretically predicted for the H^- ion [101, 102]. The results are summarised in table 9.1 for the two wavelengths of interest for GBAR. Let's note that for the $\bar{H}^+$ kinetic energy considered, the Doppler effect has negligible consequence on the photodetachment cross section.

	243 nm	410 nm
σ_{det} $(10^{-17} cm^2)$	1.2	2.4

Table 9.1: Theoretical values of the H^- photodetachment cross sections at 243 and 410 nm from [101] and [102] (only at 410 nm for the latter). The experimental data are available above 426 nm.

9.2.3 Solving

In the simulation, this system of 13 differential equations for $\bar{H}$, plus the differential equation for $\bar{H}^+$, is solved considering first a Dirac pulse of antiprotons at all possible delays. The final populations are obtained by convoluting the results by the shape of the antiproton pulse. In the case of a simulation event by event, the Dirac pulse represents one antiproton and the system is solved for each antiproton: finally, all the populations are summed, thus giving a pulse of $\bar{H}^+$: the integration of this $\bar{H}^+$ population gives the mean number of antihydrogen ion per pulse of antiprotons and the shape of the pulse represents the probability law of finding an ion at a certain time.

9.3 Parameters

9.3.1 Positron beam and positronium formation

Though the mechanisms involved in the positronium formation and desorption from the converter are quite well identified, the related dynamics is not well known. Experiments on positronium production have not been able to measure the delay between the positron implantation and the emission of the positronium from the converter surface: it is most of the time assumed to be negligible. Also, though it has been possible to measure the energy of the positronium atoms formed [44, 43], either by time of flight spectroscopy or from the γ-ray spectrum, nothing has been published concerning the time spread of the positronium pulse obtained. Again, it is usually assumed that it follows a time profile similar to the one of the positron pulse. Finally, the angular dependence of the emission is also unknown, except that there are some indications that it is not isotropic.

So far, the accumulation of the positrons in the Penning-Malmberg trap was not yet efficiently completed at CEA-Sacaly. However, we can rely on the data taken when the trap was still at RIKEN. By then, 1.34 10^{10} electrons could have been ejected in a short pulse of 76 ns FWHM, as shown in figure 9.1. [50] In the absence of large positron plasma ejection tests, it is assumed that the fast ejection of the few 10^{10} expected positrons can also produce a pulse of 75 ns typical FWHM, and that the positrons are all accelerated to 3 keV and successfully implanted into the converter.

Several materials can be used as a positron to positronium converter (metals, semiconductors,

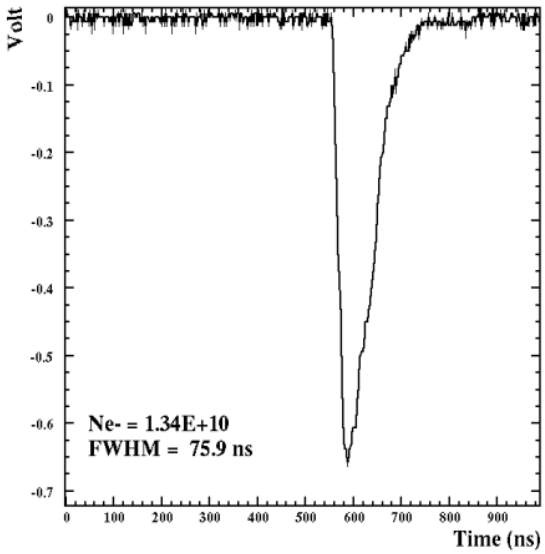


Figure 9.1: Pulse observed on a Faraday cup after fast ejection of a 1.34 10^{10} electron plasma with the RIKEN trap.

...). Members of the GBAR collaboration have acquired expertise in using nanoporous silica films [103, 43]: this material is typically 0.3 to 1 μm thick, deposited by spin-coating on a silica surface, with nanometric interconnected pores of chosen size. With pores diameter of 3-4 or 5-8 nm, it has been possible to achieve a 35 % efficiency conversion of positrons into ortho-positronium, with a re-emission energy of 48 to 73 meV (the latter has been obtained for the smaller pores, a difference probably explained by a higher confinement energy). Based on this value of 35 % efficiency, starting with $2{\cdot}10^{10}$ ejected positrons, we should be able to have $7{\cdot}10^{9}$ o-Ps atoms produced in the reaction chamber. This is thus the total number of Ps(*1s*) atoms considered in the simulation (parameter `z_Ps`). It is possible that higher conversion efficiency can be achieved before the experiment starts at CERN: a 50 % efficiency with the nanoporous films could be reached with further development, or even higher efficiency with other material, like germanium.

Under these assumptions, figure 9.2 shows the production of ground state positronium in the reaction chamber. For the convenience, the positronium production rate function has been chosen to easily define the $t = 0$ of the simulation, with a profile similar to the electron pulse shown in figure 9.1; its mathematical expression is the following:

$$prod_{Ps}(t) \;=\; \frac{4t^2}{\sqrt{\pi}(2\sigma_{Ps}^2)^{3/2}} e^{-\frac{t^2}{2\sigma_{Ps}^2}}, \tag{9.15}$$

with σ_{Ps} artificially related to the parameter `t_eimp`, the FWHM of the positron pulse, as follows: $\sigma_{Ps} = \texttt{t_eimp}/(\frac{4}{3}\sqrt{2ln2})$ (this choice allows the Ps pulse FWHM to be almost equal – in fact, slightly superior – to `t_eimp`). This `prod_Ps` function is equal to 0 at $t = 0$; all the delays and particle times of flight will thus be defined with respect to that moment when the positronium production just begins. Although we aim at a 75 ns FWHM for the positron pulse, the effect of larger or smaller width (though the latter is certainly not feasible) will be investigated. Thus, figure 9.2 also displays the positronium pulses obtained with `t_eimp` equal 60 and 100 ns.

In addition to this description of the positronium formation, we assume that the positronium

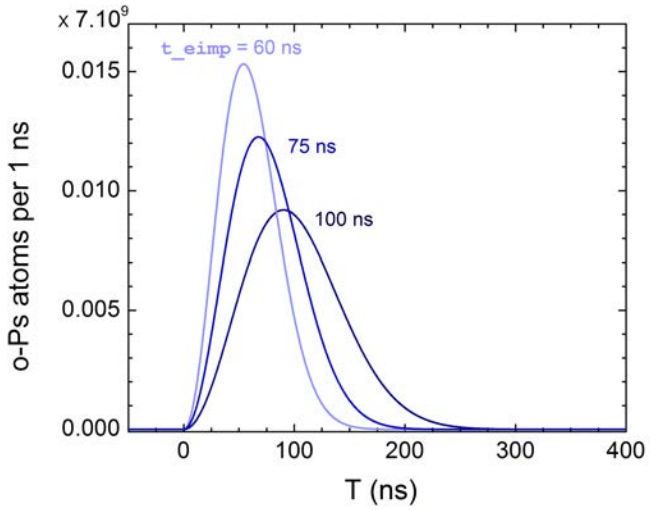


Figure 9.2: Production of ground state ortho-positronium for three different FWHM of the positron pulse.

density is homogeneous at all time all along the reaction chamber and that, as long as we work with a reaction chamber having small apertures compared to its length, the loss of positronium atoms through these apertures is negligible. Thus, it has been considered that the positronium is fully confined in the reaction chamber and fully reflected by the inner walls: no additional loss term was included in the optical Bloch equation for ground state positronium other than its annihilation into vacuum.

9.3.2 Laser beam

We mainly focussed the study on the case of positronium excitation into the 3D state. Indeed, at the time the work on the simulation began, despite the results of the cross section calculations, it had been decided to work with Ps($3d$) because the laser system required for that was already well-known, while no thorough thinking had been carried out on a laser system dedicated to the production of Ps($2p$). At the present day, excitation to the 2P state is now considered in the final experiment at CERN, requiring to be investigated through the simulation.

The laser for Ps($3d$) is designed to give one pulse each time a positronium cloud is formed in the reaction chamber. To perform a Doppler-free two-photon transition to the 3D state, the positronium is excited by two counter-propagating pulses that cross inside the reaction chamber. Precisions on this set-up are given in the following paragraph. The laser pulse has a Gaussian profile, $I_L(t)$, with a FWHM (`t_limp`) that can be chosen between 10 and 50 ns, typically. The energy per pulse can also be varied, using a parameter called `xi`, defined as the relation between the two-photon transition probability Γ_g and the width of the 3D level, Γ_e:

$$\Gamma_g \;=\; \texttt{xi}\Gamma_e. \tag{9.16}$$

The energy per pulse of the laser, $\mathcal{E}$, is given by

$$\mathcal{E} \;=\; \sqrt{\texttt{xi}}I_0 A\frac{\sqrt{\pi}}{2\sqrt{\ln 2}}\texttt{t_limp}, \tag{9.17}$$

with I_0 the previously defined intensity to have $\Gamma_g = \Gamma_e$ and A the surface lit by the laser. The delay of the laser pulse, `ldel`, is defined between $t = 0$ and the moment the maximum of the pulse enters the reaction chamber.

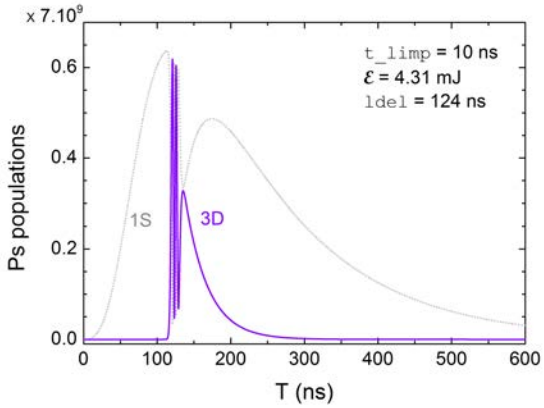
To obtain the two counter-propagating beams that permit to be free from the first order Doppler effect, the laser pulse is sent back on its track by a mirror. It is assumed that this mirror can be placed very close to the tubular reaction chamber, thus the path between the chamber and the mirror can be neglected and, since the size of the chamber is also negligible compared to the length of the laser pulse, we can assume that the light intensity in the chamber is proportional to $2I_L(t)$.

In the original proposal, the laser excitation of the positronium would be done along the axis of the reaction chamber: this would avoid hitting and damaging the nano-porous silica converter by the laser pulse, while requiring a relatively low laser intensity since the surface lit is approximatively 1 mm^2. However, with that excitation scheme, the $\bar{\mathrm{H}}^+$ ions produced would still travel in the laser beam outside of the reaction chamber, until the end of the laser pulse or until they are switched to their own beam line: this increases their chance to be photodetached. In the simulation, the photodetachment of the antihydrogen ions outside the reaction chamber is taken into account by a *survival* factor which depends on the photodetachment probability and the time the $\bar{\mathrm{H}}^+$ ion exits the reaction chamber.

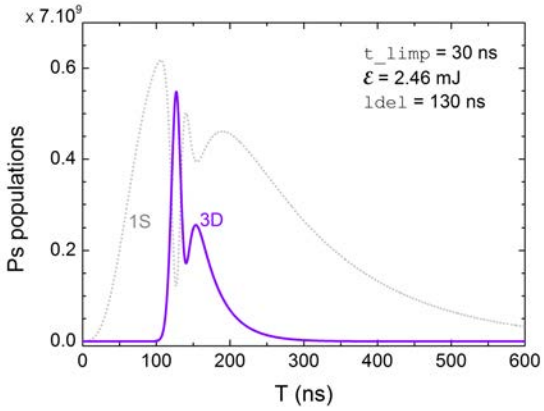
To partially circumvent this problem, the laser excitation could be done from the side of the reaction chamber, in which case the $\bar{\mathrm{H}}^+$ photodetachment can only occur while the ion is inside the reaction chamber. For that second scheme, the laser intensity should be higher than the previous case, since the surface to be lit is larger, by a factor equal to the length of the tubular cell. The laser beam should be shaped into a wide pencil of light thanks to a cylindrical mirror. Also, in order to shine the light through a window, materials should be studied; they have to: be transparent at 410 nm, withstand the radiation, the high pressure difference and be a good positronium reflector. To investigate this excitation scheme, a simple operation is done in the simulation: the *survival* factor is set to 1, since no photodetachment occurs outside the reaction chamber in that case; to retrieve the energy of the laser pulse that should be used, the previously defined $\mathcal{E}$ for the excitation on axis should be multiplied by the ratio between the length of the reaction chamber and its width.

One last proposition for the positronium excitation into state 3D is to shoot two laser pulses, the second one for example delayed by 40 ns. This could be obtained by splitting the 410 nm beam into two beams by a semi-reflecting glass, one of the beam being sent on an optical circuit of approximately 12 m long before rejoining the other path toward the reaction chamber. The idea behind this is to limit the $\bar{\mathrm{H}}^+$ photodetachment by giving the first ions produced the time to exit the reaction chamber before the second pulse. This solution might thus be more interesting than having a long laser pulse, at the sole condition to work in a side excitation scheme. The optimal delay between the two pulses, `l2del`, (as well as their energy, which could be different) can be investigated.

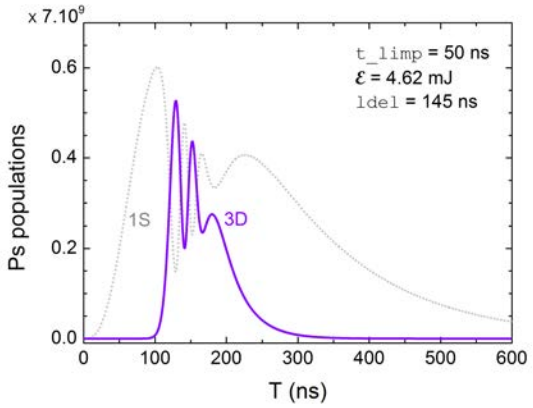
Figure 9.3 presents the positronium populations in the 1S and 3D states obtained by solving the optical Bloch equations for different values of the laser width, energy and delay parameters. For each chosen laser width (10, 30 and 50 ns) and energy per pulse (less than 5 mJ), the laser delay is the one for which the maximum of the Ps($3d$) population is the largest. For the example, a two-pulse excitation is also displayed. We can notice that the populations of the 1S and 3D undergo Rabi oscillations (oscillations in the populations of a two-level system subjected to a quasi-resonant electromagnetic field) when the energy of the pulse is high enough. These oscillations are damped by the spontaneous emission and the annihilation of the ground state.



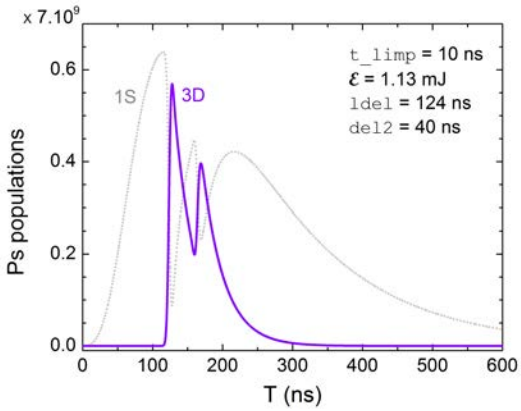
(a) Ps population evolution when excited by a 10 ns FWHM laser pulse at 410 nm, of 4.31 mJ energy.



(b) In that case, the laser width has been set to 30 ns and the energy per pulse decreased to 2.46 mJ.



(c) This Ps populations have been obtained with a 50 ns pulse of 4 mJ.



(d) In the case of two identical laser pulses of 1.13 mJ, with a 10 ns FWHM, separated by 40 ns.

Figure 9.3: Evolution of the positronium 1S and 3D populations with time for several sets of parameters.

As it has been explained in section 9.1, the main approximation concerning the laser excitation of the positronium is that we have worked exactly at resonance. This means that we neglect the width of the transition, the laser frequency width and the detuning of the laser.

9.3.3 Antiproton beam

Basically, the simulation has two ways of describing the pulse of antiprotons. The simplest form consists in a monoenergetic pulse of which time profile can be chosen. The other version of the simulation deals with a simulated pulse of decelerated antiprotons, thus closely reproducing the experimental situation.

In the case of the monoenergetic pulse, the parameters that can be continuously scanned are the full width at half maximum (`t_p`), the delay of the pulse (`pdel`) with respect to the beginning of the positronium production and obviously the energy (`Em`) of the antiprotons. The total number of antiprotons in the pulse that crosses the reaction chamber is 3.10^6, which is the number of antiprotons in one bunch delivered by ELENA every 100 s. It is thus assumed that the decelerator efficiency is 100 % and that it is possible to focus the beam inside the reaction

chamber with negligible loss. The profile, `pshape`, used to describe the time spread of the pulse has the same expression as the one chosen for the positrons:

$$pshape(t) = \frac{4(t-\texttt{pdel})^2}{\sqrt{\pi}(2\sigma_{Ps}^2)^{3/2}} e^{-\frac{(t-\texttt{pdel})^2}{2\sigma_{pbar}^2}}, \tag{9.18}$$

with, similarly, $\sigma_{pbar} = \texttt{t_p}/(\frac{4}{3}\sqrt{2ln2})$, chosen to indeed have a FWHM almost equal to `t_p`. The delay of the pulse `pdel` is then defined between $t = 0$, the beginning of the positronium production, and the time the very first antiprotons enter the reaction chamber. Figure 9.4 gives some examples of the $\bar{p}$ pulses thus obtained for various values of the parameters `t_p` and `pdel`. When `pdel` is chosen to be negative, this means that the antiproton pulse begins to enter the reaction chamber even before the positronium production has started.

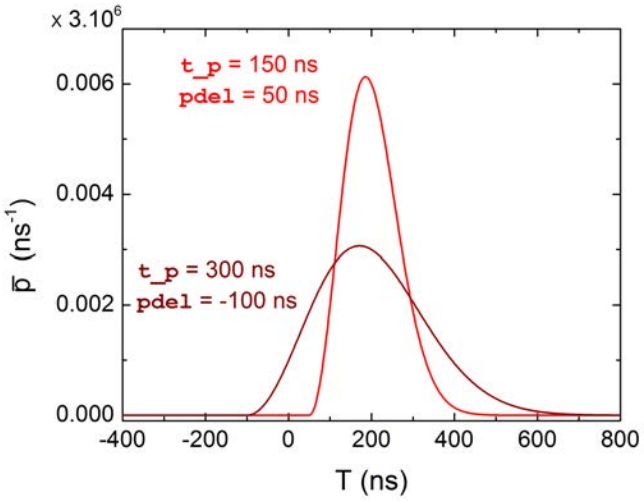
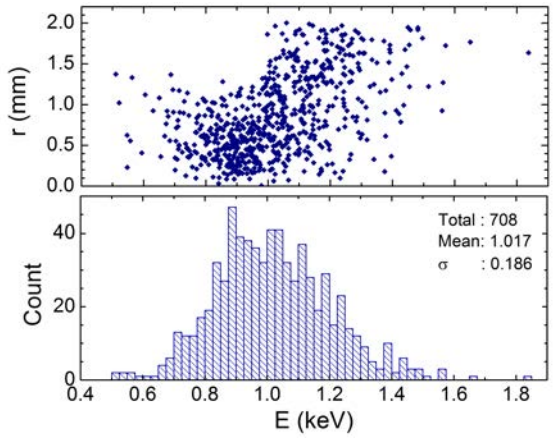


Figure 9.4: Shape of the monoenergetic antiproton pulses for two different values of the parameter `t_p`, corresponding to the FWHM, and different delays (`pdel`), chosen so that the maximum of each pulse occurs almost at the same time.

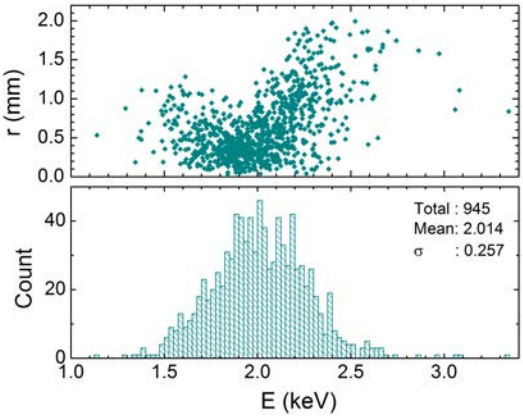
The monoenergetic pulse is useful for a first time investigation of the various experimental parameters, in particular to observe the general dependence of the $\bar{H}^+$ production with respect to the size of the reaction chamber, the energy, width and delay of the different beams: this allows to narrow down, for each of these parameters, the range that should be investigated. For experimental parts that are still under design or can be further developed, it can also give some indications on the performances that should be aimed at.

Though being convenient, the previous description of the antiproton pulse is of course weakly related to reality. To have a coherent description of the interaction region, the output data from the decelerator simulation should be used as input of the present simulation. The simulation of the antiproton decelerator using SIMION has been initiated at the CSNSM, Orsay, by Vladimir Manea and carried out by Pierre Dupré. This simulation starts with 1000 antiprotons at 100 keV, with a $\frac{\Delta p}{p}$ equal to $2.5 \cdot 10^{-3}$ (95 %) and a beam emittance of 4π mm mrad, in a 300 ns bunch, according to the specifications from ELENA. [104] The simulation includes the deceleration stage, the focusing and the transport to and right after the reaction chamber. To obtain a bunch of 1 keV antiprotons, the deceleration drift tube is switched from -99 kV to ground; for 2 keV, it

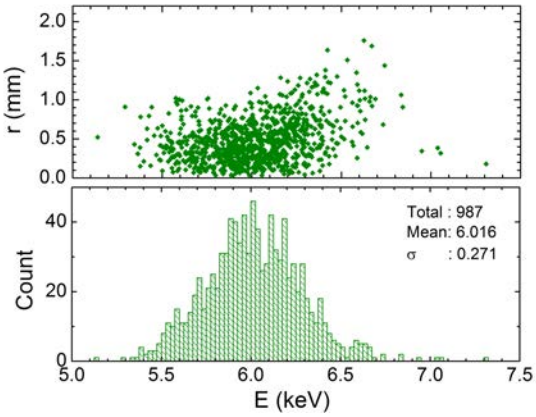
is switched from -98 kV to ground, while for 6 keV, two solutions have been tested: -94 kV to ground or -98 kV to -4 kV.



(a) Energy distribution of the antiprotons decelerated to 1 keV and their radial position just before the reaction chamber.



(b) Idem as 9.5a but for 2 keV.

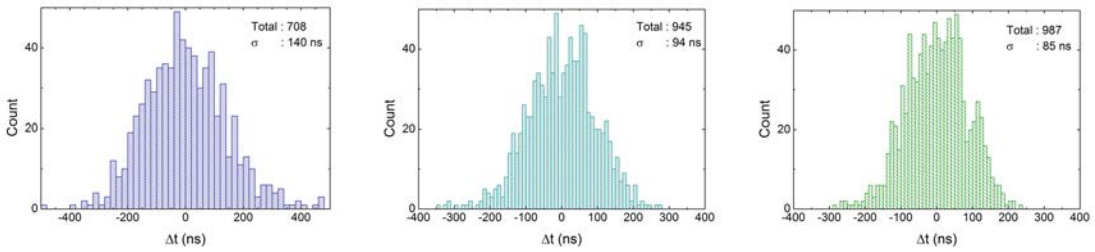


(c) Idem as 9.5a but for 6 keV.

Figure 9.5: Antiproton pulse profiles after deceleration to: (a) 1 keV, (b) 2 keV and (c) 6 keV. 1000 antiprotons have been simulated (courtesy Pierre Dupré).

Figure 9.5 assembles the beam energy profiles and the energy versus the radial position for the three cases. We shall remark that already 30 % of the antiprotons have been lost before the reaction chamber in the 1 keV case: these antiprotons have either annihilated in the decelerator as the beam emittance blows up (going from 4π mm mrad to 43π mm mrad) or have been rejected because they were not decelerated. For the 2 keV antiprotons, the beam emittance after deceleration is 30π mm mrad, while it is 16π mm mrad at 6 keV.

We note that, in this version of the simulation, since information on the phase space is now available, it is possible to correctly take into account the time dispersion of the antiproton pulse as it crosses the reaction chamber. Figure 9.6 shows the time distribution of the 1, 2 and 6 keV pulses just at the entrance of the reaction chamber.



(a) Time distribution at 1 keV. (b) At 2 keV. (c) At 6 keV.

Figure 9.6: Antiproton time distributions after deceleration to: (a) 1 keV, (b) 2 keV and (c) 6 keV. The time distribution is given just before the reaction chamber and centred on the mean time of flight value.

For the formation of the atoms and ions of antihydrogen, it has been further assumed that the inelastic collisions with the positronium have negligible effect on the total and longitudinal energy of the projectiles, due to the much lighter mass of the positronium. This assumption is totally justified and reasonable for the sole description of the interaction region; however, the knowledge of the transverse energy of the projectile is crucial to parametrise the capture trap. The general assumption would rather be that, despite the collisions individually changing the transverse energy of the particles, globally, the phase space of the antihydrogen ions remains identical to the one of the antiprotons.

9.3.4 Geometry of the reaction chamber

Prior to the 2011 proposal of the GBAR experiment, the reaction chamber was supposed to be a tube of squared section, whose walls are covered with nanoporous silica. The inner diameter of the tube was taken to be 1 mm, while the length proposed for that tube was 10 mm. This volume was chosen to keep a very high density of positronium atoms, though the 1 mm section was suspected to be an issue for the positron implantation on axis and the focussing of the antiproton beam.

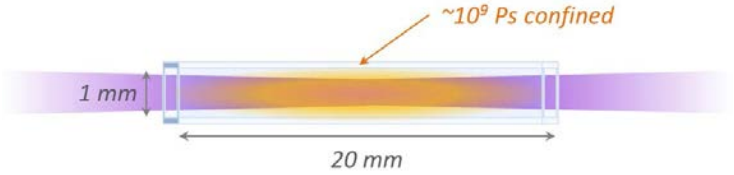
At the beginning of the present thesis, several CDW–FS cross sections had already been computed during a master's internship, mainly for l_p=0 states of positronium and l_h=0 states of antihydrogen, with the uncorrelated Chandrasekhar wave function for the second reaction. These results, combined with other theoretical studies available and remarks by GBAR collaborator Mike Charlton, already lead us to consider that antihydrogen de-excitation between the two reactions would be needed, and that having a longer tube would be helpful in that prospect. This is why the GBAR proposal describes the positronium converter structure as a tube of 1 mm^2 aperture by 20 mm length. The simulation will first be based on these values, but the influence of the tube dimension will be investigated. In the simulation, the inner section of the tube is the parameter `acell` and the length of the tube is `scell`.

Following this idea that the antihydrogen atoms must be given time between the two reactions in order to radiatively cascade down to ground state, François Biraben proposed to use two different reaction chambers instead of one. Each reaction chamber would thus dedicated to one of the two reactions, and the distance between them shall be chosen to optimise antihydrogen de-excitation. Another advantage of this solution would be the possibility, if proven of any interest, to have different states of positronium from one tube to another. However, this configuration holds several drawbacks: first, the positrons have to be distributed between the two reaction

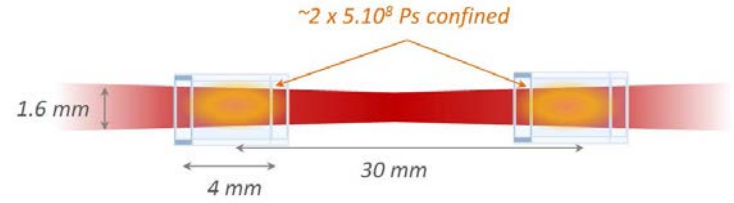
chambers, meaning that the positronium density in each chamber will be lower, unless making smaller tubes, than in the case of only one reaction chamber; second, and maybe more important, it will not be possible to focus the neutral antihydrogen atoms into the second reaction chamber. The latter constraint implies that, either we lose antiprotons in the injection into the first tube and / or antihydrogen in the second tube, or we increase the size of the reaction chambers to compensate for this focussing issue.

Finally, one last configuration can be investigated, but not for the CERN experiment any more. Indeed, before moving the positron trap to the AD hall, positronium production and excitation tests are scheduled at the CEA-Saclay facility. Also, before the positron trap moves to CERN, an attempt to measure cross sections of hydrogen formation could be made using a proton source. In the case of experiment with positronium in Saclay, no tubular reaction chamber would be available. Also, the size of the positronium cloud would be mainly defined by the positron beam size ejected from the trap. And of course, the number of trapped positrons would be at least two order of magnitude smaller than expected for the CERN experiment. For the moment, in absence of any measurement concerning the spot size of the positron pulse when it will hit the converter target at Saclay, it will be considered that a diameter of 2 or 3 mm can be achieved. The usable volume of positronium is delimited by the size of the laser beam used for excitation, which could be as big as 3 mm diameter. This gives, roughly, a 27 mm^3 volume for the "reaction chamber". Efficient accumulation of the positrons has not been performed yet, so we will make the assumption that it can reach 10^8 trapped positrons. In degraded conditions, we can considered that the trap in not used and the positrons pass through it: in that case we have to consider 10^4 positrons per pulse.

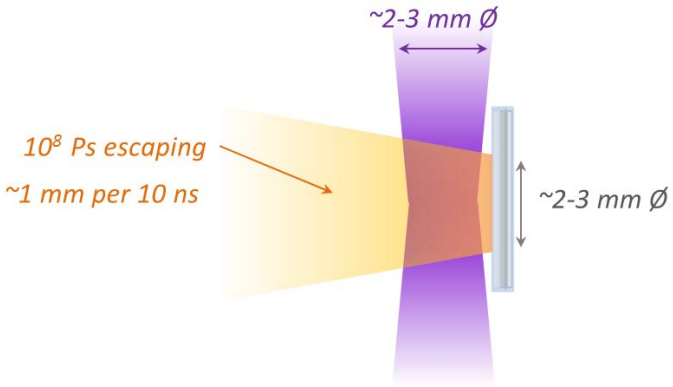
The three different set-ups are illustrated in figure 9.7: figure 9.7a represents the reaction chamber that will be used at CERN, crossed by the laser for positronium excitation on axis, figure 9.7b is the case of two separated reaction chambers, where the parameters have been chosen to keep the same angular aperture as in the previous case, with a focusing of the antiproton beam halfway between the two tubes, and figure 9.7c shows the open configuration that could be used at CEA, with positronium diffusing from the converter and laser excitation parallel to that converter. However, due to the severe constraints it imposes on the positron injection and antiproton focussing, the solution with two reaction chambers has been abandoned for this thesis.



(a) One tubular reaction chamber for the CERN experiment: the typical dimensions are 20 mm for the length and 1 mm^2 for the inner section. The violet beam corresponds to the laser beam when the positronium excitation is done on axis.



(b) Two tubular reaction chambers for the CERN experiment. The red beam represents the antiproton beam focused in the middle of the gap between the two chambers. In order to keep the same angular aperture as in the previous case, the section of the tubes has been increased and the length shortened to ensure a sufficiently high positronium density.



(c) CEA's open geometry. *A priori*, the positronium would not be confined during the positronium spectroscopy experiment; a silicon nitride window could be added in front of the converter, resulting in a longitudinal confinement, for future experiments with protons.

Figure 9.7: The three different geometries (not at scale) of the envisaged reaction chambers, with typical size parameters and number of positronium atoms.

Chapter 10

Results of the simulation

All over the chapter, the results focus on the total $\bar{H}^+$ production, since it is the main concern of the GBAR experiment. However, when estimated to be pertinent, some results will be given for the formation of the antihydrogen/hydrogen atoms, either for a proton experiment at Saclay or for projects interested in the unused $\bar{H}$ beam that will come out of the reaction chamber at CERN. The results presented here have been computed with the CDW–FS cross sections only, since the CBA cross sections were obtained only in April 2014.

10.1 Working with 6-keV antiprotons

10.1.1 First parameter scans with the monoenergetic beam

From the cross section results presented in the previous chapter, we can already restrain the energy of the antiprotons to values between 5.55 keV (see appendix B for the thresholds of each channel) and about 10 keV. To investigate the effect of parameters other than those related to the antiproton pulse, the energy will be fixed to 6 keV, `t_p` to 200 ns and `pdel` to -50 ns. First, we can work without any positronium excitation and change the dimensions of the reaction chamber, as well as the width of the positron pulse. Figure 10.1 presents the number of $\bar{H}^+$ ions per antiproton pulse obtained for different lengths of the positronium cell, and for small variations of its section. This has been obtained for `t_eimp`=75 ns. We notice the dramatic effect of variations in the inner section of the reaction chamber: a slight increase of this section induces a drop in the positronium density and thus in the production of $\bar{H}^+$. For instance, doubling the section of the reaction chamber, that is dividing the Ps density by a factor two, divides the number of ions by a factor four: this is expected since the probability of forming $\bar{H}^+$ after two consecutive reactions with the positronium is proportional to the square of the positronium density. On the other hand, lengthening the reaction chamber, though also leading to a decrease of the positronium density, permits to produce more antihydrogen ions, due to a higher number of antihydrogen atoms that were able to de-excite toward the ground state while still in the chamber. In that case, doubling the length of the positronium cell, hence dividing by two the positronium density, increase the production of $\bar{H}^+$ ions by a factor 1.2 to 1.4. Thus, at 6 keV, the gain in having more antihydrogen relaxation to ground state is less important than the gain obtained by narrowing the reaction chamber.

This leads to two remarks: first, when working at 6 keV, we obviously really need to make the reaction chamber as narrow and long as possible, of course in the range of what is feasible in terms of the beam optics to focus the antiprotons and, second, the conception of the reaction chamber must be precise at the tenth of millimetre for the inner section, which is challenging

since the cell will probably be a mechanical assembly of four different walls. Going to a length longer than 20 mm for the reaction chamber is also thought to be hardly achievable, but we will retain the possibility to go to 30 mm in the following sections and evaluate whether it could be worth the effort or not.

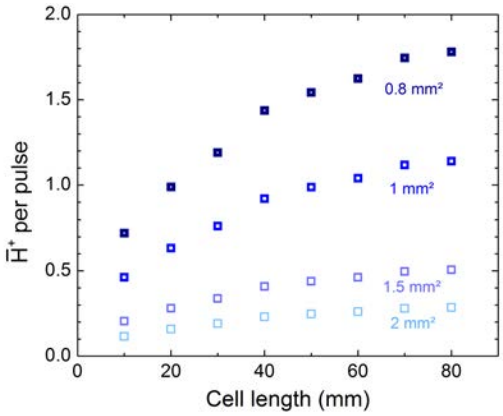


Figure 10.1: Evolution of the $\bar{H}^+$ production with the length (from 10 to 80 mm) and section (between 0.8 and 2 mm^2) of the positronium cell at 6 keV. In the present case, only ground state positronium is used.

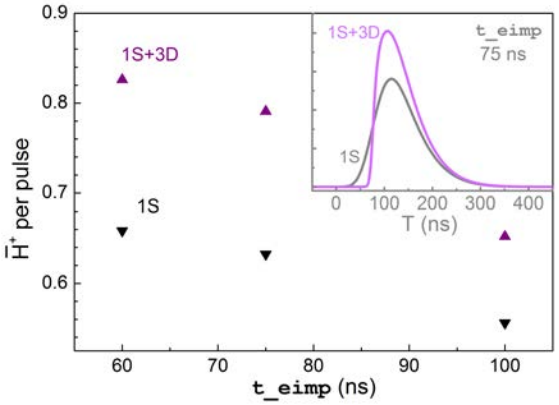


Figure 10.2: Variations in the production of antihydrogen ion for three different values of the positron pulse delay, and with (label 1S+3D) or without (label 1S) positronium excitation to state 3D. The dimensions of the reaction chamber are 1 mm^2 by 20 mm.

Now setting the reaction chamber dimensions to the ones in the proposal – 20 mm length and 1 mm^2 inner section – we present in figure 10.2 the number of antihydrogen ions obtained when the width of the positron pulse can be chosen to either 60, 75 or 100 ns, as well as an example of time profiles for the $\bar{H}^+$ pulse when `t_eimp` is 75 ns. Two sets of data are displayed: when the laser is off and only ground state positronium is used, or when a 20 ns laser pulse at 410 nm, 0.9 mJ, is sent after a delay of 75 ns in the reaction chamber to produce Ps(*3d*). We observe that, the shorter the positron pulse, the higher the $\bar{H}^+$ production: indeed, this has the effect of increasing the instantaneous positronium density. The ongoing experiments with the positron trap at CEA should thus at least try to reproduce the RIKEN results for the fast ejection of a few 10^9 particles. However, though the results presented in figure 10.2 have not been obtained for optimised parameters, the decrease in the $\bar{H}^+$ production due to the use of larger positron pulses is rather small: if we simply approximate the behaviour between 75 ns and 100 ns by a straight line, then we can estimate that an increase of `t_eimp` by 5 ns results in a loss of 0.015 $\bar{H}^+$ per pulse in the presented case. Then, aiming at a FWHM (`t_eimp`) below 90 ns is probably already sufficient.

Still in figure 10.2, the effect of positronium excitation into state 3D at 6 keV is illustrated: it leads to a significant increase of the number of antihydrogen ion per pulse (by 20 to 30 %). From the cross section calculations, we understand that it is due to a larger production of the n_h=4 and 5 states of antihydrogen with Ps(*3d*). So contrary to what figure 8.2 in section 8 was suggesting, exciting the positronium to the state 3D is even helpful at 6 keV. From now on, we will continue to consider a positronium excitation into state 3D at 6 keV. The inset graph in figure 10.2 shows the different profiles of what we will call the $\bar{H}^+$ pulse (though one pulse contains less than one particule), obtained for `t_eimp`=75 ns, when the excitation laser is either

used or not. It demonstrates that the increase of the $\bar{H}^+$ production is nonetheless accompanied by a loss of the first $\bar{H}^+$ ions formed in the reaction chamber: the cause is the photodetachment of these ions by the laser.

Now, we keep the proposal values for the dimensions of the reaction chamber, and vary the parameters related to the positronium excitation. For `t_eimp`=75 ns, the width of the laser pulse, `t_limp`, has been continuously varied while several values of the `xi` parameter have been selected; the delay `ldel` of the laser has been fixed to 75 ns. The results are shown in figure 10.3. In parallel, figure 10.4 presents the evolution of the $\bar{H}^+$ number again as a function of the laser pulse width, but when `xi` is fixed to 36 and this time, the laser delay `ldel` is set to different values.

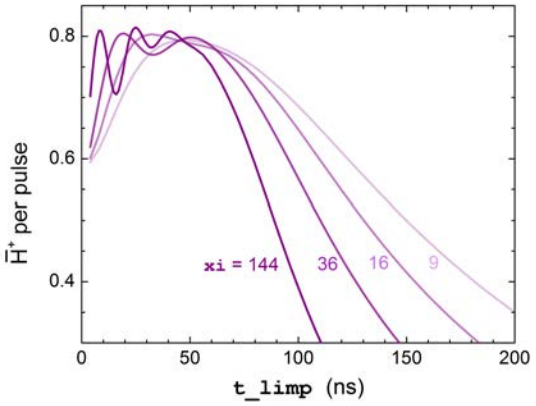


Figure 10.3: The $\bar{H}^+$ production as a function of the laser pulse FWHM for `xi`= 9, 16, 36 and 144; the laser delay has not been changed and is 75 ns.

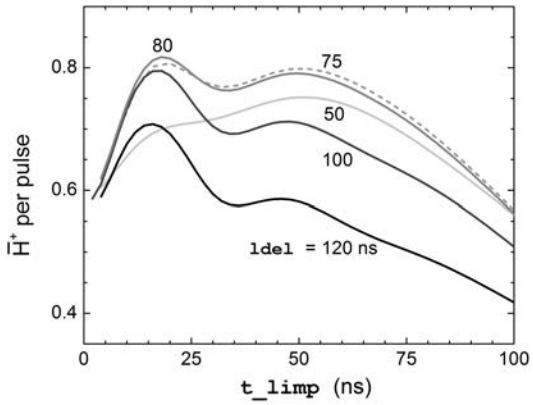


Figure 10.4: Similarly to figure 10.3, the dependence in `t_limp` is investigated, but this time, `xi` is set to 36 and several delays of the laser pulse are investigated.

The first obviously noticeable effect is the attenuation of the $\bar{H}^+$ production as the laser FWHM increases (and it is even more pronounced when `xi` increases). This comes from two reasons: as the width of the laser pulse grows larger, more $\bar{H}^+$ are subjected to a possible laser photodetachment; the other reason is that, in the presented results, varying the parameter `t_limp` corresponds to a proportional variation of the energy of the laser pulse, thus when its width increases, so does the photodetachment probability. Then, raising the parameter `xi` further augments the energy of the pulse and the photodetachment probability.

Changing `xi` is also a mean of tuning the Rabi frequency. This leads us to the second observation: the modulations in the number of $\bar{H}^+$ ions. These modulations are indirectly related to the Rabi oscillations occurring between the two levels of the positronium. Indeed, when Rabi oscillations can develop themselves in the system, they can be favourable to Ps($3d$) or on the contrary suppress its population in favour of the ground state. For instance, this is illustrated in figure 10.5 where it can be seen that going from a 10 ns to a 15 ns wide laser pulse (at fixed `xi`) results into a 3D level being significantly populated for a shorter time. Since the Rabi frequency is only linked to the parameter `xi`, the number of observable oscillations depends on the laser width, thus explaining the modulated dependence in `t_limp`. Nevertheless, in general, when the width of the laser increases, the 3D state of positronium is populated for a longer time, and the integrated population of Ps($3d$) over time is larger (this is what we see in figure 10.6), but as

it has been mentioned earlier, this positive effect for the production of $\bar{H}^+$ is overcome by the photodetachment.

Now concerning the dependence with the delay of the laser pulse presented in figure 10.4, we observe that varying the laser delay changes the modulations previously explained. This is simply because delaying the laser is like changing its efficient width, which would be defined as the portion of the pulse that actually excite the positronium.

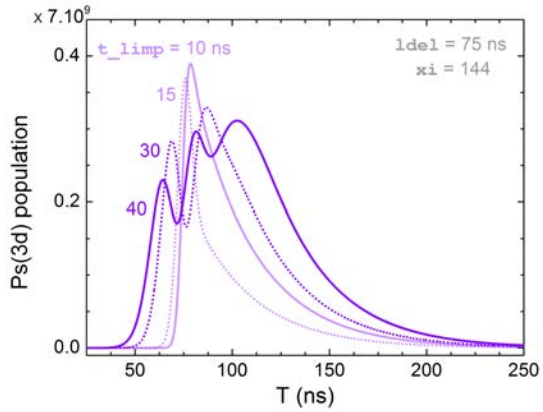


Figure 10.5: The Ps(*3d*) population evolution with time for several values of the laser width. This values of `t_limp` have been chosen close to local maxima (plain lines) and minima (dotted lines) observed in figure 10.3 for `xi`=144.

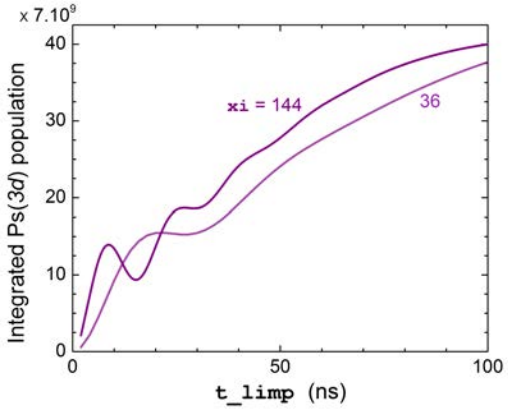


Figure 10.6: The Ps(*3d*) population has been integrated over the simulation time, while the laser width is varied, for `xi`=36 and 144. This reveals that the modulations of the $\bar{H}^+$ production observed in figure 10.3 are related to the number of excited positronium available.

In conclusion, we expect to find optimal values for each `xi`, `t_limp` and laser delay `ldel` parameter; however, it is possible that several sets of this parameters would give similar results for the total number of $\bar{H}^+$ ions per antiproton pulse. This also means that we have some flexibility concerning the laser excitation. Nonetheless, we are now able to give restrictions on the values of the laser width and of the parameter `xi`: the former should be between 10 to 50 ns and very high values of the latter should not necessarily be sought since they lead to (damped) Rabi oscillations in the positronium populations which, in fact, make the $\bar{H}^+$ yield very sensitive to jitters in the laser related parameters.

In the following, we finally consider the parameters related to the antiproton pulse. The laser pulse width has been set to 20 ns, its energy to 1.09 mJ (that is `xi`=36), and its delay to 75 ns. First, the antiproton kinetic energy is scanned between 5.6 and 8 keV. We keep in mind that, the faster the antiprotons, the longer should be the reaction chamber to sufficiently allow for antihydrogen relaxation. The results are presented in figure 10.7. Simultaneously, the same scan has been done for the case of two laser pulses (20 ns FWHM, separated by 40 ns, and `xi`=16 for each pulse) sent in the reaction chamber. In each case, laser excitation both on the axis of and perpendicular to the reaction chamber are considered, in order to investigate the importance of the losses by photodetachment outside the reaction chamber.

The results first confirm and refine the energy region of best interest: 5.8 to 6.2 keV, with only variations of 2 to 3 % of the $\bar{H}^+$ number per pulse over that range. This gives the order

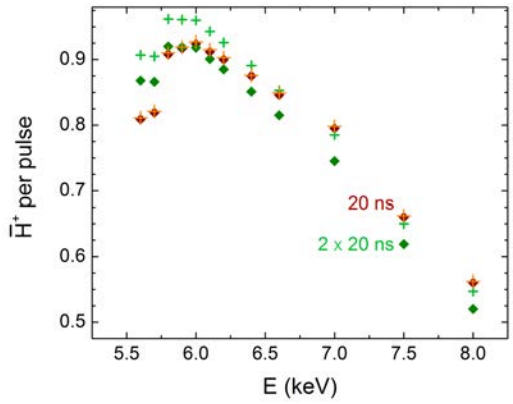


Figure 10.7: $\bar{H}^+$ production dependence with the antiproton energy around 6 keV. The square symbols are for a laser beam in the axis of the reaction chamber while the crosses are for the laser entering perpendicularly in the reaction chamber. In reddish colours, one laser pulse of 20 ns width has been used while green colours are for two pulses of 20 ns separated by 40 ns.

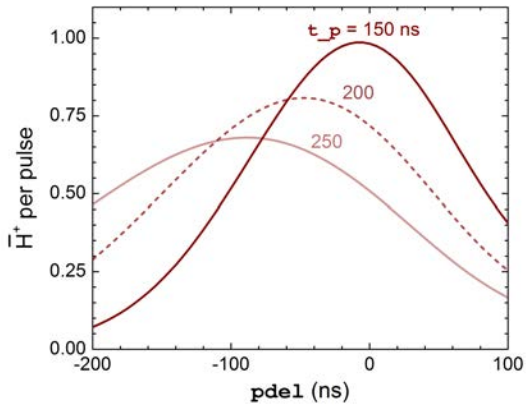


Figure 10.8: Evolution of the $\bar{H}^+$ yield with the delay of the antiproton pulse, for three values of `t_p`; so far, we had been working with a 200 ns wide pulse of antiprotons, indicated by the dashed line.

of magnitude of the acceptable energy dispersion at 6 keV: about 200 eV. The next observation concerns the excitation scheme of the positronium cloud: although not all the parameters have been optimised, we can nonetheless claim that the excitation from the side of the reaction chamber hardly limits the photodetachment of the $\bar{H}^+$ ions. Indeed, a mere 5 % gain is obtained when two laser pulses are used. Otherwise, the two laser pulse solution gives results very similar to the one pulse excitation of the positronium. In conclusion, at 6 keV, the excitation scheme with the laser entering from the side of the reaction chamber has no particular interest for increasing the number of antihydrogen ions per antiproton pulse. The choice of this solution would be mainly dictated by technical reasons.

We will now investigate the effect of varying the antiproton pulse delay and width. The energy of the antiprotons has been fixed to 6 keV. In figure 10.8, the results for three different widths of the antiproton pulse (150 ns, the already used 200 ns and 250 ns) are displayed. The laser width was 20 ns, with `xi`=36 and `ldel`=75 ns. We observe that sharper pulses of antiprotons leads to a higher yield of $\bar{H}^+$: this is simply due to the fact that compressing the antiproton pulse allows a better use of the short-lived positronium atoms, in particular of the excited positronium. As long as the antiproton pulse is wider than the lifetime of the positronium, and even larger than the lifetime of Ps($3d$), the delay of the antiproton pulse is not the parameter that will have the most influence on the production of the antihydrogen ions, hence the smooth maxima observed in figure 10.8. Note that, for an optimal production of the antihydrogen ions, the antiproton pulse should enter the reaction chamber before the positronium production has even started. For the chosen values of `t_p` presented here, reducing the antiproton pulse width by 50 ns implies an almost 25 % gain on the $\bar{H}^+$ production (when comparing the maxima obtained).

Experimentally, the width of the antiproton pulse will mainly depend on the characteristics of the pulses delivered by ELENA. However, owing to the results obtained when `t_p` is varied, it seems necessary to find a way to compress the antiproton pulses. Unfortunately, without any

cooling mechanism to compensate, the Liouville theorem imposes an increase of the momentum dispersion of the beam. This could be overcome by the use of an antiproton trap. This costly solution would also facilitate the focusing of the antiprotons into a narrow reaction chamber and the capture of the $\bar{H}^+$, thus making it worth consideration.

To conclude this section, the two most important parameters when working with antiprotons of about 6 keV are the inner section of the positronium cell, which should be made as small as possible, and the width of the antiproton pulses, which should also be decreased as much as possible. This has lead us to consider using an antiproton trap in GBAR, a solution that the decelerator was supposed to avoid. We also demonstrated that positronium excitation to the state 3D is more than welcomed at 6 keV. We showed that the length of the reaction chamber is another parameter greatly influencing the $\bar{H}^+$ production: this reaction chamber should be made as long as possible to work at 6 keV. All other parameters can be optimised but are less critical. In particular, almost any laser width between 10 to 50 ns can be used, provided that the energy of the laser is set accordingly. Finally, no particular excitation scheme of the positronium can really limit the $\bar{H}^+$ photodetachment and, in the end, the choice will rely on practical experimental considerations.

10.1.2 Antiprotons deceleration simulated at 6 keV

The positronium reaction cell is supposed to have a square section; however, the deceleration simulation used polar coordinates to describe the position of the particles and only the radial coordinate was available to set a criterion on the transmission of the antiprotons through the chamber. It has be chosen to work with the circular area equivalent to the inner section of the Ps tube; thus, for a 1 mm^2 tube, antiprotons have to be kept within a radius of 0.564 mm. It is true, however, that this slightly overestimates the number of antiprotons transmitted into the reaction chamber and, in the prospect of a consecutive simulation of the $\bar{H}^+$ capture, this modify the phase space. We keep that criterion anyway for the moment; in fact, it is applied both at the entrance and the exit of the reaction chamber to remove the particles that annihilate on the walls of the tube.

We can investigate the balance between narrowing the reaction chamber (and degrading the antiproton transmission) and increasing the antiproton transmission (while decreasing the positronium density). The length of the positronium cell being set to 20 mm, its aperture was chosen to be either 0.8, 1, or 1.33 mm^2. The results are summarised in table 10.1. We tried to push a little further by increasing the length of the reaction chamber as well, up to 30 mm; we have found earlier that at 6 keV, the reaction chamber should be as long as possible. However, to maintain a sufficient number of $\bar{p}$ crossing the chamber, the radius of this 30 mm-long chamber has not been reduced below 0.65 mm.

With a 20 mm reaction chamber of inner section equal to 0.8 mm^2 (that is 0.50 mm radius), the antiproton transmission at 6 keV is only about 50 %. In spite of this, when a 10 ns laser pulse of 0.9 mJ is used, about 2.2 10^{-4} "ion" is formed out of the 1000 antiprotons originally simulated: that is an equivalent of 0.65 $\bar{H}^+$ for a decelerated pulse of $3{\cdot}10^6$ $\bar{p}$. With a 1 mm^2 cell, the maximum obtained would be 0.48 $\bar{H}^+$, with 57 % antiproton transmission; this value is in excellent agreement with the maximum of 0.8 obtained using the simple monoenergetic description, where the antiproton transmission through the chamber was assumed to be 100 %. Let's also note that this last value is larger than the estimation used in the GBAR proposal (which was 0.3 $\bar{H}^+$ per antiproton pulse).

acell(mm^2)	0.8				1			1.33	
scell(mm)	20				20		30	20	30
$N_{\bar{p}}$	496				573		291	691	386
pdel(ns)	160	155	160	160	150	155	145	155	150
t_limp(ns)	10	20	50	$2\times$ 10	10	$2\times$ 10	10	10	10
l2del(ns)	–	–	–	40	–	40	–	–	–
xi	100	31	12	95	100	100	105	105	105
E(mJ)	0.727	0.810	1.259	2×0.709	0.909	2×0.909	0.931	1.239	1.239
ldel(ns)	90	85	80	65	95	65	95	90	95
$\bar{H}^+(10^{-4})$	2.18	2.15	2.10	2.35	1.60	1.74	1.17	1.09	0.86

Table 10.1: Examples of best $\bar{H}^+$ yield and corresponding optimal parameters obtained for an antiproton deceleration simulated at 6 keV.

The general effect of using larger laser pulse is to slightly decrease the $\bar{H}^+$ yield, as it is shown here for the smaller positronium cell. However, this is a very small effect in the range 10 to 50 ns for t_limp, so the simulation does not place strong constraints concerning the laser pulse parameters. We notice that the use of two laser pulses to excite the positronium leads to an increase $\bar{H}^+$ production by roughly 10 %. This may not be enough to justify implementing this solution, but should be kept in mind if some new experimental constraints require to look for any improvement in the total yield.

Finally, we observe that increasing the length of the positronium cell always leads to a lower $\bar{H}^+$ yield (for a given aperture size). When, in the previous section, we demonstrated that lengthening of the reaction chamber was beneficial to the antihydrogen de-excitation and would overcome the decrease in the positronium density, here, we now take into account the transmission losses as the aperture angle of the reaction chamber is reduced: the resulting effect is a slightly smaller $\bar{H}^+$ production which suggests that, contrary to the simple mono-energetic simulation results, it is not worth trying to build a reaction chamber longer than 20 mm.

The results presented here show that, at 6 keV, we can afford degrading the antiproton transmission by decreasing the inner section of the reaction chamber: the loss is largely compensated by the gain offered by the increase of the positronium density. For instance, going from a 0.8 mm^2 chamber to one with a 1 mm^2 inner section increases the antiproton transmission by 15 %, but for any laser excitation scheme employed, the total number of antihydrogen ion produced then drops by one fourth. This confirms earlier conclusions drawn in the previous section: the design of the reaction chamber should aim at having it as narrow as possible.

10.2 Working with 1 keV antiprotons and 3D-state positronium

10.2.1 First investigations with a mono-energetic beam

The complete description of the parameters which influence the number of $\bar{H}^+$ produced per antiproton pulse will not be carried out again for this case, since some of the effects have already been detailed and should be independent from the energy of the antiprotons. Only a few topics have been selected: the dimensions of the cell, the consequences of the $\bar{H}^+$ photodetachment, the importance of the width of the antiproton pulse and variation of the antiproton energy around 1 keV. At these low energies, the excitation of the positronium is mandatory and we will work

with Ps($3d$).

By default, the laser parameters have been set to 20 ns FWHM, `xi`=36 and the delay of the pulse is 75 ns. When it is not scanned, the width of the antiproton pulse is chosen to be 300 ns (when it was 200 ns at 6 keV); the delay of the antiproton pulse is then set to -180 ns. These parameters will be optimised in the following section using the data from the simulation of the decelerator.

We first consider the dimensions of the reaction chamber. At 6 keV, we concluded that we had to increase as much as possible the length of the positronium cell (at least up to 80 mm), but, more importantly, to reduce as much as possible the section of this reaction chamber. Similarly to figure 10.1, figure 10.9 shows the evolution of $\bar{H}^+$ yield with the dimensions of the positronium cell for the previously given parameters of the antiproton and laser beams. We observe that the behaviour at 1 keV is different from 6 keV: for any aperture size of the cell, there is an optimal length of the positronium cell occurring at around 30 mm. In the range 20 to 45 mm, the production of $\bar{H}^+$ remains above 90 % of the maximum value: the value of 20 mm chosen in the proposal is thus a good compromise. However, if the length of the cell is made shorter than 20 mm, then the number of antihydrogen ions per antiproton pulse drops quickly; 20 mm should be kept as the minimum accepted value for the parameter `scell`. Concerning the inner section of the reaction chamber, the effects and conclusions are here similar to the 6 keV case results: the aperture of the positronium cell should be made as small as possible. One remark: since we work at a fixed value of `xi`, the energy of the laser pulse per unit of surface remains constant when we change the parameter `acell`.

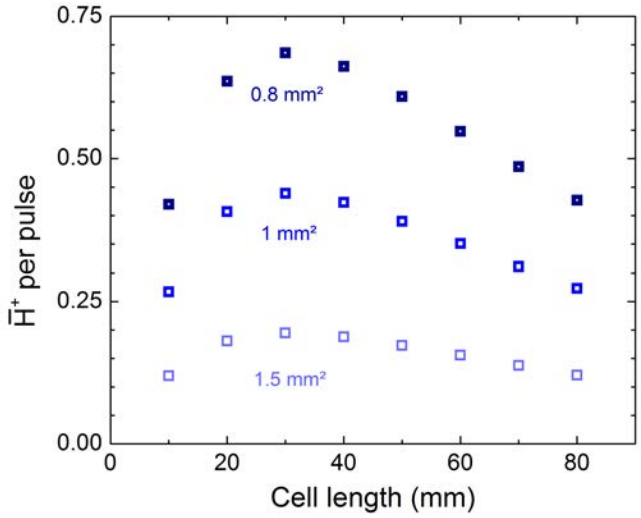


Figure 10.9: Evolution of the $\bar{H}^+$ production with the length (`scell`) and section (`acell`) of the positronium cell at 1 keV, with laser excitation of the positronium to the state 3D.

We now keep the dimensions of the reaction chamber to 20 mm for its length and 1 mm^2 for its inner section. Keeping `xi`=36 for both a 20 and a 50 ns laser pulse width, the delay of the pulse is varied, and the laser excitation is either done on axis or perpendicularly to the reaction chamber: like it has been done at 6 keV, this will allow us to investigate the relative importance of the $\bar{H}^+$ photodetachment at 410 nm when working with 1 keV antiprotons. The results are displayed in figure 10.10. A case of two-laser pulses excitation is also displayed, for two pulses of 20 ns FWHM separated by a 40 ns delay.

We see that the choice of the laser delay has great consequences on the production of $\bar{H}^+$ at 1 keV: varying this delay by 20 ns can do more than doubling the number of antihydrogen ions per antiproton pulse (for `ldel` below 100 ns in the case of the 20 ns laser pulse). A maximum is reached for an optimal value of the laser delay; this is a flat maximum, meaning that, once around that maximum, a jitter of 10 ns in the laser delay should only have a very limited effect.

Suppressing the photodetachment outside the reaction chamber by exciting the positronium from the side of the cell has no significant effect for a short laser pulse (at most a few percent gain for larger laser pulses). Indeed, at 1 keV, it takes 42 ns for an antiproton to cross the reaction chamber: for most of the $\bar{H}^+$ ions, the laser pulse is already over when they exit the positronium cell.

This leads to the following conclusion concerning the utility of exciting the positronium from a side window in the reaction chamber: either we work with very short laser pulses or use longer ones (around 50 ns), the side excitation has no particular advantage, except that it avoids having to place a mirror in the path of the antihydrogen atoms. So only practical reasons lead to this solution of transverse excitation.

The results presented in figure 10.10 for a two laser pulse excitation shows a higher number of antihydrogen ions per pulse than with only one laser pulse. In the present case, a gain of about 10 % is obtained. The interest of this solution has to be confirmed once all the parameters have been optimised. Other laser widths and delay between the two pulses should also be investigated.

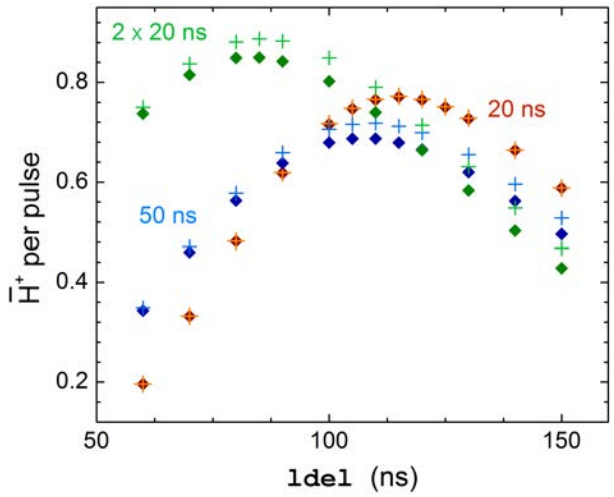


Figure 10.10: Variations of the $\bar{H}^+$ production with the delay of the 410 nm laser; the square signs are for laser excitation on the axis of the reaction chamber (thus parallel to the antiproton beam) and the "+" signs for excitation from the side of the positronium cell. Two sets of data are displayed corresponding to two different laser widths: 20 and 50 ns. The 20 ns points for the two laser orientations are merged.

Having set the laser parameters to 20 ns for `t_limp`, 36 for `xi` and 100 ns for `ldel`, we now focus on the parameters related to the antiproton beam. In figure 10.11, the energy of the antiproton beam has been varied between 0.4 and 2 keV, while the width of the antiproton pulse was maintained to 300 ns, and it is delayed by 180 ns with respect to the beginning of the positronium production. As the calculations of the cross sections have shown, in that energy

range, any decrease of the antiproton energy is in favour of the $\bar{H}^+$ production. In particular, for the results shown in figure 10.11 below 1 keV, decreasing the energy of the antiprotons by 200 eV results, at least, into a 20 % increase of the $\bar{H}^+$ number per pulse. Between 1 and 2 keV, the number of antihydrogen ions per pulse is divided by more than a factor two. One observe that the behaviour of the $\bar{H}^+$ production in that energy region guarantees that the results are almost independent from the energy dispersion of the antiprotons; the important parameter is mainly the mean energy of the antiprotons.

Though it is probably very difficult, experimentally, to decelerate the antiprotons below 1 keV, this goal should not be abandoned because of the expected gain in the $\bar{H}^+$ yield. Again, an antiproton trap (either a Penning trap or, as it is currently investigated, an electrostatic ion beam trap – EIBT) could be the necessary tool to reach this goal.

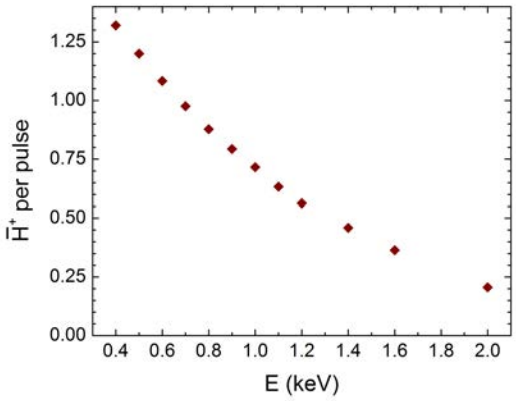


Figure 10.11: The general dependence of the $\bar{H}^+$ yield with the energy of the antiprotons.

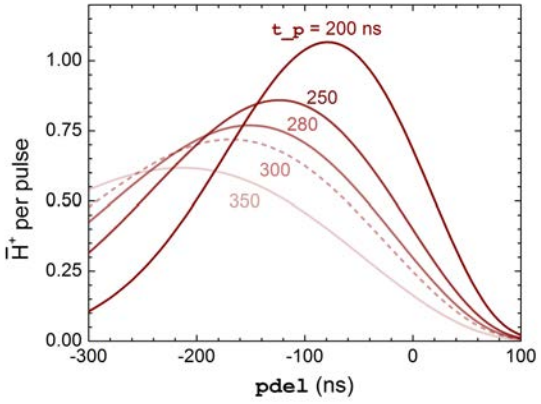


Figure 10.12: The evolution of the antihydrogen production when the delay of the antiproton is varied, for different values of the $\bar{p}$ pulse width.

We set the antiproton energy back to 1 keV, and, like it was done at 6 keV, the delay `pdel` of the antiproton pulse is continuously varied for several values of the antiproton pulse width `t_p` (200, 250, 280, 300 and 350 ns). We remind that the value of `t_p` previously used was 300 ns, while the default value of this parameter at 6 keV was 200 ns. The results are displayed in figure 10.12.

The conclusions are identical to the 6 keV case: by varying the antiproton pulse delay, a maximum is observed in the antihydrogen ion production. For long pulses of antiprotons, this maximum is very smooth and the tuning of the parameter `pdel` does not require special care. When the antiproton pulse is compressed, the acceptable jitter on `pdel` is reduced but still not critical. More importantly, shortening the antiproton pulse induces a rise in the $\bar{H}^+$ yield (typically, a gain of about 20 % when `t_p` is reduced by 50 ns).

If we now look at the number of $\bar{H}^+$ per pulse and make a comparison between the 1 keV and the 6 keV results, for the same width of the antiproton pulse, and the same laser parameters, we observe that the number of antihydrogen ion produced per pulse is greater for 1 keV antiprotons. For instance, with `t_p`=250 ns, the calculation gives 0.85 $\bar{H}^+$ per pulse at 1 keV, while at 6 keV, it reaches at most 0.65 ions per antiproton pulse. So, in similar conditions, the 1 keV solution using Ps($3d$) is better than any configuration around 6 keV. However, experimentally, we do not expect to have the same widths for the antiproton pulse decelerated to 1 and 6 keV: the pulse

decelerated to 6 keV should be significantly shorter than the one at 1 keV.

The benefit of the 1 keV solution is thus questioned. Only a simulation based on the output data of the decelerator can settle the case. Nonetheless, in tables 10.2 and 10.3, we make a comparison between several configurations respectively for a 300 ns antiproton pulse at 1 keV and a 200 ns pulse at 6 keV, with a 100 % transmission efficiency of the antiprotons through the reaction chamber (1 mm^2 aperture by 20 mm length). The positronium excitation is only considered on the axis of the reaction chamber, but the possibilty to send two delayed pulses is taken into account.

We first observe that for a unique laser pulse, whatever its width and for its optimal energy, the highest number of $\bar{H}^+$ obtained is 0.8 ions per antiproton pulse, either at 1 or 6 keV, with a relative maximum obtained with a 20 ns laser pulse at 1 keV and a 10 ns pulse at 6 keV. This confirms the former conclusion: the choice between the two cases mainly relies on the performances of the antiproton decelerator. However, there is one option that points toward the 1 keV solution as the most interesting one: by implementing a two laser pulse excitation, carried out with two 10 ns pulses of 0.76 mJ each and separated by 40 ns, the simulation predicts 1 $\bar{H}^+$ per antiproton pulse. From an earlier result concerning a laser excitation from the side of the positronium cell, this number can be increased by 4 % when the two laser pulses are send perpendicularly to the antiproton beam; this may seems to be a very minor gain but, nonetheless, it represents about 4 more possible events every 3 h of continuous beam-time.

	1 keV (t_p = 300 ns)								
t_limp(ns)	10	20	30		50		2×10		2×20
l2del(ns)	–	–	–	–	–	–	30	40	40
xi	95	28	15	95	7	38	44	70	16
E(mJ)	0.886	0.962	1.056	2.657	1.202	2.801	2×0.603	2×0.760	2×0.727
ldel(ns)	120	120	120	115	115	110	100	90	90
pdel(ns)	−150	−148	−146	−150	−148	−142	−150	−154	−150
$\bar{H}^+$	0.82	0.84	0.81	0.81	0.73	0.71	0.96	1.00	0.89

Table 10.2: Number of $\bar{H}^+$ expected per mono-energetic antiproton pulse at 1 keV, for several configurations of laser excitation; parameters other than the laser pulse width have been optimised.

	6 keV (t_p = 200 ns)								
t_limp (ns)	10	20	30		50		2×10		2×20
l2del (ns)	–	–	–	–	–	–	30	40	40
xi	105	32	16	101	11	45	81	95	27
E (mJ)	0.931	1.028	1.091	2.740	1.507	3.048	2×0.818	2×0.886	2×0.944
ldel (ns)	85	85	85	80	80	75	65	60	55
pdel (ns)	−44	−44	−44	−38	−38	−34	−42	−38	−38
$\bar{H}^+$	0.83	0.82	0.81	0.82	0.80	0.81	0.86	0.88	0.86

Table 10.3: Number of $\bar{H}^+$ expected per mono-energetic antiproton pulse at 6 keV, for the same laser excitation configurations as the ones used in table 10.2.

In conclusion, when working at about 1 keV, effort should be made experimentally to both reduce the width of the antiproton pulse and the mean energy of the antiprotons. In the sole prospect of $\bar{H}^+$ production (i.e. without any consideration on the capture efficiency downstream), this can be done to the detriment of the energy dispersion since the higher cross sections for the lower energy antiprotons will compensate for the smaller cross sections of the more energetic ones. Nonetheless, decelerating the antiprotons to energies even lower than 1 keV implies increasing the beam emittance: all the effort put into having the highest cross sections might be lost to a poor transmission efficiency through the reaction chamber. To verify this, a complement to the simulation of the antiproton decelerator would be required.

As seen before, the tuning of the laser parameters, though crucial to optimise the yield of antihydrogen ion production, is less critical since, experimentally, they will be more easily adjustable. Only the jitter on the laser delay can cause significant loss, especially for short laser pulses with high values of the `xi` parameter.

Now, comparing the 1 keV solution to the 6 keV solution, it is the former one that yields to the highest number of antihydrogen ions per antiproton pulse, when a two-laser pulse excitation is used. However, this result highly depends on the real antiproton beam parameters: if it appears that decelerating the antiprotons to 1 keV implies having much longer $\bar{p}$ pulses and decreasing too much the antiproton transmission through the reaction chamber, then the 6 keV solution (with Ps excitation) would be better. This is the "lesser effort" solution.

Another point of view is to look at the promises held by a short (less than 250 ns) 1 keV antiproton beam (or even lower energy if possible); this has lead the collaboration to think about a new apparatus in replacement or in addition to the decelerator, that could improve the beam quality. Technical considerations lead to the development of an electrostatic ion beam trap (EIBT) that is presently tested.

10.2.2 Results with a realistic simulation of an antiproton pulse decelerated to 1 keV

We use here results from the CSNSM decelerator simulation dating from June 2013. At 1 keV, the emittance of the antiproton pulse blows up (from 4π mm·mrad to 40π mm·mrad) and thus the transmission of the antiprotons through the reaction chamber is drastically degraded: for instance, only 16 % of the pulse coming from ELENA would make it through a 1 mm^2 by 20 mm positronium cell. The simulation of the decelerator device is still in development, but no other data were made available, as the transmission, after the deceleration and focussing stages, was not improved.

As for the 6 keV case, four different sizes of the reaction chamber have been evaluated. We first worked with a 20 mm-long cell, with inner sections of 0.8, 1 or 1.33 mm^2 (which correspond respectively to radii of 0.50, 0.56 and 0.65 mm). A two laser-pulse excitation has been considered for the two smallest sections. Finally, keeping the inner section to 1.33 mm^2, the length of the cell is increased to 30 mm, which, according to the previous section, is the optimal length at 1 keV. A summary of the results is presented in table 10.4.

With a single laser pulse, the highest number of $\bar{H}^+$ ion per antiproton pulse is obtained for a 20 ns laser pulse of 0.98 mJ: out of the 1000 $\bar{p}$ simulated, 123 were able to exit and 8.6 10^{-5} antihydrogen ion were produced. Extrapolated to a $3{\cdot}10^6$ pulse of antiprotons, that is 0.26 $\bar{H}^+$. Although it is comparable to the 0.3 antihydrogen ion announced in the GBAR proposal, this is much smaller than the 0.8 predicted by the simple monoenergetic antiproton pulse simulation; but, here, only 12 % of the antiprotons are transmitted. This means, that, in fact, if the

acell(mm^2)	0.8				1		1.33	
scell(mm)	20				20		20	30
$N_{\bar{p}}$	123				159		218	91
pdel(ns)	165	165	170	165	190	185	195	150
t_limp(ns)	10	20	50	$2\times$ 10	20	$2\times$ 10	20	25
l2del(ns)	–	–	–	40	–	40	–	–
xi	100	29	7	72	28	73	29	20
E(mJ)	0.727	0.783	0.962	2×0.617	0.962	2×0.777	1.302	1.351
ldel(ns)	120	120	115	90	120	90	120	150
$\bar{H}^+(10^{-5})$	8.54	8.58	6.75	9.27	6.35	6.80	4.54	2.38

Table 10.4: Examples of best $\bar{H}^+$ yield and corresponding optimal parameters obtained for an antiproton deceleration simulated at 1 keV.

transmission could be increased to 50 %, we would have about 1 $\bar{H}^+$ per antiproton pulse, i.e. more than the first simple predictions! This could be explained by the fact that, on one side, the 123 antiproton pulse has a mean energy below 1 keV (so higher cross sections in average), and, on theother side, it has a width smaller that the 300 ns used in the monoenergetic case (thus a more efficient use of the antiprotons).

More generally, a 10 to 25 ns laser pulse of 0.7 to 0.9 mJ gives about 8.5 10^{-5} $\bar{H}^+$ per pulse. Longer laser pulse are less efficient for the production of the antihydrogen ions. A further 8 to 9 % can be gained by using two laser pulses of 10 ns FWHM, 0.6 mJ, with a 40 ns delay between them. Now, increasing the diameter of the reaction chamber does not greatly improve the antiproton transmission efficiency, but, moreover, decreases the positronium density, resulting in a decreased $\bar{H}^+$ yield. For instance, increasing the radius of the cell by 30 %, from 0.50 mm to 0.65 mm, leads to $\bar{H}^+$ production almost divided by a factor 2. In that case, going to a longer reaction chamber is of no help since it further degrades the positronium density. So, in the end, if we have to choose between a degraded transmission of the antiprotons due to a narrower positronium cell or an improved transmission obtained by opening the aperture angle of the reaction chamber, it is better to afford losing some antiprotons at the injection but keep a positronium density as high as possible. The present results also reinforce the choice of a 20 mm long positronium cell.

10.3 Positronium excitation at Saclay and hydrogen production

Before installing the experiment at CERN, starting from 2016, the linac-based positron source demonstrator and the positron accumulation trap will remain available at CEA during the next two years. This is an opportunity to perform experiments on positronium, such as positronium spectroscopy in the 3D state or cross section measurements using protons instead of antiprotons, in order to confront the theoretical predictions. For the latter, since the positronium density at Saclay would be several order of magnitude lower than it will be at CERN, it is probably illusory to undertake a measurement of the H^- production cross sections, unless buying an intense proton source. However, an experiment focussing on the production of hydrogen should be within reach. This type of experiment would thus be very similar to the one of Merrison *et al.* [64], and could give cross sections values for proton energies lower than 10 keV. It would also be the first experiment to measure this cross section with excited positronium.

Studying the spectroscopy of positronium and measuring the cross sections needs to con-

centrate on signal detection. For the positronium spectroscopy, there are two different ways to detect and quantify the formation of excited positronium: either in the positronium lifetime spectrum, where excited positronium appears to change the positronium annihilation rate (this is what is usually done [44, 24]), either by detecting the fluorescence of the positronium as it relaxes to ground state (which is the method we will try to implement at CEA, in complement to lifetime measurements; see further). For a cross section experiment, we probably want to have the highest event rate possible to limit statistical error, and of course be able to efficiently detect and identify the hydrogen atoms.

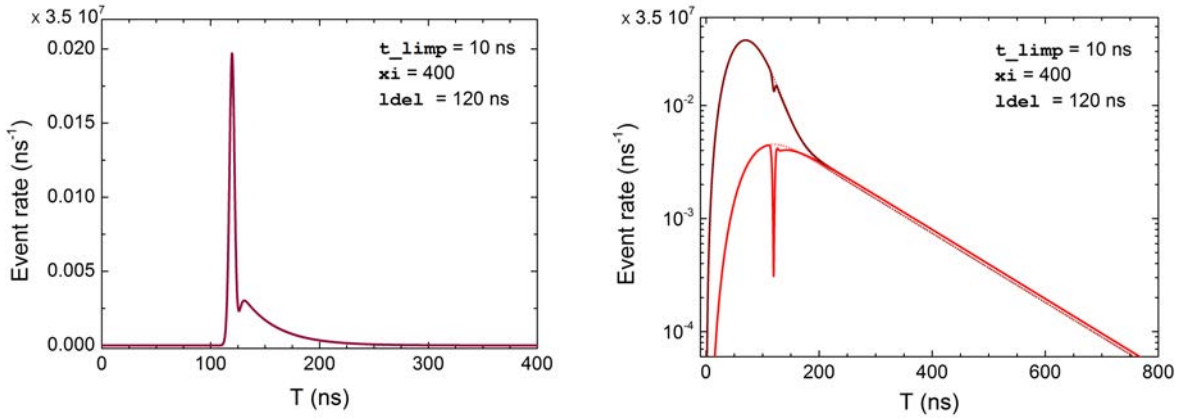
We remind here that for the Saclay set-up, a maximum of 10^8 accumulated positrons can be expected, resulting in a cloud of $3.5 \cdot 10^7$ ortho-positronium. This is 200 times lower than the density foreseen at CERN.

10.3.1 Positronium spectroscopy experiment

The simulation previously described can easily be adapted to extract the ground state positronium annihilation signal, as well as the fluorescence signal from the 3D state of positronium. In the latter case, one should note that this simulation does not taken into account the fact that the relaxation of the 3D state first populates the 2P state of positronium, which then de-excites to ground state. The 3D to 2P transition leads to the emission of an infra-red photon at 1312 nm, while the 2P to 1S transition gives a UV photon at 243 ns. For the moment, we do not discuss which fluorescence transition will be detected. Since the lifetime of the 3D state is 31 ns while it is 3.2 ns for the 2P state, we assume that the fluorescence signal at 243 nm will be similar and almost simultaneously with the 1312 nm signal.

In order to have the brightest fluorescence signal, we need to optimise the laser pulse width `t_eimp` and its energy, as well as the delay. The other possibility is to have a less intense fluorescence signal, but more excited positronium over a longer period of time. The background at 243 ou 1312 nm in the reaction chamber has not been measured yet, so it is not included in the discussion. Figures 10.13 to 10.15 present several signals obtained for each possibility, along with the corresponding annihilation signal. For the moment, it is assumed that the laser can lit the whole positronium cloud formed out of the 10^8 positrons ejected from the trap. Concerning the annihilation signals, their principle is comparable to the ones published by Cassidy *et al.* [44], called single-shot lifetime spectra.

In figure 10.13, a 10 ns laser pulse of 1.82 mJ has been used, with `ldel` = 120 ns. On the fluorescence rate (figure 10.13a), we observe that a bright but short signal is produced: this flash has a width of 5 ns, for a total number of 4.16 10^6 fluorescence photons emitted. With the adequate detection system based on a photomultiplier tube, it should be possible to record and use this fluorescence signal. Now looking at the corresponding annihilation rate (figure 10.13b), we notice that the positronium excitation occurred while the positron pulse was only partially implanted into the converter, and thus, the effect on the positronium annihilation rate is diluted into the prompt annihilation signal – it is the small decreased in the total annihilation rate that can be seen around 120 ns. This would have to be confirmed experimentally or with a more detailed simulation, but it is likely that this small decrease would not be distinguishable from the background (mainly the direct annihilation of the positrons) fluctuations. We can nonetheless observe that the positronium excitation has a second effect on the annihilation spectrum: the tail of the spectrum is longer, corresponding to more positronium atoms being still available at longer time, since the atoms that have been excited were momentary subtracted from annihilation. This effect is the reversed of the one reported by Cassidy *et al.*, where the resonant transition to the

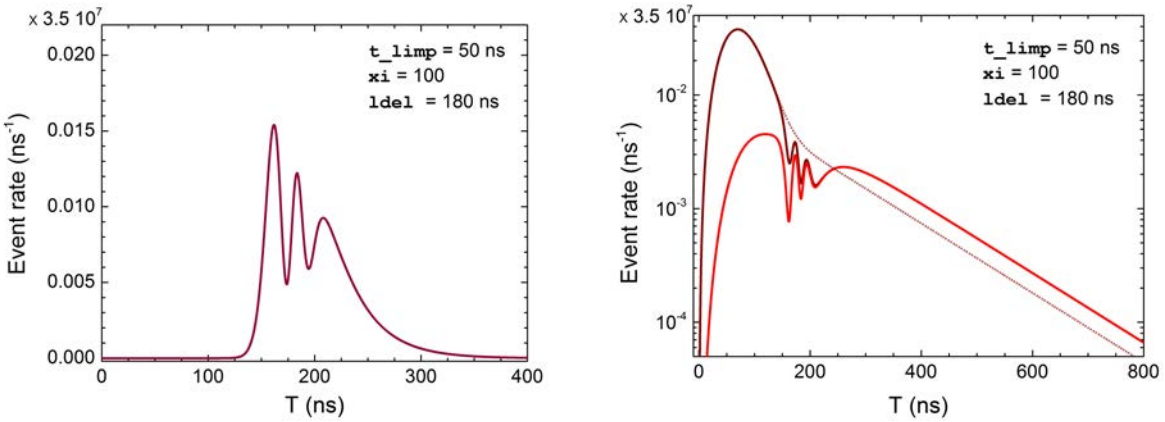


(a) Photon emission rate from the fluorescence of Ps(*3d*).

(b) Positron and positronium annihilation event rate.

Figure 10.13: The fluorescence signal (a) and annihilation spectrum (b) simulated for an intense (`xi`=400) 10 ns laser pulse, used 120 ns after the beginning of positronium formation. In the annihilation spectrum, the red curves correspond to ortho-positronium annihilation only while the dark red curves take into account the background formed by the prompt annihilation of the positrons and of the para-positronium; the dotted lines indicate what the signals would look like without laser excitation.

2P state of positronium performed in a 700 G magnetic field was accompanied by a mixing with the 2S singlet state and thus by an increased annihilation rate of the positronium: subsequently, less positronium atoms were left afterwards. However, this lifetime extension due to excitation into state 3D is a very small effect in the case of the 10 ns laser pulse presented here, and it would be difficult to exploit in order to quantify the laser transition efficiency.



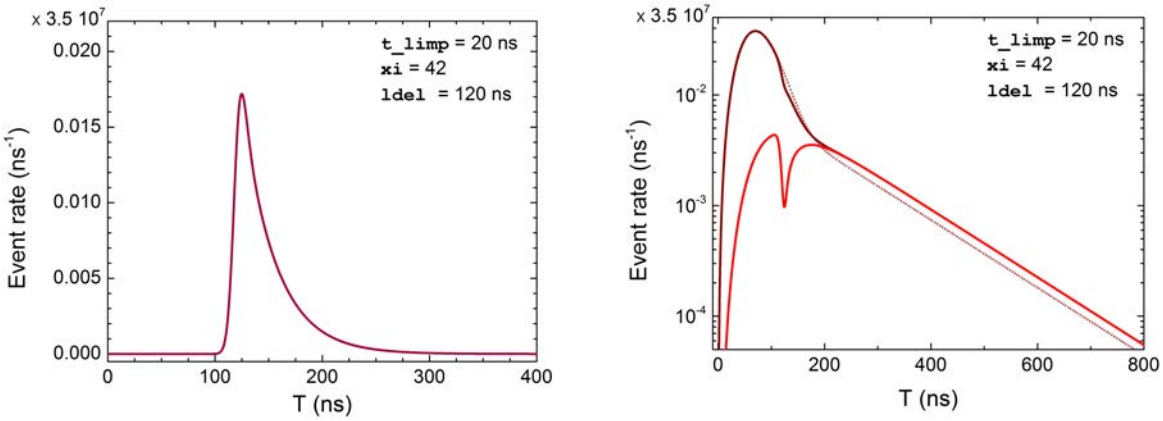
(a) Photon emission rate from the fluorescence of Ps(*3d*).

(b) Positron and positronium annihilation event rate.

Figure 10.14: Same as figure 10.13 but for an intense (`xi`=100) 50 ns laser pulse sent after of greater delay (`ldel`=180 ns).

Figure 10.14 shows the case of a 50 ns laser pulse, its energy being 4.54 mJ; this time, the excitation of the positronium takes place slightly later, at `ldel` = 180 ns. The damped Rabi

oscillations are the cause of the three-pulse structure of the fluorescence, each peak being less intense than in the results presented in figure 10.13a. But if the fluorescence of the positronium cloud is not as bright in this case, here, the Rabi oscillations have the advantage of stretching the time during which the Ps(*3d*) level is highly populated: thus the fluorescence signal lasts much longer. In particular, a fluorescence event rate greater than 10^5 ns^{-1} should be observed at least during 100 ns. This would probably simplify the detection of the fluorescence. The detection of the positronium excitation from the annihilation γ-ray spectrum is also more convenient: due to the longer delay chosen for the laser, the associated drop in the annihilation rate occurs after the prompt positron annihilation peak and the corresponding number of excited positronium atoms can thus be determined. We also notice that the effect on the tail of the annihilation spectrum is larger in that case. It would then be possible to deduce the fraction of excited positronium by adapting the method presented in [44]. Strictly from the point of view of the detection, a long and energetic laser pulse seems to be the best solution, since both the fluorescence and the annihilation of the positronium can be (simultaneously) used. The drawback comes from the Rabi oscillations themselves since they highly depends on the laser parameters.



(a) Photon emission rate from the fluorescence of Ps(*3d*).

(b) Positron and positronium annihilation event rate.

Figure 10.15: Same as figure 10.13 but for a less intense laser pulse with `xi`=42, 20 ns FWHM, delayed by 120 ns with respect to the positronium production.

Finally, in figure 10.15, it has been chosen to present the case of a 20 ns laser pulse of 1.18 mJ, delayed by 120 ns with respect to the beginning of the positronium production. In that case, Rabi oscillations did not established in the system and the fluorescence signal displays a simpler form with a $\frac{1}{\tau_{3D}}$ decay rate clearly defined. The event rate is greater than 2.6 10^5 ns^{-1} for more than 25 ns (and exceeds 10^5 ns^{-1} during 60 ns). This is probably sufficient to make the fluorescence signal directly detectable (always depending on the actual light background in the positronium chamber after the positron trap). However, this time, simultaneously recording the positronium lifetime spectrum (figure 10.15b) is probably of no help since the decrease in the annihilation rate related to the fraction of positronium excited is hardly distinguishable in the prompt annihilation signal. Only the tail of the spectrum, that is for long lifetimes, could be used to estimate the number of excited positronium produced; but since this methods relies of the low event rate part of the spectrum, its interest strongly depends on the gamma-ray background in the chamber.

The usual way to detect and quantify the positronium excitation from the annihilation signal does not use the annihilation spectra presented here. The best way to extract information on the positronium excitation from the gamma ray detection is to perform positronium lifetime spectroscopy. In a few words, the methods consists, for each positron implanted into the converter, into detecting the emission of a secondary electron, which gives the $t = 0$, and then detecting the gamma rays from the annihilation of the positronium at a certain $t = \Delta T$ later, ΔT thus being the lifetime of the positronium atom formed. However, the corresponding set up cannot be used at Saclay after the positron trap, simply because a secondary electron emission detection system has not been implemented there, but a lifetime spectroscopy experiment could be carried out on the "materials science beamline" if the integration of the laser on this beamline is thoroughly thought. The downside of operating the laser on the materials science beamline would be the challenge of detecting the light from the positronium de-excitation since the photon emission rate would be at most of the order of 50 ns^{-1} (corresponding to one pulse coming from the linac, i.e. approximately 10^4 positrons) in a large volume (the diameter of the positron spot at the end of this beamline is about 10 mm).

Already for 10^8 accumulated positrons, the detection would be challenging, since the fluorescence of the positronium cloud indeed only concerns the volume that has been lit by the laser, that is a 8 to 27 mm^3 volume. For one pulse of about 10^4 positrons only, a lesser fluorescence signal would be obtained. Also, the fluorescence will in fact be quite diffuse and requires to design a light collection system that can cover the largest possible solid angle. For all these reasons, in the following, we do not consider a positronium spectroscopy experiment at the materials science beamline any more. To give a final conclusion on the possibility to detect the faint and ephemeral fluorescence of the positronium cloud, and to find the best laser excitation scheme to use, an experimental simulation of the detection could be envisaged using another fluorescent gas. This will be discussed in the next part dedicated to the laser.

We finally note that further work would be needed on the simulation if we want to measure the line-shape of the 1S-3D transition and compare it with its predictions; in particular, the detuning of the laser should be included in the optical Bloch equations (both to take into account the laser spectral width and to simulate a scan of the transition frequency).

10.3.2 Hydrogen production cross section experiment

If the progress in positron trapping at Saclay allows it, the positronium cloud produced at the exit of the RIKEN trap could be used to measure the cross sections of hydrogen and H^- formation before the trap is moved to CERN; it would also be an opportunity to test the antiproton decelerator with protons. We thus assume that we can again use the data from the decelerator simulation (at 1, 2 and 6 keV) as input for a hydrogen experiment at Saclay, although this supposes a proton source with an emittance and a momentum dispersion similar to the ones of the antiproton beam from ELENA. Beside, the notable difference is that we do not have to inject the proton pulse through a 1 mm^2 hole, thus a much larger fraction of them will be efficiently used. On the other hand, one should keep in mind that the linac installed at Saclay is only a demonstrator and produces a lower positron flux compared to the CERN experiment goal: like for the positronium spectroscopy experiment, only 10^8 positrons would be trapped – in the most optimistic scenario – and the positronium density will be much lower than the one in the final antimatter experiment.

This is particularly true for the "open geometry" configuration shown in figure 9.7c. In order to avoid losing too many positronium atoms in the interaction region due to their free diffusion into vacuum, we will assume from the beginning that the positronium will be (weakly) confined

in a tube, similarly to what will be done at CERN. Following the idea originally discussed within the collaboration and that has been demonstrated at ETH Zürich by Paolo Crivelli [105] (see figure 10.16), the positrons would be implanted through a silicon nitride (SiNi) window and the frame of the window would be shaped as a tube, so that the laser and the proton beams could go through, perpendicularly to the positron implantation direction. With the set-up at Saclay, the expected positron spot-size on the converter is 2 to 3 mm in diameter, which fixes the size of the SiNi window; the distance between the window and the converter could be set to 2 mm: the inner section of the tube would thus be comprised between 4 and 6 mm^2. The tube length would be mainly determined by the frame of the window. Nonetheless, it should be short enough in order to keep the positronium density as high as possible, but still long enough to minimise positronium diffusion out of the tube and to provide a longer interaction time. The simulations are run with 6 and 8 mm.



Figure 10.16: The positron to positronium converter enclosed in a tube tested by P. Crivelli, with the silicon nitride window for the positron implantation.

The total cross section measurement could be realised in two phases: first, the measurement of the hydrogen production, where no distinction would be made between the states of hydrogen (unless implementing an optical detection of the excited state fluorescence), and afterwards, if feasible, a measurement of the H^- production cross section from the two consecutive reactions combined. The former would be very similar to the experiment performed by Merrison *et al.* [64] and should be compared to the simulation estimation provided by summing the populations in $\boldsymbol{p}_{\bar{\mathrm{H}}}$ (sum over the excited states of hydrogen considered), just at the exit of the interaction region. Also, for the first time, this cross section measurement could be done with excited positronium (into state 3D to start at CEA): in particular, below 6 keV, we expect the number of hydrogen atoms measured to almost only depend on the cross sections for Ps($3d$); we will mainly focus on the case of excited positronium in the results below. Due to the enclosure of the interaction region in a tube, it will not be possible to monitor the positronium excitation from its fluorescence; we will thus have to rely on the positronium lifetime spectrum.

Since the count rate would be extremely low and time is limited by the installation at CERN, a H^- production experiment is certainly out of reach at Saclay; we will thus focus the results of this section on the hydrogen production. The results obtained are summarised in tables 10.5 to 10.9, for the case of 10^8 trapped positrons.

It is found that, either for a 6 or 8 mm tube length, whether the size of the hole for the protons is 4 or 6 mm^2, the transmission of the protons through the tube is maximal whatever their energy. This corresponds to 709 protons out of 1000 simulated for a deceleration at 1 keV, 946 out of 1000 at 2 keV and 987 out of 1000 for 6 keV; the missing particles are in fact protons

that have either hit the walls of the decelerator or have not been properly decelerated and thus cross the interaction region way before the main proton pulse.

6 keV – 4 mm^2× 6 mm						
t_limp(ns)	10	30	50		100	
xi	100	16	9	36	9	36
E(mJ)	3.64	4.36	5.45	10.91	10.91	21.81
ldel(ns)	125	125	120	125	135	140
pdel(ns)	155	150	150	165	170	165
H(10^{-3})for : $10^8 e^+$	8.58	9.12	9.80	11.20	13.06	15.30

Table 10.5: Total number of hydrogen atoms obtained for 1000 protons, simulated with the same characteristics as the antiproton pulse from ELENA, for several sets of parameters; the delays have been optimised. Here the protons have been decelerated to 6 keV and injected in a tube of 4 mm^2 aperture by 6 mm length.

6 keV – 4 mm^2× 8 mm			
t_limp(ns)	30	50	100
xi	16	36	9
E(mJ)	4.36	10.91	10.91
ldel(ns)	125	120	135
pdel(ns)	150	160	170
H(10^{-3})for : $10^8 e^+$	9.10	11.17	13.04

Table 10.6: Same as table 10.5 with 6 keV protons, but the tube is now 8 mm long.

6 keV – 6 mm^2						
scell(mm)	6			8		
t_limp(ns)	30	50	100	30	50	100
xi	16	36	9	16	36	9
E(mJ)	6.54	16.36	16.36	6.54	16.36	16.36
ldel(ns)	125	125	135	125	125	135
pdel(ns)	150	165	170	150	165	170
H(10^{-3})for : $10^8 e^+$	6.08	7.47	8.71	6.07	7.46	8.69

Table 10.7: Same as table 10.5 with 6 keV protons, but a larger SiNi window has been used, thus the aperture of the tube is now 3 mm × 2 mm; its length is either set to 6 or 8 mm.

We observe that for longer pulses of laser, for instance a 100 ns pulse, the total number of hydrogen atoms produced is significantly increased. And though it is not displayed here, this yield

1 keV						
acell (mm^2)	4			6		
scell (mm)	6			8		
t_limp (ns)	30	50	100	30	50	100
xi	16	36	9	16	36	9
E (mJ)	4.36	10.91	10.91	6.54	16.36	16.36
ldel (ns)	120	125	135	120	130	135
pdel (ns)	185	175	180	185	175	180
H (10^{-3}) for : $10^8 e^+$	2.77	3.64	4.45	1.84	2.42	2.96

Table 10.8: Same as table 10.5 but this time with 1 keV protons; only the smallest (4 mm^2 $\times$ 6 mm) and the largest (6 mm^2 $\times$ 8 mm) tube dimensions have been considered here.

2 keV						
acell (mm^2)	4			6		
scell (mm)	6			8		
t_limp (ns)	30	50	100	30	50	100
xi	16	36	9	16	36	9
E (mJ)	4.36	10.91	10.91	6.54	16.36	16.36
ldel (ns)	120	125	135	120	130	135
pdel (ns)	165	150	170	165	150	170
H (10^{-3}) for : 10^8 e^+	3.54	4.94	6.04	2.36	3.28	4.02

Table 10.9: Same as table 10.8 but with protons decelerated to 2 keV.

can be further augmented with even larger and more intense laser pulses. This is the reverse behaviour compared to the results obtained for $\bar{H}^+$; the reason is the absence of photo-detachment for the hydrogen atoms. Such long pulses cannot be done with the foreseen laser system for the CERN experiment. And, obviously, the required power (of the order of 100 kW) is much too high to be obtained from CW laser, even if the interaction region was placed in a very high finesse optical cavity. We should thus aim for a 50 ns laser pulse, with at least an energy per pulse of 10 mJ, but, depending on the intensity of the proton source and the total number of positron used, a 30 ns laser of 5-6 mJ can be sufficient. The simulation shows, with such laser pulses, that the expected number of hydrogen atoms produced ranges between 10 to 30 atoms, if the proton source delivers pulses of $3{\cdot}10^6$ particles and for 10^8 accumulated positrons.

One comment should be made on the possibility to work with a single pulse of 10^4 positrons. This solution should not be completely ruled out, in the case of no laser excitation of the positronium at all. It would require a much more intense source of protons in order to reach an event rate of a few hydrogen atoms per pulse. However, the experimental scheme could be completely changed: operating the linac at 200 Hz, and, optionally stretching the 10^4 positron pulses, we could work with a quasi continuous positron beam, and do the same for the proton beam – in which case the decelerator cannot be tested. This possibility has not been taken into account here and needs to be investigated in the near future. Its main interest is that it can still be used

for cross section measurements after the antiproton decelerator and the positron trap have been moved to CERN.

Concerning the simulation with the 10^8 accumulated positrons and the decelerated proton pulses, at 6 keV, there is no meaningful difference between a 6 mm and a 8 mm long tube; though not being shown here, this is also true at 1 and 2 keV. We can thus aim at 8 mm in length if this is easier to assembly. Also, if the positron spot size can not be smaller than 3 mm in diameter and the SiNi window is then chosen to be 3 mm $\times$ 3 mm, the degradation of the positronium density would be responsible for a one third loss in the total number of events: the possibility to use of such a degraded event rate depends on the proton source intensity.

In conclusion, with 10^8 trapped positron and a proton source at least complying with the characteristics of the antiproton beam from ELENA, we should be able to produce a few tens of hydrogen atoms every 100 s (e^+ accumulation time) and thus carried out the measurement of the quantity $\sum_{n_h,l_h} \sigma^{3B,2}_{n_h l_h;n_p l_p}$, while simultaneously testing the antiproton decelerator. The detection of the hydrogen atoms themselves has not been discussed here.

Although the measurement of the different hydrogen excited states is not envisaged, we give here for information the typical repartition of the hydrogen population between the first thirteen states considered, right after the exit of the tube. This is shown in figure 10.17, in the case of a 50 ns laser pulse of 10.9 mJ for 1 keV protons. We notice that the hydrogen atoms that will be detected after the interaction region are still in a state $n_h = 5$; the ground state is already well populated thanks to the radiative transition of the higher excited states. Obviously, if the detection system is placed far from the interaction region, for instance half a meter away, most of the hydrogen will be in the ground state. In order to quantify the fraction of hydrogen atoms in the state $n_h = 5$, we could for instance add a second laser to the system (perpendicular to the proton beam, just at the exit of the tube of positronium), tuned to the photo-ionisation threshold of these states, that is 2.278 μm (obtained for instance with a Cr:ZnSe/S based laser [106]), and detect the resulting free electrons.

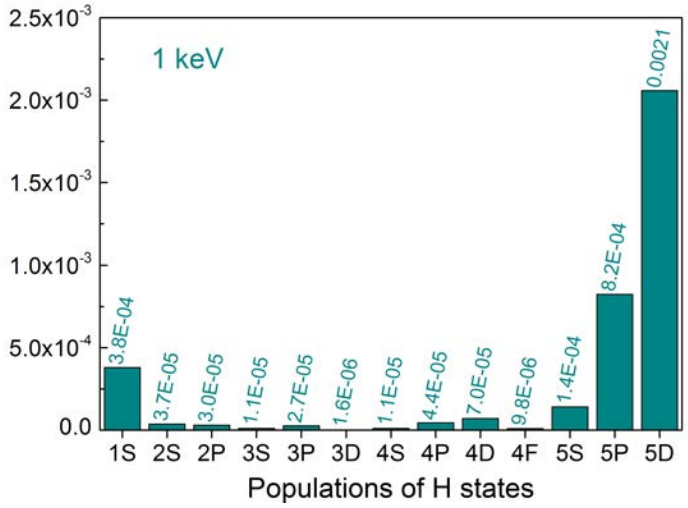


Figure 10.17: Repartition of the hydrogen population between the excited states at 1 keV; this is a picture of the hydrogen pulse content right at the exit of the interaction region.

Following these last remarks, it is important to note the big distinction between the $H^-/\bar{H}^+$ production experiment and the hydrogen production. In the first one, we want the de-excitation of the excited states of hydrogen/antihydrogen to occur as soon as possible so that a sufficient number of ground state atoms can interact with the positronium for the second reaction. In that case, it is perfectly understandable that long-lived hydrogen states (roughly starting from $n_h = 6$) can be discarded from consideration. In the second case, however, we just want to count the number of hydrogen atoms formed from the first reaction, regardless of their state. The simulation stopped at H(*5d*) because we have not yet computed the cross sections for other higher states, but if we extrapolate the behaviour of the cross sections to these states, we expect them to be copiously produced. All this to remark that the simulated numbers of hydrogen atoms given here do not take into account the H states above 5D, and thus are probably underestimated. Also, the suggested photo-ionisation experiment of the $n_h = 5$ would have to cope with the ionisation of the higher excited states...

Finally, we also give some results when there is no laser excitation in table 10.10; in fact, we will most certainly start the cross section experiment by this measurement, since it is simpler to implement, in particular because the problem of the laser pulse synchronisation is removed. The main interest of the experiment relies in the fact that there will only be ground state positronium available in the tube, making it easier to deduce the quantity $\sum_{n_h,l_h} \sigma^{3B,2}_{n_h l_h;1\ 0}$ from the results. This experiment would be directly comparable to and complete the results from Merrison *et al.* [64]. One last advantage: this measurement can still be done once the laser is also moved to CERN.

As expected from the cross section calculations, there will not be much hydrogen atoms to detect at 1 and 2 keV: unless having access to a very high intensity proton source, we cannot expect reaching a precise measurement of the summed cross sections at these energies. This is thus an experiment that should done for energies above 6 keV. In that case, the summed cross section related to Ps(*3d*) only – that is $\sum_{n_h,l_h} \sigma^{3B,2}_{n_h l_h;3\ 2}$ – can be deduced from the difference between the results obtained when the laser is either ON or OFF.

	1 keV		2 keV		6 keV	
`acell` (mm^2)	4	6	4	6	4	6
`scell` (mm)	6	8	6	8	6	8
`pdel` (ns)	340		230		175	
H	$1.05\ 10^{-9}$	$6.96\ 10^{-10}$	$1.75\ 10^{-6}$	$1.16\ 10^{-6}$	10.4	6.87

Table 10.10: Number of hydrogen atoms (up to H(*5d*) included) predicted when only ground state positronium is used (formed out of 10^8 accumulated positrons and $3{\cdot}10^6$ protons); the delay of the proton pulse has been optimised.

Chapter 11

Conclusions and suggested future developments

11.1 Proposition for the design and realisation of reaction chamber based on the simulation results

In the present thesis, the values of the proposal for the interaction region of GBAR have been used as benchmarks. Thus, the default parameters for the reaction chamber dimensions were set to 1 mm^2 inner section and 20 mm length. It appears from the simulation, and based on what seems to be experimentally feasible, that the optimal realisable dimensions are indeed 0.8 to 1 mm^2 by 20 mm. The importance of having a long reaction chamber was a result foreseen at the beginning of the thesis, based on the first cross section calculations, that lead to change the foreseen 10 mm length to 20 mm before submitting the GBAR proposal. The simulation has validated this suggestion.

It has also been shown that the gain obtained by having a longer reaction chamber cannot compensate for a larger aperture of the tubular chamber, since the final result is proportional to the square of the positronium density. Thus, the inner section of the reaction chamber should be made as small as possible. This, however, greatly limits the injection efficiency of the positron and antiprotons inside the chamber. Nonetheless, it has been demonstrated that, without any improvement on the $\bar{p}$ focussing, it is better to afford losing antiprotons at the injection and keep a high positronium density. Thus the value of 0.8 mm^2 has been recommended. For the positrons, the difficulties raised by the strong focusing required (in addition to the lack of solution for the subsequent implantation into the converter) forced the collaboration to find another solution for the positron implantation: this resulted in a successful attempt in transmitting a positron pulse through a SiNi window, that will allow us to implant the positrons perpendicularly to the chamber axis.

It has been demonstrated that the photodetachment of the $\bar{H}^+$ causes significant losses. Obviously, that cannot be avoided while the particles are inside the reaction chamber; we thought we could minimise the photodetachment outside the positronium cell by placing the laser beam off the antiproton beam axis, and then gain on the total $\bar{H}^+$ yield. However, we demonstrated that the gain is at most a few percent. Except if it is proven that any small gain is required for the GBAR experiment, it seems not worth to pursue this idea. In fact, it should not be fully discarded since, experimentally, it has the advantage of keeping the beam paths, after the reaction chamber, free of any mirror that the laser excitation needs. One should nonetheless

note that this laser excitation from the side of the reaction chamber requires twenty (that is, the length of the chamber) times more energy than for the excitation on axis. The other drawback is finding the correct material(s) to transform two walls of the reaction chamber into two laser windows (or one window and one mirror).

11.2 Ameliorations to the simulation

Although spanning all over the experimental parameters, this simulation is based on several approximations that can be discussed. For the positronium excitation, the simulation has not considered a realistic laser pulse with its frequency width and its detuning with respect to the frequency of the transition aimed at: we only worked at resonance. For the excitation into state 3D, the possibility to excite simultaneously the 3S state has not been treated, and the intermediate relaxation to the 2P state has not been taken into account.

The excitation of the positronium into the 2P state has not been studied yet. This was mainly a lack of experimental input concerning the laser system that would be used. This study can now be undertaken and should be the priority regarding the simulation development since the cross sections with the 2P state of positronium are higher than the one with Ps($3d$).

For the CEA experiments on positronium spectroscopy and cross section measurements, it has not been taken into account that the positronium atoms formed and excited will still be in a 100 to 300 G magnetic field. It was also assumed that all the positronium atoms produced were confined in a small volume, when, for the fluorescence detection, they will in fact probably freely diffuse into vacuum. However, it lacks some experimental description on how the positronium is emitted from the converter's surface to fully include the diffusion problem in the simulation.

In general, the absence of experimental input is the reason for most of the approximations that have been adopted. The future developments of the simulation should include a finer description of the positronium excitation, and implement the simulation each time new informations are available from the experiment. In particular, the data used from the simulation of the antiproton decelerator need to be up-dated.

Finally, we also recommend that the simulations are rerun using the CBA cross sections for the first reaction instead of the CDW–FS cross sections, since the results of Part II suggest that CBA could be more appropriate than CDW–FS at low energies.

Even in its simplest form, this simulation has already pointed out which parameters should be carefully tuned, or, on the contrary, which ones offer some flexibility, and it has underlined the importance of improving some of the current performances of the experimental equipment. In particular, new solutions are being considered around the antiproton decelerator in order to either reduce the beam emittance or compress the bunch.

Part IV

Laser for positronium excitation into the state 3D

Chapter 12

Description of the laser

12.1 Requirements

In this section, we give some further precisions about the transition 1S-3D that we want to observe in the positronium. In particular, the values of the natural linewidth and Doppler broadening which were not taken into account in the simulation. Then, we discuss the differences between the positronium excitation configuration at CERN and the one in CEA where the first tests will be made. This changes the characteristics of the laser which has to be used.

12.1.1 Natural linewidth of the transition and Doppler broadening

As already said in part III, the 1S-3D transition in positronium is reached via a two-photon transition at 410 nm (410.095 nm, $\nu_0 = 731.031$ THz). The de-excitation of the 3D level leads to the emission of 1312 nm light from the 3D-2P spontaneous transition and 243 nm light from the 2P-1S relaxation. The lifetime of the 3D level of positronium is $\tau_{3D} = 31$ ns. Due to this short lifetime, the absorption line is broadened into a Lorentzian profile of width $\Delta\nu_{3D}$, called the natural linewidth. Using the Heisenberg Uncertainty Principle in its "time-energy" formulation, we can express the natural linewidth $\Delta\nu_{3D}$ as:

$$\Delta\nu_{3D} = \frac{\Delta E}{h} \approx \frac{h}{2\pi\Delta t} \cdot \frac{1}{h} \approx \frac{1}{2\pi\tau_{3D}}. \tag{12.1}$$

This gives a natural linewidth of approximatively 5 MHz. Since the positronium is moving, the linewidth is also broadened by the Doppler effect. The shift $\delta\nu_1$ due to the first order Doppler effect is given by

$$\frac{\delta\nu_1}{\nu_0} \sim \frac{v}{c}. \tag{12.2}$$

If the positronium was re-emitted at room temperature (let's take 293 K) from the nanoporous silica converter, then its mean speed would be

$$v \sim \sqrt{\frac{2kT}{m_{Ps}}} \approx 6.636\ 10^4 m/s \tag{12.3}$$

which corresponds to a kinetic energy of 25 meV. In which case the corresponding Doppler shift would be

$$\delta\nu_1 \approx 731.2 \cdot 10^{12} \frac{6.636\ 10^4}{2.998\ 10^8} \approx 161.8\ GHz, \tag{12.4}$$

and, assuming a thermal distribution of the velocities, the Doppler broadening $\Delta\nu_1$ (FWHM) would be:

$$\Delta\nu_1 = \frac{2\nu_0}{c}\sqrt{2\ln 2\frac{kT}{m_{Ps}}} \approx 269.4\ GHz, \tag{12.5}$$

However, the positronium is not thermalised when exiting the pores of the converter and according to the measurements made by Cassidy *et al.* [44] and Crivelli *et al.* [43], its energy is at least about 45 meV. This excess of energy is due to the confinement of the positronium atoms in the pores; the larger the pore, the lower is the additional kinetic energy (it was found for instance that pores of roughly 4 nm diameter re-emit positronium at 48 meV while 3 nm diameters pores lead to 73 meV positronium). Then, the corresponding Doppler effect is

$$\delta\nu_1 \approx 731.2 \cdot 10^{12}\frac{8.896\ 10^4}{2.998\ 10^8} \approx 217.0\ GHz, \tag{12.6}$$

which is much more important than the natural linewidth.

In the case of positronium emission from the pores, the thermal distribution of the velocities cannot be used; the positronium are in fact monoenergetic and the velocity distribution along the axis of the laser beam is mainly due to the geometry of the pores at the surface of the converter. [44] It is indeed known that the positronium re-emission from the converter is not isotropic, but nonetheless, it is not unidirectional, and in particular, it is not perpendicular to surface of the converter. As a consequence, one cannot assume that having the laser beam parallel to the converter would sufficiently minimise the Doppler broadening.

In fact, the first order Doppler effect can be cancelled by using two counter-propagating beams. [107] Indeed, in the referential of a positronium atom of any speed $\vec{v}$, the apparent frequency of one beam will be $\omega + \vec{k}\cdot\vec{v}$ while for the other beam, it will be $\omega - \vec{k}\cdot\vec{v}$. Then, for the simultaneous absorption of a photon from each beam, the first order Doppler effects exactly compensate and the excitation frequency is 2ω (with ω equal to half the frequency of the transition). Experimentally, this can be done by using a mirror to send the laser back on its track. This was already taken into account in the simulation in which the first order Doppler effect is not considered and the photon density used to excite the positronium is twice the photon density of the laser beam.

Cancelling the first order Doppler effect, which is the usual main source for line broadening, implies now to take into account the second order Doppler effect, $\delta\nu_2$. For a two photon transition, it results into a shift given by

$$\frac{\delta\nu_2}{\nu_0} \sim -\frac{1}{2}\frac{v^2}{c^2} \tag{12.7}$$

then

$$\delta\nu_2 \approx -731.2 \cdot 10^{12}\frac{1}{2}\left(\frac{8.896\ 10^4}{2.998\ 10^8}\right)^2 \approx -32.19\ MHz \tag{12.8}$$

It is the most prominent effect which affects the search for the transition or a measurement of the positronium velocity distribution (using the 1S-2P transition at 243 nm). The idea in the GBAR experiment is slightly different, since we want to excite as many positronium atoms as possible for the $\bar{H}^+$ production. This means that the frequency and the spectral width of the laser pulse should be set according to the second order Doppler effet.

Other effects are supposed to be neglected in the configuration of the CERN experiment, one of the reason being the absence of strong magnetic field where the reaction chamber will be located.

12.1.2 In the prospect of an experiment at CEA

The purpose of the positronium study and the experimental conditions at CEA-Saclay are different from the future ones in the CERN configuration. At Saclay, the aim will be to test the laser, quantify the excitation efficiency and perhaps study the positronium re-emission dynamics. More important, the positronium density will be much lower than the one expected at CERN and, probably at the beginning, the positronium atoms will not be produced in a small tube but emitted from the nanoporous silica converter in an open configuration. The number of trapped positrons at Saclay during 100 s can be estimated at 10^8, maximum (we keep here the time between two antiproton pulse, 100 s: in Saclay, to reach a reasonable number of trapped positrons, long accumulation times are needed, although they should not exceed the positron lifetime in the trap, and since we want to be able to build up statistics on the observation of the 1S-3D transition, longer accumulation time would mean longer data taking). This is two order of magnitude lower than the number intended at CERN, and it has not been reached yet. Furthermore, the positronium in the GBAR experiment will be confined (thought loosely) in, roughly, the 20 mm^3 volume of the tubular reaction chamber. At CEA-Saclay, the positron beam diameter will be at least 2 mm, leading to approximatively the same diameter for the positronium cloud, and the positronium will diffuse into the vacuum as soon as it is produced.
Contrary to the CERN expected set-up, in Saclay, the positronium will be produced and excited right at the exit and on the axis of the 5 T positron trap: the Zeeman splitting effect will to be taken into account. The converter will have to be in the 300 G region. However, a recent scheme has arisen for the positron implantation: this scheme involves a positron remoderator placed between the trap and the converter target, adding a further 500 mm distance between these two. In that case, the converter is in the 100 G region, and we expect that the Zeeman splitting effect is reduced. This will have to be confirmed by calculations which have not been done here.

12.2 General description of the laser system

According to the results of the simple simulation presented in part III, the laser for the positronium excitation into state 3D shall deliver 410 nm pulses of 10 to 20 ns width, with an energy of the order of 1 mJ, for the CERN experiment. If a two-laser pulse solution is chosen for the excitation, then, we have to aim at 10 ns pulses and the total energy for the two pulses should be of the order of 2 mJ. For the purpose of an experiment at CEA-Saclay, it should be possible to easily adapt the previous system in order to produce longer laser pulses (if possible up to 50 ns FWHM) and much more intense (between 5 to 15 mJ).

To aim at the 1S-3D transition, and eventually perform a spectroscopy measurement of this transition, the laser shall be highly stable in wavelength, but also tunable, first because the speed of the positronium re-emitted from the nanoporous silicate is not precisely known and second because we may want to determine the lineshape of the transition by scanning the wavelength.

The laser system presented in the following has been realised in order to meet all these requirements. It is basically constituted of three different parts:

- the 410 nm pulsed laser itself, obtained from the frequency doubling of a 820 nm pulsed laser, after an amplification stage if needed (see section 12.2.3);

- the 820 nm pulsed laser (see section 12.2.2), which acquires is pulsed structure from a commercial pump laser and has its wavelength defined by the light coming from a 820 nm

continuous wave (CW) laser;

- this CW laser at 820 nm, that we will describe first (section 12.2.1), whose role is to ensure the wavelength selection and stability of the whole laser system.

Figure 12.1 schematically represents the disposition of the different laser parts on the laser table.

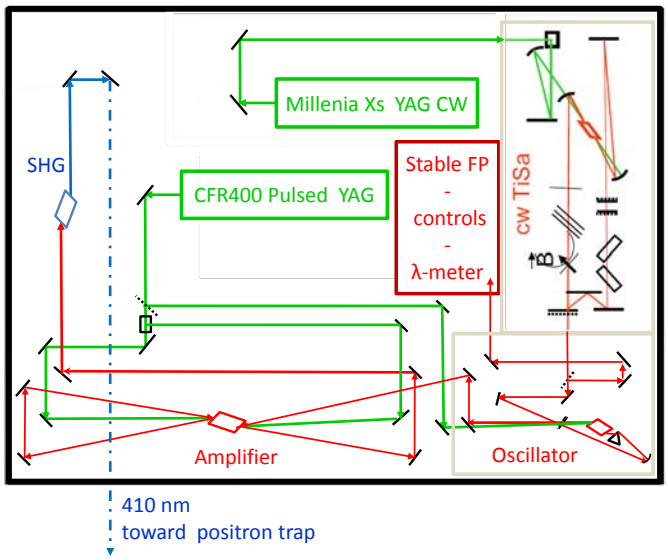


Figure 12.1: A schematic representation of the laser system.

12.2.1 CW Ti:Sa laser

A. Description of the cavity

In order to produce a monomode, tunable laser around 820 nm, we use a solid-state gain medium: it is a sapphire crystal (alumina Al_20_3 in a trigonal lattice) that has been doped with ions of Ti^{3+}. In the following, we note this titanium-doped sapphire as Ti:Sa. Ti:Sa lasers can cover a large range of wavelengths, typically from 650 to 1100 nm, but the maximum gain and efficiency are obtained around 800 nm [108]. To obtain this fluorescence, the crystal is optically pumped with green light lasers. In particular, we will work with a CW laser at 532 nm. The refractive index of Ti:Sa is 1.76 at 800 nm and 1.77 at 532 nm. The Brewster angles at 532 and 820 nm are respectively 60.53°and 60.39°.

The Ti:Sa crystal (15×5×5 from Roditi company) is placed in a ring cavity which mirrors are chosen for their total reflectance around 820 nm, in order to limit losses (while inducing losses for more remote wavelengths, thus participating into the wavelength selection). Six mirrors are used to build this cavity, that we will note as M1 to M6, M6 being the output coupler that allows the exit of the laser beam. This output coupler has a transmission of 3 % around the desired wavelength. M1 and M2 are two spherical mirrors (with a curvature radius of 0.15 m) placed on each side of the Ti:Sa crystal. The disposition of the mirrors is shown in figure 12.2, along with the other elements inserted into the cavity and that will be discussed below. Except mirror M5,

all the other mirrors belong to the same plane with the Ti:Sa crystal. M5 is above this plane, the segment M4-M5 making a 11° angle with this plane. M5 along with the Faraday rotator ensure the selection of the rotation direction of the light in the cavity; the other elements, namely the thick Fabry-Perot, the thin etalon and the Lyot filter are used to select the wavelength among all the longitudinal modes authorised in the cavity, while the bi-plates is used to scan the length of the Ti:Sa cavity. Keeping this distinction between rotation selection and wavelength selection, all these elements are described in the following. Also shown in figure 12.2, the mirrors (m4 to m1) used to inject the pump laser in the cavity, aiming at the Ti:Sa crystal through mirror M1. The Ti:Sa crystal mount is water cooled and set on a horizontal translation stage. Mirrors m1, m2, M1 and M2 are mounted on translation stages to modify the focusing; with the exception of M5, as well as m3 and m4, which are fixed, each mirror is set on a left-right and up-down adjustable mount for the alignment of the cavity.

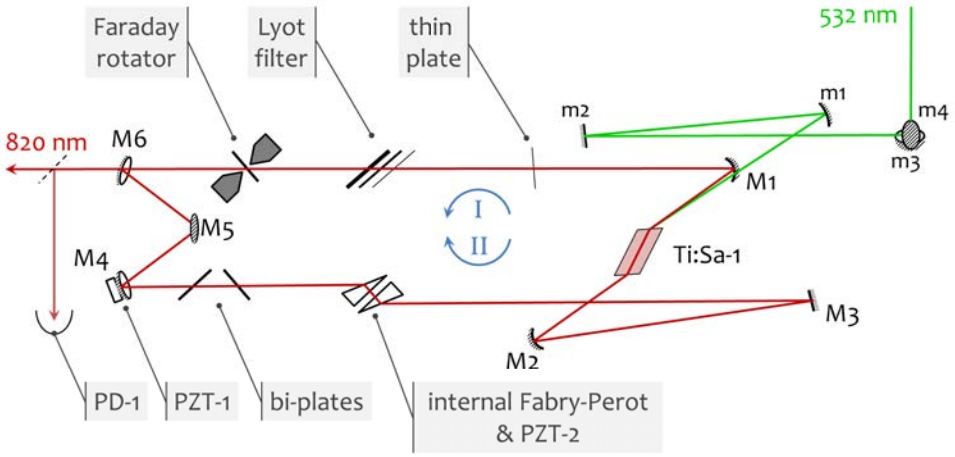


Figure 12.2: Schematic drawing of the CW Ti:Sa laser cavity showing, in particular, the disposition of the mirrors and the optical elements for the tuning of the wavelength.

This type of Ti:Sa laser has been chosen since it was already developed by LKB physicist François Biraben. At the origin, it was a dye laser [109]. This laser has been widely used by the team for their spectroscopy experiments (for example 2S-nD [110] and 1S-3S [111] in the hydrogen atom, and even in the proton radius experiment at PSI with muonic hydrogen [112]): it is thus a well-known tool. Other advantage: one of these Ti:Sa laser cavities was available at LKB, though it was dismantled. A large part of the work on the laser system for positronium excitation was thus to reassemble and realign the CW Ti:Sa laser, testing and changing its components when required. For instance, all the mirrors were replaced, in particular M1, M2 and the output coupler M6, since the original laser was supposed to work at 780 nm; the Faraday rotator was also redesigned and changed; three Lyot filter were tested; the internal Fabry-Perot had to be fully reassembled. The final – and operating – result is pictured in figure 12.3. The whole cavity has been built on a thick granite pedestal, itself being posed on the laser table with rubber absorber pads in between: all this is made to isolate the CW Ti:Sa from the mechanical vibrations of the table, which could change the length of the cavity and thus the wavelength of the laser. A Plexiglas box also limits the acoustical vibrations. The box has an entry for an air (or nitrogen) flow in order to create a small overpressure that will keep dust out of it.

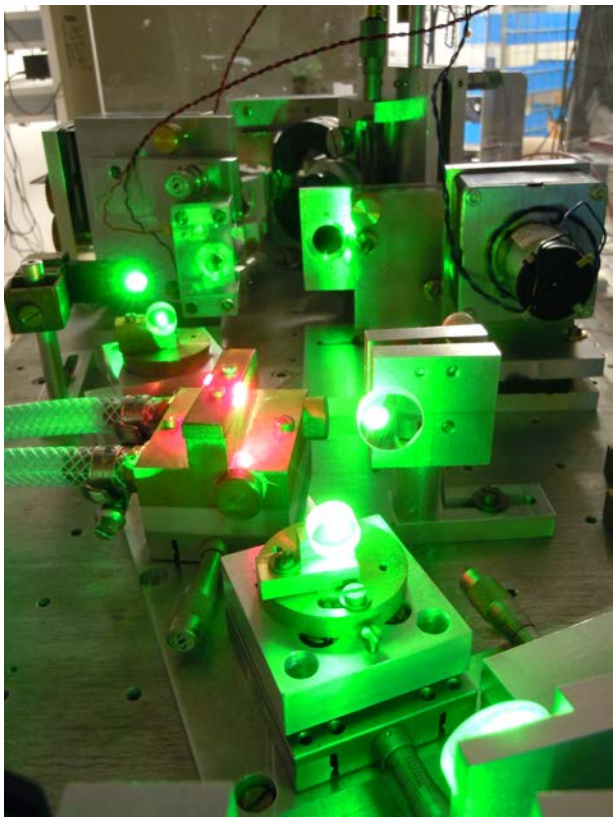


Figure 12.3: Picture of the CW Ti:Sa laser cavity, running.

B. CW pump laser

The pump laser for the CW Ti:Sa is a commercial frequency doubled continuous YAG laser from SpectraPhysics, called the Millennia X*s*. It can deliver 10 W at 532 nm. The beam at the exit is polarised vertically, while the pumping of the CW Ti:Sa crystal requires it to be horizontally polarised; a set of two R*max* mirrors at 532 nm are used to both turn the polarisation by $\pi/2$ and change the height of the pump laser beam.

In the Millennia, the YAG crystal is pumped by two diode lasers with which we experienced some troubles. At the beginning, we were using the Millennia at 8.5 W but in November 2013, the power kept dropping below 1 W after only 20 min of use. It appeared that the spectrum of one of the pump diode had shifted, rendering the pumping less efficient. The diode has been replaced in December 2013 and the Millennia was again able to stably deliver 10 W. However, we expect the second diode to cause the same problem in a near future: we thus decided to lower the power used to pump the CW Ti:Sa. Since then, we use the Millennia at 6 W.

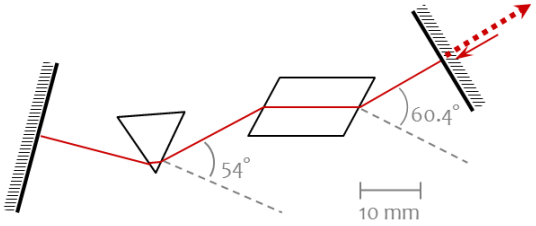
12.2.2 Oscillator

A. The oscillator cavity

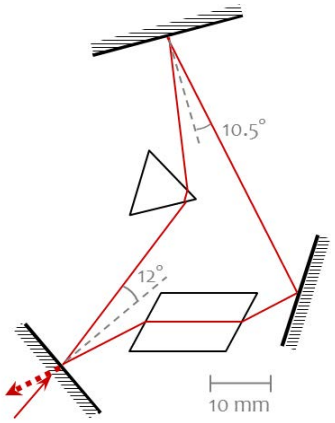
The oscillator cavity is basically made of another Ti:Sa crystal, an output coupler, a spherical mirror for the focusing and a prism. The prism ensures a rough wavelength selection in the light coming from the Ti:Sa fluorescence. The Ti:Sa crystal (dimensions 15×9×5) is pumped by a frequency doubled pulsed YAG laser; this pump laser is also a commercial laser (CFR400 by Quantel – see the description below). It defines the repetition rate of the 820 nm laser. The

energy of the 820 nm pulses, as well as their duration, at the output of the oscillator also depends on the pumping energy. The oscillator is seeded by the CW Ti:Sa laser: this excess of photons at the exactly wanted wavelength is used to force the stimulated emission at the same wavelength. By sending the 820 nm CW laser in the oscillator, we also make the cavity alignment at 820 nm more convenient and precise.

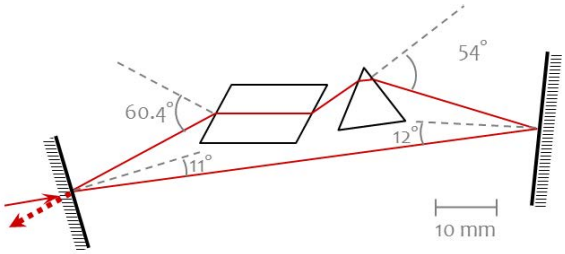
Several designs were considered for the oscillator. The general idea was to keep the length of the cavity as small as possible, since this is what will allow us to keep the 820 nm pulses short. However, shortening the oscillator cavity is limited by its elements' bulk (the crystal and the prism holders, the mirror mounts). We had the choice between two cavity configurations: either a linear cavity or a ring cavity, knowing that, for the ring cavity, the incidence angles on the spherical mirror and the output coupler should be as small as possible to avoid losses; the possibility to add a flat mirror with R*max* coating at 45°was envisaged. The three designs originally proposed are given in figure 12.4. The linear cavity design (figure 12.4a) is based on the oscillator used at the PSI for the muonic hydrogen spectroscopy experiments. We finally chose the design of figure 12.4c, since it has the advantage of a ring cavity in order to have separated beam paths, while still having a short cavity length, similar to what we could have achieved with a linear cavity. One should however note that the prism and the non-normal incidence on the spherical mirror are a source of astigmatism in the oscillator.



(a) The simplest and compact linear cavity design, identical to the one used for the muonic hydrogen spectroscopy [112]. On figures 12.4a to 12.4c, the output coupler is identified by laser beams coming in (thin solid arrow for the CW laser) and out (thick dashed arrow for the 820 nm pulsed beam) of the cavity.



(b) First ring cavity design, requiring a third mirror, this one flat, to make a 90 turn in the cavity.



(c) Second ring cavity design, this time only using the output coupler and the spherical mirror.

Figure 12.4: Design study of the oscillator.

There remains one practical problem to be solved: the light has to pass close to the Ti:Sa crystal, leaving very few space for the usual crystal clamp on that side. We came up with the

following solution: a 3 mm high by 12 mm long hole has been drilled in the corresponding crystal clamp. This hole has been made large enough in order to ease the passage of the beam, knowing that its position may significantly change during the alignment of the cavity and taking into account a possible translation of the crystal, in particular in the case of any damage occurring in it. The resulting oscillator cavity is shown in figure 12.5, with a representation of the beam paths. The output coupler used (OC in the picture) has a 20 % transmission efficiency. The curvature radius of the spherical mirror (Ms) is 5 m: for a cavity length of 200 mm, this implies a beam waist of 0.41 mm (if the cavity was linear, the waist would be located on the output coupler but here, it is a little bit ahead); we started with a cavity length of 228 mm, hence a beam waist w_0^{osc} of 0.44 mm. In the latest configuration of the oscillator, the cavity length has been shortened to 175 mm. The beam waist is then w_0^{osc} of 0.43 mm. As shown in figure 12.5, the pump laser injection in done through the output coupler, almost on the same track as the red pulsed light coming out of the oscillator. We thus need to separate the two beams. This is achieved by a pick-up Rmax820 mirror that sends the outgoing 820 nm pulsed laser toward the next stage, while the incoming pump laser goes integrally through it. The 532 nm pulsed beam is focused behind the Ti:Sa crystal, in order to have at most 5 J/cm^2 at its input surface (it is commonly admitted that above 10 J/cm^2, the crystal can be damaged).

The oscillator has been assembled on a separate plate that is attached to the table; this gives the flexibility to displace the oscillator easily without changing the alignment of the cavity. The mirror and coupler are mounted on a three-adjuster low-drift mirror mount from Thorlabs. The spherical mirror Ms has been stuck to a piezoelectric translator (PZT-4) that allows us to sweep the length of the cavity and which will be used for the control of the length of the oscillator cavity. The light leaking through the spherical mirror is detected by a photo-diode (PD-3). The crystal (Ti:Sa-2) holder is mounted on a translation stage and is pierced in order to implemented water cooling if needed. The incident angle on the prism (Pr) can be varied thanks to its rotating mount. Finally, the whole oscillator is enclose in a small box of Plexiglas to attenuate acoustical vibrations and dust deposition.

B. The pulsed pump laser

We bought a CFR400 pulsed YAG laser from Quantel, which is frequency doubled in order to emit light at 532 nm. The beam is vertically polarised when it exits the laser head. Its nominal energy is 230 mJ per pulse, each pulse being 7 ns wide, for a repetition rate of 10 Hz. This repetition rate is determined by the flash lamp used to pump the Nd:YAG crystal. A Q-switch system is used to control the light emission. The Q-switch (Q standing for *quality factor*) works as follows: a voltage controllable attenuator – the Q-switch – is inserted in the resonator cavity, preventing the light emitted from the crystal to be send back to the gain medium: these high losses block the light amplification and the energy is accumulated in the YAG crystal. When the attenuator is set at minimal losses, the gain is then high enough and a pulse is generated. Very high peak powers are reached by the process, as well as pulse widths of a few nanoseconds like in the case of the CFR400.

In order to decrease the output energy, it is possible to choose the delay between the flash lamp and the Q-switch, but this has the effect of increasing the pulse width and also degrading the transverse profile of the laser (the transverse profiles of a laser are described by Laguerre-Gauss modes [113]; the fundamental mode has a circular section and is designated as the TEM00 mode). We thus decided to avoid this solution. In order to get the 20 mJ pulse at 532 nm to pump the Ti:Sa crystal in the oscillator, we tested, in the pulsed beam, both the reflectance (and transmittance) of several mirrors available, as well as their capacity to stand at full power. We selected one mirror that reflected 20 mJ (and transmitted about 180 mJ that will be dedicated

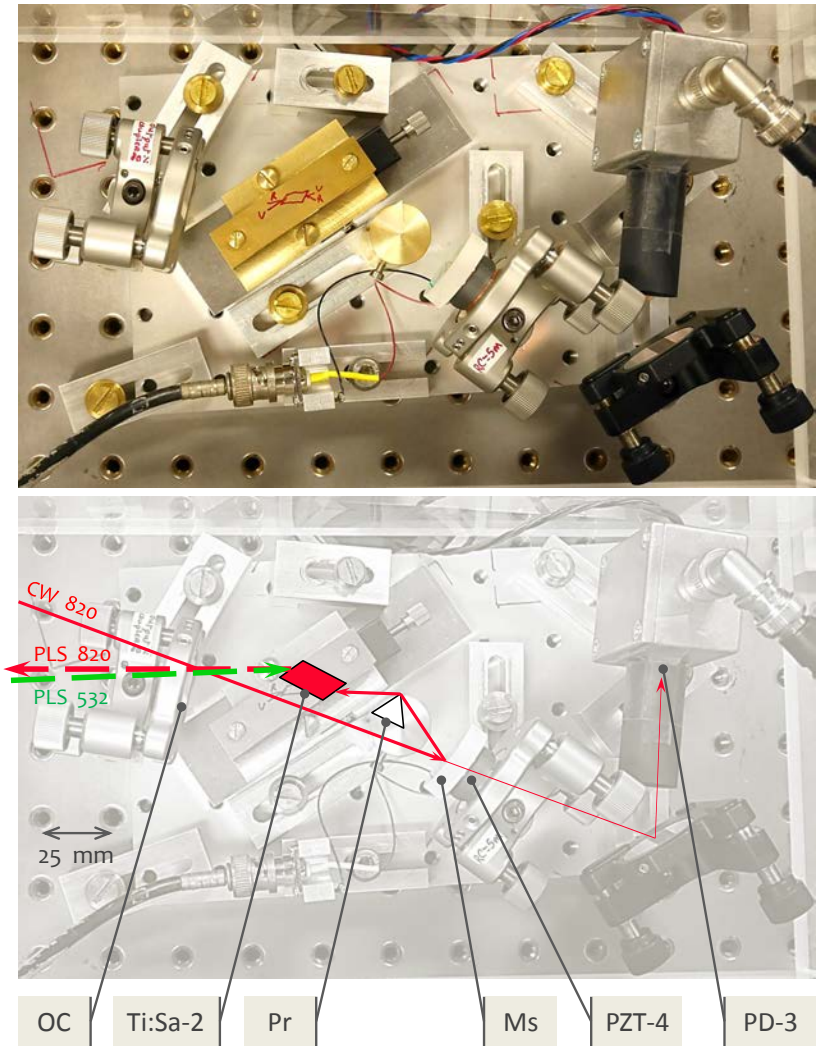


Figure 12.5: Up: picture of the oscillator cavity. Down: annotated picture identifying the elements of the oscillator and indicating the different beam paths.

to the amplification system described in section 12.2.3), and whose coating appeared to remain unaltered by the intense beam. This mirror, used as a beam splitter, is installed after an assembly of two R*max*-45° mirrors that permits both to turn the polarisation from vertical to horizontal and to change the height of the beam.

12.2.3 Amplification and frequency doubling

If the energy per pulse obtained at the exit of the oscillator is not enough either for CERN or CEA-Saclay set-ups, then an amplifying stage can be added. The 820 nm pulsed laser from the oscillator is sent through another Ti:Sa crystal (dimensions $15 \times 9 \times 5$); the supplementary amount of energy is supplied by the same pump laser as before. Indeed, we use the 180 mJ

that were not utilised for the pumping of the oscillator. This 180 mJ beam at 532 nm first has its polarisation turned by a half-wave plate ($\lambda/2$ plate) before passing through a variable beam-splitter cube that separates the vertical and the horizontal components of the polarisation. This gives two pulsed beams at 532 nm, of 80 mJ each. The beam polarised vertically is turned by $\pi/2$ by another $\lambda/2$ plate. With these two beams, the Ti:Sa crystal is pumped from both sides. In order to withstand the intensity of the pumping, the crystal is water cooled.

In order to optimally take advantage of the energy deposited in the Ti:Sa crystal, the 820 nm laser beams makes at least two passages in it, thanks to a "butterfly"-shaped path. In this multi-passage scheme, it is not possible for the laser to enter the Ti:Sa crystal at Brewster angle upon each passage. We thus tried to keep the incidence angles as small as possible, imposing long wings for this "butterfly". A general scheme and a picture of the amplifier are shown in figure 12.6. If necessary, the amplifier can be upgraded to four passages in the crystal; this, however, requires more space on the laser table.

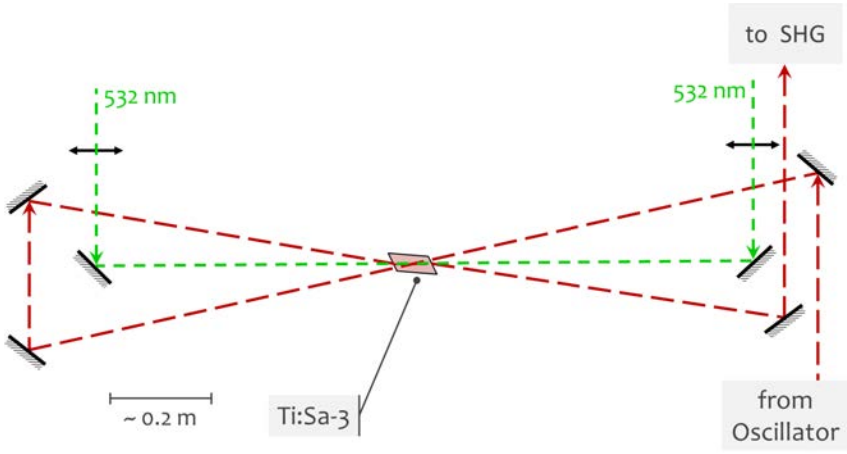


Figure 12.6: Schematic drawing of the light amplification stage; the scale indicated gives a general idea of space occupied by this amplifier on the laser table (the Ti:Sa crystal is not at scale).

Either directly after the oscillator or after amplification, the 820 nm pulsed laser is sent to the last part of the laser system: the second harmonic generation (SHG or frequency doubling) stage. The 410 nm pulsed beam is obtained by doubling the frequency of the 820 nm pulsed laser into a non-linear crystal, presently a crystal of lithium triborate (LBO). The SHG is a non-linear effect arising when a non-linear material is subjected to intense laser power densities. This can only be observed under certain condition, in particular the *phase matching*. This condition is fulfilled when the speed of the 410 nm wave in the SHG crystal is equal to the speed of the 820 nm wave. In our case, in the LBO crystal, the 410 nm wave has its polarisation perpendicular to the polarisation of the 820 nm wave; since a birefringent crystal like the LBO possesses different refractive indexes depending on the polarisation, there is a particular incident angle for which the condition is indeed met: it is the phase matching angle. Experimentally, we need to optimise the size of the crystal and finely tuned its orientation with respect to the incident laser beam (a precision better to 1° is required).

In order to choose the type of crystal, its size and predict its efficiency, we can use the SNLO software. If the frequency doubling efficiency is maximal, then, the energy of the 410 nm pulses is around half the energy of the 820 nm pulses. This means that, with a goal of 10 mJ pulses at 410 nm for instance, we have to obtain at least 20 mJ after the amplification. Another effect

of the SHG is a slight shortening of the pulses. Most of the time, there is still 820 nm light emerging from the LBO: it is removed by picking-up the 410 nm beam thanks to a Rmax mirror at 410 nm.

12.3 Alignment diagnostics, selective elements and controls

12.3.1 Alignment diagnostics

In order to check that the CW Ti:Sa laser is indeed mono-mode, an external Fabry-Perot interferometer (label FPe) has been used to observe the longitudinal modes of the CW Ti:Sa laser at the scope. This confocal cavity is enclosed in an aluminium cylinder, with a centred hole in each end-cap for the entry and exit of the light. The light sent to this Fabry-Perot is sampled from the beam exiting the CW Ti:Sa cavity; the intensity of the light coming out of the Fabry-Perot is monitored with a photo-diode (PD-2). Inside, two spherical mirrors of curvature radius equal to 100 mm, with a reflection coefficient of R=0.95, are fixed to the end-caps; in addition, one of the mirror is fixed to a piezoelectric translator (PZT-3) in order to modulate the cavity length. Between the two coated surfaces of the mirrors, the measured cavity length is 97.6 mm (in fact making the cavity not exactly confocal), which corresponds to a free spectral range $\Delta\lambda_{FPe}$ of 1.536 GHz. The finesse of this Fabry-Perot (defined as $\frac{\Delta\lambda_{FPe}}{\delta\lambda_{FPe}}$ where $\delta\lambda_{FPe}$ is the FWHM of the peaks of the Fabry-Perot) can be estimated from the reflection coefficient R of the mirrors by a simple formula (only valid when $1 - R << 1$):

$$\mathcal{F} \approx \frac{\pi\sqrt{R}}{1-R} = 61. \tag{12.9}$$

Optionally, the signal of FPe displayed at the oscilloscope was also used for a visual demonstration concerning the necessity of isolating the CW Ti:Sa laser from vibrations...

In a similar way, the modes in the oscillator cavity are visualised thanks to PD-2, when the signal coming from this photo-diode is triggered by the modulation sent to the piezoelectric translator of the spherical mirror. We thus observed that the longitudinal modes of the oscillator where accompanied by transverse modes, which can be easily discriminated, as it can be observed in figure 12.7.

12.3.2 Rotation direction and wavelength selection for the CW Ti:Sa laser

A. Rotation direction selection: the Faraday rotator

The pumped Ti:Sa crystal emits fluorescence light in every space direction and only a part is collected by the mirrors M1 and M2 to circulate in the ring cavity. Therefore, the light can propagate in the cavity in two directions: from the crystal to M1 to M6 (direction I in figure 12.2) or from the crystal toward M2 to M3 (direction II); consequently, a stationary wave is produced in the cavity, and it can also happen that the laser becomes highly unstable, constantly switching between one rotation direction to the other with a laser beam exiting the output coupler in two different directions.

To suppress this undesirable effect, we can force the light into a one-way circulation, thanks to the Faraday rotator, the idea being to cause considerable losses on each interface at Brewster angle, but only for the beam with the unwanted rotation direction, which is direction II. The Faraday rotator works in association with a passive element formed by the mirrors M5 and M4

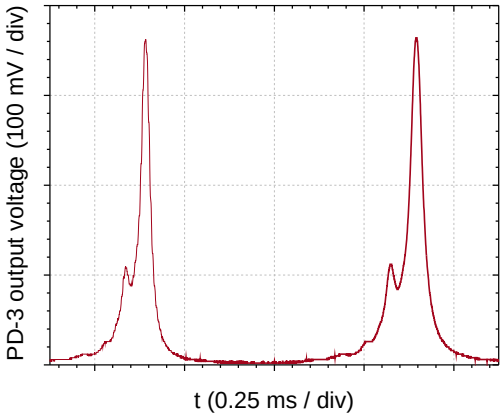


Figure 12.7: The cavity modes of the oscillator as observed at the scope; one can see the transverse modes on the left of the main peaks, the latter ones corresponding to the longitudinal modes TEM00; the first transverse mode is probably a TEM10, due to the non-perfect mode matching, either in size or curvature, of the incoming beam.

and the output coupler M6, which are tilted in order to send the light to M5, above the plane to which belong all the other mirrors. [114] Doing so, the polarisation of the fluorescence light is turned by a small angle θ_G that can be computed from geometrical considerations. In our case, $\theta_G = 4.5°$. Depending on the direction of the light propagation, the polarisation plane is turned by either $+\theta_G$ or $-\theta_G$.

The Faraday rotator itself, based on the Faraday effect, is made of a 4 mm thick terbium-doped borosilicate glass plate from HOYA (reference FR-5, $n = 1.69$), placed at Brewster angle in the beam and plunged in a normal magnetic field of 0.4 T. Under these conditions, the HOYA glass, becomes birefringent and turns the polarisation plane of the light independently from its propagation direction, by an angle equal to θ_F. θ_F is related to the strength of the magnetic field B by:

$$\theta_F = \mathcal{V}.d.B, \tag{12.10}$$

with d the distance travelled by the light in the Hova glass and $\mathcal{V}$ the Verdet constant of the HOYA glass: at room temperature and for $\lambda = 820$ nm, it is equal to -0.113 min.G^{-1}.cm^{-1} (value obtained from the formula given in [115]). This gives $\theta_F \approx -3.5°$. The HOYA glass and its magnet can be rotated to change d.

This thus approximatively compensates the $+\theta_G$ deviation in the desired propagation direction (I) while it results into a total $\theta_G + \theta_F$ polarisation rotation for the other propagation direction after one turn in the cavity. Since the polarisation now has a non-negligible vertical component, the latter will be mostly reflected when the beam encounters a surface at Brewster angle, thus inducing losses that will kill off propagation direction II. Because θ_G and θ_F do not exactly compensate, some losses are also to be expected in the desired propagation direction I, but with a lesser impact.

We note that, in order to avoid the instabilities mentioned earlier, it is further required that any reflective element in the cavity, in particular the thin etalon, shall not be placed in the beam at normal incidence. We also added an optical isolator on the beam path between the exit of the CW Ti:Sa and the oscillator to suppress any light that might be sent upstream and would perturb the functioning of the CW Ti:Sa laser.

B. Wavelength selection: the Lyot filter, internal Fabry-Perot, thin etalon and bi-plates

The total length of the CW Ti:Sa laser cavity is about 1.85 m. The interval between two consecutive longitudinal modes of the cavity is thus of the order of 160 MHz. In order to have a single mode laser, new constraints are added to progressively select the wavelength allowed to propagate in the cavity. One of the main idea to achieve this goal is to insert smaller cavities/interferometers in the cavity, which are the following:

- The Lyot filter is a passband filter made of birefringent quartz plates, each of these plates having twice the thickness of the previous one. The optic axis of each birefringent plate are parallel to their surfaces (and parallel from one plate to another) and makes a 45° angle with the polarisation of the light circulating inside the cavity. Due to the different refractive indices in the ordinary and extraordinary directions of the birefringent plate, each corresponding component of the linear polarisation of the incident beam experiences a different phase delay: therefore, the polarisation at the exit of the plate has either turned or become circular, and losses are induced by the polarisation selection in the cavity. However, the relative phase delay also depends on both the thickness of the plate and the wavelength. If the optical path difference between the two polarisation components appears to be a multiple of the wavelength, then the polarisation of the incident light is unchanged and the light proceed to the next birefringent plate without any losses. Since all the plates have a thickness which is a multiple of the smallest one, this transmission without losses will appear for several common wavelengths. The thickest plate will set the width of the transmission peaks while the thinnest plate (410 μm) sets the free spectral range; the other plates allows to narrow the transmission filter function. This is explained and illustrated in [116, p. 312 to 314]. In practice, the Lyot filter intercepts the light beam at Brewster angle, and is mounted on a motorised rotating frame. Rotating the filter allows to select the peak transmission wavelengths. The typical width of the Lyot bands is 0.05 nm, while the free spectral range can be of the order of 100 nm.

- A thin etalon of fused silica (thickness 0.7 mm, $n = 1.45$ at 820 nm) is added, and used as a very low finesse Fabry-Perot interferometer to modulate the spectrum. The frequency of this modulation is the free spectral range of the thin etalon interferometer, 147 GHz; in order to tune the modulation, the angle of the plate can be tuned thanks to an electric motor, thus varying the apparent length of this Fabry-Perot. With the exception of the mirrors, this is the only optical element which is not inserted in the beam at Brewster angle, but needs to be close to normal incidence for interferences to build up.

- The thick internal Fabry-Perot interferometer is made of two right prisms in silica, with a summit angle of 34°, which adjacent sides placed in regard are coated to offer a 30 % reflection efficiency at 820 nm. The gap between these two parallel mirrors is 8 mm, which corresponds to an interval between orders of 18.7 GHz. Each prism can be independently orientated for the alignment; before placing the interferometer in the CW Ti:Sa cavity, a first alignment is performed outside the laser with an auxiliary HeNe laser. One of the prism of the internal Fabry-Perot is mounted on a piezoelectric translator (PZT-2) thus allowing to establish a control loop, described below.

- Finally, a continuous scan of the laser wavelength is obtained by the bi-plates, which

are used to smoothly change the total length of the laser cavity without perturbing the alignment of all its other elements. The symmetrical rotation of the plate is driven by another electric motor.

The wavelength selection is thus obtained as follow: thanks to the Lyot filter, a short range of wavelength (about 0.05 nm) is selected among all the possible wavelengths emitted by the Ti:Sa crystal, which are already restrained by the maximum reflectivity range of the mirrors in the cavity. The internal Fabry-Perot then selects the modes that comply with its mode spacing requirement (multiples of 19 GHz approximately). The intensity of these selected modes is modulated by the thin etalon: the mode matching the maximum of the thin etalon transmission is the one that will be the least attenuated in the cavity. This leads to the selection of one fringe of the internal Fabry-Perot, with a width of about 8 GHz. The number of the CW laser cavity modes, separated by 160 MHz, is now restrained to this bandwidth. But, actually, the internal Fabry-Perot works itself like the thin etalon: the laser cavity mode that corresponds to the maximum of the Fabry-Perot peak is the least attenuated and will therefore be the final mode of the laser. To scan the frequency of the laser, the position of mirror M4 is scanned with PZT-1 (see figure 12.2); a larger excursion can be done with a rotation of the bi-plates system (about 200 GHz).

12.3.3 Servo loop

A. Description

The monomode running of the CW Ti:Sa laser is ensured with a control loop of the internal Fabry-Perot. The thickness of this air-interferometer is swept at 10 kHz (in that case, the reference output of a lock-in amplifier) thanks to the piezoelectric translator PZT-2 aforementioned. The resulting modulated intensity of the laser is recorded by photodiode PD-1, whose signal is sent to the lock-in amplifier. The resulting error signal is amplified and sent back to the PZT-2, thus dynamically compensating for any low frequency drift of this Fabry-Perot. The internal Fabry-Perot is therefore servo-looped on a fringe of the CW Ti:Sa ring cavity. The frequency of the CW laser is stabilised with PZT-1.

The same principle is applied to the oscillator: like for the simple mode observation described earlier, the piezoelectric translator, PZT-4, positioned at the back of Ms is used to modulate the length of the oscillator cavity, but this time, the signal from PD-3 is sent to another lock-in amplifier and the error signal is amplified and sent back to the PZT-4. This is used to keep the oscillator cavity resonant with the CW laser frequency. The servo-control of the oscillator has not achieved the same stability as the one ot the CW Ti:Sa because of the housing of this pulsed laser.

The servo control of the Ti:Sa laser can be further refined, as it is described in [117] for instance. In particular, when we will implement the experiment with the caesium (see chapter 13), it will be possible to lock the frequency of the laser on the fluorescence signal from the caesium to remain constantly at resonance. Later, this will be used as a frequency standard to calibrate the wavelength-meter that can be included in the control loop. This would allow us to lock the laser on the frequency of the 1S-3D transition in positronium.

B. Functioning principle of a lock-in amplifier

The usual application of lock-in amplifiers concerns the extraction of a small signal (with pulsation ω_S, amplitude A_S) from a noise background. The signal to be analysed, once sent to the lock-in amplifier, is multiplied by a wave carrier of pulsation ω_R, which is the reference (usually

internal but possibly external) of the lock-in amplifier. The resulting signal is then integrated over a period that has to be longer than the ones of reference or the signal of interest; due to the orthogonality properties of sinusoidal functions, the integrated quantity is non-zero only if ω_R is equal to ω_S and is maximum if the phase difference between the two of them is null; to comply with this conditions, ω_R is set equal to ω_S and the phase of the reference is tuned. The lock-in amplifier thus provides a DC signal that is directly proportional to the amplitude A_S of the signal of interest; other components with frequency different from ω_S are filtered.

In the particular application of stabilising a laser frequency, ω_S is imposed by modulating the length of the laser cavity. For instance, in the case of the CW Ti:Sa laser, the voltage (V) applied on PZT-2 is modulated at 10 kHz. This small modulation on V, that can be writen $\delta V \cos(\omega_S t)$, is a modulation of the internal Fabry-Perot length, i. e. a modulation of the frequency f_{FP} of its fringe. This results into a small modulation of the CW laser frequency f_{CW} – seen in the laser intensity $I(V)$ – which gets smaller and smaller as the modulation is made close to the maximum of a peak of the internal Fabry-Perot (the duty point). This is illustrated in figure 12.8.

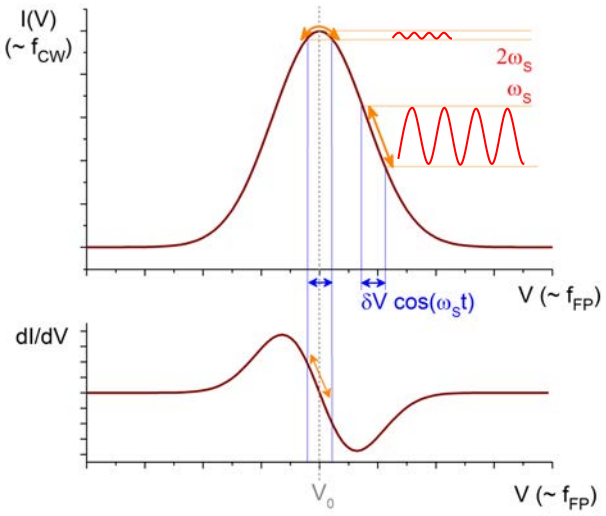


Figure 12.8: Illustration of the intensity modulation depending on the small voltage modulation applied on a piezoelectric translator.

Since the modulation is small with respect to the laser intensity, we can make a Taylor expansion of I:

$$I(V + \delta V \cos(\omega_S t)) \simeq I(V) + \delta V \cos(\omega_S t) \frac{dI}{dV}.$$

Now sending this modulated signal to the lock-in amplifier and tuning the phase of the reference signal, we deduce that the output signal will be proportional to the first order derivative of the laser intensity, $\frac{dI}{dV}$. Therefore, in the central part of the signal, there is a linear dependency between the frequency of the CW laser and the frequency of the internal Fabry-Perot fringe, as it is also illustrated in figure 12.8. This produces an *error* signal that is amplified and fed-back to PZT-2. Each time a perturbation induces a variation of the laser intensity, the error signal fed-back to PZT-2 will modify V and bring the Fabry-Perot back to the duty point. Therefore, the internal Fabry-Perot is *locked* on the maximum of a fringe of the CW Ti:Sa laser cavity.

12.4 Characterisation of the laser beam

12.4.1 Wavelength measurement

To measure the wavelength of the CW Ti:Sa laser to a precision up to a few tens of MHz, we used a commercial lambda-metre from HighFinesse, model WS-7 (10 MHz resolution, 60 MHz accuracy). This lambda-metre is able to determine the wavelength of both continuous and pulsed lasers. It works by comparing the interference patterns made by a solid-state Fizeau interferometer, the pattern being imaged by a CCD photo-diode array, to the recorded pattern used for the calibration. Another WS-7 lambda-meter which includes an option to use it in the control loop of the Ti:Sa laser has been bought.

The light is sent to the wavelength meter via an optical fibre. Only a few microwatts or microjoules are required for the measurement. For the wavelength measurement of the CW Ti:Sa laser, the light is sampled from the beam going to the external Fabry-Perot cavity; in the case on the pulsed Ti:Sa laser, we consider, as a first approximation, that the wavelength is the same as the CW seed laser. We will see that it is not exactly the case in section 12.4.3. Figure 12.9 gives an example of the wavelength stability obtained for the CW Ti:Sa at 822.469 nm (364.503 THz), locked on the Cs two-photon transition (reference standard at 364.503080 THz), for 12 min.

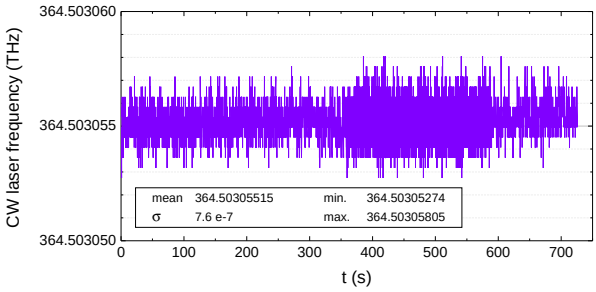


Figure 12.9: Wavelength of the CW Ti:Sa recorded for 12 min; here, as in all the following figures, the statistical values are given in THz.

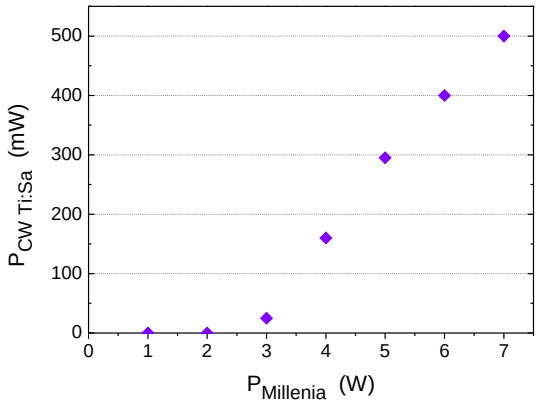
12.4.2 Power, energy and pulse length

A. Output power of the CW Ti:Sa laser

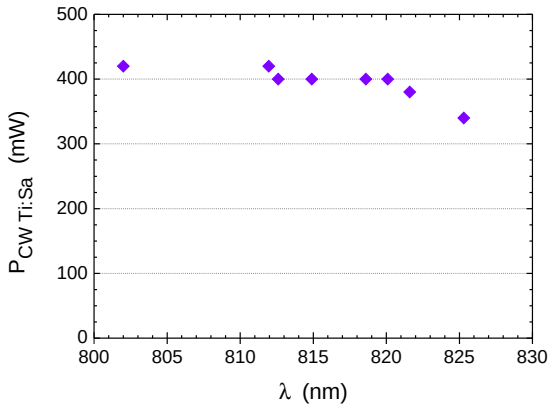
After optimal alignment of the CW Ti:Sa laser, we measured, at a fixed wavelength around 800 nm (the lambdameter was not used at that time), its output power as a function of the pump power chosen from the Millennia. The corresponding graphics is displayed in figure 12.10a (the laser threshold is observed at 2.6 W pump power). We usually run at 6 W pump power for the CW Ti:Sa laser; once the laser wavelength set at 820 nm, we had about 400 mW output power, measured after an optical isolator placed between the CW Ti:Sa and the oscillator. This can be seen in figure 12.10b, where we give the output power of the CW Ti:Sa pumped at 6 W when the wavelength of the laser is scanned between 800 and 830 nm. In that range, we observe that the output power is quite stable.

B. Energies of the pulsed lasers

The measured output energy of the CFR400 was 236 mJ instead of the 232 mJ given in the specification sheet. In order to measure the average pulsed energy, as the repetition rate of the



(a) Output power of the CW Ti:Sa laser at about 800 nm versus the 532 nm pump power of the Millennia.



(b) Output power of the CW Ti:Sa laser when its wavelength is varied around 820 nm.

CFR400 is fixed and known, we used a power-metre whose sensitivity (in V/W) is known. With the same power-metre, we also measured the energies after splitting the beam into one pump beam for the oscillator and two pump beams for the amplifier. For usual running conditions, we thus measured 21 mJ pump energy for the Ti:Sa-2 crystal (assuming the output coupler OC does not absorb at 532 nm) and two times 80 mJ dedicated to the pumping of the crystal in the amplifier.

The measurement of the smaller output energy of the oscillator and of the amplifier could be done using a more precise Joule-meter. For the usual 21 mJ pumping energy used in the oscillator, and without the amplifier, we are able to produce pulses of 4 mJ energy at 820 nm, with a 9 ns FWHM duration, as it will be shown in the next paragraph. This means that, according to the simulation results, we have already met the laser pulse width and energy requirements for the positronium excitation at CERN.

The measurement of the SHG efficiency has yet to be done, once the LBO crystal is installed on the laser table.

B. Pulse length at 820 nm

The length of the red light pulses coming out of the oscillator has been measured using a fast photo-diode. The fast photo-diode (from Thorlabs) has a 0.8 mm^2 biased silicon detector which exhibits a rise time of 1 ns. According the specification sheet, this fast photodiode has a maximum responsivity (measured anode current per light power in A/W) around 730 nm; its responsivities at 410, 532 and 820 nm are respectively about 0.10, 0.25 and 0.40 A/W. The anode current is converted into a voltage signal using an internal resistance from the oscilloscope that records the pulses.

We made a primary measurement of the pulse length when the oscillator cavity was 228 mm long, shown in figure 12.10; the signal intensity is given in Volt, although no conversion from Volt to mJ can be made, even knowing the photo-diode responsivity, because a diffusive material has been used in front of the silicon detector to avoid its saturation. The recorded signal exhibited two peaks, labelled 1 and 2. Peak 1 is the actual laser pulse, with a FWHM found to be 18 ns, thus meeting the recommendations drawn from the simulation. Peak 2 corresponds to a 532 nm pulse from the CFR400, not efficiently screened.

It was then decided to reduce the length of the oscillator cavity, in order to try reaching pulses of 10 ns (still following the simulation recommendations for the CERN experiment, in

particular if a two pulse excitation has to be applied). Getting the output coupler and mirror Ms closer to the crystal and the prism, we obtained a cavity length of 175 mm and we were able to record laser pulses as short as 9 ns FWHM at 820 nm, as shown in figure 12.11.

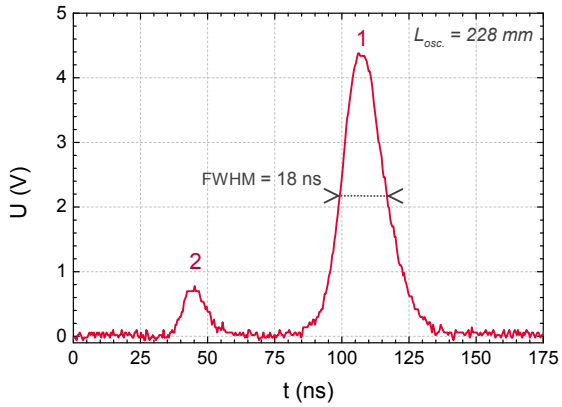


Figure 12.10: First laser pulse recorded at 820 nm, with a FWHM of 18 ns.

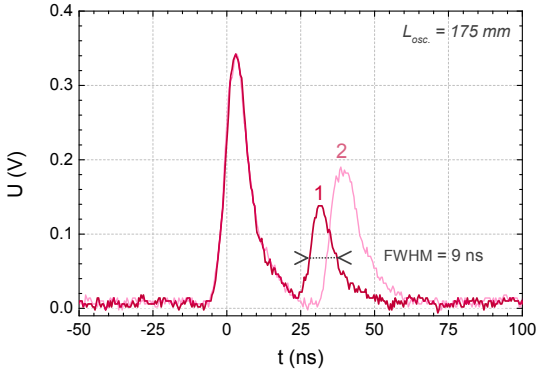


Figure 12.11: A 9 ns pulse at 820 nm (label 1) and a pulse obtained when there is no CW laser beam to seed the oscillator cavity (label 2): in the latter case, the stimulated emission is further delayed with respect to the 532 nm pump pulse (first pulse on the left).

12.4.3 Chirp

Despite the use of the CW Ti:Sa laser to seed the oscillator, the frequency of the pulsed laser can still be shifted with respect to the frequency of the CW laser. This effect is called *frequency chirp*, a frequency modulation that is inherent to pulsed lasers. Indeed, while pumping the Ti:Sa crystal with a pulse at 532 nm, its refractive index varies with time. The consequence is that, when the laser power builds up in the cavity, the latter is "not resonant" with the CW laser any more. The resulting shift in the output frequency is expected to be of the order of 100 MHz, which is in fact larger than the second-order Doppler shift estimated for the positronium. Further details on the origin of the chirp and a possible compensation of the effect are given for instance by Eikema *et al.* [118]; in the case of the 1S-2S two-photon transition in positronium, see for example Danzmann *et al.* [119].

We need to know the chirp of the pulsed laser at 820 nm in order, either to take it into account for future measurements on the positronium or to compensate its mean effect. The WS-7 lambda-meter mentioned earlier is able to record the frequency of a pulsed laser.

In order to measure this chirp effect, we first verified the accuracy of the WS-7 lambda-meter, using a well-know atomic transition close to 820 nm: the 6S-8S two-photon transition in atomic caesium (Cs). The measured frequency for this transition is 364.5030803(1) THz [120].

Only the CW Ti:Sa laser is used for this verification. The main CW laser beam is sent to an enhancement cavity (a linear Fabry-Perot of 280 mm length), where a caesium cell (150 mm long, 20 mm diameter, windows at Brewster angle) has been placed. The enhancement cavity is kept resonant with the CW Ti:Sa laser using a piezoelectric translator (noted PZT-5) and a lock-in amplifier: when the frequency of the CW laser is swept, the feedback on PZT-5 allows to change the length of the enhancement cavity to maintain the resonant conditions.

During the frequency sweeping, the frequency of the CW Ti:Sa laser becomes resonant with the 6S-8S two-photon transition in Cs: this is observed thanks to the resulting fluorescence of the caesium atom at 456 nm (see figure 13.1 in chapter 13 for the energy diagram), which is detected by a photomultiplier (PM, IP28 from RCA) placed above the Cs cell. If necessary, by modulating the voltage on PZT-1 (mirror M4 of the CW laser cavity) and using another lock-in amplifier, one can lock the CW Ti:Sa laser on the 6S-8S resonance of caesium by sending the error signal, obtained from the fluorescence signal, back to PZT-1. This is what has been done for the wavelength stability measurement presented in figure 12.9, and we use these results to give the laser frequency measured by the WS-7 lambda-metre:

- the frequency of the CW Ti:Sa laser locked on the two-photon transition is 364.5030551(8) THz when measured with the WS-7;
- we remind that the measured frequency of the transition is 364.5030803(1) THz [120].

This 35 MHz discrepancy should not be surprising since the lambda-metre is based on an optical interferometer which is sensible, for instance, to temperature variations, noise, etc. Also, the sensitivity announced by the constructor is 10 MHz with a guaranteed accuracy of 60 MHz. The value given by the WS-7 is thus compatible with the measured 6S-8S transition in caesium. However, this can prove insufficient when we will be searching for the 1S-3D transition in positronium. Therefore, we will frequently use the Cs 6S-8S transition to check the indication given by the lambda-metre. Since the 6S-8S two-photon transition in Cs happens to be close enough to the 1S-3D transition in Ps, it will be sufficient to apply an off-set correction to the measurements obtained with positronium.

The frequency of the 6S-8S transition in caesium is close to the one of the Ps 1S-3D transition, but is still different. During an experiment with positronium, we cannot lock the CW Ti:Sa laser on the Cs 6S-8S transition any more. Instead, we will use the WS-7 lambda-metre to make the control loop: it can provide a frequency reference, to which we have to add the off-set regularly measured.

We can now measure the chirp itself. The CW Ti:Sa frequency is locked on the lambda-metre: the WS-7 gives the error signal between the reference frequency set by the user on the lambda-metre and the frequency of the CW laser; this error signal is fed-back to PZT-1 to correct the frequency of the CW Ti:Sa laser, which seeds the Ti:Sa oscillator. The pulsed pump laser is turned on, and low intensity pulsed beam is sampled from the pulsed beam coming out of the oscillator. This low energy beam is sent in a 1.3 μm monomode fibre connected to a second WS-7 lambda-metre. Simultaneously, another low intensity beam is sampled from the CW Ti:Sa laser and injected in another monomode optical fibre. By alternating the fibres connected to the second WS-7, we can successively measure the frequency of either the pulsed laser or the CW laser.

The chirp has been measured at a frequency close to the 6S-8S two-photon transition frequency in caesium; figures 12.12 to 12.15 show the different measurements taken to deduce the frequency chirp. In figure 12.12, we display the frequency of the CW Ti:Sa laser recorded by the first WS-7 lambda-metre. We observe that this frequency, measured to be 364.615410(1) THz, is highly stable: this is due to the fact that the laser is locked on this lambda-metre.

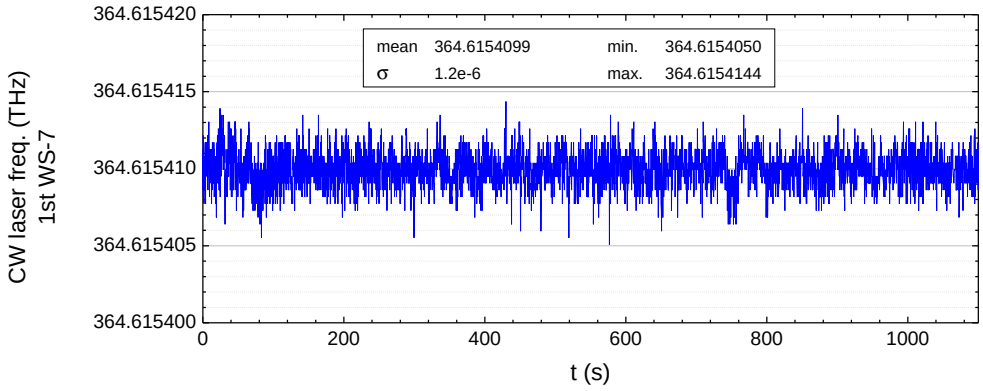


Figure 12.12: Measurement, with the first WS-7, of the frequency of the CW Ti:Sa laser locked on the very same lambda-metre.

Figure 12.13 shows again the frequency of the CW Ti:Sa laser, which is kept locked on the first WS-7, but this time measured by the second WS-7 lambda-metre. The mean value is 364.615455 THz, with a standard deviation of 3 MHz. We observe that the frequency is less stable than what is indicated by the first lambda-metre, and also that it is shifted by 45 MHz compared to the previous value. We already noticed a similar shift when we measured the frequency of the 6S-8S transition in caesium and compared it with the published value, but, as it was then concluded, the effect remains compatible with the 60 MHz accuracy announced by the constructor.

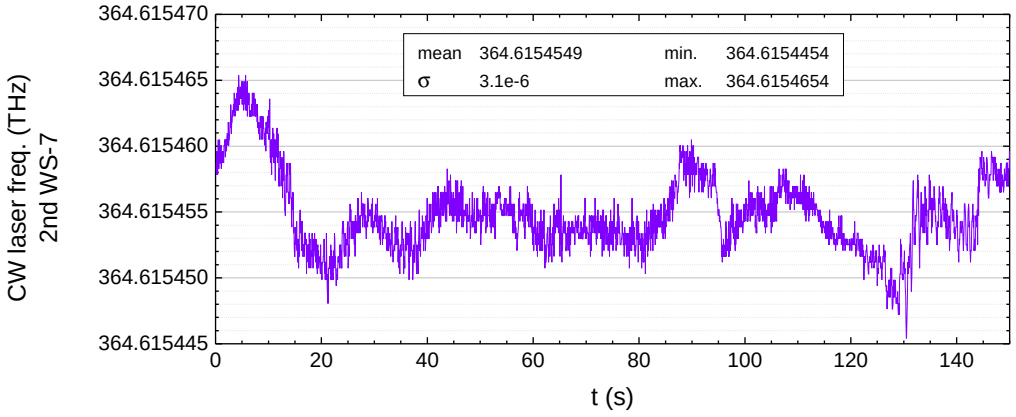


Figure 12.13: Frequency measurement, with the second WS-7, of the CW Ti:Sa laser locked on the first lambda-metre.

In figure 12.14, the second WS-7 lambda-metre gives the frequency of the pulsed Ti:Sa laser recorded during, roughly, 6 min. For the measurement with the pulsed laser, whose repetition rate is 10 Hz, the lambda-metre was set to acquire data every 465 ms (exposure time), which means that each data point is the average frequency of four to five pulses. Over the run presented in figure 12.14, the mean frequency of the pulsed laser was 364.615533(9) THz.

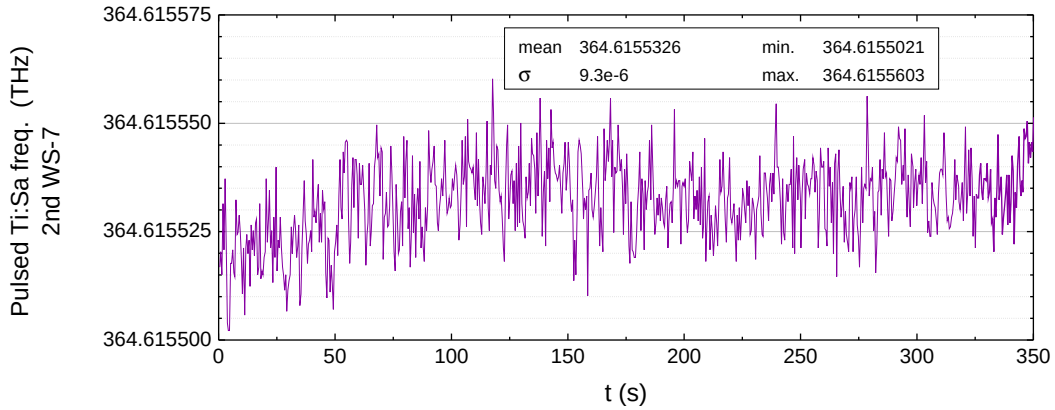


Figure 12.14: Measurement, with the second WS-7, of the frequency of the pulsed Ti:Sa laser which is locked on the CW Ti:Sa laser.

Figure 12.15 has been obtain by changing the optical fibre connected to the second lambda-metre while acquiring data: we started with the fibre guiding the pulsed light and then switched to the fibre with the CW laser light (simultaneously, the lambda-metre is switched from pulsed to continuous mode). This gives a clear visualisation of the frequency chirp. Using the data presented in figures 12.13 and 12.14, we deduce that the mean value of the frequency chirp is 78(12) MHz, in agreement with the order of magnitude expected.

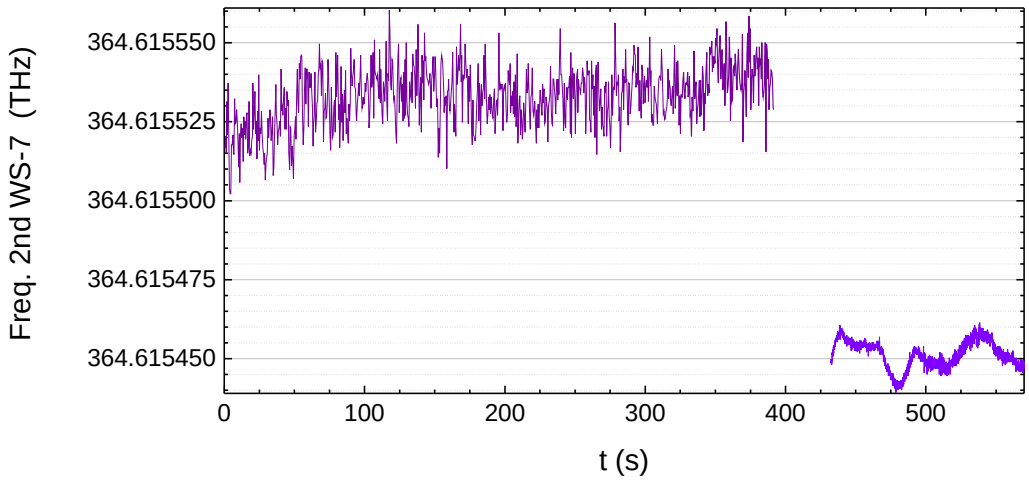


Figure 12.15: Visualisation of the frequency chirp between the pulsed Ti:Sa laser (first measured, on the left) and the CW Ti:Sa laser (second to be measured, on the right).

Chapter 13

Preparation of the positronium spectroscopy experiment at CEA

13.1 The Saclay set-up simulated with a caesium cell

In the simulation part, when we discussed the use of the fluorescence light from the Ps($3d$) de-excitation, we raised some concerns on the possibility to actually efficiently detect this fluorescence light. In order to address this question, we decided to conceive a test experiment at LKB using the two-photon transition (6S-8S) in caesium already introduced for the chirp measurement (12.4.3).

13.1.1 Atomic caesium

For the chirp measurement, we used the caesium as a frequency standard at 822 nm in order to control the wavelength of the CW Ti:Sa laser and calibrate the wavelength-meter. The transition was done using the CW laser beam and happened in a Fabry-Perot cavity in order to excite the two-photon transition. For the test, in order to approach the experimental conditions of the positronium spectroscopy at Saclay, we consider that the excitation is done with the pulsed laser and that no cavity is used.

The advantage of the 6S-8S transition in caesium is that the frequency is well known and we can easily search for the transition. The fluorescence signal obtained with the pulsed Ti:Sa laser can be compared to the one obtained with the CW laser. The energy level diagram of caesium, for the transitions of interest, is given in figure 13.1. Also, the density of caesium in a cell can be controlled with the temperature of the tip of the cell: this allow us to simulate the positronium density in the Saclay experiment.

This leads to the estimation of the caesium density in a caesium cell. In the best scenario at CEA-Saclay, we considered that 10^8 positrons could be ejected from the positron trap after accumulation. Then, if the positronium is formed in some kind of tube confining it in a 4 mm^2 by 10 mm volume, the maximum positronium density would be 8.7 10^{14} m^{-3}. However, if we cannot work with this tube geometry and have the positronium atoms freely diffusing into vacuum, then we would have to deal with lower Ps density. The density of caesium atoms in the cell that are in a gaseous state is determined by the saturated vapour pressure, which only depends on the temperature. Usually, in order to get a bright fluorescence, the caesium is heated at 80 to 90 °C; this corresponds to a saturated vapour pressure of about 2.7 10^{-2} Pa [121], and thus a Cs density of 5.5 10^{18} m^{-3}. In order to mimic the low positronium density that will be available

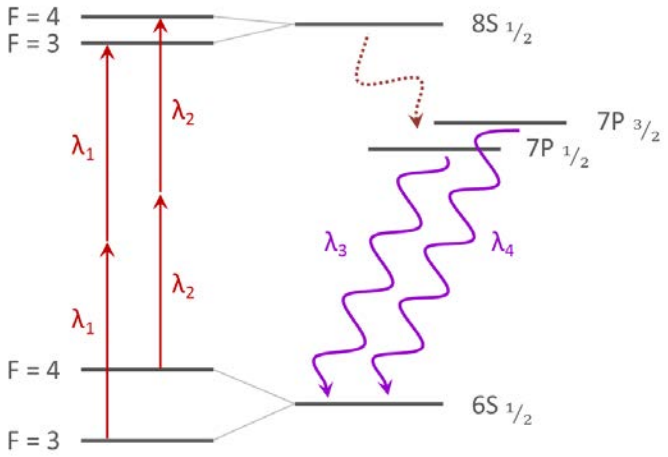


Figure 13.1: Optical transition between the 6S and 8S levels of caesium. We remind that F is the total angular momentum including the nuclear spin. The values of the different wavelengths indicated are: $\lambda_1 = 822.459$ nm, $\lambda_2 = 822.468$ nm (both frequencies measured at a 0.1 MHz precision by Hagel *et al.* [120]), $\lambda_3 = 459.3$ nm and $\lambda_4 = 455.5$ nm. The 6S-8S two-photon transition that we use is for F = 4, at 822.468 nm (364.508030 THz) and we detect the fluorescence at 456 nm.

at CEA, we should lower the caesium density as much as possible, which is done by lowering the temperature of the tip of the Cs cell. At room temperature, the saturated vapour pressure is 9.3 10^{-5} Pa, giving a Cs density of 2.3 10^{16} m^{-3}. We can consider further decreasing the cell temperature (to 0 °C, for instance, or even lower if using a Peletier cooling element; at 0 °C, the Cs density is about 3.5 10^{15} m^{-3}, hence four times the maximum Ps density). From the data obtained at different temperatures, that is different Cs densities, we could extrapolate to the case of the positronium excitation at Saclay.

13.1.2 Description of the future set-up at LKB

The set-up for this experiment mainly re-employs the elements described earlier when the measurement of the frequency chirp has been presented: the Brewster caesium cell, the fluorescence detection system and, just at the beginning, the 280 mm Fabry-Perot cavity. However, a few additions have to be made: a special Cs cell has been designed and realised, and the detection system will make use of a bundle of optical fibres. We present these new elements in the following.

In the prospect of the positronium spectroscopy experiment at Saclay, we had to think about a new fluorescence detection system that can accommodate with the physical constraints of the positronium chamber designed at CEA. This positronium chamber is 200 mm in diameter for 100 mm in length, with eight flanges (four CF40 and four CF63) providing access into it. The positrons arrive on the axis of this chamber at the centre of which the positronium converter is placed. The converter is secured by a sample holder fixed at the bottom of the chamber, above the bottom flange that is dedicated to the feedthroughs; a sample manipulator inserts or removes the converter samples from the upper CF63 flange. Two horizontal CF63 flanges have been assigned to the excitation laser access. Two of the diagonal smaller flanges are used for the charge measurement and imaging of the positron pulse: on one side is a retractable microchannel

plate detector (MCP, acting similarly to a photomultiplier by multiplying charges in cascade) with a phosphor screen just behind and a mirror that sends the image of the phosphor screen to a camera placed outside the opposite flange. This leaves two possible CF40 flanges for the detection of the fluorescence light of the positronium.

From the description, we understand that the space available around the positronium converter is very limited (see figure 13.2) and, therefore, it will not be possible to place a collector lens or mirror (and the photomultiplier all the more) close to the positronium cloud, when the faint fluorescence signal expected requires otherwise. In addition of the bulk problem, all the materials used for the detection system must be compatible with the ultra-high vacuum (10^{-9} mbar) in the chamber. We have thus envisaged a light collection system based on optical fibres.

By using a bundle of optical fibres, we could collect the fluorescence light just a few millimetres away from the positronium cloud, and send it through a window mounted on one of the CF40 flange: the last part of the optical detection (condensers, filter and photomultiplier previously mentioned for the chirp measurement) would then be outside of the vacuum chamber. The downside of using optical fibres is that, generally, the coating of the fibres is not compatible with ultra-high vacuum: we should then probably work with bare fibres, which are much more fragile. The fibre holder and the connection at the exit window are still to be designed for the Saclay experiment.

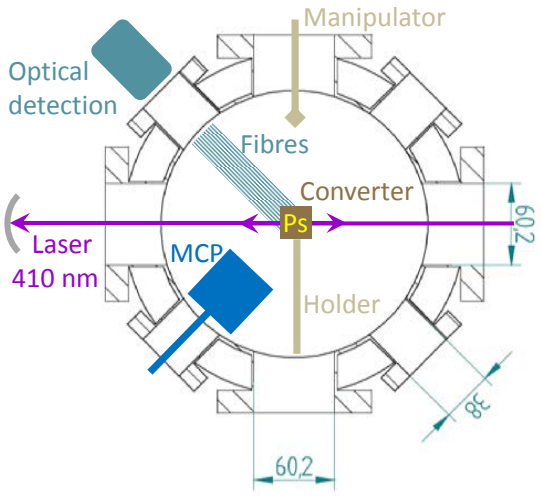


Figure 13.2: A simple drawing of the positronium chamber designed for the Saclay experiment; in the chosen point of view, the positron trap is situated behind.

To investigate the efficiency of such a light collection system with the caesium cell at LKB, about 200 optical fibres of 180 mm length have been cut: assembled together, they form a 3 by 40 mm bundle that fills the three fourth of the pre-existing detection window. For this experiment at LKB, the fibres keep their Tefzel coating. The multi-mode fibres chosen have a numerical aperture (NA) of 0.48; $NA = \sqrt{n_{core}^2 - n_{clad}^2}$, where n_{core} is the refractive index of the fibre core, pure silica, and n_{clad} is the refractive index of the cladding. The maximum acceptance angle θ_{max} is defined as $NA = n.sin\theta_{max}$; for $n = 1$ and $NA = 0.48$, $\theta_{max} = 28.7°$. The diameter of the core is 0.40 mm while the total diameter of the fibre with the cladding and Tefzel buffer is 0.73 mm; the long term minimum bend radius is 130 mm. Working with bigger

fibres, for instance with a 1 mm diameter core, would greatly diminish the number of fibres needed to cover the largest solid angle possible; however, in that case, their long term minimum bend radius is about 300 mm, a condition that will probably not be achievable in the 200 mm diameter vacuum chamber.

The caesium cell previously used for the chirp measurement is 20 mm in diameter, which means that the fluorescing region of the gas is almost 10 mm away from the light collection optics. Since the available space around the positronium converter forces us to get the optical fibres as close as possible to the Ps cloud in order to cover the largest solid angle, we designed a new Cs cell accordingly. This new cell is made of three different segments: the segments at the extremities have a 20 mm diameter (decreasing to 4 mm toward the middle of the cell) and are 39 and 41 mm long, while the middle segment is a 4 mm diameter tube, of inner diameter 2.4 mm, and is 41 mm long. This narrow tube thus simulates a gas lit by a 2 mm diameter laser beam, like we intend to do at Saclay, and allows to approach the optical fibres at about 1 mm from the fluorescing region. Due to technical constraints foreseen by the LKB glass-blower, this cell does not have windows welded at Brewster angle but rather shaped with a right angle; these windows needs to have a constant thickness (1 mm here), at least on the area hit by the laser beam, in order to avoid lensing effect. A picture of this new caesium cell is displayed in figure 13.3.

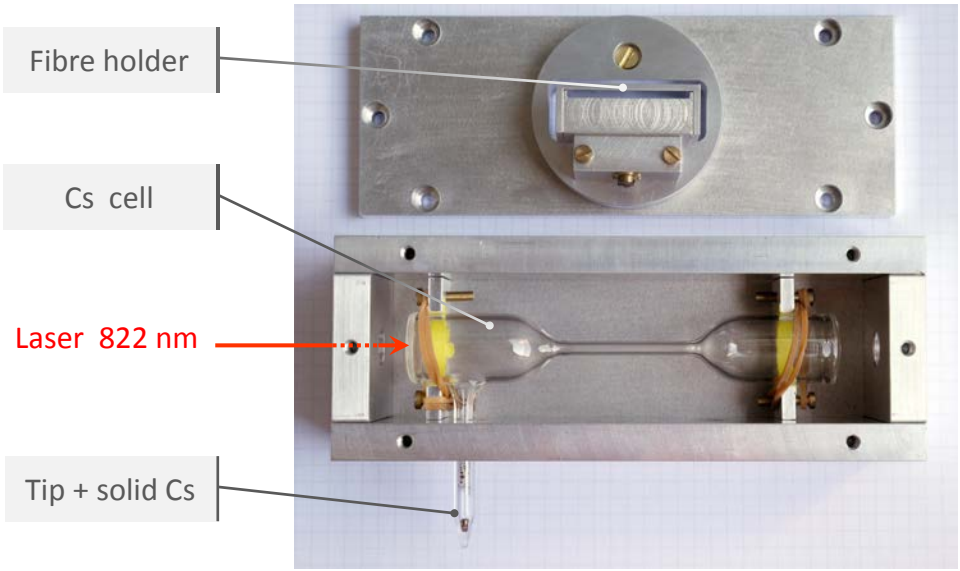


Figure 13.3: The specially realised caesium cell with its narrow section of 4 mm diameter.

We remind that the aim of the experiment, which will be realised at the end of year 2014, is to estimate the feasibility of using optical fibres to detect the fluorescence signal from a thin positronium cloud excited with a single laser shot. The set-up shares similarities with the one used for the frequency chirp measurement. The CW Ti:Sa laser is locked on one of the WS-7 lambda-metre and a correcting off-set is applied to be resonant with the 6S-8S transition. In

particular, the off-set takes into account the mean frequency chirp. The Ti:Sa oscillator is locked on the CW Ti:Sa laser and the pulsed laser is sent to the Cs cell; the intensity of the fluorescence is recorded at the scope. The set-up is graphically summarised in figure 13.4.

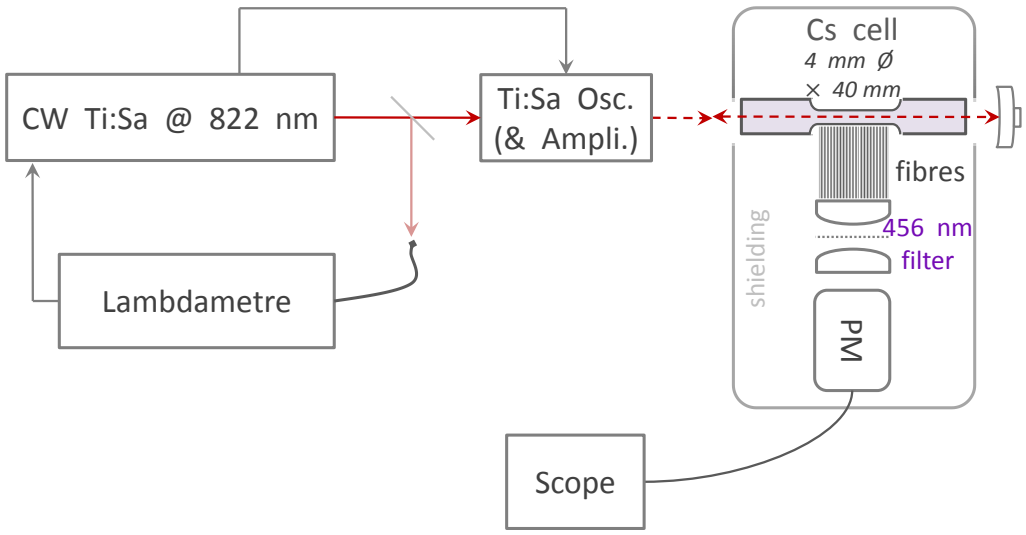


Figure 13.4: A schematic representation of the set-up used to estimate the efficiency of a bundle of optical fibres for the fluorescence light collection; the use of the lambdameter is indicated for the monitoring of the laser excitation frequency.

In figure 13.5, we present the intensity of the Cs fluorescence signal detected by the IP28 photomultiplier when the voltage applied on the dynodes is 500 V; the caesium cell is the one used for the chirp measurement and is at room temperature. This is for the CW laser, whose frequency is scanned to search for the transition. We observe that we already reached about 300 mV intensity for the fluorescence signal (corresponding to an anode current of 14 μA), which gives encouraging signs for the detection with the optical fibres using the pulsed laser.

13.1.3 Supplementary remarks

In the experimental test of fluorescence detection, we will use a bundle of identical fibres, since we only need to detect the Cs fluorescence at 456 nm. For the positronium experiment at Saclay, we either need to choose between the 243 and the 1312 nm fluorescence wavelengths or we need to make a bundle of mixed fibres if we want to detect both, since no multi-mode fibres efficiently spanning the UV to IR range are readily available. Mixing the fibres means that, for the same solid angle covered, the fluorescence signal for each wavelength would be at least divided by two. Unless the results of the test shows that the signal-to-noise ratio is still acceptable in that case, we will probably focus our effort on detecting only one of the fluorescence wavelengths

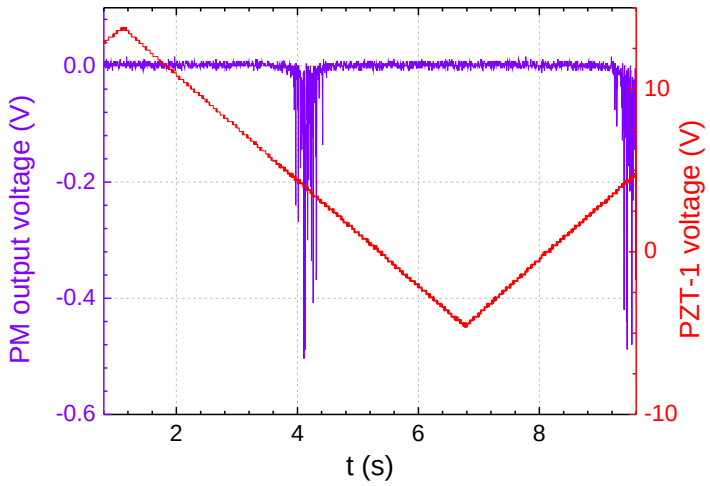


Figure 13.5: The Cs fluorescence signal (violet pulses) detected when the frequency of the CW Ti:Sa laser is swept (the voltage ramp on PZT-1 is shown in red).

of the positronium. Prior to choosing between 243 and 1312 nm, a measurement of the light background in the vacuum chamber of the positronium experiment at Saclay should be done.

Concerning the laser pulses used for the caesium excitation, we have not given any precision regarding their duration. Since the oscillator is currently aligned to deliver pulses of 9 ns FWHM, we will start the fluorescence detection test with these short pulses. If the test proves that, in that case, the fluorescence signal is too faint to be detected or the signal-to-noise ratio too low for the purpose of the spectroscopy measurement, then we will have to change the configuration of the oscillator, i.e. increase the cavity length, in order to produce wider laser pulses. We remind that the results presented in the simulation part suggested that longer pulses of laser (for instance 20 to 50 ns FWHM) should be more interesting for the spectroscopy experiment. Alternatively and/or simultaneously, the energy of the pulses can also be varied. In fact, if the caesium fluorescence detection test is conclusive and easy to implement, we could investigate several laser pulse widths and energies, and confront the experimental results with the simulation results; this would help for a better determination of the laser parameters that should be used for the positronium experiment at Saclay.

Independently, we can also check the out-gassing of a bundle of a few hundred fibres in a separated vacuum chamber at CEA-Saclay. The coating of the fibres is made of Tefzel, a fluoropolymer: the properties handbook for Tefzel from manufacturer DuPont indicates that an average weight loss of 0.07 % is observed in hard vacuum (no further precision), when heated at 150 °C, for 24 hrs. This seems to be a low out-gassing rate, and it gets certainly even lower as the time spent in vacuum is prolonged, but for many fibres (with a length of, at least, 120 to 150 mm), the total out-gassing may remain to high. If it is confirmed that Tefzel is incompatible with long use in ultra-high vacuum, we will indeed have to work with bare fibres, which have to be handle with extreme care: they easily break when bent or pinched. In order to hold the bundle together, we can try carefully clenching them with an indium ring. Another or complementary solution should be investigated: the epoxy resin Torr Seal, for instance, is claimed to be usable at 10^{-9} torr. We could test it and, if revealed to be suitable, use it to glue together the bare fibres.

13.2 Preparation of the experiment at CEA-Saclay

While the assembly and alignment of the laser was carried out at LKB, the GBAR experimental zone at CEA-Saclay was prepared for the arrival of the laser. Space had to be found for a laser hut and a study of the safety equipments needed has been made. We describe here the specificities of the laser hut and its equipments and give a status of its realisation progress.

13.2.1 Installation of the laser hut on the GBAR zone

The GBAR experimental zone at Saclay, where are installed the linac-based positron source demonstrator and the positron trap, is a rather small area in a so-called "hall of accelerators" surrounded by other experiments, test-benches for accelerator parts and exhibition area for public visits. The installation of a laser hut in that area required to gain some space on this public communication area. The laser table used at LKB, originally given by the SIS (*Service d'ingénierie des systèmes*, part of the Irfu), is 1.8 m long by 1.3 m wide: in order to have easy circulation around the table with space for electronic racks and an entry vestibule with curtains at the door, the dimensions chosen for the hut are 5 m long by 3 m wide. The location of the laser hut on the GBAR zone can be visualised in figure 13.6.

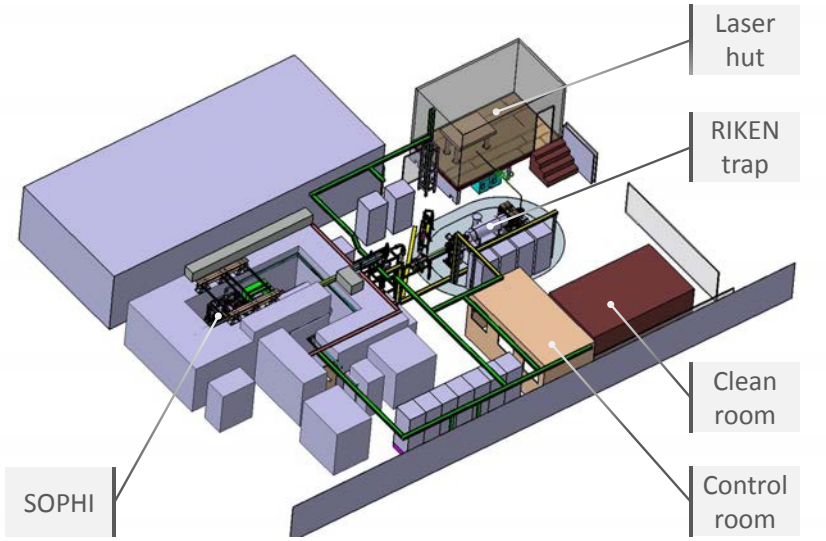


Figure 13.6: The 3D visualisation of the GBAR zone including the laser hut.

Since the hall is a rather noisy environment, and we want to limit the vibrations of the laser system to ensure wavelength stability during the spectroscopy measurements, we decided to bolt the table legs on a long concrete block of 0.4 m height, itself laying on a second identical concrete block: between the two concrete blocks and between the floor and the blocks, vibration absorber pads have been placed to isolate as much as possible the table from the vibrations of the ground. Surrounding the concrete blocks, the laser hut has been built on a light structure 0.9 m above the ground and the floor of the hut is in light contact with the concrete blocks via other absorber pads; this floor has been cut away at the locations of the table legs. When the laser table is moved to CEA, two side panels of the hut will be removed so the laser table can be inserted in

the hut without removing all the optics installed on it. Only the pump lasers will have to be transported separately. This solution will save time for the realignment of the laser system.

The laser is also sensitive to temperature variations (inducing deformation of the cavities), therefore, a 6 kW air conditioning unit has been installed to regulate the temperature at 21±1 °C. Again, we took care to isolate the hut from the air conditioner vibrations: the unit has thus been installed outside the hut, on a pillar, and the connection with the hut is made by a flexible vent hose. A line providing dry air has to be installed: this will be used for keeping a small overpressure in the laser boxes. In order to be independent from the water circuit of the hall, it has been decided to use a derivation on the pump laser chiller for the cooling of the Ti:Sa crystals.

The cables for the hut equipment power supply are currently being installed. Other general equipments to be installed are a shelf above the table and the automate controlling the safety organs in the hut that is described in the next section. Figure 13.7 shows the laser hut installed in the GBAR zone at CEA-Saclay.



Figure 13.7: The laser hut built in the GBAR zone (the positron trap can be seen on the left); picture taken during the installation of the air conditioning unit.

13.2.2 Operation of the laser at CEA-Saclay and safety procedures

All the lasers operating in the hut are classified as class 4 lasers, requiring the maximum protection (lab coat and adequate laser glasses for the individual protection) and active safety equipments to avoid any accidental exposition to the laser. For the laser hut itself, the access is limited to authorised persons in possession of a transponder. Moreover, when any of the pump laser is switch on in the laser hut, it is mandatory to have the authorisation of the person working inside the hut to enter without activating the laser shutters. At the entrance, a vestibule made with fireproof curtains adds further protection; in the vestibule, the laser goggles are available, with a LED display indicating which type of goggles should be used. The selection of the goggles has been particularly meticulous since it is possible to be exposed to three different wavelengths (410, 532 and 820 nm) and to both continuous and pulsed lasers.

In normal running conditions, all the lasers are locked in totally opaque boxes, whose opening panels are equipped with a contact switch: in case the opening of a box is forced, all the lasers are shut down. An emergency stop button is also installed to shut down all the power inside the hut. A key switch is used to change the automate mode from *normal running* to *alignment*

phase. In that case, it is allowed to open the laser boxes. A total of seven boxes are supervised by the automate in the laser hut. Before exiting the hut, the 410 nm laser beam is blocked by a shutter (default position): this allows to be still working on the laser system in the hut while an intervention on the positronium chamber is done.

The laser beam will exit the hut from the side close to the positron trap, about 2 m above the ground. The beam will travel inside a tube, and three mirrors will be needed to send it in the positronium chamber, where is enters through a fused silica window mounted on a CF63 flange. A fourth mirror, spherical, is placed outside the vacuum chamber, behind a second silica window mounted on the opposite side of the laser entry window. In order to access these mirrors – and additional focussing optics – for a first rough alignment, each one of them is enclosed in a box, otherwise locked during normal operation (any attempt to open a box without prior switching to the alignment mode in the hut results in the shut down of the pump lasers). For the precision alignment, remote control of the mirror mounts has been planned. The safety committee at CEA also required a monitoring of the laser power, at the exit of the hut and behind the positronium chamber, in order to alert the users of a misaligned beam in the tube outside the hut.

The realisation of the automate managing all the active safety equipments has been fully supported by the SIS; the automate is currently being installed and tested.

Chapter 14

Conclusion: status of laser system

The last part of the present thesis has been dedicated to the building of a pulsed 410 nm laser system for the excitation of positronium into state 3D in the GBAR experiment at CERN. Presently, we have built a pulsed laser at 820 nm which matches the requirements of this 410 nm laser as it is described in the proposal.

- First, we have assembled a continuous-wave (CW) Ti:Sa laser, which delivers 400 mW at 820 nm, when pumped with 6 W of 532 nm light power. The wavelength of this laser can be chosen in a wide range around 820 nm and also finely tuned around the desired wavelength.

- Using this tunable laser at 822 nm, we carried out the 6S-8S two-photon transition in caesium. This allowed us to verify the accuracy of the reference lambda-metre. We measured the error made by the lambda-metre with respect to the published value of the 6S-8S transition frequency: the error found was 35 MHz, which is compatible with the 60 MHz accuracy announced by the constructor.

- A pulsed Ti:Sa laser has been specifically designed for the GBAR experiment. When its oscillator cavity is pumped at 21 mJ with a frequency doubled YAG laser from Quantel, it delivers pulses of 4 mJ with a full width at half maximum of 9 ns. The frequency of this pulsed laser is set by the one of the CW laser since the latter is used to seed the oscillator cavity.

- There is nevertheless a discrepancy between the frequencies of the CW and the pulsed lasers, due to a frequency excursion occurring during the pumping of the Ti:Sa crystal with the 532 nm pulses. This effect, called chirp, has been characterised using two lambda-metres: it induces an average 75 MHz shift for our usual running conditions.

- Finally, we implemented a control-loop on the frequency of the CW Ti:Sa laser using a lambda-metre: this set-up will be used as a reference when we will search for the 1S-3D transition in positronium, either at CERN or at CEA-Saclay.

To produce the final 410 nm pulses needed to excite the positronium, we still have to install the non-linear crystal for the second harmonic generation. We will also probably have to increase the energy of the 820 nm pulses for the preliminary experiment at CEA-Saclay. This requires to build a new stage in the laser system: a multi-passage Ti:Sa amplifier. The goal is to go from the current 4 mJ pulses to pulses of 10 to, more difficult, 20 mJ at 820 nm.

A picture of the current laser set-up is shown in figure 14.1.

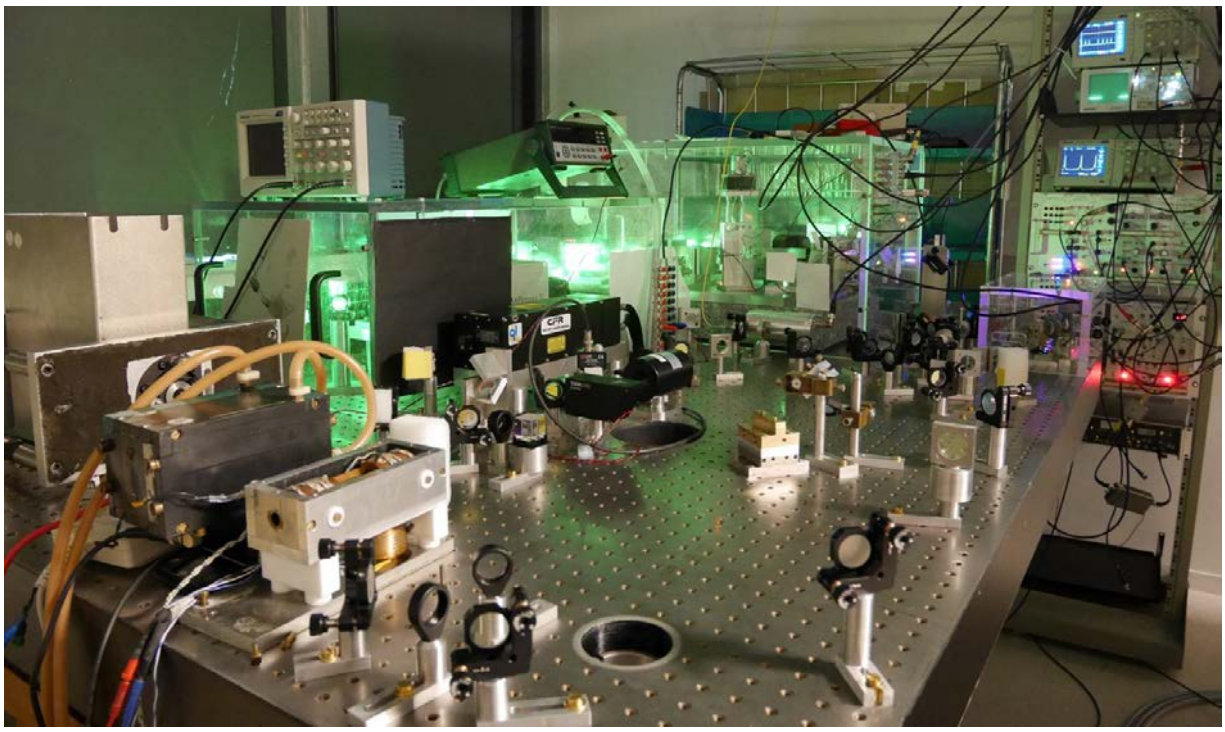


Figure 14.1: The laser system currently running at LKB.

Part V

Conclusion

1. Summary of the achieved work

The GBAR experiment is a recently approved CERN experiment that proposes to measure the gravitational acceleration of antimatter on Earth by performing the free fall of antihydrogen atoms. In order to get cold antihydrogen atoms, an intermediate state, the antihydrogen positive ion, must be produced by the successive collisions of antiprotons with positronium atoms. The present thesis encompasses the theoretical study of the collisional processes leading to the production of the antihydrogen ion, by both calculating the cross sections of the corresponding reactions and simulating the physical processes in the interaction volume, and the building of a laser system to excite the positronium. The aim is to optimise the production of the $\bar{H}^+$ antihydrogen positive ions.

We have adapted the Continuum Distorted Wave – Final State (CDW–FS) perturbation theory to compute the cross sections at low energy for: *i*) first reaction, the antihydrogen formation in collisions between antiproton and positronium, and *ii*) second reaction, the antihydrogen ion formation in the subsequent collisions between the antihydrogen atoms and the positronium. We also derived the Coulomb-Born Approximation cross sections. Particular attention has been paid to the treatment of long-range Coulomb interaction and of the electronic correlations in $\bar{H}^+$. We also extensively computed the cross sections for many excited states of both antihydrogen and positronium. The present work completes existing studies on the first reaction and constitutes the largest study undertaken on the second reaction.

From the cross section results, we have isolated three different interesting states of positronium and three possible ranges of kinetic energy for the CERN antiprotons used in the GBAR experiment. Depending on the performances of the GBAR antiproton decelerator, we suggest to use either 6 keV antiprotons (with possible excitation of the positronium into state 3D), 2 keV antiprotons with the 2P state of positronium or antiprotons below 1 keV with the 3D state of positronium; we expect the latter two possibilities to give the highest production rates of $\bar{H}^+$.

We then integrated these cross sections into a preliminary simulation of the interaction region, in order, for instance, to account for the time evolution of the positronium and antihydrogen excited states. This allowed us to assess the influence of several experimental parameters on the total $\bar{H}^+$ production. We concluded that the reaction chamber – a tube in which the positronium is formed – should be 20 mm long and should not exceed 1 mm^2 in section. In particular, this latter parameter is the most important as it governs the positronium density. We showed that it should be as small as possible, even if the transmission of the antiprotons through the tube is hence degraded. We also emphasised the interest of employing short pulses of antiprotons.

In this simulation, we only considered positronium excitation into state 3D. We determined that the laser pulses used for the positronium excitation in the CERN experiment should be 10 to 20 ns wide (FWHM) and have an energy of about 1 mJ. We also suggested to use two consecutive laser pulses of 10 ns and about 0.8 mJ energy to further enhance the $\bar{H}^+$ production. Finally, we demonstrated that the $\bar{H}^+$ losses induced by laser photo-detachment cannot be reduced much by changing the positronium excitation scheme.

Having determined the parameters for the laser of positronium excitation into state 3D, we have undertaken the building of this pulsed laser system at 410 nm. The 410 nm beam is obtained by the frequency doubling of a pulsed Ti:Sa laser at 820 nm. This 820 nm pulsed laser has been built and characterised.

The pulsed beam at 820 nm is formed in a short cavity oscillator, where the Ti:Sa crystal is

pumped by a pulsed doubled YAG. The oscillator cavity is seeded by a stable and tunable CW Ti:Sa laser. Using this laser system, we were able to produce 820 nm pulses having an energy of 4 mJ and a FWHM of 9 ns; extrapolating the second harmonic generation efficiency, this result matches the requirements for the positronium excitation in the GBAR experiment at CERN.

Before moving the laser at CERN, it will be used at CEA-Saclay for the spectroscopy of the 3D level of positronium. The laser system can be adapted to this experiment by adding an amplification stage and lengthening the oscillator cavity to obtain longer laser pulses. In the prevision of the laser coming at the GBAR experimental zone at Saclay, a laser hut has been installed and the study and the realisation of the safety equipment control has been done.

2. Continuity

The present thesis has addressed many topics related to the production of antihydrogen and its positive ion for the GBAR experiment. It offers both the references and the tools (either theoretical or experimental with the laser) for anyone willing to continue the task. It has also laid the foundations of further developments. Indeed, the cross section calculations and the simulation, for instance, could receive a deeper exploration.

We know that the theoretical models used to compute the cross sections of the $\bar{H}$ and $\bar{H}^+$ formation reactions have a post-prior discrepancy that should be investigated. The CDW–FS model, used here in its *prior* formulation, could be derived in its *post* form. Because of this post-prior discrepancy, the argument of micro-reversibility put forward to inverse the cross sections is not fully justified any more. Therefore, a new development of the CDW–FS model could be done for the direct sense of the GBAR reactions. But this is certainly not enough, since our pertubation theory models also have a limited validity toward the thresholds of the reactions. This calls for other calculations using more accurate low energy models. However, these models often only give cross section values for the energies laying just above the thresholds, which is not sufficient for GBAR. The idea would be to combine these highly accurate low energy results with those of perturbation theory models. It is worth mentioning that a new PhD thesis has started in Strasbourg to continue the work on the subject of the cross sections. Other complementary studies could be dedicated to the differential cross sections and to the parasitic reactions.

In order to precise its results, the simulation awaits for new experimental input or data from simulations of other parts of the experiment, in particular regarding the antiproton beam sent to the reaction chamber. New cross sections could also be used. The dynamics of the positronium emission and diffusion in the converter tube could be better described. Also, the simulation for the case of the positronium being excited into state 2P must be done.

The work on the laser is not achieved yet. Currently, the laser set-up lacks its frequency doubling stage, and probably an amplifier. They should be implemented by the end of year 2014. An experiment is also being prepared in order to assess the feasibility of positronium fluorescence detection using optical fibres in a future experiment at CEA-Saclay.

We focussed on the 3D state of positronium, but the results from the theoretical study suggests that the 2P state might be more interesting for the production of $\bar{H}^+$ in GBAR. Recently, a French ANR proposal concerning the laser excitation of positronium (and also including hydrogen and H^- production cross section measurement) has been approved. The project intends to build another laser system, dedicated to the Lyman-α transition in positronium (1S-2P, at 243 nm). For that purpose, part of the laser system presented here could be re-employed.

Bibliography

[1] P. A. M. Dirac. The quantum Theory of the Electron. *Proc. R. Soc. Lond. A*, 117:610–624, 1928.

[2] C. D. Anderson. The apparent existence of easily deflected positives. *Science*, 9:238–239, 1932.

[3] M. Deutsch. Evidence for the Formation of Positronium in Gases. *Phys. Rev.*, 82:455–456, 1951.

[4] O. Chamberlain, E. Segrè, C. Wiegand, and T. Ypsilantis. Observation of Antiprotons. *Phys. Rev.*, 100:947–950, 1955.

[5] B. Cork, G. R. Lambertson, O. Piccioni, and W. A. Wenzel. Antineutrons Produced from Antiprotons in Charge-Exchange Collisions. *Phys. Rev.*, 104:1193–1197, 1956.

[6] G. Baur, G. Boero, A. Brauksiepe, A. Buzzo, W. Eyrich, R. Geyer, D. Grzonka, J. Hauffe, K. Kilian, M. LoVetere, M. Macri, M. Moosburger, R. Nellen, W. Oelert, S. Passaggio, A. Pozzo, K. Rhrich, K. Sachs, G. Schepers, T. Sefzick, R. S. Simon, R. Stratmann, F. Stinzing, and M. Wolke. Production of antihydrogen. *Physics Letters B*, 368:251–258, 1996.

[7] T. Massam, Th. Muller, B. Righini, M. Schneegans, and A. Zichichi. Experimental observation of antideuteron production. *Il Nuovo Cimento*, 39:10–14, 1965.

[8] J. H. Christenson, J. W. Cronin, V. L. Fitch, and R. Turlay. Evidence for the 2π decay of the K_2^0 Meson. *Phys. Rev. Lett.*, 13:138–140, 1964.

[9] A. Alavi-Harati *et al.* Observation of Direct CP Violation in $k_{s,l} \to \pi\pi$ decays. *Phys. Rev. Lett.*, 83:22–27, 1999.

[10] V. Fanti *et al.* A new measurement of direct CP violation in two pion decays of the neutral kaon. *Phys. Lett. B*, 465:335–348, 1999.

[11] R. P. Feynman. The Theory of Positrons. *Phys. Rev.*, 76:749–759, 1949.

[12] M. S. Fee, S. Chu, A. P. Mills, R. J. Chichester, D. M. Zuckerman, E. D. Shaw, and K. Danzmann. Measurement of the positronium $1\ ^3\ s_1 - 2\ ^3\ s_1$ interval by continuous-wave two-photon excitation. *Phys. Rev. A*, 48:192–219, 1993.

[13] G. Gabrielse, A. Khabbaz, D. S. Hall, C. Heimann, H. Kalinowsky, and W. Jhe. Precision Mass Spectroscopy of the Antiproton and Proton Using Simultaneously Trapped Particles. *Phys. Rev. Lett.*, 82:3198–3201, 1999.

[14] M. Hori, A. Sótér, D. Barna, A. Dax, R. Hayano, S. Friedreich, B. Juhász, T. Pask, E. Widmann, D. Horváth, L. Venturelli, and N. Zurlo. Two-photon laser spectroscopy of antiprotonic helium and the antiproton-to-electron mass ratio. *Nature*, 475:484488, 2011.

[15] K. A. Olive *et al.* Review of Particle Physics. *Chin. Phys. C*, 38:090001, 2014.

[16] V. B. Berestetskiĭ, E. M. Lifshitz, and L. P. Pitaevskiĭ. *Relativistic Quantum Theory*, volume 4 of *Course of Theoretical Physics*. Pergamon Press, 1971.

[17] E. E. Salpeter and H. A. Bethe. A Relativistic Equation for Bound-State Problems. *Phys. Rev.*, 84:1232–1242, 1951.

[18] A. Messiah. *Mécanique quantique*, volume 1. Dunod, 1964.

[19] H. A. Bethe and E. E. Salpeter. *Quantum Mechanics of One- and Two-Electron Systems*. Springer, 1957.

[20] R. Ley and G. Werth. *The Hydrogen Atom*, volume 570 of *Lecture Notes in Physics*, chapter Positroniu: Theory Versus Experiment. Springer, 2001.

[21] R. Ley. Atomic physics of positronium with intense slow positron beams. *Appl. Surf. Sci.*, 194:301306, 2002.

[22] M. W. Ritter, P. O. Egan, V. W. Hughes, and K. A. Woodle. Precision determination of the hyperfine-structure interval in the ground state of positronium. *Phys. Rev. A.*, 30:1331–1338, 1984.

[23] D. Hagena, R. Ley, D. Weil, G. Werth, W. Arnold, and H. Schneider. Precise Measurement of n=2 Positronium Fine-Structure Intervals. *Phys. Rev. Lett.*, 71:2887–2890, 1993.

[24] D. B. Cassidy, M. W. J. Bromley, L. C. Cota, T. H. Hisakado, H. W. K. Tom, and A. P. Mills Jr. Cavity Induced Shift and Narrowing of the Positronium Lyman-α Transition. *Phys. Rev. Lett.*, 106:023401, 2011.

[25] S. Karshenboim. Precision physics of simple atoms: QED tests, nuclear structure and fundamental constants. *Phys. Rept.*, 422:1–63, 2005.

[26] M. Amoretti *et al.* Production and detection of cold antihydrogen atoms. *Nature*, 419:456–459, 2002.

[27] G. Gabrielse, N. S. Bowden, P. Oxley, A. Speck, C. H. Storry, J. N. Tan, M. Wessels, D. Grzonka, W. Oelert, G. Schepers, T. Sefzick, J. Walz, H. Pittner, T. W. Hänsch, and E. A. Hessels. Background-Free Observation of Cold Antihydrogen with Field-Ionization Analysis of Its States. *Phys. Rev. Lett.*, 89:213401, 2002.

[28] The ALPHA Collaboration. Confinement of antihydrogen for 1,000 seconds. *Nature Physics*, 7:558564, 2011.

[29] C. Amole *et al.* Resonant quantum transitions in trapped antihydrogen atoms. *Nature*, 483:439443, 2012.

[30] N. Kuroda *et al.* A source of antihydrogen for in-flight hyperfine spectroscopy. *Nature Communications*, 5:3089, 2014.

[31] M. M. Nieto and T. Goldman. The arguments against antigravity and the gravitational acceleration of antimatter. *Phys. Rept.*, 205:221–281, 1991.

[32] F. S. Dzheparov Y. G. Abov and L. B. Okun'. Test of the equality of the particle and antiparticle masses in neutronantineutron oscillations. *JETP Lett.*, 39:599–600, 1984.

[33] P. Crivelli, D. A. Cooke, and S. Friedreich. Experimental considerations for testing antimatter antigravity using positronium 1S-2S spectroscopy. *International Journal of Modern Physics: Conference Series*, 20:1460257, 2014.

[34] R. J. Hughes and M. H. Holzscheiter. Constraints on the Gravitational Properties of Antiprotons and Positrons from Cyclotron-Frequency Measurements. *Phys. ReV. Lett.*, 66:854–857, 1991.

[35] The ALPHA collaboration and A. E. Charman. Description and first application of a new technique to measure the gravitational mass of antihydrogen. *Nature comm.*, 4:1785, 2013.

[36] A. Kellerbauer *et al.* Proposed antimatter gravity measurement with an antihydrogen beam. *Nucl. Instr. Meth. Phys. Res. B*, 266:351–356, 2008.

[37] J. Walz and T. W. Hänsch. A Proposal to Measure Antimatter Gravity Using Ultracold Antihydrogen Atoms. *Gen. Relat. Gravit.*, 36:561–570, 2004.

[38] P. Pérez, L. Liszkay, J.-M. Rey, V. Blideanu, M. Carty, A. Curton, O. Delferrierre, P. Dupré, T. Muranaka, N. Ruiz, and Y. Sacquin. A mini linac based positron source. *Phys. Status Solidi C*, 6:2462–2464, 2009.

[39] L. Liszkay, P. Comini, C. Corbel, P. Debu, P. Dupré, P. Grandemange, Pérez, J.-M. Rey, N. Ruiz, and Y. Sacquin. Linac-based positron source and generation of a high density positronium cloud for the GBAR experiment. *J. Phys.: Conf. Ser.*, 443:012006, 2013.

[40] P. Dupré. *Piégeage de positons dans un piège de Penning-Malmberg, en vue de leur accumulation avec un faisceau pulsé.* PhD thesis, Université Pierre et Marie Curie - Paris 6, 2011.

[41] P. Grandemange. *Piégeage et accumulation de positons issus d'un faisceau pulsé produit par un accélérateur pour l'étude de l'interaction gravitationnelle de l'antimatière.* PhD thesis, Université Paris-Sud 11, 2013.

[42] L. Liszkay, , C. Corbel, Pérez P. Desgardin, M.-F. Barthe, T. Ohdaira, A. Rubbia M. Etienne S. Suzuki P. Crivelli, U. Gendotti, and A. Walcarius. Positronium reemission yield from mesostructured silica films. *Appl. Phys. Lett.*, 92:063114, 2008.

[43] P. Crivelli, U. Gendotti, A. Rubbia, L. Liszkay, P. Pérez, and C. Corbel. Measurement of the ortho-positronium confinement energy in mesoporous thin films. *Phys. Rev. A*, 81:052703, 2010.

[44] D. B. Cassidy, P. Crivelli, T. H. Hisakado, L. Liszkay, V. E. Meligne, P. Pére, H. W. K. Tom, and A. P. Mills Jr. Positronium cooling in porous silica measured via Doppler spectroscopy. *Phys. Rev. A*, 81:012715, 2010.

[45] O. Morandi, P.-A. Hervieux, and G. Manfredi. Study of the positronium thermalization in porous materials. *Eur. Phys. J. D*, 68:84, 2014.

[46] O. Morandi, P.-A. Hervieux, and G. Manfredi. Bose-einstein condensation of positronium in silica pores. *Phys. Rev. A*, 89:033609, 2014.

[47] ELENA parameter list. Technical report, 2012.

[48] C. Monroe, D. M. Meekhof, B. E. King, S. R. Jefferts, W. M. Itano, D. J. Wineland, and P. Gould. Resolved-Sideband Raman Cooling of a Bound Atom to the 3D Zero-Point Energy. *Phys. Rev. Lett.*, 75:4011–4014, 1995.

[49] G. Dufour, R. Guérout, A. Lambrecht, V. Nesvizhevsky, S. Reynaud, and A. Voronin. Quantum Reflection of Antihydrogen in the GBAR Experiment. *Int. J. Mod. Phys.: Conf. Ser.*, 30:1460265, 2014.

[50] The GBAR Collaboration. Proposal to measure the Gravitational Behaviour of Antihydrogen at Rest - GBAR, 2011. CERN-SPSC-2011-029, SPSC-342.

[51] A. R. P. Rau. The Negative Ion of Hydrogen. *J. Astrophys. Astr.*, 17:113–145, 1996.

[52] H. A. Bethe. The Electron Affinity of Hydrogen. *Zeits. Physik*, 57:815, 1929.

[53] S. J. Smith and D. S. Burch. Relative Measurement of the Photodetachment Cross Section for H^-. *Phys. Rev.*, 116:1125–1131, 1959.

[54] S. Chandrasekhar. Some remarks on the negative hydrogen ion and its absorption coefficient. *Astrophys. J.*, 100:176–180, 1944.

[55] J. W. Humberston, M. Charlton, F. M. Jacobsen, and B. I. Deutch. On antihydrogen formation in collisions of antiprotons with positronium. *J. Phys. B: At. Mol. Phys.*, 20:L25–L29, 1987.

[56] A. Igarashi, N. Toshima, and T. Shirai. Hyperspherical coupled-channel calculation for antihydrogen formation in antiproton-positronium collisions. *J. Phys. B: At. Mol. Opt. Phys.*, 27:L497–L501, 1994.

[57] J. Mitroy. Formation of antihydrogen by the charge-transfer reaction. *Phys. Rev. A*, 52(4):2859–2864, 1995.

[58] J. Mitroy and G. Ryzhikh. The formation of antihydrogen by the charge transfer reaction. *J. Phys. B: At. Mol. Opt. Phys.*, 30:L371–L375, 1997.

[59] M. Weber, A. Hofman, W. Raith, W. Sperber, F. Jacobsen, and K. G. Lynn. Results of the Bielefeld–Brookhaven e^+–H experiment. *Hyperfine Interact.*, 89:221–242, 1994.

[60] S. Zhou, H. Li, W. E. Kauppila, C. K. Kwan, and T. S. Stein. Measurements of total and positronium formation cross sections for positrons and electrons scattered by hydrogen atoms and molecules. *Phys. Rev. A*, 55:361–368, 1997.

[61] H. R. J. Walters, A. A. Kernoghan, and M. T. McAlinden. Overview of the Present Theoretical Status of Positron-Atom Collisions. *AIP Conf. Proc.*, 360:397–412, 1996.

[62] J. Mitroy. An L^2 calculation of positronhydrogen scattering at intermediate energies. *J. Phys. B: At. Mol. Opt. Phys.*, 29:L263–L269, 1996.

[63] A. A. Kernoghan, D. J. R. Robinson, M. T. McAlinden, and H. R. J. Walters. Positron scattering by atomic hydrogen. *J. Phys. B: At. Mol. Opt. Phys.*, 29:2089–2102, 1996.

[64] J. P. Merrison, H. Bluhme, J. Chevallier, B. I. Deutch, P. Hvelplund, L. V. Jørgensen, H. Knudsen, M. R. Poulsen, and M. Charlton. Hydrogen Formation by Proton Impact on Positronium. *Phys. Rev. Lett.*, 78:2728–2731, 1997.

[65] A. S. Kadyrov and I. Bray. Two-center convergent close-coupling approach to positron-hydrogen collisions. *Phys. Rev. A*, 66:012710, 2002.

[66] C.-Y. Hu, D. Caballero, and Z. Hlousek. Low-energy antihydrogen formation cross sections and differential cross sections via the modified Faddeev equations. *J. Phys. B: At. Mol. Opt. Phys.*, 34:331–338, 2001.

[67] C.-Y. Hu and D. Caballero. Low-energy anti-hydrogen formation differential cross sections from Ps(n = 2) via the modified Faddeev equations. *J. Phys. B: At. Mol. Opt. Phys.*, 35:3879–3886, 2002.

[68] P. A. Macri, J. E. Miraglia, J. Hanssen, O. A. Fojón, and R. D. Rivarola. Evidence of two-channel distortion effects in positronium formation reactions. *J. Phys. B: At. Mol. Opt. Phys.*, 37:L111–L119, 2004.

[69] L. Jiao, Y. Wang, and Y. Zhou. Positronium formation for positron scattering from hydrogen: Maximum positions and scaling law. *Phys. Rev. A*, 84:052711, 2011.

[70] J. C. Straton and R. J. Drachman. Formation of positronium in $e^+ + H^-$ collisions. *Phys. Rev. A*, 44:7335–7342, 1991.

[71] P. Chaudhuri. Positronium Formation from Hydrogen Negative Ion, H^-. *Braz. J. Phys.*, 31:1–7, 2001.

[72] P. K. Biswas. Effect of H^- ion formation on positronium-hydrogen elastic scattering. *J. Phys. B: At. Mol. Opt. Phys.*, 34:4831–4844, 2001.

[73] M. T. McAlinden, J. E. Blackwood, and H. R. J. Walters. Positron scattering by the negative hydrogen ion. *Phys. Rev. A*, 65:032715, 2002.

[74] S. Roy and C. Sinha. Formation of negative hydrogen ion in positronium-hydrogen collisions. *Eur. Phys. J. D*, 47:327–334, 2008.

[75] I. M. Cheshire. Continuum distorted wave approximation; resonant charge transfer by fast protons in atomic hydrogen. *Proc. Phys. Soc.*, 84:89–98, 1964.

[76] Dž. Belkić. *Quantum Theory of High-Energy Ion-Atom Collisions.* CRC Press, 2008.

[77] Dž. Belkić. A quantum theory of ionisation in fast collisions between ions and atomic systems. *J. Phys. B: At. Mol. Phys.*, 11:3529–3552, 1978.

[78] D. S. F. Crothers. Refined orthogonal variational treatment of continuum distorted waves. *J. Phys. B: At. Mol. Phys.*, 15:2061–2074, 1982.

[79] D. S. F. Crothers and J. F. McCann. Ionisation of atoms by ion impact. *J. Phys. B: At. Mol. Phys.*, 16:3229–3242, 1983.

[80] M. Abramowitz. *Handbook of mathematical functions with Formulas, Graphs, and Mathematical Tables*, chapter Coulomb Wave Functions. 1964.

[81] O. A. Fojón, R. D. Rivarola, R. Gayet, J. Hanssen, and P.-A. Hervieux. Continuum-distorted-wavefinal-state approximation in positron-hydrogenic atom (ion) collisions with positronium formation. *Phys. Rev. A*, 54:4923–4930, 1996.

[82] C. R. Mandal, M. Mandal, and S. C. Mukherjee. Excited-state positronium formation from positron–atomic-hydrogen collisions. *Phys. Rev. A*, 44(5):2968–2974, 1991.

[83] J. Hanssen, P.-A. Hervieux, O. A. Fojón, R. D. Rivarola, and R. Gayet. Inner-shell contribution to electron capture in positronalkali collisions. *J. Phys. B: At. Mol. Opt. Phys.*, 31:1313–1319, 1998.

[84] O. A. Fojón, J. Hanssen, P.-A. Hervieux, and R. D. Rivarola. Transfer excitation in collisions of positrons with He and alkaline-earth metals. *J. Phys. B: At. Mol. Opt. Phys.*, 33:3093–3105, 2000.

[85] J. Hanssen, P.-A. Hervieux, O. A. Fojón, and R. D. Rivarola. Positronium formation in positron-metastable-helium collisions. *Phys. Rev. A*, 63:012705, 2000.

[86] B. H. Bransden, C. J. Joachain, and J. F. McCann. Positronium formation in positron-atom collisions at intermediate energies. *J. Phys. B: At. Mol. Opt. Phys.*, 25:4965–4979, 1992.

[87] P. Comini and P.-A. Hervieux. ion production from collisions between antiprotons and excited positronium: cross sections calculations in the framework of the GBAR experiment. *New J. Phys.*, 15:095022, 2013.

[88] A. Franz and P. Altick. Electron impact ionization of helium: coplanar, triply differential cross sections at high and intermediate energies. *J. Phys. B*, 25:1577–1590, 1992.

[89] A. Messiah. *Mécanique quantique*, volume 2. Dunod, 1964.

[90] C. L. Pekeris. Ground State of Two-Electron Atoms. *Phys. Rev.*, 112:1649–1658, 1958.

[91] C. Le Sech. Accurate analytic wavefunctions for two-electron atoms. *J. Phys. B: At. Mol. Opt. Phys.*, 30:L47–L50, 1997.

[92] C. Le Sech. private communication. 2012.

[93] A. Sarsa and C. Le Sech. Variational Monte Carlo Method with Dirichlet Boundary Conditions: Application to the Study of Confined Systems by Impenetrable Surfaces with Different Symmetries. *J. Chem. Theory Comput.*, 7:2786–2794, 2011.

[94] K. Fujiwara. Coulomb-Born Calculation of Charge Transfer Cross Sections of Highly-Ionized Atoms. *J. Phys. Soc. Jpn.*, 41:1350–1355, 1976.

[95] S. Mukherjee, K. Bahdra, N. C. Sil, and D. Basu. Capture in proton-He^+ collisions. *Phys. Lett.*, 65A:285–286, 1978.

[96] C. J. Joachain. *Quantum Collision Theory.* North-Holland, 1975. p. 654.

[97] J. E. Blackwood, M. T. McAlinden, and H. R. J. Walters. Importance of the H^- channel in ps-H scattering. *Phys. Rev. A*, 65:032502(R), 2002.

[98] F. Biraben. *Spectroscopie à deux et trois photons sans élargissement Doppler. Application à létude des collisions sodium-gaz rare.* Thèse d'état, Université Pierre et Marie Curie - Paris 6, 1977.

[99] Y. Gontier and M. Trahin. On the multiphoton absorption in atomic hydrogen. *Phys. Lett.*, 36A:463–464, 1971.

[100] Y. F. Verolaĭnen and A. Y. Nikolaich. Radiative lifetimes of excited states of atoms. *Sov. Phys. Usp.*, 25:431–447, 1982.

[101] M. A. C. Nascimento and W. A. Goddard. The photodetachment cross section of the negative hydrogen ion. *Phys. Rev. A*, 16:1559–1567, 1977.

[102] M. Crance and M. Aymar. Two-photon detachment of H^-. A model calculation. *J. Phys. B: At. Mol. Opt. Phys.*, 28:3529–3536, 1985.

[103] L. Liszkay, C. Corbel, L. Raboin, J.-P. Boilot, P. Pérez, A. Brunet-Bruneau, P. Crivelli, U. Gendotti, A. Rubbia, T. Ohdaira, and R. Suzuki. Mesoporous silica films with varying porous volume fraction: Direct correlation between orthopositronium annihilation decay and escape yield into vacuum. *Appl. Phys. Lett.*, 95:124103, 2009.

[104] W. Bartman *et al.* Progress in ELENA design. *Proceedings of IPAC-2013*, 2013.

[105] P. Crivelli. collaboration meeting communication. 2014.

[106] IPG Photonics. TM:ZnSe/S series. Datasheet, 2012.

[107] B. Cagnac, G. Grynberg, and F. Biraben. Spectroscopie d'absorption multiphotonique sans effet Doppler. *J. Physique*, 34:845–858, 1973.

[108] P. F. Moulton. Spectroscopic and laser characteristics of Ti:Al_2O_3. *J. Opt. Soc. Am. B*, 3:125–132, 1986.

[109] F. Biraben and P. Labastie. Balayage d'un laser à colorant continu monomode sur 150 GHz. *Optics Comm.*, 41:49–51, 1982.

[110] B. de Beauvoir, C. Schwob, O. Acef, L. Jozefowski, L. Hilico, F. Nez, L. Julien, A. Clairon, and F. Biraben. Metrology of the hydrogen and deuterium atoms: determination of the Rydberg constant and Lamb shifts. *Eur. Phys. J. D*, 12:61–93, 2000.

[111] O. Arnoult, F. Nez, L. Julien, and F. Biraben. Optical frequency measurement of the 1S–3S two-photon transition in hydrogen. *Eur. Phys. J. D*, 60:243–256, 2010.

[112] A. Antognini *et al.* Proton Structure from the Measurement of 2S-2P Transition Frequencies of Muonic Hydrogen. *Science*, 339:417–420, 2013.

[113] H. Kogelnik and T. Li. Laser Beams and Resonators. *Appl. Opt.*, 5:1550–1567, 1966.

[114] F. Biraben. Efficacité des systèmes unidirectionnels utilisables dans les lasers en anneau. *Optics Comm.*, 29:353–356, 1979.

[115] A. Balbin Villaverde and E. C. C. Vasconcellos. Magnetooptical dispersion of Hoya glasses: AOT-5, AOT-44B, and FR-5. *Appl. Opt.*, 21:1347–1348, 1982.

[116] B. Cagnac and J.-P. Faroux. *Lasers: interaction lumière-atomes*. Savoirs actuels. EDP Science, 2002.

[117] S. Bourzeix, M. D. Plimmer, F. Nez, L. Julien, and F. Biraben. Efficient frequency doubling of a continuous wave titanium: sapphire laser in an external enhancement cavity. *Opt. Commun.*, 99:89–94, 1993.

[118] K. S. E. Eikema, W. Ubachs, W. Vassen, and W. Hogervorst. Lamb shift measurement in the 1 ^{1}S ground state of helium. *Phys. Rev. A*, 55:1866–1884, 1997.

[119] K. Danzmann, M. S. Fee, and S. Chu. Doppler-free laser spectroscopy of positronium and muonium: Reanalysis of the 1S-2S measurements. *Phys. Rev. A*, 39:6072–6073(R), 1989.

[120] G. Hagel, C. Nesi, L. Jozefowski, C. Schwob, F. Nez, and F. Biraben. Accurate measurement of the frequency of the 6S–8S two-photon transitions in cesium. *Opt. Commun.*, 160:1–4, 1999.

[121] R. E. Honig and D. A. Kramer. Vapor Pressure Data for the Solid and Liquid Elements. *RCA Review*, 30:285–305, 1969.

Part VI

Appendices

Appendix A

Wave functions for hydrogen-like atoms

We reproduce here a part of appendix B-3 of *Mécanique quantique* by Albert Messiah [18]: it gives the general expression of the wave functions for hydrogen-like atoms, which can be used for both positronium and hydrogen. In spherical coordinates, the general form of the wave function for the hydrogen-like atoms is:

$$\psi_{nlm}(r,\theta,\varphi) \;=\; a^{-\frac{3}{2}} N_{nl} F_{nl}\left(\frac{2r}{na}\right) Y_{lm}(\theta,\varphi), \tag{A.1}$$

where a is equal to $\frac{\hbar^2}{Z\mu e^2}$, with Z the charge of the nucleus and μ the reduced mass of the "electron"; in the case of the hydrogen atom, H, $Z = 1$ and $\mu = 1$, while for positronium, Ps, we have $Z = 1$ and $\mu = \frac{1}{2}$. We introduce $\rho = \frac{r}{a}$: $\rho_{Ps} = \frac{1}{2}\rho_H$. The coefficient $N_n l$ is equal to:

$$N_{nl} \;=\; \frac{2}{n^2}\sqrt{\frac{(n-l-1)!}{[(n+l)!]^3}}, \tag{A.2}$$

and $F_{nl}\left(\frac{2\rho}{n}\right)$ can be computed with the following equation

$$F_{nl}(x) \;=\; x^l e^{-\frac{1}{2}x} L_{n-l-1}^{2l+1}(x), \tag{A.3}$$

where $L_{n-l-1}^{2l+1}(x)$ is a generalised Laguerre polynomial defined as

$$L_{n-l-1}^{2l+1}(x) \;=\; (n+l)!\frac{1}{(n-l-1)!} e^x x^{-(2l+1)} \frac{d^{n-l-1}}{dx^{n-l-1}}\left(x^{n+l} e^{-x}\right). \tag{A.4}$$

One should note that, regarding the generalised Laguerre polynomials, there is a difference between the conventions used by Messiah in [18] (L_k^{2l+1}) and by Abramowitz and Stegun in [80] ($\mathcal{L}_k^{(2l+1)}$). The relation between the two convention is the following:

$$L_k^{2l+1}(x) \;=\; (2l+1+k)!\; \mathcal{L}_k^{(2l+1)}(x). \tag{A.5}$$

Appendix B

Reaction thresholds

B.1 Thresholds of the GBAR reactions

B.1.1 Antihydrogen formation

In the reaction of antihydrogen formation

$$\bar{p} \ + \ \mathrm{Ps}(n_p) \ \rightarrow \ \bar{\mathrm{H}}(n_h) \ + \ e^{-}, \tag{B.1}$$

the available energy in the centre of mass of the initial state at rest is equal to the energy in level n_p of the positronium:

$$-\frac{1}{4n_p^2} \tag{B.2}$$

in atomic units. This energy is sufficient to produce antihydrogen if and only if

$$-\frac{1}{4n_p^2} \geq -\frac{1}{2n_h^2}. \tag{B.3}$$

This gives a simple condition on the principle quantum numbers of Ps and $\bar{\mathrm{H}}$ for the latter to be produced at zero impact kinetic energy:

$$n_p \geq \frac{n_h}{\sqrt{2}}. \tag{B.4}$$

From this formula (but also from the energy diagrams of hydrogen and positronium), one can see that ground state antihydrogen can always be produced. If the channel is not open with positronium and antiproton being at rest, then the minimal additional energy needed in the centre of mass, T_{CM} is

$$T_{CM} = +\frac{1}{4n_p^2} - \frac{1}{2n_h^2}. \tag{B.5}$$

Table B.1 summarises the values of T_{CM} depending on n_p and n_h. In the centre of mass, T_{CM} is almost equal to the kinetic energy of the positronium. This table also gives the equivalent threshold energy in the laboratory frame, T_{3B}, where the positronium is almost at rest (a few tens of meV compared to the keV energy of the antiproton).

n_p	n_h	T_{CM} (eV)	T_{3B} (keV)
	1	0	0
	2	3.401	3.122
1	3	5.291	4.858
	4	5.953	5.465
	5	6.259	5.746
	1 & 2	0	0
2	3	0.189	0.174
	4	0.850	0.780
	5	1.156	1.061
3	1 to 4	0	0
	5	0.212	0.195

Table B.1: Thresholds values for the 3-body reaction of antihydrogen production: T_{CM} in the centre of mass and T_{3B} for the antiproton energy in the laboratory frame.

B.1.2 Antihydrogen plus formation

Similarly to the 3-body reaction, the 4-body reaction of antihydrogen plus formation,

$$\bar{\mathrm{H}}(n_h) \ + \ \mathrm{Ps}(n_p) \ \rightarrow \ \bar{\mathrm{H}}^+ \ + \ e^-, \tag{B.6}$$

sometimes need extra kinetic energy to happen, resulting in a threshold for the reaction. In the centre of mass, when the antihydrogen atom and the positronium are at rest, the available energy is

$$-\frac{1}{2n_h^2} - \frac{1}{4n_p^2}. \tag{B.7}$$

In these conditions, to form the $\bar{\mathrm{H}}^+$ ion which binding energy is 0.5277 au, the principal quantum numbers must fulfil the following relation:

$$\frac{1}{2n_h^2} + \frac{1}{4n_p^2} \leq \ 0.5277. \tag{B.8}$$

This relation is verified for any state of positronium, provided that $n_h \geq 2$ for the antihydrogen. When the antihydrogen is in its ground state, the additional kinetic energy T_{CM} required to make the reaction is

$$T_{CM} = \frac{1}{4n_p^2} + \frac{1}{2n_h^2} \ - \ 0.5277. \tag{B.9}$$

The numerical values of the energy thresholds are given in table B.2, for the values of n_p and n_h that have been considered throughout this thesis. This was obtained using the exact value of the H^- binding energy; for the three wave functions that we employed for H^-, the values of the thresholds are shifted by 0.373, 0.049 and 0.018 eV in the centre of mass respectively for the UC, CC and LS wave functions.

B.2 Thresholds of the break-up reactions

For the 3-body reaction of anithydrogen production, the only break-up channel corresponds to the break-up of the positronium atom:

$$\mathrm{Ps}(n_p) \ + \ \bar{p} \ \rightarrow \ e^- \ + \ e^+ \ + \bar{p}. \tag{B.10}$$

n_p	n_h	T_{CM} (eV)	T_{4B} (keV)
1	1	6.049	5.553
1	≥ 2	0	0
2	1	0.947	0.869
2	≥ 2	0	0
3	1	0.002	0.002
3	≥ 2	0	0

Table B.2: Thresholds values for the 4-body reaction of antihydrogen plus production: T_{CM} in the centre of mass and T_{4B} for the antihydrogen energy in the laboratory frame.

This occurs as soon as the kinetic energy in the centre of mass is equal to the binding energy of the positronium:

$$T_{CM}^{break} = \frac{1}{4n_p^2}. \tag{B.11}$$

Numerical values are given in table B.3.

n_p	T_{CM}^{break} (eV)	T_{3B}^{break} (keV)
1	6.803	6.246
2	1.701	1.562
3	0.756	0.694

Table B.3: Break-up energy values for the 3-body reaction: T_{CM}^{break} in the centre of mass and T_{3B}^{break} for the antiproton energy in the laboratory frame.

In the case of the 4-body reaction, there are three different break-up channels:

$$\bar{\mathrm{H}}(n_h) \ + \ \mathrm{Ps}(n_p) \ \rightarrow \ \bar{\mathrm{H}}(n_h') \ + \ e^- \ + \ e^+ \tag{B.12}$$

$$\bar{\mathrm{H}}(n_h) \ + \ \mathrm{Ps}(n_p) \ \rightarrow \ \bar{p} \ + \ e^+ \ + \ \mathrm{Ps}(n_p') \tag{B.13}$$

$$\bar{\mathrm{H}}(n_h) \ + \ \mathrm{Ps}(n_p) \ \rightarrow \ \bar{p} \ + \ e^+ \ + \ e^- \ + \ e^+ \tag{B.14}$$

The break-up channel B.12 opens as soon as the available kinetic energy in the centre of mass $T_{CM}^{break,1}$ verifies:

$$T_{CM}^{break,1} - \ \frac{1}{4n_p^2} \ - \ \frac{1}{2n_h^2} \ = - \ \frac{1}{2n_h'^2}. \tag{B.15}$$

For channel B.13, $T_{CM}^{break,2}$ is given by

$$T_{CM}^{break,2} - \ \frac{1}{4n_p^2} \ - \ \frac{1}{2n_h^2} \ = - \ \frac{1}{4n_p'^2} \ ; \tag{B.16}$$

and for channel B.14, $T_{CM}^{break,3}$ simply verifies:

$$T_{CM}^{break,3} - \ \frac{1}{4n_p^2} \ - \ \frac{1}{2n_h^2} \ = \ 0. \tag{B.17}$$

In the following tables, only a few values will be given, for threshold remaining below about 10 keV antiproton energy, since this is the energy range of interest for GBAR, and limited to n_h

n_p	n_h	n'_h	$T_{CM}^{break,1}$ (eV)	$T_{3B}^{break,1}$ (keV)
1	n_h	n_h	6.803	6.246
1	2	1	0	0
1	2	3	8.688	7.976
1	3	1	0	0
1	3	2	4.913	4.511
2	n_h	n_h	1.701	1.562
2	2	3	3.589	3.295
2	3	1	0	0
2	3	2	0	0
3	n_h	n_h	0.756	0.694
3	1	2	10.95	10.05
3	2	1	0	0
3	2	3	2.646	2.429
3	3	1	0	0
3	3	2	0	0

Table B.4: Break-up energy values corresponding to the break-up channel B.12: $T_{CM}^{break,1}$ is the value in the centre of mass and $T_{4B}^{break,1}$ for the antihydrogen energy in the laboratory frame.

n_h	n_p	n'_p	$T_{CM}^{break,2}$ (eV)	$T_{3B}^{break,2}$ (keV)
1	2	1	8.504	7.807
1	3	1	7.559	6.939
2	n_p	n_p	3.401	3.122
2	1	2	8.504	7.807
2	1	3	9.448	8.674
2	2	1	0	0
2	2	3	4.346	3.990
2	3	1	0	0
2	3	2	2.457	2.255
3	n_p	n_p	1.512	1.388
3	1	2	6.614	6.072
3	1	3	7.559	6.939
3	2	1	0	0
3	2	3	2.457	2.255
3	3	1	0	0
3	3	2	0.567	0.520

Table B.5: Break-up energy values corresponding to the break-up channel B.13: $T_{CM}^{break,2}$ is the value in the centre of mass and $T_{4B}^{break,2}$ for the antihydrogen energy in the laboratory frame.

and $n'_h \leq 3$.

From this results, it should be noticed that the break-up channels opens at very low energies when the positronium is excited, in particular for $n_p = 3$, and this is true for both reactions. However, when working at 1 keV for Ps($3d$) or 2 keV for Ps($2p$), we remain below most of the

n_h	n_p	$T_{CM}^{break,3}$ (eV)	$T_{3B}^{break,3}$ (keV)
2	1	10.204	9.368
2	2	5.102	4.684
2	3	4.157	3.817
3	1	8.315	7.633
3	2	3.212	2.949
3	3	2.268	2.082

Table B.6: Break-up energy values corresponding to the break-up channel B.14: $T_{CM}^{break,3}$ is the value in the centre of mass and $T_{4B}^{break,3}$ for the antihydrogen energy in the laboratory frame.

break-up channel thresholds. In fact, for the second reaction of $\bar{H}^+$ production, we remember that the almost only ground state antihydrogen leads to significant cross sections, and in that case, only the break-up channel B.12 – which is the positronium ionisation channel – is opened at the optimal antiproton energies found in this thesis. For the first reaction of antihydrogen production, the break-up channel is also the positronium ionisation, and it occurs to happen just below or above the optimal antiproton energy values. It could then be worth computing the cross section for these particular break-up channels (B.10 and B.12).

A last comment on the break-up channels concerns future work on the GBAR cross sections that have been initiated by collaborators in Strasbourg. Due to these many break-up channels opened at zero or very low energies, the cross section calculations based of the Faddeev equations that they have undertaken cannot be done for some excited states of positronium and will have a very limited energy range.

Appendix C

Mathematical tools

In part II of the thesis, we used the Wigner symbols in the analytical expressions of the cross sections. These symbols are related to the Clebsch-Gordan coefficients, but with their more graphical disposal, they helps to immediately visualise and identify the relations between the angular momenta. Following appendix C of *Mécanique quantique* by Messiah [89], we give here the most common definitions and properties of the Wigner symbols and the relations that we used to compute the cross sections. More details can be found in the aforementioned reference.

C.1 *3j* symbols

The first and most important symbols introduced are the *3j* Wigner symbols. They appear when three angular momentum are coupled and are therefore directly related to the Clesch-Gordan coefficients. For a direct comparison with the cross sections, we will work here with the orbital angular momenta, but every formula given can be used with the total angular momenta.

Considering two quantum systems with respective orbital angular momenta l_1 and l_2 (and magnetic quantum numbers $-l_1 \leq m_1 \leq l_1$ and $-l_2 \leq m_2 \leq l_2$); the reunion of the two systems has an orbital angular momentum $L = l_1 + l_2$ and magnetic quantum number M. This global system can be described by the operators $\mathbf{l_1}^2$, $\mathbf{l_2}^2$, $\mathbf{l_1}_z$ and $\mathbf{l_2}_z$ and has $(2l_1{+}1)(2l_2{+}1)$ eigenvectors written as $|l_1 l_2 m_1 m_2\rangle$, but it can also be described with the operators $\mathbf{l_1}^2$, $\mathbf{l_2}^2$, $\mathbf{L}^2$ and $\mathbf{L}_z$, in which case the eigenvectors are noted $|l_1 l_2 L M\rangle$. These two sets of eigenvectors are linked by a unitary transformation:

$$|l_1 l_2 L M\rangle \;=\; \sum_{m_1 m_2} \langle l_1 l_2 m_1 m_2 | J M\rangle \, |l_1 l_2 m_1 m_2\rangle \,. \tag{C.1}$$

The coefficients $\langle l_1 l_2 m_1 m_2 | J M\rangle$ are the Clebsch-Gordan coefficients, and the Wigner *3j* symbols are defined as

$$\begin{pmatrix} l_1 & l_2 & L \\ m_1 & m_2 & -M \end{pmatrix} \equiv \frac{(-1)^{l_1 - l_2 + M}}{\sqrt{2L+1}} \langle l_1 l_2 m_1 m_2 | J M\rangle \,. \tag{C.2}$$

In the following, we re-introduce the notation used in part II: $\hat{l} = 2l + 1$.

In general, for a *3j* symbol written

$$\begin{pmatrix} l_1 & l_2 & l_3 \\ m_1 & m_2 & m_3 \end{pmatrix}, \tag{C.3}$$

the orbital angular momenta verify the inequalities:

$$\begin{array}{l} |l_1 - l_2| \leq l_3 \leq l_1 + l_2; \\ |l_1 - l_3| \leq l_2 \leq l_1 + l_3; \\ |l_2 - l_3| \leq l_1 \leq l_2 + l_3; \end{array} \tag{C.4}$$

and the relation $m_1+m_2+m_3 = 0$. The Wigner *3j* symbol is invariant with a circular permutation of its columns; exchanging two columns leads to the appearance of a factor $(-1)^{l_1+l_2+l_3}$. If one of the orbital angular momentum is equal to zero, for instance l_3, then we have $l_1 = l_2$ and $m_1 = -m_2$, and the value of the *3j* symbol is

$$\begin{pmatrix} l_1 & l_1 & 0 \\ m_1 & -m_1 & 0 \end{pmatrix} = \frac{(-1)^{l-m}}{\sqrt{\hat{l}}}. \tag{C.5}$$

If $m_1 = m_2 = m_3 = 0$, then the *3j* symbol is null when the sum $l_1 + l_2 + l_3$ is odd.

From the orthogonality relations satisfied by the Clesch-Gordan coefficients, we deduce the following relations for *3j* symbols:

$$\sum_{m_1=-l_1}^{l_1} \sum_{m_2=-l_2}^{l_2} \begin{pmatrix} l_1 & l_2 & l_3 \\ m_1 & m_2 & m_3 \end{pmatrix} \begin{pmatrix} l_1 & l_2 & l_4 \\ m_1 & m_2 & m_4 \end{pmatrix} = \frac{1}{\hat{l_3}} \delta_{l_3 l_4} \delta_{m_3 m_4} \tag{C.6}$$

and

$$\sum_{l_3=|l_1-l_2|}^{l_1+l_2} \sum_{m_3=-l_3}^{l_3} \hat{l_3} \begin{pmatrix} l_1 & l_2 & l_3 \\ m_1 & m_2 & m_3 \end{pmatrix} \begin{pmatrix} l_1 & l_2 & l_3 \\ m'_1 & m'_2 & m_3 \end{pmatrix} = \delta_{m_1 m'_1} \delta_{m_2 m'_2}. \tag{C.7}$$

In the analytical developments of the cross sections, the *3j* symbols were also used to express the product of two spherical harmonics or the composition of three spherical harmonics. We have:

$$Y_{l_1 m_1}(\Omega) Y_{l_1 m_1}(\Omega) = \sum_{L=|l_1-l_2|}^{l_1+l_2} \sum_{M=-L}^{L} (-1)^M \left(\frac{\hat{l_1}\hat{l_2}\hat{L}}{4\pi} \right)^{\frac{1}{2}} \begin{pmatrix} l_1 & l_2 & L \\ 0 & 0 & 0 \end{pmatrix} \begin{pmatrix} l_1 & l_2 & L \\ m_1 & m_2 & M \end{pmatrix} Y_{LM}(\Omega) \tag{C.8}$$

and

$$\int Y_{l_1 m_1}(\Omega) Y_{l_1 m_1}(\Omega) Y_{l_3 m_3}(\Omega) d\Omega = \left(\frac{\hat{l_1}\hat{l_2}\hat{l_3}}{4\pi} \right)^{\frac{1}{2}} \begin{pmatrix} l_1 & l_2 & l_3 \\ 0 & 0 & 0 \end{pmatrix} \begin{pmatrix} l_1 & l_2 & l_3 \\ m_1 & m_2 & m_3 \end{pmatrix}. \tag{C.9}$$

C.2 *6j* symbols

The *6j* symbols of Wigner correspond to the coupling of four (orbital) angular momenta. In the computation of the cross sections, they are introduced because of special relations appearing between the *3j* symbols. For instance, we have:

$$\begin{aligned} \sum_{m_1 m_2 M_1 M_2 M_3} (-1)^{L_1+L_2+L_3+M_1+M_2+M_3} & \begin{pmatrix} L_1 & L_2 & l_3 \\ M_1 & -M_2 & m_3 \end{pmatrix} \begin{pmatrix} L_2 & L_3 & l_1 \\ M_2 & -M_3 & m_1 \end{pmatrix} \\ & \times \begin{pmatrix} L_3 & L_1 & l_2 \\ M_3 & -M_1 & m_2 \end{pmatrix} \begin{pmatrix} l_1 & l_2 & l_4 \\ m_1 & m_2 & m_4 \end{pmatrix} \end{aligned} \tag{C.10}$$

$$= \delta_{l_3 l_4} \delta_{m_3 m_4} \frac{1}{\hat{l_3}} \begin{Bmatrix} l_1 & l_2 & l_3 \\ L_1 & L_2 & L_3 \end{Bmatrix}, \tag{C.11}$$

or

$$\sum_{M_1M_2M_3}(-1)^{L_1+L_2+L_3+M_1+M_2+M_3}\begin{pmatrix} L_1 & L_2 & l_3 \\ M_1 & -M_2 & m_3 \end{pmatrix} \times\begin{pmatrix} L_2 & L_3 & l_1 \\ M_2 & -M_3 & m_1 \end{pmatrix}\begin{pmatrix} L_3 & L_1 & l_2 \\ M_3 & -M_1 & m_2 \end{pmatrix} = \begin{pmatrix} l_1 & l_2 & l_3 \\ m_1 & m_2 & m_3 \end{pmatrix}\begin{Bmatrix} l_1 & l_2 & l_3 \\ L_1 & L_2 & L_3 \end{Bmatrix}. \tag{C.12}$$

The *6j* symbols are invariant when two column are exchanged and by the exchange of two orbital angular momentum from the first row with the corresponding two placed in the row below. The inequality relations between the orbital angular momentum can be deduced from the *3j* symbols. If one of the angular momentum is null, the *6j* symbol is easily computed; for example:

$$\begin{Bmatrix} l_1 & l_2 & 0 \\ L_1 & L_2 & L_3 \end{Bmatrix} = (-1)^{l_1+L_1+L_3}\frac{\delta_{l_1l_2}\delta_{L_1L_2}}{(\hat{l_1}\hat{L_1})^{\frac{1}{2}}} \tag{C.13}$$

with $|l_1 - L_1| \leq L_3 \leq l_1 + L_1$.

C.3 *9j* symbols

Finally, when we computed the cross sections for the antihydrogen ion formation, we also introduced the *9j* symbols, which arise from the coupling of five orbital angular momenta. In particular, the *9j* symbol appeared with the following relation obtained on *3j* symbols:

$$\sum_{m_1m_2m_3m_4M_{12}M_{34}}\begin{pmatrix} l_1 & l_2 & L_{12} \\ m_1 & m_2 & M_{12} \end{pmatrix}\begin{pmatrix} l_3 & l_4 & L_{34} \\ m_3 & m_4 & M_{34} \end{pmatrix} \times\begin{pmatrix} l_1 & l_3 & L_{13} \\ m_1 & m_3 & M_{13} \end{pmatrix}\begin{pmatrix} l_2 & l_4 & L_{24} \\ m_2 & m_4 & M_{24} \end{pmatrix}\begin{pmatrix} L_{12} & L_{34} & L \\ M_{12} & M_{34} & M \end{pmatrix} = \begin{pmatrix} L_{13} & L_{24} & L \\ M_{13} & M_{24} & M \end{pmatrix}\begin{Bmatrix} l_1 & l_2 & L_{12} \\ l_3 & l_4 & L_{34} \\ L_{13} & L_{24} & L \end{Bmatrix}. \tag{C.14}$$

The *9j* symbol is invariant by reflection with respect to its diagonals and, when two columns or rows are exchanged, it is multiplied by $(-1)^{\Sigma}$, where Σ is the sum of all the orbital angular momenta. Finally, when one orbital angular momentum is equal to zero, we have:

$$\begin{Bmatrix} l_1 & l_2 & L_{12} \\ l_3 & l_4 & L_{34} \\ L_{13} & L_{24} & 0 \end{Bmatrix} = \delta_{L_{12}L_{34}}\delta_{L_{13}L_{24}}\frac{(-1)^{l_2+l_3+L_{12}+L_{13}}}{(\hat{L}_{12}\hat{L}_{13})^{\frac{1}{2}}}\begin{Bmatrix} l_1 & l_2 & L_{12} \\ l_4 & l_3 & L_{13} \end{Bmatrix}. \tag{C.15}$$

Appendix D

CDW–FS analytical expressions for particular cases

D.1 Particular cases of antihydrogen formation

The simplified expressions of the cross sections for different cases of excitation states of Ps or H are particularly useful in the case of the 3-body reaction since they do not depend on the magnetic quantum numbers any more: for these cases, they thus limit the number of partial cross sections to compute and the computation itself is also faster.

D.1.1 Only *s*-states of positronium

This case corresponds to $l_p = 0$ and $l_h \geq 0$, and is very useful to compute the GBAR cross section (since there is no restriction on the produced states of antihydrogen) in the case of ground state positronium, and also *2S* and *3S* excited states. In this particular case, the transition matrix element reads

$$T_{\alpha\beta}^{(-)} = \frac{(4\pi)^{\frac{3}{2}}}{k_\alpha k_+ k_-}\ \hat{l}_h^{\frac{1}{2}}\ \sum_{l_i L}\ i^{l_i}\ e^{i\delta_{l_i}} \hat{l}_i \hat{L}^{\frac{1}{2}}\ \mathcal{P}_{l_i L}\ Y_{L m_h}(\hat{\boldsymbol{k}_\beta}) \tag{D.1}$$

with

$$\begin{aligned}
\mathcal{P}_{l_i L} &= \sum_{l l' l_f} i^{-l-l_f}\ e^{i(\delta_l + \delta_{l_f})}\ \mathcal{A}_{l_i L}^{l l' l_f}\ \mathcal{R}_{l_i l_f}^{l l'}, \\
\mathcal{A}_{l_i L}^{l l' l_f} &= (-1)^{L+l'}\ \hat{l}\hat{l}'\hat{l}_f \begin{pmatrix} l_h & l & l' \\ 0 & 0 & 0 \end{pmatrix} \begin{pmatrix} l_i & l' & l_f \\ 0 & 0 & 0 \end{pmatrix} \\
&\times \begin{pmatrix} l & l_f & L \\ 0 & 0 & 0 \end{pmatrix} \begin{pmatrix} l_i & L & l_h \\ 0 & -m_h & m_h \end{pmatrix} \begin{Bmatrix} l_i & L & l_h \\ l & l' & l_f \end{Bmatrix}, \\
\mathcal{R}_{l_i l_f}^{l l'} &= \int_0^\infty dR\ F_{l_f}(k_+ R)\ \mathcal{V}_{l l'}(R)\ F_{l_i}(k_\alpha R), \\
\mathcal{V}_{l l'}(R) &= \int_0^\infty dr\ r\ F_l(k_- r)\ \mathcal{J}_{l'}(r, R)\ R_{n_h l_h}(r), \\
\mathcal{J}_{l'}(r, R) &= \frac{1}{2} \int_{-1}^{1} du\ R_{n_p 0}(\rho)\ \left(\frac{1}{R} - \frac{1}{\rho}\right) P_{l'}(u).
\end{aligned} \tag{D.2}$$

The differential and total cross sections are given by

$$\left[\frac{d\sigma}{d\Omega}\right]_{n_h l_h m_h} = \frac{1}{4\pi^2}\,\frac{k_\beta}{k_\alpha}\,\mu_\alpha\mu_\beta\,\left|\,T^{(-)}_{\alpha\beta}\right|^2 \tag{D.3}$$

and

$$\begin{aligned}\sigma^{3B,1}_{n_h l_h;\ n_p 0} &= \frac{1}{\hat{l}_h}\,\frac{1}{4\pi^2}\,\frac{k_\beta}{k_\alpha}\,\mu_\alpha\mu_\beta\,\sum_{m_h}\int d\boldsymbol{k}_\beta\,\left|T^{(-)}_{\alpha\beta}\right|^2 \\ &= \frac{1}{4\pi^2}\,\frac{k_\beta}{k_\alpha}\,\mu_\alpha\mu_\beta\,\frac{(4\pi)^3}{(k_\alpha k_+ k_-)^2}\,\sum_{l_i L}\,\hat{l}_i\hat{L}\,\left(\tilde{\mathcal{P}}^*_{l_i L}\times\tilde{\mathcal{P}}_{l_i L}\right),\end{aligned} \tag{D.4}$$

with

$$\begin{aligned}\tilde{\mathcal{P}}_{l_i L} &= \sum_{l l' l_f}\,i^{-l-l_f}\,e^{i(\delta_l+\delta_{l_f})}\,(-1)^{l'}\,\hat{l}_f\hat{l}\hat{l}'\,\mathcal{R}^{l l'}_{l_i l_f} \\ &\quad\times\begin{pmatrix} l_h & l & l' \\ 0 & 0 & 0\end{pmatrix}\begin{pmatrix} l_i & l' & l_f \\ 0 & 0 & 0\end{pmatrix}\begin{pmatrix} l & l_f & L \\ 0 & 0 & 0\end{pmatrix}\begin{Bmatrix} l_i & L & l_h \\ l & l' & l_f\end{Bmatrix}.\end{aligned} \tag{D.5}$$

D.1.2 Only *s*-states of antihydrogen

Another simplified expression of the cross section is given here for $l_h = 0$ and $l_p \geq 0$. The production of only s-states of antihydrogen has no real interest for GBAR. However, when the inverse reaction of positronium formation is considered, this case can be usefully compared to theoretical and experimental studies which have used only ground state (anti)hydrogen. We have

$$T^{(-)}_{\alpha\beta} = \frac{(4\pi)^{\frac{3}{2}}}{k_+ k_- k_\alpha}\,(\hat{l}_p!)^{\frac{1}{2}}\hat{l}_p^{\frac{1}{2}}\,\sum_{l_i L}(-1)^{l_i}\,i^{l_i}\,e^{i\delta_{l_i}}\,\hat{L}^{\frac{1}{2}}\hat{l}_i\,\mathcal{U}_{l_i L}\,Y_{L\ -m_p}(\boldsymbol{k}_\beta), \tag{D.6}$$

with

$$\begin{aligned}\mathcal{U}_{l_i L} &= \sum_{l_f l l' L'}\sum_{\lambda=0}^{l_p}\,i^{-l-l_f}\,e^{i(\delta_l+\delta_{l_f})}\,\mathcal{C}^{l_f l l' L'\lambda}_{l_i L}\,\mathcal{R}^{\lambda l l'}_{l_f l_i}, \\ \mathcal{C}^{l_f l l' L'\lambda}_{l_i L} &= \frac{\hat{l}_f\hat{l}\hat{l}'\hat{L}'}{((2\lambda)!(2(lp-\lambda))!)^{\frac{1}{2}}}\,\begin{pmatrix} l_f & l & L \\ 0 & 0 & 0\end{pmatrix}\begin{pmatrix} l_p-\lambda & l' & L' \\ 0 & 0 & 0\end{pmatrix} \\ &\quad\times\begin{pmatrix} \lambda & l & L \\ 0 & 0 & 0\end{pmatrix}\begin{pmatrix} l_f & L' & l_i \\ 0 & 0 & 0\end{pmatrix}\begin{pmatrix} L & l_p & l_i \\ m_p & -m_p & 0\end{pmatrix} \\ &\quad\times\begin{Bmatrix} L & l_p & l_i \\ L' & l_f & l\end{Bmatrix}\begin{Bmatrix} l & L' & l_p \\ l_p-\lambda & \lambda & l'\end{Bmatrix}, \\ \mathcal{R}^{\lambda l l'}_{l_f l_i} &= \int_0^\infty dR\,R^{l_p-\lambda}\,F_{l_f}(k_+R)\,\mathcal{V}_{\lambda l l'}(R)\,F_{l_i}(k_\alpha R), \\ \mathcal{V}_{\lambda l l'}(R) &= \int_0^\infty dr\,r^{\lambda+1}\,F_l(k_-r)\,\mathcal{J}^{l_p}_{l'}(r,R)\,R_{n_h 0}(r), \\ \mathcal{J}^{l_p}_{l'}(r,R) &= \frac{1}{2}\int_{-1}^{1}du\,\rho^{-l_p}\,R_{n_p l_p}(\rho)\,\left(\frac{1}{R}-\frac{1}{\rho}\right)\,P_{l'}(u).\end{aligned} \tag{D.7}$$

This gives a total cross section summed over the degenerated states of the positronium atom

$$\begin{aligned}\sigma^{3B,1}_{n_h0;\ n_pl_p} &= \frac{1}{4\pi^2}\,\frac{k_\beta}{k_\alpha}\,\mu_\alpha\mu_\beta\,\sum_{m_p}\int d\boldsymbol{k}_\beta\,\left|T^{(-)}_{\alpha\beta}\right|^2 \\ &= \frac{1}{4\pi^2}\,\frac{k_\beta}{k_\alpha}\,\mu_\alpha\mu_\beta\,\frac{(4\pi)^3}{(k_+k_-k_\alpha)^2}\,\hat{l}_p!\hat{l}_p\,\sum_{l_iL}\,\hat{l}_i\hat{L}\,\left(\tilde{\mathcal{U}}^*_{l_iL}\times\tilde{\mathcal{U}}_{l_iL}\right),\end{aligned} \tag{D.8}$$

with

$$\begin{aligned}\tilde{\mathcal{U}}_{l_iL} &= \sum_{l_fll'L'}\sum_{\lambda=0}^{l_p}\,i^{-l-l_f}\,e^{i(\delta_l+\delta_{l_f})}\,\tilde{\mathcal{C}}^{l_fll'L'\lambda}_{l_iL}\,\mathcal{R}^{\lambda ll'}_{l_fl_i}, \\ \tilde{\mathcal{C}}^{l_fll'L'\lambda}_{l_iL} &= \frac{\hat{l}_f\hat{l}\hat{l}'\hat{L}'}{((2\lambda)!(2(lp-\lambda))!)^{\frac{1}{2}}}\,\begin{pmatrix} l_f & l & L\\ 0 & 0 & 0\end{pmatrix}\begin{pmatrix} l_p-\lambda & l' & L'\\ 0 & 0 & 0\end{pmatrix}\begin{pmatrix} \lambda & l & L\\ 0 & 0 & 0\end{pmatrix} \\ &\quad\times\begin{pmatrix} l_f & L' & l_i\\ 0 & 0 & 0\end{pmatrix}\begin{Bmatrix} L & l_p & l_i\\ L' & l_f & l\end{Bmatrix}\begin{Bmatrix} l & L' & l_p\\ l_p-\lambda & \lambda & l'\end{Bmatrix}.\end{aligned} \tag{D.9}$$

D.1.3 *s*-states of both positronium and antihydrogen

This simple case in very convenient to compute the cross section for ground state antihydrogen formation from ground state positronium. Though, alone, it has no interest for the GBAR problem, this case is the most investigated in the literature and having a simplified expression of the cross section, easy and fast to numerically compute, allows for rapid comparison between CDW–FS and other theories. In this case we thus have $l_p = l_h = 0$, and the transition matrix element writes

$$T^{(-)}_{\alpha\beta} = \frac{(4\pi)^{\frac{3}{2}}}{k_+k_-k_\alpha}\,\sum_{l_i}\,i^{l_i}\,e^{i\delta_{l_i}}\,\hat{l}_i^{\frac{1}{2}}\,\mathcal{X}_{l_i}\,Y_{l_i0}(\boldsymbol{k}_\beta), \tag{D.10}$$

with

$$\begin{aligned}\mathcal{X}_{l_i} &= \sum_{l_fl}\,i^{-l-l_f}\,e^{i(\delta_l+\delta_{l_f})}\,\mathcal{D}^{l_fl}_{l_i}\,\mathcal{R}_{l_fll_i}, \\ \mathcal{D}^{l_fl}_{l_i} &= \hat{l}_f\hat{l}\,\begin{pmatrix} l_i & l & l_f\\ 0 & 0 & 0\end{pmatrix}^2, \\ \mathcal{R}_{l_fll_i} &= \int_0^\infty dR\;F_{l_f}(k_+R)\;\mathcal{V}_l(R)\;F_{l_i}(k_\alpha R), \\ \mathcal{V}_l(R) &= \int_0^\infty dr\;F_l(k_-r)\;\mathcal{J}_l(r,R)\;R_{n_h0}(r), \\ \mathcal{J}_l(r,R) &= \frac{1}{2}\int_{-1}^{1}du\;R_{n_p0}(\rho)\;\left(\frac{1}{R}-\frac{1}{\rho}\right)\;P_l(u).\end{aligned} \tag{D.11}$$

The total cross section is then given by

$$\begin{aligned}\sigma^{3B,1}_{n_h0;\ n_p0} &= \frac{1}{4\pi^2}\,\frac{k_\beta}{k_\alpha}\,\mu_\alpha\mu_\beta\,\int d\boldsymbol{k}_\beta\,\left|T^{(-)}_{\alpha\beta}\right|^2 \\ &= \frac{1}{4\pi^2}\,\frac{k_\beta}{k_\alpha}\,\mu_\alpha\mu_\beta\,\frac{(4\pi)^3}{(k_+k_-k_\alpha)^2}\,\sum_{l_i}\,\hat{l}_i\left(\mathcal{X}^*_{l_i}\times\mathcal{X}_{l_i}\right). \end{aligned} \tag{D.12}$$

D.2 Particular cases of antihydrogen plus formation

D.2.1 Only *s*-states of positronium

In the case of $l_p = 0$, while $l_h \geq 0$, the different terms of the 4-body reaction can also be simplified. The pure *capture* term reads

$$\sum^{m_h}\int d\hat{\boldsymbol{k}}_\beta\;t^*_{cap,l_p=0}\times t_{cap,l_p=0} \;=\; 2\,\frac{(4\pi)^5}{(k_+k_-k_\alpha)^2}\,\hat{l}_h\,\sum_{l_iL}\hat{l}_i\hat{L}\;\left(\mathcal{P}^*_{l_iL}\times\mathcal{P}_{l_iL}\right), \tag{D.13}$$

with

$$\begin{aligned}\mathcal{P}_{l_iL} &= \sum_{l_fll'}\,i^{-l-l_f}\;e^{i(\delta_l+\delta_{l_f})}\;\mathcal{B}^{l_fll'}_{l_iL}\;\mathcal{R}^{ll'}_{l_fl_i}\;, \\ \mathcal{B}^{l_fll'}_{l_iL} &= (-1)^{l_f}\;\hat{l}_f\hat{l}\hat{l}'\begin{pmatrix} l' & l & l_h\\ 0 & 0 & 0\end{pmatrix}\begin{pmatrix} l_f & l' & l_i\\ 0 & 0 & 0\end{pmatrix}\begin{pmatrix} l & l_f & L\\ 0 & 0 & 0\end{pmatrix}\begin{Bmatrix} L & l_i & l_h\\ l' & l & l_f\end{Bmatrix}, \\ \mathcal{R}^{ll'}_{l_fl_i} &= \int_0^\infty dR\;F_{l_f}(k_+R)\;\mathcal{V}_{ll'}(R)\;F_{l_i}(k_\alpha R), \\ \mathcal{V}_{ll'}(R) &= \int_0^\infty dr_1\;r_1\;F_l(k_-r_1)\;\mathcal{L}_{n_hl_h}(r_1)\;\mathcal{J}_{l'}(r_1,R), \\ \mathcal{L}_{n_hl_h}(r_1) &= \int_0^\infty dr_2\;r_2^2\;R_{n_hl_h}(r_2)\;\tilde{h}_{l_h}(r_1,r_2), \\ \mathcal{J}_{l'}(r_1,R) &= \frac{1}{2}\int_{-1}^{1}du\;\tilde{R}_{n_p0}(\rho_1)\left(\frac{1}{R}-\frac{1}{\rho_1}\right)P_{l'}(u). \end{aligned} \tag{D.14}$$

The pure *excitation* term is given by

$$\sum_{m_h}\int d\hat{\boldsymbol{k}}_\beta\;t^*_{exc,l_p=0}\times t_{exc,l_p=0} \;=\; 2\,\frac{(4\pi)^5}{(k_+k_-k_\alpha)^2}\,\hat{l}_h\,\sum_{l_i\tilde{l}}\hat{l}_i\hat{\tilde{l}}\;\left(\tilde{\mathcal{P}}^*_{l_i\tilde{l}}\times\tilde{\mathcal{P}}_{l_i\tilde{l}}\right), \tag{D.15}$$

with

$$
\begin{aligned}
\tilde{\mathcal{P}}_{l_i\tilde{l}} &= \sum_{l_f l_t \Lambda l l' L} i^{-l-l_f}\, e^{i(\delta_l+\delta_{l_f})}\, \tilde{\mathcal{B}}^{l_f l_t \Lambda l l' L}_{l_i\tilde{l}}\, \tilde{\mathcal{R}}^{l_t \Lambda l l'}_{l_f l_i}\ , \\
\tilde{\mathcal{B}}^{l_f l_t \Lambda l l' L}_{l_i\tilde{l}} &= \hat{l}_f \hat{l}_t \hat{l} \hat{l}' \hat{L} \begin{pmatrix} l_h & \Lambda & l_t \\ 0 & 0 & 0 \end{pmatrix} \begin{pmatrix} l & l_t & l' \\ 0 & 0 & 0 \end{pmatrix} \begin{pmatrix} l' & l_i & L \\ 0 & 0 & 0 \end{pmatrix} \\
&\quad \times \begin{pmatrix} l_f & \Lambda & L \\ 0 & 0 & 0 \end{pmatrix} \begin{pmatrix} l & l_f & \tilde{l} \\ 0 & 0 & 0 \end{pmatrix} \begin{Bmatrix} \Lambda & l_f & L \\ l_t & l & l' \\ l_h & \tilde{l} & l_i \end{Bmatrix}, \\
\tilde{\mathcal{R}}^{l_t \Lambda l l'}_{l_f l_i} &= \int_0^\infty dR\ F_{l_f}(k_+ R)\ \tilde{\mathcal{V}}_{l_t \Lambda l l'}(R)\ F_{l_i}(k_\alpha R), \\
\tilde{\mathcal{V}}_{l_t \Lambda l l'}(R) &= \int_0^\infty dr_1\ r_1\ F_l(k_- r_1)\ \tilde{\mathcal{L}}^{n_h l_h}_{l_t \Lambda}(r_1, R)\ \tilde{\mathcal{J}}_{l'}(r_1, R), \\
\tilde{\mathcal{L}}^{n_h l_h}_{l_t \Lambda}(r_1, R) &= \int_0^\infty dr_2\ r_2^2\ R_{n_h l_h}(r_2)\ \left(\frac{r_<^\Lambda}{r_>^{\Lambda+1}} - \frac{\delta_{\Lambda 0}}{R} \right)\ \tilde{h}_{l_t}(r_1, r_2), \\
\tilde{\mathcal{J}}_{l'}(r_1, R) &= \frac{1}{2} \int_{-1}^{1} du\ \tilde{R}_{n_p 0}(\rho_1)\ P_{l'}(u),
\end{aligned}
\tag{D.16}
$$

and the cross terms are of the form

$$
\sum_{m_h} \int d\hat{\boldsymbol{k}}_\beta\ t^*_{cap, l_p=0} \times t_{exc, l_p=0} = 2\, \frac{(4\pi)^5}{(k_+ k_- k_\alpha)^2}\, \hat{l}_h \sum_{l_i \tilde{l}}\, \hat{l}_i \hat{\tilde{l}}\, \left(\mathcal{P}^*_{l_i\tilde{l}} \times \tilde{\mathcal{P}}_{l_i\tilde{l}} \right). \tag{D.17}
$$

The cross section is thus

$$
\begin{aligned}
\sigma^{4B,3}_{n_h l_h;\ n_p 0} &= \frac{1}{4\pi^2}\, \frac{k_\beta}{k_\alpha}\, \mu_\alpha \mu_\beta \int d\boldsymbol{k}_\beta\ \left| T^{(-)}_{\alpha\beta} \right|^2 \\
&= \frac{1}{4\pi^2}\, \frac{k_\beta}{k_\alpha}\, \mu_\alpha \mu_\beta\, \frac{2(4\pi)^5}{(k_+ k_- k_\alpha)^2}\, \hat{l}_h \\
&\quad \times \sum_{l_i \tilde{l}}\, \hat{l}_i \hat{\tilde{l}} \left(\mathcal{P}^*_{l_i\tilde{l}} \times \mathcal{P}_{l_i\tilde{l}} + \tilde{\mathcal{P}}^*_{l_i\tilde{l}} \times \tilde{\mathcal{P}}_{l_i\tilde{l}} + \left[\tilde{\mathcal{P}}^*_{l_i\tilde{l}} \times \mathcal{P}_{l_i\tilde{l}} + c.c. \right] \right).
\end{aligned}
\tag{D.18}
$$

D.2.2 Only *s*-states of antihydrogen

This case of $l_h = 0$, $l_p \geq 0$ is especially useful when only the production of $\bar{\mathrm{H}}^+$ from $\bar{\mathrm{H}}$ in its ground state is considered, for any excited state of positronium. Indeed, it has been demonstrated that excited states of antihydrogen do not contribute much to the production of $\bar{\mathrm{H}}^+$, so for faster numerical computations, this is a convenient restriction. The different terms in the total cross section now write (for any value of n_h)

$$
\sum_{m_p} \int d\hat{\boldsymbol{k}}_\beta\ t^*_{cap, l_h=0} t_{cap, l_h=0} = 2\, \frac{(4\pi)^5}{(k_+ k_- k_\alpha)^2}\, \hat{l}_p! \hat{l}_p \sum_{l_i \mathcal{L}}\, \hat{l}_i \hat{\mathcal{L}}\, \left(\mathcal{U}^*_{l_i \mathcal{L}} \times \mathcal{U}_{l_i \mathcal{L}} \right) \tag{D.19}
$$

with

$$\begin{aligned}
\mathcal{U}_{l_i\mathcal{L}} &= \sum_{l_f l l' L' \lambda} i^{-l-l_f}\; e^{i(\delta_l+\delta_{l_f})}\; \mathcal{B}_{l_i\mathcal{L}}^{l_f l l' L' \lambda}\; \mathcal{R}_{l_f l l' \lambda l_i}^{l_h=0}, \\
\mathcal{B}_{l_i\mathcal{L}}^{l_f l l' L' \lambda} &= (-1)^{l_f+L'}\; \frac{\hat{l}_f \hat{l} \hat{l}' \hat{L}'}{((2\lambda)!(2(l_p-\lambda))!)^{\frac{1}{2}}} \begin{Bmatrix} l_f & l_p-\lambda & L' \\ l & \lambda & l' \\ \mathcal{L} & l_p & l_i \end{Bmatrix} \\
&\quad \times \begin{pmatrix} l & \lambda & l' \\ 0 & 0 & 0 \end{pmatrix} \begin{pmatrix} l' & l_i & L' \\ 0 & 0 & 0 \end{pmatrix} \begin{pmatrix} l_f & l_p-\lambda & L' \\ 0 & 0 & 0 \end{pmatrix} \begin{pmatrix} l_f & l & \mathcal{L} \\ 0 & 0 & 0 \end{pmatrix}, \qquad \text{(D.20)}
\end{aligned}$$

$$\sum_{m_p} \int d\hat{\boldsymbol{k}}_\beta\; t^*_{exc,l_h=0} t_{exc,l_h=0} \;=\; 2\; \frac{(4\pi)^5}{(k_+k_-k_\alpha)^2}\; \hat{l}_p! \hat{l}_p \sum_{l_i \tilde{l}}\; \hat{l}_i \hat{\tilde{l}}\; \left(\tilde{\mathcal{U}}^*_{l_i\tilde{l}} \times \tilde{\mathcal{U}}_{l_i\tilde{l}} \right) \qquad \text{(D.21)}$$

with

$$\begin{aligned}
\tilde{\mathcal{U}}_{l_i\tilde{l}} &= \sum_{l_f l l' l_t \lambda \tilde{L} L L'} i^{-l-l_f}\; e^{i(\delta_l+\delta_{l_f})}\; \tilde{\mathcal{B}}_{l_i\tilde{l}}^{l_f l l' l_f \lambda \tilde{L} L L'}\; \tilde{\mathcal{R}}_{l_f l_t, \Lambda=l_t, l l' \lambda l_i}^{l_h=0}, \\
\tilde{\mathcal{B}}_{l_i\tilde{l}}^{l_f l l' l_f \lambda \tilde{L} L L'} &= (-1)^{\lambda+L+\tilde{L}}\; \frac{\hat{l}_f \hat{l}_t \hat{l} \hat{l}' \hat{\tilde{L}} \hat{L} \hat{L}'}{((2\lambda)!(2(l_p-\lambda))!)^{\frac{1}{2}}} \begin{pmatrix} l' & l_t & \tilde{L} \\ 0 & 0 & 0 \end{pmatrix} \begin{pmatrix} l & \lambda & \tilde{L} \\ 0 & 0 & 0 \end{pmatrix} \\
&\quad \times \begin{pmatrix} l_t & l_i & L \\ 0 & 0 & 0 \end{pmatrix} \begin{pmatrix} l' & L & L' \\ 0 & 0 & 0 \end{pmatrix} \begin{pmatrix} l_f & l_p-\lambda & L' \\ 0 & 0 & 0 \end{pmatrix} \\
&\quad \times \begin{pmatrix} l_f & l & \tilde{l} \\ 0 & 0 & 0 \end{pmatrix} \begin{Bmatrix} l_i & L' & \tilde{L} \\ l' & l_t & L \end{Bmatrix} \begin{Bmatrix} l_f & l_p-\lambda & L' \\ l & \lambda & \tilde{L} \\ \tilde{l} & l_p & l_i \end{Bmatrix}, \qquad \text{(D.22)}
\end{aligned}$$

$$\sum_{m_p} \int d\hat{\boldsymbol{k}}_\beta\; t^*_{cap,l_h=0} t_{exc,l_h=0} \;=\; 2\; \frac{(4\pi)^5}{(k_+k_-k_\alpha)^2}\; \hat{l}_p! \hat{l}_p \sum_{l_i \tilde{l}}\; \hat{l}_i \hat{\tilde{l}}\; \left(\mathcal{U}^*_{l_i\tilde{l}} \times \tilde{\mathcal{U}}_{l_i\tilde{l}} \right), \qquad \text{(D.23)}$$

and thus

$$\begin{aligned}
\sigma^{4B,3}_{n_h 0;\; n_p l_p} &= \frac{1}{4\pi^2}\; \frac{k_\beta}{k_\alpha}\; \mu_\alpha \mu_\beta\; \frac{2(4\pi)^5}{(k_-k_\alpha k_+)^2}\; \hat{l}_p! \hat{l}_p \sum_{l_i \tilde{l}}\; \hat{l}_i \hat{\tilde{l}} \\
&\quad \times \left\{ \mathcal{U}^*_{l_i\tilde{l}} \times \mathcal{U}_{l_i\tilde{l}} + \tilde{\mathcal{U}}^*_{l_i\tilde{l}} \times \tilde{\mathcal{U}}_{l_i\tilde{l}} + \left[\mathcal{U}^*_{l_i\tilde{l}} \times \tilde{\mathcal{U}}_{l_i\tilde{l}} + c.c. \right] \right\}. \qquad \text{(D.24)}
\end{aligned}$$

D.2.3 *s*-states of both positronium and antihydrogen

When both l_p and l_h are equal to zero, further simplifications can be found for the different terms of the 4-body reaction. Again, this particular case gives a rapid computation of the cross section for antihydrogen plus production from ground state positronium and ground state anithydrogen, which corresponds to the first case investigated by other works. The pure *capture* term reads

$$\int d\hat{\boldsymbol{k}}_\beta\; t^*_{cap} \times t_{cap} \;=\; 2\; \frac{(4\pi)^5}{(k_+k_-k_\alpha)^2} \sum_{l_i}\; \hat{l}_i \left(\mathcal{X}^*_{l_i} \times \mathcal{X}_{l_i} \right), \qquad \text{(D.25)}$$

with

$$\begin{aligned}
\mathcal{X}_{l_i} &= \sum_{l_f l} i^{-l-l_f}\ e^{i(\delta_l+\delta_{l_f})}\ \mathcal{B}_{l_i}^{l_f l}\ \mathcal{R}_{l_f l_i}^{l}\ , \\
\mathcal{B}_{l_i}^{l_f l} &= \hat{l}_f \hat{l} \begin{pmatrix} l_f & l & l_i \\ 0 & 0 & 0 \end{pmatrix}^2, \\
\mathcal{R}_{l_f l_i}^{l} &= \int_0^\infty dR\ F_{l_f}(k_+ R)\ \mathcal{V}_l(R)\ F_{l_i}(k_\alpha R), \\
\mathcal{V}_l(R) &= \int_0^\infty dr_1\ r_1\ F_l(k_- r_1)\ \mathcal{L}_{n_h 0}(r_1)\ \mathcal{J}_l(r_1, R), \\
\mathcal{L}_{n_h 0}(r_1) &= \int_0^\infty dr_2\ r_2^2\ R_{n_h 0}(r_2)\ \tilde{h}_0(r_1, r_2), \\
\mathcal{J}_l(r_1, R) &= \frac{1}{2}\int_{-1}^{1} du\ \tilde{R}_{n_p 0}(\rho_1) \left(\frac{1}{R} - \frac{1}{\rho_1}\right) P_l(u).
\end{aligned} \tag{D.26}$$

The pure *excitation* term is given by

$$\int d\hat{\boldsymbol{k}}_\beta\ t^*_{exc} \times t_{exc} = 2\ \frac{(4\pi)^5}{(k_+ k_- k_\alpha)^2}\ \sum_{l_i}\ \hat{l}_i\ \left(\tilde{\mathcal{X}}^*_{l_i} \times \tilde{\mathcal{X}}_{l_i}\right), \tag{D.27}$$

with

$$\begin{aligned}
\tilde{\mathcal{X}}_{l_i} &= \sum_{l_f l_t l l' L} i^{-l-l_f}\ e^{i(\delta_l+\delta_{l_f})}\ \tilde{\mathcal{B}}_{l_i}^{l_f l_t l l' L}\ \tilde{\mathcal{R}}_{l_f l_i}^{l_t l l'}\ , \\
\tilde{\mathcal{B}}_{l_i}^{l_f l_t l l' L} &= (-1)^{l_t}\ \hat{l}_f \hat{l} \hat{l}' \hat{L} \begin{pmatrix} l & l_t & l' \\ 0 & 0 & 0 \end{pmatrix} \begin{pmatrix} l' & l_i & L \\ 0 & 0 & 0 \end{pmatrix} \\
&\quad \times \begin{pmatrix} l_f & l_t & L \\ 0 & 0 & 0 \end{pmatrix} \begin{pmatrix} l & l_f & l_i \\ 0 & 0 & 0 \end{pmatrix} \begin{Bmatrix} l_f & L & l_t \\ l' & l & l_i \end{Bmatrix}, \\
\tilde{\mathcal{R}}_{l_f l_i}^{l_t l l'} &= \int_0^\infty dR\ F_{l_f}(k_+ R)\ \tilde{\mathcal{V}}_{l_t l l'}(R)\ F_{l_i}(k_\alpha R), \\
\tilde{\mathcal{V}}_{l_t l l'}(R) &= \int_0^\infty dr_1\ r_1\ F_l(k_- r_1)\ \tilde{\mathcal{L}}_{l_t}^{n_h 0}(r_1, R)\ \tilde{\mathcal{J}}_{l'}(r_1, R), \\
\tilde{\mathcal{L}}_{l_t}^{n_h 0}(r_1, R) &= \int_0^\infty dr_2\ r_2^2\ R_{n_h 0}(r_2)\ \left(\frac{r_<^{l_t}}{r_>^{l_t+1}} - \frac{\delta_{l_t 0}}{R}\right)\ \tilde{h}_{l_t}(r_1, r_2), \\
\tilde{\mathcal{J}}_{l'}(r_1, R) &= \frac{1}{2}\int_{-1}^{1} du\ \tilde{R}_{n_p 0}(\rho_1)\ P_{l'}(u),
\end{aligned} \tag{D.28}$$

and the cross terms are of the form

$$\int d\hat{\boldsymbol{k}}_\beta\ t^*_{cap} \times t_{exc} = 2\ \frac{(4\pi)^5}{(k_+ k_- k_\alpha)^2}\ \sum_{l_i}\ \hat{l}_i\ \left(\mathcal{X}^*_{l_i} \times \tilde{\mathcal{X}}_{l_i}\right). \tag{D.29}$$

This leads to the cross section

$$\begin{aligned}\sigma^{4B,3}_{n_h0;\ n_p0} &= \frac{1}{4\pi^2}\,\frac{k_\beta}{k_\alpha}\,\mu_\alpha\mu_\beta\,\int d\boldsymbol{k}_\beta\,\left|T^{(-)}_{\alpha\beta}\right|^2 \\ &= \frac{1}{4\pi^2}\,\frac{k_\beta}{k_\alpha}\,\mu_\alpha\mu_\beta\,\frac{2(4\pi)^5}{(k_+k_-k_\alpha)^2} \\ &\quad\times\sum_{l_i}\,\hat{l}_i\left(\mathcal{X}^*_{l_i}\times\mathcal{X}_{l_i}+\tilde{\mathcal{X}}^*_{l_i}\times\tilde{\mathcal{X}}_{l_i}+\left[\tilde{\mathcal{X}}^*_{l_i}\times\mathcal{X}_{l_i}+c.c.\right]\right). \qquad \text{(D.30)}\end{aligned}$$

List of Figures

1.1 The energy levels of ortho-positronium arranged according their orbital quantum number, l_p: in black, the Schrödinger levels, in blue, the fine structure obtained from [19]. In red, the ground state of para-positronium is also displayed. The transition frequencies for the transitions identified with a letter are reported in table 1.2 below. 6

1.2 Transition frequencies in MHz for several transitions in ortho-positronium and for the ground state hyperfine splitting. In [24], a wavelength measurement of the $1^3S - 2^3P$ transition is reported (243.024(0.002) nm). The last two values, computed from the values obtained with the formulas in [19] are given for information. 6

2.1 The production of $\bar{\mathrm{H}}^+$ ions in GBAR at CERN. 12

2.2 The cooling of $\bar{\mathrm{H}}^+$ ions in GBAR and the free fall of cold antihydrogen. 13

3.1 Examples of radial parts of continuum Coulomb wave functions for a 1 eV positron moving in the Coulomb potential of a proton. The first maximum of $F_l(kr)$ corresponds to the classical turning point. 23

4.1 Coordinates used for reaction (2.5). 27

4.2 Coordinates used for reaction (2.7). 32

5.1 Illustration of the f and g processes. 42

6.1 Antihydrogen production cross sections from ground state positronium as a function of antiproton impact energy. 46

6.2 Antihydrogen production cross sections from positronium excited in a state $n_p = 2$ as a function of antiproton impact energy. 47

6.3 Antihydrogen production cross sections from positronium excited in a state $n_p = 3$ as a function of antiproton impact energy. 48

6.4 Cross sections of antihydrogen production in the states $n_h = 4$ for Ps(*2p*), as a function of the antiproton impact energy. 49

6.5 Summed cross sections of antihydrogen production from Ps(*3d*), up to the states $\bar{\mathrm{H}}$(*3d*), $\bar{\mathrm{H}}$(*4f*) and $\bar{\mathrm{H}}$(*5d*), as a function of the antiproton impact energy. 49

6.6 Cross sections of antihydrogen production up to $\bar{\mathrm{H}}$(*5d*) for Ps(*1s*) to Ps(*3d*), as a function of antiproton impact energy. 50

6.7 $\bar{\mathrm{H}}$ production cross sections from ground state positronium (n_p=1), obtained in the framework of the CBA theory. For each n_h state of antihydrogen, the cross sections have been summed over the l_h states. 51

6.8 Same as for Figure 6.7 but for n_p=2. 51

6.9 Same as for Figure 6.7 but for n_p=3. 52
6.10 CBA cross sections of total antihydrogen production, the contribution of the different states of antihydrogen being summed up to $\bar{H}(4f)$, for Ps(*1s*) to Ps(*3d*), and as a function of antiproton impact energy. 53
6.11 $\bar{H}^+$ production cross sections from ground state positronium as a function of antihydrogen impact energy; the arrow indicates the threshold of the $\bar{H}(1s)$ channel. 53
6.12 $\bar{H}^+$ production cross sections from positronium excited in a state n_p=2 as a function of antihydrogen impact energy; the arrows mark the threshold of the $\bar{H}(1s)$ channel. 54
6.13 $\bar{H}^+$ production cross sections from positronium excited in a state n_p=3 as a function of antihydrogen impact energy. 55
6.14 Comparison between the different positronium states for reaction (2.6) when $\bar{H}$ is in the ground state, in the case of the uncorrelated Chandrasekhar wave function. 56
6.15 $\bar{H}^+$ production cross sections from Ps(*2p*) and the different n_h=4 states of antihydrogen. 57
6.16 Contributions of the different processes involved in the formation of $\bar{H}^+$ from Ps(*2p*) and $\bar{H}(4s)$. 58
6.17 $\bar{H}^+$ production cross sections from ground state positronium (n_p=1). Comparison between the three H^- wave functions investigated: (grey) dotted lines for UC , (blue) dash-dot lines for CC and (black) solid lines for LS. The upper lines correspond to ground state antihydrogen in the entrance channel and the lines below are for the *2s*-state of antihydrogen. 58
6.18 Same as for Figure 6.17 but for n_p=2. 59
6.19 Same as for Figure 6.17 but for n_p=3. 60
6.20 Comparison between the different positronium states for reaction 2.6 when $\bar{H}$ is in the ground state - the Le Sech wave function has been used for H^-. 61

7.1 CDW–FS (black) and CBA (teal) $\bar{H}$ production cross sections compared for ground state positronium. The dotted lines correspond to the formation of ground state antihydrogen only while the solid lines are the summed cross sections of antihydrogen production up to $\bar{H}(4f)$. 63
7.2 Same as for Figure 7.1 but for n_p=2. 64
7.3 Same as for Figure 7.1 but for n_p=3. 64
7.4 Comparison of the theoretical results for Ps(*1s*) in the entrance channel of the first reaction. The solid black line corresponds to the CDW-FS results taking into account the hydrogen states up to H(*5d*) whereas the grey dotted line is the CC estimation of the total hydrogen production from Mitroy & Ryzhikh [58], using the $\frac{1}{n^3}$ scaling for the states above H(*3d*). Our CBA results, summed over the states of hydrogen up to H(*5d*) are also included (teal dashed line). 66
7.5 Comparison of the CDW–FS (solid black line) and CBA (teal dashed line) results to the modified Faddeev results of Hu and Caballero [67] (grey dotted line), in the case of positronium in a state n_p=2 and antihydrogen in a state $n_h \leq 2$ (summed cross sections of Ps(*2s*) and Ps(*2p*) for the summed contributions of $\bar{H}(1s)$, ($2s$) and ($2p$)). 67

7.6 Comparison between the CDW–FS (solid black line), CBA (teal dashed line) and UBA [57] (grey dotted line) results of total hydrogen formation cross section when the positronium is excited into state 3D. The contributions of the hydrogen states have been summed up to n_4=4 and n_h=5 (except for CBA); this corresponds respectively to labels (4) and (5) in the figure. 68

7.7 The cross sections relative to the four body reaction for ground state (anti)hydrogen and ground state positronium computed with different models. The present CDW–FS calculations are represented by the black solid line labelled *LS* for the Le Sech wave function and the grey solid line with label *UC* for the uncorrelated Chandrasekhar wave function. For the other theoretical calculations, in figure 7.7a, a small *d* (for *direct*) in exponent indicates that the cross sections have been computed for the direct reaction of H^- production, while a small *r* means that the reverse reaction, that is the positronium production, was considered. The light red dashed line labelled CMEA^d is for the results of Roy and Sinha [74] and the pseudo-state approach results of McAlinden *et al.* [73] correspond to the light green dotted line labelled CC^r (shortened to CC in figure 7.7b); the dark green dotted line with label CC^d is the calculation at threshold done by Blackwood *et al.* [97]. The CBA results of Straton and Drachman [70] are the square scatter points: pink and labelled $Pr\mathrm{CBA}^r$ for the *prior* form, and crimson with label $Ps\mathrm{CBA}^r$ for the *post* form. By the same author, the orthogonalised Fock-Tani calculations in their *post* and *prior* forms are represented by left turned triangles respectively dark yellow with label $Ps\mathrm{CDO}^{(r)}$ and brown with label $Pr\mathrm{CDO}$; the *post* iso-orthogonalised results are the orange right turned triangles labelled $Ps\mathrm{CDIO}^r$. Finally, the close-coupling calculations of Biswas [72], both two channel and two channel model exchange, are the blue dash-dot lines labelled $\mathrm{2CH}^d$. . . . 69

7.8 $\bar{H}^+$ production cross sections from ground state antihydrogen and n_p=2 states of positronium computed with different models. The present CDW–FS calculations are represented by the black solid line labelled *LS* for the Le Sech wave function and the grey solid line with label *UC* for the uncorrelated Chandrasekhar wave function. The light red dashed line labelled CMEA is for the results of Roy and Sinha [74] and the pseudo-state approach results of McAlinden *et al.* [73] correspond to the green dotted line labelled CC^r. 70

7.9 Comparison between experimental data available concerning reactions 2.4 and 2.5, and the related CDW–FS and CBA results. The CDW–FS calculations are represented by the black solid line and CBA by the teal solid lines. 72

8.1 Comparison between the global $\bar{H}^+$ production cross sections, in the case of the UC wave function, when a fraction of the excited antihydrogen atoms had time to radiatively cascade down to ground state for the second reaction (solid curves) or not (dashed curves). Antihydrogen production up to $\bar{H}(4f)$ has been taken into account. The influence of positronium excitation is also demonstrated with either 100 % of Ps(*1s*) (black) or 30 % of Ps(*2p*) (red). 77

8.2 Comparison between the global $\bar{H}^+$ production cross sections, in the case of the Le Sech wave function, for different simple solutions of positronium excitation; it has been assumed that 20% of all the antihydrogen produced are in the ground state for the second reaction and that they are the only one to contribute to the $\bar{H}^+$ formation. Antihydrogen production up to $\bar{H}(5d)$ has been taken into account here. 78

9.1 Pulse observed on a Faraday cup after fast ejection of a 1.34 10^{10} electron plasma with the RIKEN trap. 86
9.2 Production of ground state ortho-positronium for three different FWHM of the positron pulse. 87
9.3 Evolution of the positronium 1S and 3D populations with time for several sets of parameters. 89
9.4 Shape of the monoenergetic antiproton pulses for two different values of the parameter `t_p`, corresponding to the FWHM, and different delays (`pdel`), chosen so that the maximum of each pulse occurs almost at the same time. 90
9.5 Antiproton pulse profiles after deceleration to: (a) 1 keV, (b) 2 keV and (c) 6 keV. 1000 antiprotons have been simulated (courtesy Pierre Dupré). 91
9.6 Antiproton time distributions after deceleration to: (a) 1 keV, (b) 2 keV and (c) 6 keV. The time distribution is given just before the reaction chamber and centred on the mean time of flight value. 92
9.7 The three different geometries (not at scale) of the envisaged reaction chambers, with typical size parameters and number of positronium atoms. 94

10.1 Evolution of the $\bar{H}^+$ production with the length (from 10 to 80 mm) and section (between 0.8 and 2 mm^2) of the positronium cell at 6 keV. In the present case, only ground state positronium is used. 96
10.2 Variations in the production of antihydrogen ion for three different values of the positron pulse delay, and with (label 1S+3D) or without (label 1S) positronium excitation to state 3D. The dimensions of the reaction chamber are 1 mm^2 by 20 mm. 96
10.3 The $\bar{H}^+$ production as a function of the laser pulse FWHM for `xi`= 9, 16, 36 and 144; the laser delay has not been changed and is 75 ns. 97
10.4 Similarly to figure 10.3, the dependence in `t_limp` is investigated, but this time, `xi` is set to 36 and several delays of the laser pulse are investigated. 97
10.5 The Ps(*3d*) population evolution with time for several values of the laser width. This values of `t_limp` have been chosen close to local maxima (plain lines) and minima (dotted lines) observed in figure 10.3 for `xi`=144. 98
10.6 The Ps(*3d*) population has been integrated over the simulation time, while the laser width is varied, for `xi`=36 and 144. This reveals that the modulations of the $\bar{H}^+$ production observed in figure 10.3 are related to the number of excited positronium available. 98
10.7 $\bar{H}^+$ production dependence with the antiproton energy around 6 keV. The square symbols are for a laser beam in the axis of the reaction chamber while the crosses are for the laser entering perpendicularly in the reaction chamber. In reddish colours, one laser pulse of 20 ns width has been used while green colours are for two pulses of 20 ns separated by 40 ns. 99
10.8 Evolution of the $\bar{H}^+$ yield with the delay of the antiproton pulse, for three values of `t_p`; so far, we had been working with a 200 ns wide pulse of antiprotons, indicated by the dashed line. 99
10.9 Evolution of the $\bar{H}^+$ production with the length (`scell`) and section (`acell`) of the positronium cell at 1 keV, with laser excitation of the positronium to the state 3D. 102

10.10Variations of the $\bar{H}^+$ production with the delay of the 410 nm laser; the square signs are for laser excitation on the axis of the reaction chamber (thus parallel to the antiproton beam) and the "+" signs for excitation from the side of the positronium cell. Two sets of data are displayed corresponding to two different laser widths: 20 and 50 ns. The 20 ns points for the two laser orientations are merged. 103
10.11The general dependence of the $\bar{H}^+$ yield with the energy of the antiprotons. . . . 104
10.12The evolution of the antihydrogen production when the delay of the antiproton is varied, for different values of the $\bar{p}$ pulse width. 104
10.13The fluorescence signal (a) and annihilation spectrum (b) simulated for an intense (`xi`=400) 10 ns laser pulse, used 120 ns after the beginning of positronium formation. In the annihilation spectrum, the red curves correspond to ortho-positronium annihilation only while the dark red curves take into account the background formed by the prompt annihilation of the positrons and of the para-positronium; the dotted lines indicate what the signals would look like without laser excitation. 109
10.14Same as figure 10.13 but for an intense (`xi`=100) 50 ns laser pulse sent after of greater delay (`ldel`=180 ns). 109
10.15Same as figure 10.13 but for a less intense laser pulse with `xi`=42, 20 ns FWHM, delayed by 120 ns with respect to the positronium production. 110
10.16The positron to positronium converter enclosed in a tube tested by P. Crivelli, with the silicon nitride window for the positron implantation. 112
10.17Repartition of the hydrogen population between the excited states at 1 keV; this is a picture of the hydrogen pulse content right at the exit of the interaction region.115

12.1 A schematic representation of the laser system. 124
12.2 Schematic drawing of the CW Ti:Sa laser cavity showing, in particular, the disposition of the mirrors and the optical elements for the tuning of the wavelength. 125
12.3 Picture of the CW Ti:Sa laser cavity, running. 126
12.4 Design study of the oscillator. 127
12.5 Up: picture of the oscillator cavity. Down: annotated picture identifying the elements of the oscillator and indicating the different beam paths. 129
12.6 Schematic drawing of the light amplification stage; the scale indicated gives a general idea of space occupied by this amplifier on the laser table (the Ti:Sa crystal is not at scale). 130
12.7 The cavity modes of the oscillator as observed at the scope; one can see the transverse modes on the left of the main peaks, the latter ones corresponding to the longitudinal modes TEM00; the first transverse mode is probably a TEM10, due to the non-perfect mode matching, either in size or curvature, of the incoming beam. 131
12.8 Illustration of the intensity modulation depending on the small voltage modulation applied on a piezoelectric translator. 135
12.9 Wavelength of the CW Ti:Sa recorded for 12 min; here, as in all the following figures, the statistical values are given in THz. 136
12.10First laser pulse recorded at 820 nm, with a FWHM of 18 ns. 138

12.11A 9 ns pulse at 820 nm (label 1) and a pulse obtained when there is no CW laser beam to seed the oscillator cavity (label 2): in the latter case, the stimulated emission is further delayed with respect to the 532 nm pump pulse (first pulse on the left). 138
12.12Measurement, with the first WS-7, of the frequency of the CW Ti:Sa laser locked on the very same lambda-metre. 140
12.13Frequency measurement, with the second WS-7, of the CW Ti:Sa laser locked on the first lambda-metre. 140
12.14Measurement, with the second WS-7, of the frequency of the pulsed Ti:Sa laser which is locked on the CW Ti:Sa laser. 141
12.15Visualisation of the frequency chirp between the pulsed Ti:Sa laser (first measured, on the left) and the CW Ti:Sa laser (second to be measured, on the right). . . . 141

13.1 Optical transition between the 6S and 8S levels of caesium. We remind that F is the total angular momentum including the nuclear spin. The values of the different wavelengths indicated are: $\lambda_1 = 822.459$ nm, $\lambda_2 = 822.468$ nm (both frequencies measured at a 0.1 MHz precision by Hagel *et al.* [120]), $\lambda_3 = 459.3$ nm and $\lambda_4 = 455.5$ nm. The 6S-8S two-photon transition that we use is for F = 4, at 822.468 nm (364.508030 THz) and we detect the fluorescence at 456 nm. 144
13.2 A simple drawing of the positronium chamber designed for the Saclay experiment; in the chosen point of view, the positron trap is situated behind. 145
13.3 The specially realised caesium cell with its narrow section of 4 mm diameter. . . 146
13.4 A schematic representation of the set-up used to estimate the efficiency of a bundle of optical fibres for the fluorescence light collection; the use of the lambdameter is indicated for the monitoring of the laser excitation frequency. 147
13.5 The Cs fluorescence signal (violet pulses) detected when the frequency of the CW Ti:Sa laser is swept (the voltage ramp on PZT-1 is shown in red). 148
13.6 The 3D visualisation of the GBAR zone including the laser hut. 149
13.7 The laser hut built in the GBAR zone (the positron trap can be seen on the left); picture taken during the installation of the air conditioning unit. 150

14.1 The laser system currently running at LKB. 154

List of Tables

5.1 Convergence of the H^- partial wave expansion. 38

9.1 Theoretical values of the H^- photodetachment cross sections at 243 and 410 nm from [101] and [102] (only at 410 nm for the latter). The experimental data are available above 426 nm. 85

10.1 Examples of best $\bar{H}^+$ yield and corresponding optimal parameters obtained for an antiproton deceleration simulated at 6 keV. 101

10.2 Number of $\bar{H}^+$ expected per mono-energetic antiproton pulse at 1 keV, for several configurations of laser excitation; parameters other than the laser pulse width have been optimised. 105

10.3 Number of $\bar{H}^+$ expected per mono-energetic antiproton pulse at 6 keV, for the same laser excitation configurations as the ones used in table 10.2. 105

10.4 Examples of best $\bar{H}^+$ yield and corresponding optimal parameters obtained for an antiproton deceleration simulated at 1 keV. 107

10.5 Total number of hydrogen atoms obtained for 1000 protons, simulated with the same characteristics as the antiproton pulse from ELENA, for several sets of parameters; the delays have been optimised. Here the protons have been decelerated to 6 keV and injected in a tube of 4 mm^2 aperture by 6 mm length. 113

10.6 Same as table 10.5 with 6 keV protons, but the tube is now 8 mm long. 113

10.7 Same as table 10.5 with 6 keV protons, but a larger SiNi window has been used, thus the aperture of the tube is now 3 mm $\times$ 2 mm; its length is either set to 6 or 8 mm. 113

10.8 Same as table 10.5 but this time with 1 keV protons; only the smallest (4 $mm^2 \times 6$ mm) and the largest (6 $mm^2 \times 8$ mm) tube dimensions have been considered here. . . 114

10.9 Same as table 10.8 but with protons decelerated to 2 keV. 114

10.10 Number of hydrogen atoms (up to H($5d$) included) predicted when only ground state positronium is used (formed out of 10^8 accumulated positrons and $3{\cdot}10^6$ protons); the delay of the proton pulse has been optimised. 116

B.1 Thresholds values for the 3-body reaction of antihydrogen production: T_{CM} in the centre of mass and T_{3B} for the antiproton energy in the laboratory frame. . . 172

B.2 Thresholds values for the 4-body reaction of antihydrogen plus production: T_{CM} in the centre of mass and T_{4B} for the antihydrogen energy in the laboratory frame. 173

B.3 Break-up energy values for the 3-body reaction: T_{CM}^{break} in the centre of mass and T_{3B}^{break} for the antiproton energy in the laboratory frame. 173

B.4 Break-up energy values corresponding to the break-up channel B.12: $T_{CM}^{break,1}$ is the value in the centre of mass and $T_{4B}^{break,1}$ for the antihydrogen energy in the laboratory frame. 174
B.5 Break-up energy values corresponding to the break-up channel B.13: $T_{CM}^{break,2}$ is the value in the centre of mass and $T_{4B}^{break,2}$ for the antihydrogen energy in the laboratory frame. 174
B.6 Break-up energy values corresponding to the break-up channel B.14: $T_{CM}^{break,3}$ is the value in the centre of mass and $T_{4B}^{break,3}$ for the antihydrogen energy in the laboratory frame. 175